# Investigation of Transition Metal Based Magnetic Nanostructures and Their Applications in Storage Devices

*A thesis submitted for the award of the degree of*

**Doctor of Philosophy**

*in*

**Physics (Experimental)**

*by*

**Ashutosh Kumar Singh**

**July 2015**

Department of Physics

**University of Calcutta**

Kolkata, India

*Dedicated to my beloved parents…*

# Acknowledgements

In full gratitude, I would like to acknowledge the following individuals who encouraged, inspired, supported, assisted, and sacrificed themselves to help my pursuit of a higher education degree.

First of all, I would like to express my special appreciation and thanks to my PhD supervisor *Professor Dr. Kalyan Mandal*, he has been a tremendous mentor for me. I must thank him for encouraging my research and for allowing me to do my research with full freedom. His valuable guidance and discussion always gives me a new angle to tackle the hurdles in my research problems. He has been provided me tremendous academic support and so many wonderful opportunities.

I am grateful to *S.N. Bose National Centre for Basic Sciences* for providing me all research facilities and healthy research environment since I joined this research centre as a research scholar.

I would like to express my deepest gratitude and thanks to *Dr. Gobinda Gopal Khan* and *Dr. Debasish Sarkar*, DST Inspire Faculty at CRNN- University of Calcutta and IISc.-Bangalore, respectively, for their encouraging and humble guidance as collaborator, friend and elder brothers. Their innovative ideas and valuable discussions always motivated me to dig deeper into my research problem. We together have melted many tough research problems on the rocks.

I am grateful to all my school and college teachers who motivated me to choose research as a career. I feel myself blessed to have their true and unconditional guidance. I am also grateful to my college friend *Chandan Mishra* for his moral support since I met him.

I am really thankful to my lab mates *Madhuri Di, Bipul, Arka, Shyam, Debasish, Rajashree, Arup, Monalisa, Rupali, Mahebub, Keshab, Souvanik, Indranil*. It is my pleasure to have such a cooperative lab mates who provided me a wonderful research environment. Specially, one of my best friend Arup, I must thank him for

listening my problem, offering me advice and standing by my side in difficult situations. I wish every research scholar could have a friend like him during their PhD life.

I must thank to my SNB seniors outside my lab *Prashant, Kapil, Amartya, Rajiv, Abhinav, Rudra, Surajit* and many more. I enjoyed a wonderful time with them. I am also thankful to my *PBIR-2009* batch mates. I have shared joyful times with them during my *M.Sc.* days.

I am thankful to my SNB friends *Ravi, Vibhuti, Neha, Juriti, Ransell, Poonam, Shaili, Neeraj, Ankan, Balwant, Avinash, Ritam* and many more. I am really thankful to God for having such a wonderful people in my friend circle during my PhD life. These people really made me feel that PhD life is not that boring.

I must thank *Shakti, Surojit, Samik, Dipankar, Amit and Urmi* for their technical assistance in the material characterization during PhD work at *S. N. Bose National Centre for Basic Sciences*. Without their support, encouragement, and dedication to assist me, this dissertation would not have been possible.

A special thanks to my family. Words cannot express how grateful I am to *my mother and father* for all of the sacrifices that they have made on my behalf. Their prayer for me was what sustained me thus far. They are the most important people for me in this world and I dedicate this thesis to them. I am very fortunate to have my elder brother *Sandeep*, my sister-in-law *Sumi*, my sweet niece *Manya* and my uncle *Chandrama* who supported me in writing, and encouraged me to strive towards my goal. At the end, but by no means least, I am really thankful to my dearest one *Anshu* who has always my support in the moments when there was no one to answer my queries.

_____

**Ashutosh Kumar Singh**

# List of publications related to thesis work


[1] **A. K. Singh**, D. Sarkar, G. G. Khan and K. Mandal, "Unique Hydrogenated Ni-NiO Core-Shell 1D Nano-heterostructures With Superior Electrochemical Performance as Supercapacitor", ***Journal of Materials Chemistry A***, *1*, 12759 (2013).

[2] G. G. Khan, **A. K. Singh**, and K. Mandal, "Structure dependent Photo-luminescence of nanoporous amorphous AAO membranes: Role of $F^+$ center defects", ***Journal of Luminescence***, *134*, 772 (2013).

[3] **A. K. Singh** and K. Mandal, "Effect of aspect ratio and temperature on magnetic properties of permalloy nanowires", ***Journal of Nanoscience and Nanotechnology***, *7*, 5036 (2014).

[4] **A. K. Singh**, D. Sarkar, G. G. Khan and K. Mandal, "Designing one dimensional Co-Ni/$Co_3O_4$-NiO core/shell nano-heterostructure electrodes for high-performance pseudocapacitor", ***Applied Physics Letter***, *104*, 133904 (2014).

[5] **A. K. Singh**, B. Das, P. Sen, S. K. Bandopadhyay and K. Mandal, "Effect of alpha-particle irradiation on magnetic properties of Ni nanowires", ***IEEE Transactions on Magnetics***, *50(11)*, 2302104 (2014).

[6] **A. K. Singh**, D. Sarkar, G. G. Khan and K. Mandal, "Hydrogenated NiO Nanoblocks Architecture for High Performance Pseudocapacitor", ***ACS Applied Materials & Interfaces***, *6*, 4648 (2014).

[7] **A. K. Singh** and K. Mandal, "Engineering of High Performance Supercapacitor Electrode based on Fe-Ni/$Fe_2O_3$-NiO Core/Shell Hybrid Nanostructures", ***Journal of Applied Physics***, *117*, 105101 (2015).

[8] **A. K. Singh**, G.G. Khan, B. Das and K. Mandal, "Growth and Magnetic characterization of 1D Permalloy nanowires using self-developed anodic aluminium oxide templates", ***IOP Conf. Series: Materials Science and Engineering***, *73*, 012125 (2015).

[9] **A. K. Singh** and K. Mandal, "High performance supercapacitor electrodes based on metal/metal-oxide core/shell nano-heterostructures", ***AIP Conference Proceedings,*** *1665*, 050003 (2015).

[10] **A. K. Singh**, D. Sarkar, G. G. Khan and K. Mandal, "High performance supercapacitor electrode based on porous $Co_3O_4$-$MnO_2$-NiO ternary hybrid nanotubes", 2015 (**Communicated**).

[11] **A. K. Singh** and K. Mandal, "Study of aspect ratio and temperature dependent magnetic properties of CoNi alloy nanotube arrays", 2015 (**Communicated**).

# List of publications apart from thesis work

[1] A. Sarkar, **A. K. Singh**, G. G. Khan, D. Sarkar and K. Mandal, "TiO2/ZnO core/shell nano-heterostructure arrays as photo-electrodes with enhanced visible light photoelectrochemical performance", ***RSC Advances***, *4*, 55629 (2014).

[2] M. Pal, **A. K. Singh**, R. Rakshit and K. Mandal, "Surafec chemistry modulated introduction of multifunctionality within $Co_3O_4$ nanocubes", ***RSC Advances***, *5*, 16311 (2015).

[3] D. Sarkar, G. G. Khan, **A. K. Singh** and K. Mandal, "High Performance Pseudocapacitor Electrodes Based on $Fe_2O_3$/$MnO_2$ Core–Shell Nanowire Heterostructure Arrays", ***Journal of Physical Chemistry C***, *117*, 15523 (2013).

[4] G. G. Khan, D. Sarkar, **A. K. Singh** and K. Mandal, "Enhanced band gap emission and ferromagnetism of Au nanoparticle decorated α-$Fe_2O_3$ nanowires due to surface plasmon and interfacial effects", ***RSC Advances***, *3*, 1722 (2013).

[5] D. Sarkar, G. G. Khan, **A. K. Singh** and K. Mandal, "Enhanced electrical, optical and magnetic properties in multifunctional ZnO/α-$Fe_2O_3$ semiconductor nanoheterostructures by heterojunction engineering", ***Journal of Physical Chemistry C***, *116*, 23540 (2012).

# List of attended conferences

**International:**

[1] European Material Research Society –Spring 2015 Meeting- Grand Palace-Lille, France, 11-15 May 2015.

[2] International Conference on Nanoscience and Nanotechnology– INST Mohali, Chandigarh, 3-5 March 2014.

[3] International Conference on Material Sciences and Technology– St. Thomas College, Kottayam, Kerala 10-14 June 2012.

[4] International conference on Advance Functional Materials S.N. Bose National Centre for Basic Sciences, India- 1-2 March 2012.

[5] International Conference on Nanomaterials & Nanotechnology -University of Delhi, 18-21 Dec 2011.

[6] Workshop on advanced magnetic measurement techniques- OIST, Okinawa-Japan, 10-14 July 2012.

[7] Workshop on materials for energy storage device fabrication-Forschungszentrum, Juelich- Germany, 1-7 March 2013.

**National:**

[1] DAE-Solid State Physics Symposium-VIT- Vellore, India, 16-20, Dec 2014.

[2] Nano Days -2015, S.N. Bose National Centre for Basic Sciences, India- 16-18 Feb 2015.

[3] National Workshop on Application of Radiation in Physical, Chemical & Life Sciences –UGC- DAE, Kolkata Centre & CRNN- University of Calcutta, 4-6 September 2013.

[4] Conference on Magnetic Material and Applications-– S.N. Bose National Centre for Basic Sciences, Kolkata- India, 24-25 Jan 2011.

# CONTENTS

# Chapter 1 | Introduction

This introductory chapter consists of the detailed literature review of various works that motivated me to work in this specific field and also a brief outline of the entire work done by me.

## 1.1. Transition Metals

The transition metals have great importance in our lives. They are building blocks for life and are found directly in the center (d-block) of the periodic table. The d-block simply means that the element's d-orbitals are the last to get occupied, according to the building-up principle. The transition metals give off electrons from their outer s-orbital, but most can lose a multiple number of d-orbital electrons. Because of this many of the d-block metals have multiple oxidation numbers. The transition elements are both ductile and malleable, and conduct electricity and heat. Anything that needs electricity has metal components because of their electrical conductivity. Metals have another great characteristic, they easily mix. This is because all the d-block metals have about the same atomic size. This allows them to replace one another easily in a crystal lattice. When two or more metals mix, or replace one another, we call the new metal an alloy. These elements and alloys are fundamental for the existence of life, and also for its progression through time. The transition metals, and some of its key alloys, shaped the Bronze Age, Iron Age, and most importantly the steel age. Transition metals are in top demand because of their tremendous technological application. There are three noteworthy elements in the transition metals family. These elements are iron, cobalt, and nickel, and they are the only elements known to produce a magnetic effect called ferromagnetism and are used for permanent magnets and magnetic storage devices. With ferromagnetism, the unpaired electrons have aligned spins forming domains that survive even after the applied field is turned off. For this reason, ferromagnetic materials are used in coating cassette tapes, computer disks, and other devices that use magnetic codes and signals [1, 2]. In addition, transition metal based oxides such as NiO, $Co_3O_4$, $Fe_2O_3$, etc. have gained tremendous application towards the development of clean and sustainable energy. Transforming natural energy, such as wind, tide, and solar energies can generate large amounts of clean and sustainable energy. The development of efficient energy storage devices is extremely important to store the harvested energy for wide applications [3, 4].

## 1.2. Nanostructures

Interest in nanotechnology is growing rapidly. Nanostructured materials may be defined as those materials whose structural element clusters, crystallites or molecules—have dimensions in the 1 to 100 nm range. Now it is possible to arrange atoms into structures that are only a few nanometers in size. The explosion in both academic and industrial interests in these materials over the past decade arises from the remarkable variations in fundamental electrical, optical, electrochemical and magnetic properties that occur as one progresses from an 'infinitely extended' solid to a particle of material consisting of a countable number of atoms. Reduction of the size introduces physical and chemical constraints along one or more dimensions of the nanostructured materials leading to some novel, even completely new properties in these materials in comparison to their bulk counterpart. These novel properties arise in these functional nanomaterials when their size becomes comparable to or less than a certain characteristic length scales such as carrier mean free path, superconducting coherence length, magnetic domain wall width, spin diffusion length etc. [5]. Due to the complex design of the nanostructures and also the interplay between the constituent materials, they exhibit various properties depending on their size, shape and morphology. It has been found that materials having building blocks with the same composition but different morphology can have different properties [6, 7]. Magnetic behaviour, chemical reactivity, colour, electronic excitation, charge transport, etc. of metal have been found to be influenced significantly by their size. With the reduction of the size it has been observed that metals show non-metallic band gaps and thus showing electronic absorption spectra, clusters of non-magnetic materials show magnetic ordering, hence leading to giant magnetoresistance, enhanced coercivity and remanance and other properties of magnetic materials. These novel properties of the functional materials can also be tailored by manipulating self-assembly and self-organizing techniques of their nanoscale building blocks to produce a self-sustaining well-defined nanostructure [5]. Not only the fabrication of nanostructures of different functional materials is

important, their characterization is much more challenging. It is very important to fabricate the arrays of ultrafine nanostructures over macroscopic areas; i.e. ordered arrays of nanostructures is much more needed because one can then probe the individual and collective behaviour of the nanomaterials in a well-defined and reproducible fashion.

## 1.3. One-dimensional (1-D) Nanostructures

Recently, one-dimensional (1-D) nanostructures such as nanowires, nanorods, nanobelts, and nanotubes have become the focus of intensive research owing to their unique application in the mesoscopic physics and fabrication of nanoscale devices [8], it is generally accepted that 1D nanostructures provide a good system to investigate the dependence of electrical, magnetic and mechanical etc. properties on dimensionality and size reduction (or quantum confinement). They are also expected to play an important role as both interconnects and functional units in fabricating electronics, magnetic, optoelectronics and electrochemical devices with nanoscale dimensions. In comparison with quantum well and dots, the advancement of 1D nanostructures have been slow until very recently, as hindered by the difficulties associated with the synthesis and fabrication of these nanostructures with well-controlled dimension, morphology, phase purity and chemical composition. Although 1D nanostructures can now be fabricated using a number of advanced nanolithography techniques [9], such as electron-beam or focused ion beam writing, X-ray or UV lithography, further development of these techniques into practical routes to large quantities of 1D nanostructures from a diversified range of materials, rapidly, and at reasonably low costs, still requires great ingenuity. In contrast, unconventional methods based on chemical synthesis might provide an alternative and intriguing strategies for generating 1D nanostructures in terms of material diversity, cost, and the potential for high volume production [10]. In 1995, Masuda and Fukuda in Japan developed highly ordered nanoporous alumina membranes via electrochemical anodization of aluminum. Since the time, highly ordered porous alumina membranes have attracted many international groups as a template

material for the synthesis of magnetic nanowires [11]. Among the various methods for preparing 1D nanostructures, template assisted electrodeposition is widely used because of its simplicity and low cost.

### 1.3.1. One dimensional (1-D) nanostructures for magnetic storage application

High aspect-ratio magnetic nanomaterials, especially magnetic nanowires (NWs) arrays have generated growing interest in the scientific community due to their potential applications in magnetic sensors, high-density magnetic recording [12-16]. The magnetic nanowires possess unique properties which are quite different from those of their thin film, nanoparticle, and nanotube counterparts. The magnetic nanowires possess quasi-one dimensional (1D) anisotropic structures along the wire axis, resulting in their anisotropic magnetic properties. The magnetic properties of the nanowires are governed by several material parameters, such as diameter, length, and composition. It has been reported that the coercivity (*Hc*), remanent magnetization (*Mr*), and saturation magnetization (*Ms*) are dependent on the direction of an externally applied field. There have been numerous reports on electrodeposited Co, Ni, and Fe nanowires and their alloys with large crystalline anisotropies [17-21]. Wire shaped ferromagnetic materials that have been researched since the last century and are also at the center of attraction of today's research in material science such as: *nanowires* (NWs). The NWs have diameters typically order of 100 nm and their length could be several micrometers. The main interest in the research on ferromagnetic NWs is due to their potential applications in recording media[10-12] and spintronics systems [22-25]. In case of magnetic storage media, the magnetization of a single NW treated as a single bit of data which is either '0' or '1' depending upon the direction of magnetization which may be 'up' or 'down' respectively. Propagation of domain walls along the NWs by sending spin polarized current pulse current pulse or applying a magnetic field is the basic concept of spintronics. Permalloy NWs show large anisotropic magnetoresistance and hence easy to probe in the investigation of domain wall dynamics in the NWs make them

important for spintronics applications. The arrays of NWs show unique magnetic behavior depending upon NWs diameter, length, and material of the NWs and on inter NW separation. Highly ordered arrays of NWs as can be used as data storage media in perpendicular magnetic recording systems. The NWs are polycrystalline or single crystalline and made of ferromagnetic metals and their alloys. Magnetic nanowires can be prepared by various methods, such as E-beam lithography, chemical routes, electrochemical deposition etc. [26]. Among which, the electrochemical deposition is proved to be the modest, simplest and cost effective synthesis procedure. In this process, a porous diamagnetic membrane (few microns thick) is used to deposit metal NWs within the pores (diameter ~ few nanometers) of the membrane electrochemically. The membranes that are generally used for the purpose can be made of alumina or polycarbonate. The NWs have the same diameter as nano pores and are uniform in length throughout the membranes.

### 1.3.2. One dimensional (1-D) nano-heterostructures for electrochemical energy storage applications.

One-dimensional (1D) heterostructured nanomaterials have been of great scientific and technological interests due to their high versatility and applicability as essential components in energy conversion, storage devices [27-29]. Currently, tremendous efforts have been devoted to the rational synthesis of advanced core/shell nanowire heterostructures with fascinating synergistic properties or multifunctionalities offered by the composite nanostructures. Various core/ shell nanowire heterostructures such as metal/metal oxide, metal/metal and metal oxide/metal oxide have been explored, and enhanced properties have been demonstrated [30-34]. The heterostructured nanowire architecture can make use of the advantages of both components and offer special properties through a reinforcement or modification of each other. Transition metal oxides such as $Co_3O_4$, NiO, $Fe_2O_3$ and ZnO are technologically important materials for applications in electrochemical energy storage devices such as supercapacitors and lithium-ion batteries. To meet these applications, it is desirable to integrate these oxides into

core/ shell nanowire arrays to achieve enhanced electrical, electrochemical, and mechanical properties. The fabrication of core/shell nanowire arrays with well-defined morphologies and tunable functions still remains a challenge. Progress has been achieved in developing cost-effective and simple methods for controlling nanowire growth as well as creating more complex heterostructures. Core/ shell nanowire arrays are generally grown by the catalyst-assisted vapor, liquid, solid mechanism and template-based approaches. However, there is still no simple and high-efficiency method to synthesize transition metal oxide or hydroxide core/ shell nanostructure arrays with precise structure control, even though a few successful strategies (electrodeposition, oxidation, wet-chemical methods based on sacrificial templates, and physical technique such as sputtering and pulsed laser deposition) have been reported [33, 34].

# 1.4. Magnetic Properties

## 1.4.1. Magnetic Anisotropy Energy

Magnetic anisotropy is the dependence of magnetic energy on the relative orientation of the magnetization direction to the crystal axis. The associated energy is called the anisotropy energy. In a material, the magnetic anisotropy may arise due to the symmetry of the crystalline lattice or due to the specific shape of that particular piece of material. In the absence of any external magnetic field, there is an energetically favorable direction of spontaneous magnetization, called the easy axis of that particular material that can be determined by sources of various magnetic anisotropy energies as given below.

### 1.4.1.1. Magnetocrystalline Anisotropy

Magnetocrystalline anisotropy is the most prominent contribution to the magnetic anisotropy which arises due to the symmetry axis of the local atomic structure. It arises because of spin-orbit coupling which is the exchange interaction via spin-spin coupling between neighboring spins. This strong spin-orbit coupling

keeps the neighboring spins to be parallel or anti-parallel to each other. However, the associated energy is isotropic and therefore the coupling cannot contribute to the crystal anisotropy. The magnitude of this magnetocrystalline anisotropy depends on the ratio of the crystal field energy and spin orbit coupling [35]. There are two models to describe the magnetic anisotropy; (a) Néel model which says that the magnetic anisotropy arises due to pair interactions between two essentially magnetic ions [36] and (b) Single-ion or crystal field model which describes crystal field interactions with atoms that are not essentially magnetic [37]. As the magnetocrystalline energy is associated with the relative orientation of the total magnetization with respect to the magnetic easy axis of the crystal, i.e. $\theta$, the magnetocrystalline anisotropy energy can be expressed as,

$$E_k = V(K_0 + K_1 \sin^2\theta + K_2 \sin^4\theta) \qquad (1.1)$$

Where, $K_n$ ($n$= 0, 1, 2…) are the magnetocrystalline anisotropy constants. $K_0$ is $\theta$ independent, arbitrary and thus an irrelevant parameter.

The dependence of the magnetic properties in the direction of the applied field with respect to the crystal lattice represents the magnetocrystalline anisotropy. It turns out that depending on the orientation of the field with respect to the crystal lattice one would need a lower or a higher magnetic field to reach the saturation magnetization. *Easy axis* is the direction inside a crystal, along which small applied magnetic field is sufficient to reach the saturation magnetization. *Hard axis* is the direction inside a crystal, along which large applied magnetic field is needed to reach the saturation magnetization.

#### 1.4.1.2. Shape Anisotropy

In case of polycrystalline material with no preferred direction of its grains, has no overall crystalline anisotropy. If the material is perfectly spherical in shape, then the external applied field will magnetize it in every possible direction in the same extent. However, if the material is not spherical but having a preferred growth

direction, then it is easy to magnetize it along the long axis than along the short one. This type of crystalline anisotropy is known as shape anisotropy.

#### 1.4.1.3. Magneto-elastic Anisotropy

Strain in a ferromagnet changes the magnetocrystalline anisotropy and may thereby alter the direction of the magnetization. This effect is the 'inverse' of magnetostriction, the phenomenon that the sample dimensions change if the direction of the magnetization is Altered. The energy per unit volume associated with this effect can, for an elastically isotropic medium with isotropic magnetostriction, be written as : $E_{me} = -k_{me}\cos^2\theta$, where $k_{me} = -(3/2)\lambda\sigma$, Here $\sigma$ is the stress which is related to the strain, $\varepsilon$, via the elastic modulus $E$ E by $\sigma = E\varepsilon$. The magnetostriction constant $\lambda$ depends on the orientation and can be positive or negative. The angle $\theta$ measures the direction of the magnetization relative to the direction of uniform stress. If the strain in the film is non-zero, the magneto-elastic coupling contributes in principle to the effective anisotropy.

### 1.4.2. Magnetic Domain

Magnetic domains are the regions within a magnetic material that have distinct magnetization directions where all the magnetic spins are parallel to each other. The domains are separated by boundaries where the spins slowly rotate from one particular direction to other (i.e. The transition from one domain to another) and are called domain wall. The dimension of a typical domain is of the order of 10 nm and the domain walls have the typical dimension of few atomic layers to several nanometers. In a ferromagnetic material, the domains are formed due to the ferromagnetic exchange interaction and the anisotropy energy of the materials. The positive exchange interaction, which is an inherent characteristic of all the ferromagnetic materials, tries to orient the neighboring spins parallel to each other within a domain. Whereas, the anisotropy energy, that may originate due to the peculiar shape, stress or crystalline structure of the material, try to orient the neighboring spins along the anisotropic direction within the domain. Shape

anisotropy originates from the asymmetry in shape of a magnetic material. The demagnetizing field due to the free magnetic charges on the surface of the material is found to be different in different directions of the material. Whereas, different interaction of orbital and spin magnetic moment along different direction of a particular crystal lattice generates the magnetocrystalline anisotropy within a material. Thus, within a ferromagnetic material, the exchange interaction and the anisotropy field compete with each other and form a peculiar domain and domain wall distribution within a particular magnetic material. Ideally NWs have uniaxial anisotropy with a preferential magnetization direction along the axis of the NW. The anisotropy originates from the self-demagnetizing field due to their cylindrical shaped structure and depends on the aspect ratio (length/diameter) of the NWs. Other anisotropies also present in the NWs. The magnetic spins near the surfaces of NWs realize less coordination numbers than the spins in the inner portions of the NWs. Thus, due to the large surface to volume ratio in NWs compared to bulk systems, the anisotropy corresponds to surface energy has a significant contribution to the magnetic free energy of the NWs. The controlled synthesis of the NWs promotes crystallinity in the NWs and single crystal NWs can easily be obtained. Hence the magnetocrystalline anisotropy can have significant role depending on the crystal structure of the NWs. The domain size is comparable to the sizes of the NWs and the interplay among the exchange interaction and various anisotropies within the NWs gives unique spin distributions to them. Their remanent states have been calculated using micromagnetic framework by various researchers [38-45].

### 1.4.3. Magnetostatic Interaction Field

Electrodeposition technique of synthesizing NWs in porous membranes produces arrays of NWs. That means, millions of NWs are arranged in a hexagonal or squared mesh or random. Here it is obvious, if the NWs are closely spaced, they should interact with each other magnetostatically. If the NW is assumed as a single magnetic dipole then the simplest form of the magnetostatic interaction is the dipolar interaction. But, the dipole assumption of individual NWs and dipolar

approximation does not hold when the length of the NWs are many orders of magnitude longer than their diameters and inter-wire spacing [46-48]. In the ideal case the dipoles should have low aspect ratios and should be infinitely far away from each other [46]. Using the assumption, it was shown earlier in 1998 that the dipolar magnetostatic interaction between nanodots in array changes the magnetization process compared to the one of a single neighbor [49]. Later in 2000s, the dipolar approximation extensively used for explaining the magnetic properties of arrays of NWs even when their lengths are comparable to the NW diameter and interwire spacings [50, 51]. The studies established that, the dipolar interaction among the NWs play the dominating role in determining the magnetic properties of arrays of NWs which are significantly different from the individual NWs. But, it may not true if the NWs are closely spaced and very long compared to their diameters. However, at the same time, other approaches also made by other researchers. M. Vazquez at. Al. (2000) works on a model, which divides a NW into thousands of cubic cells, each of which contains a point dipole parallel to each other and then consider the dipolar interaction between the nearest neighbor inter-wire point dipoles [47]. This approach was more realistic approach compared to the dipolar interaction considering the NWs as dipoles as described earlier. The nature of magnetostatic interaction is difficult to simulate when the pores are randomly distributed in the membranes, but possible considering the average inter-wire distance [47]. The other way to calculate the magnetostatic interaction field was introduced by Clime et al (2006) where the field produced by a single NW was calculated and then for the whole array on a particular test NW was calculated [48]. In this regard, the whole array can be divided into two regions. One is the nearest neighbor discrete distribution of the NWs. For longer NWs, it was seen that the field produced by it and hence the interaction with other NWs is more concentrated at the ends of the NWs, breaking its dipolar approximation. Beyond the discrete region, the NWs can be considered as continuously distributed and their effect, the same as that of a thin film. This mean field approach is more realistic to calculate the interaction at saturation taking both dipolar and non-dipolar interaction among the NWs

depending on its length. It shows an increase in the axial saturation field of the NWs with the length dominated by the axial interaction between the NWs whereas, the transverse saturation field decreases upon increasing the length of NWs. The field acted on a particular NW by the others, opposes (antiferromagnetic-"AFM" coupling) and supports (ferromagnetic-"FM" coupling) the magnetization along the axial and transverse direction respectively. The interaction field strength along the transverse direction is half of the axial direction.

### 1.4.4. Saturation Magnetization

Saturation magnetization ($M_s$) is the maximum possible magnetization of a magnetic material under a large external field. Assuming each atom has the same magnetic moment; $M_s$ is dependent on the magnitude of the atomic moment ($\mu$) and also the density of atoms ($n$). $M_s$ of nanomaterials is found to be affected significantly by their size and their synthesis procedure as there is a large fraction of superficial ions in nanomaterials. As we move from bulk to nanoscale, $M_s$ decreases, which may be due to different reasons. According to Gangopadhay et al. [52] this reduction in $M_s$ is due to the formation of a disordered nonmagnetic shell layer over the magnetically aligned core in nanomaterials. According to other models this reduction in magnetization was due to surface spin canting. A similar argument was given by Parker et al. [53] where it has been suggested that the spin canting occurs in the whole sample due to quantum size effects.

### 1.4.5. Magnetic Hysteresis

Magnetic hysteresis loop which is a plot of the variation of magnetization under applied magnetic field is the most common way to represent the bulk properties of a magnetic material. This hysteresis behavior, i.e. the inability to trace back the same magnetization curve is related to the presence of domains within the material. When these domains are magnetized in one direction, it needs some energy to turn them back again. This property of magnetic materials is very useful for magnetic storage application. Magnetic anisotropy yields easy magnetization

directions corresponding to local energy minima and energy barriers that separate the easy directions in a single domain particle. On an atomic scale, the barriers are easily overcome by thermal fluctuations, but on the nanoscale or macroscopic length scales excitations are usually too weak to overcome the barriers. This is observed as magnetic hysteresis. The most useful information that one can get from the hysteresis loop is the maximum energy product which is the product of the maximum field ($H_{max}$) and the maximum magnetization ($M_{max}$). This is a measure of the maximum amount of work that can be performed by the magnetic material. Coercive field ($H_C$) is the field that is required to reduce the remanance magnetization ($M_R$) to zero. It is a measure of how strongly a magnetic material can oppose an external magnetic field. $M_R$ is the magnetization of a magnetic material when the field is reduced to zero after its complete magnetization.

## 1.5. Electrochemical Properties

### 1.5.1. Electrochemical Capacitors (Supercapacitors)

Diminishing reserves of fossil fuels and severe impacts of burning fossil fuels on both human beings and environment have been increasingly driving the world towards the development of clean and sustainable energy. Transforming natural energy, such as wind, tide, and solar energies can generate large amounts of clean and sustainable energy. The development of energy storage devices is extremely important to store the harvested energy for wide applications. Supercapacitors, batteries, and conventional capacitors are commonly used energy storage devices. Among these energy storage devices, supercapacitors (also known as electrochemical capacitors or ultracapacitors) have attracted rapidly growing attention due to their unique features, such as high power density, long cycle life, and small size. Nowadays, supercapacitors are exhibiting wide applications in electric vehicles, pacemakers, consumer electronic devices and so on. The specific energy and power capabilities of several energy storage and conversion systems (conventional capacitors, supercapacitors, batteries, and fuel cells) are shown in

Figure 1.1. It should be noted that no single energy source can match all power and energy region. Supercapacitors and batteries, filling up the gap between conventional capacitors and fuel cells, are ideal electrochemical energy-storage systems [54, 55].

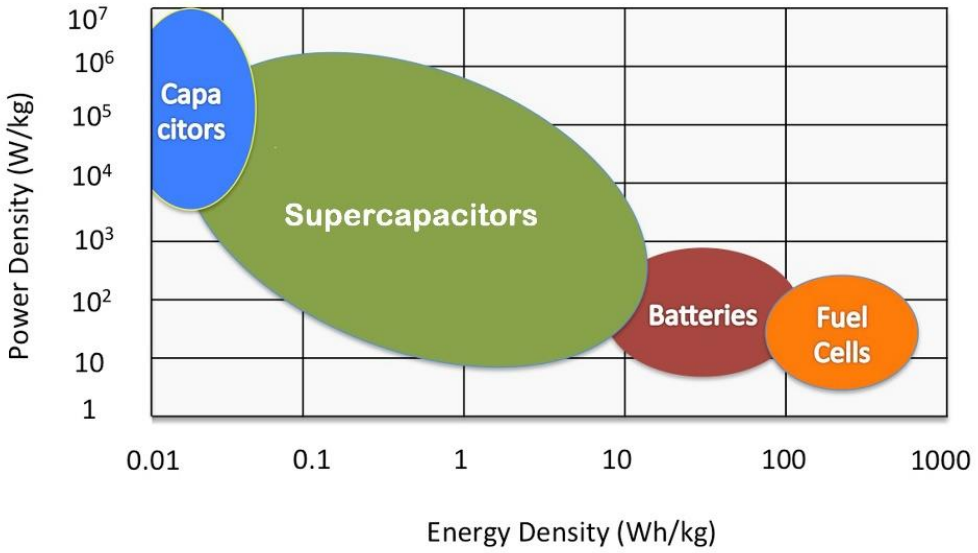


**Figure 1.1** Schematic Ragone plot of specific energy and power capabilities for various energy storage and conversion devices

The common features of both systems are that energy release takes place at the interface of electrode and electrolyte, and that electron and ion transports are separated [56]. Owing to the inherent differences between batteries and supercapacitors with respect to the energy storage mechanism and electrode materials, the characteristic performance of supercapacitors sets them apart from batteries. Table 1.1 summarizes the inherent differences between batteries and supercapacitors as well as the conventional capacitors (electrolytic capacitors) [57]. In a battery, energy is stored in chemical form, whereas energy is released in an electrical form by connecting a load across the terminals of a battery. The electrochemical reactions of electrode materials with ions in an electrolyte occur, leading to the conversion of chemical energy to electrical energy [58]. Lithium-ion batteries (LIBs) are the most popular rechargeable batteries. A battery mainly consists of an anode, a cathode, an electrolyte, and a separator. When a LIB is cycled, Li ions exchange between anode and cathode. The discharge rate and power

performance of batteries are determined by the reaction kinetics of active materials as well as mass transport.

**Table 1.1** The basic characteristics of supercapacitors, batteries, and electrolytic capacitors

| Parameters | Supercapacitor | Battery |
|---|---|---|
| Storage mechanism | Physical | Chemical |
| Charge time | 1~30 Sec | 1~5 hrs |
| Discharge time | 1~30 Sec | 0.3~3 hrs |
| Energy density (Wh/kg) | 1~10 | 20~100 |
| Power density (kW/kg) | 5~10 | 0.5~1 |
| Charge/Discharge Efficiency (%) | 75~95 | 50~90 |
| Cycle life | > 500 000 | 500~2000 |
| Max. voltage determinants | Electrode and electrolyte stability window | Thermodynamics of phase reactions |
| Charge stored determinants | Electrode microstructure and electrolyte | Active mass and thermodynamics |

Therefore, batteries generally yield high energy densities (150 Wh/kg is possible for LIBs), rather low power rates, and limited cycle life. The even-increasing demand for power requirements is a great challenge to the capability of battery design [3]. Conventional capacitors store energy physically as positive and negative charges on two parallel conductive plates, offering a high power density but a low energy density.

Supercapacitors offer a higher specific power density than most batteries and a higher energy density than conventional capacitors. The configuration of a typical supercapacitor consists of a pair of polarizable electrodes with current collectors, a separator, and an electrolyte, similar to that of a battery. The fundamental difference between supercapacitors and batteries lies in the fact that energy is physically stored in a supercapacitor by means of ion adsorption at the electrode/electrolyte interface (namely, electrical double-layer capacitors, EDLCs). As a result, the supercapacitor offers the ability to store/release energy in timescales of a few seconds with extended cycle life (Table 1.1) [59]. Generally, carbon materials (e.g. activated carbon,

porous carbon, carbon nanotubes) are used as electrode materials of EDLCs [3, 60]. Metal oxides and conducting polymers are also used as the active materials for supercapacitors, of which energy storage is based on the reversible redox reactions. This class of supercapacitors is represented as pseudocapacitor. The electrolytes of supercapacitors can be aqueous or organic. The aqueous electrolyte offers a low internal resistance, but limits the operating potential window to be about 1.0 V determined by the thermodynamic electrochemical window of water (1.23 V). Organic electrolytes with a broader electrochemical window can significantly enhance the electrical charge (or energy) accumulated in supercapacitors than aqueous electrolytes.

The rapid growth of clean and sustainable energy industry requires energy storage devices of high energy density, high power density, and long cycle life. This has greatly promoted the development of next-generation supercapacitors. In addition, the availability of advanced electrode materials, such as graphene has provided unprecedented opportunities for researchers to design and fabricate innovative electrode materials for high-performance supercapacitors.

### 1.5.2. Classification of Supercapacitors

Depending on the charge storage mechanism supercapacitors have been classified into two categories, electrical double layer capacitors (EDLCs) and pseudocapacitors (or redox supercapacitors) [4]. EDLCs, using carbon-based active materials with high surface area, build up an electrical charge at the electrode/electrolyte interface. Charge separation occurs on polarization at the electrode–electrolyte interface, producing what Helmholtz described in 1853 as the double layer capacitance *C*:

$$C = \frac{\varepsilon_0 \varepsilon_r A}{d} \tag{1.1}$$

Where, $\varepsilon_r$ is the electrolyte dielectric constant, $\varepsilon_0$ is the dielectric constant of the vacuum, $d$ is the effective thickness of the double layer (charge separation distance)

and *A* is the electrode surface area. On the other hand, pseudo-capacitors utilize fast and reversible surface or near surface reactions for charge storage. Metal oxides such as $RuO_2$, $Fe_3O_4$, $MnO_2$, NiO or $Co_3O_4$ [61-63], as well as electronically conducting polymers, have been studied extensively during the past few decades because of their high theoretical specific capacitance [4]. The specific pseudo-capacitance exceeds that of the carbon based EDLCs. They can complement or replace batteries in electrical energy storage and harvesting applications, when high power delivery or uptake is required. A notable improvement in performance has been achieved through recent advances in understanding charge storage mechanisms and the development of advanced nanostructured materials. As the pseudocapacitors store charges in the first few nanometers from surface, decrease of the particle size will increase the usage of active material. Recent reports suggest that supercapacitors based on thin films (thickness about several tens of nanometers) exhibit high specific capacitance due to their high specific surface area.

## 1.6. Transition Metal based materials for storage devices

Transition metal based ferromagnetic nanowires due to the unique combination of magnetic, transport and structural properties are in a focus of many scientific groups as potential candidates for applications in patterned magnetic recording media with density beyond $2Tb/in^2$ [1, 2], and high energy and power density energy storage devices [3, 4].

### 1.6.1. Materials for Magnetic storage devices

There are three noteworthy elements in the transition metals family. These elements are iron, cobalt, nickel, and their alloys and they are the only elements known to produce a magnetic effect called ferromagnetism and are used for permanent magnets and magnetic storage devices. With ferromagnetism, the unpaired electrons have aligned spins forming domains that survive even after the applied field is turned off. For this reason ferromagnetic materials are used in

coating cassette tapes, computer disks, and other devices that use magnetic codes and signals.

Piraux et al. [64] realized a comparative study of ferromagnetic Co, Ni, Fe nanowires grown by electrodeposition in polycarbonate membranes of various pore diameters, ranging from 30 to 500 nm. Using low porosity membranes for low dipolar interactions, the researchers observed that all Co, Ni and Fe nanowires exhibited an increase in coercivity as the pore diameter decreases. However, for Co and Ni nanowires, the remanent magnetization decreased with pore diameter, which suggests that wires split into domains when the pores were large. In the case of Co only nanowires, the shape anisotropy competed with the crystal anisotropy, which led to a specific magnetic behavior. Piraux et al. concluded that Ni and Fe nanowire magnetic properties were governed by the shape anisotropy.

In a recent review, Sellmyer et al [65] analyzed transition metal arrays of nanowires electrodeposited in self-assembled aluminum oxide membranes. They concluded that porous aluminum oxide templates, obtained by electrochemical anodization of aluminium in acidic electrolytes, were excellent mediums for nanowires electrodeposition due to high pore density, uniform pore distribution and high aspect ratios. Sellmyer et al. showed that large aspect ratio Co, Ni and Fe nanowires showed magnetization anisotropy, having an easy magnetization axis along the wires axis and 0.9 remanence ratios. The maximum coercivity was shown by Fe nanowires (3000 Oe), followed by Co nanowires (2600 Oe) and lastly by Ni nanowires (950 Oe). In their review, Sellmyer et al. highlighted the crucial effect of wire imperfections which led to the curling behavior, controlling the nanowires coercivity and magnetic viscosity. Using a magnetic model simulation, Sellmyer et al. also showed wire interactions could be approximated by a demagnetizing field.

Zhu et al. [66] studied the effect of applied magnetic field during CoNi alloy nanowire electrodeposition in AAO templates (200 nm pore diameter). Their examination showed that the perpendicular applied magnetic field during electrodeposition not only reduced the ($B_H$) saturation fields, but also enhanced squareness.

In a different study, Zhu et al. [67] looked at magnetic properties of FeNi nanowires of very high aspect ratios (>1000). The FeNi nanowires were electroplated in self-prepared AAO of highly ordered pores (43 nm pore diameters and 60 nm distance between pores). Enhanced coercivity of 769 Oe and 70 % remanent magnetization was observed when the magnetic field was applied parallel to the wires. Wang et al. [68] analyzed the structure and magnetic anisotropy of compositionally modulated FeNi alloy nanowires electrodeposited in AAO. Using XRD and Mossbauer spectroscopy, the obtained wires (16 nm diameter and 4 μm length) showed a polycrystalline structure along the (110) direction. The Fe component proved to have magnetic moments parallel to the wires in contrast to bulk Fe that showed (100) as the easy magnetization axis. The authors stated that the change in the preferred magnetization axis was due to the large shape anisotropy. Moreover, Wang et al. confirmed that the Ni component showed a disordered placement along the wires.

### 1.6.2. Electrode Materials for Supercapacitors

Common transition metal oxides that are currently researched for pseudocapacitive electrodes are $RuO_2$ [69], $Co_3O_4$ [70], $MnO_2$ [71], NiO [72], and $V_2O_5$ [73]. These metal oxides undergo multiple oxidation states at specific potentials, leading to increased capacitance. $RuO_2$ is one of the most popular pseudocapacitive materials because of its good reversibility, three oxidation states within a potential range of 1.2 V, and an acceptable life cycle [4].

For example, Hu, Chen, and Chang [74] maximized the performance of hydrous $RuO_2$ by annealing it at high temperature and achieved a capacitance of 1340 F/g. Unfortunately, ruthenium metal is toxic and expensive due to scarce availability. This shifted the attention of researchers toward nonprecious metals that are more commercially available, including cobalt, manganese and nickel oxides. Nanoporous nickel hydroxide films were electrodeposited on a titanium substrate by using Brij 56 (polyoxyethylene cetyl ether) as a template [75,76]. Such a nanoporous film displayed a specific capacitance as high as 578 F/g. Porous NiO microspheres

with a specific capacitance of 710 F/g at a current density of 1 A/g and a capacitance retention of 98% after 2000 continuous charge/discharge cycles were reported [77]. Loosely packed NiO nanoflakes were prepared using a chemical precipitation method, achieving a specific capacitance as high as 942 F/g [78].

Although these nickel oxide/hydroxides exhibit high specific capacitances, they suffer from the limited potential window (< 0.6 V), much lower than 1.0 V, which would limit their energy densities when used as electrode materials in supercapacitors because the energy density is proportional to the squared potential window. Mesoporous $Co_3O_4$ nanocrystals with well-controlled shapes were prepared by using a solvothermal method [70]. The specific capacitance was measured to be about 92 F/g at a current density of 5 mA/cm$^2$. Cobalt oxide aerogel was synthesized with propylene oxide as an additive and used as a supercapacitor electrode. A high specific capacitance of 623 F/g and good cycle stability were observed [79]. The specific capacitance of cobalt oxide aerogel is much higher than that of loosely packed cobalt oxide nanocrystals and xerogels. Cobalt hydroxide thin films were also prepared using a nonionic surfactant (Brij 56) as a template [80]. The maximum specific capacitance of 1084 F/g was realized in a 2 M KOH electrolyte solution at a current density of 4 A/g.

Nonetheless, metal oxides generally suffer performance loss for possessing poor electrical conductivity. Overall, a variety of electrode materials, such as carbon-based materials, conducting polymers, transition-metal-oxides, and their composite materials have been tested as electrode materials for supercapacitors. The diversity of electrode materials in chemical and physical properties, preparation methods, as well as the evaluation methods render the reported electrochemical performances highly variable. With respect to transition-metal-oxide-based materials, it is expected to fully exploit as promising materials for supercapacitors.

## 1.7. Motivation and Objectives of Thesis

Nanostructured materials have become an arena of vast research interest as they supply the underlying building block for Nanoscience and nanotechnology. Due to their extremely small dimension as comparable to some characteristic length scales of materials such as Bohr exciton radius, spin diffusion length, carrier mean free path, magnetic domain wall width, etc. they often exhibit some novel and enhanced properties over their bulk counterpart [26, 81-83]. Specially, transition metal based nanostructured materials have attracted significant research attention due to their tremendous technological applications in sensors, magnetic and energy storage devices [1-4].

Ordered assembly of nanostructures is particularly interesting because one can probe the individual as well as collective behavior of the samples in a well-defined and reproducible fashion. There are several chemical and physical methods commonly used for the fabrication of ordered nanostructures. Among them anodized alumina oxide (AAO) assisted electrodeposition method is very popular [84]. Self-organized nanoporous anodized alumina oxide template synthesized by controlled electrochemical anodization of pure aluminium in acidic medium [11] have been employed extensively as the host for nanostructures like nanowires, nanotubes and nanorods of different metal, semiconductor and polymers [85, 86] because of its uniform structure and stability

Magnetic cylindrical nanostructures have recently attracted tremendous attention because of their potential applications in various fields, particularly in high density perpendicular magnetic storage. Highly ordered arrays of such cylindrical nanostructures show novel and interesting magnetic properties different from those of bulk and thin films and sensitively depend on their sizes, shapes, and the interactions among them. Magnetic properties of such nanostructures are governed by various anisotropy energies such as shape, magnetocrystalline and surface anisotropies [49]. However the magnetic behaviour of the ordered arrays of nanostructures is determined by the magnetic nature of individual nanostructure as

well as by the interactions among them. The direction of the magnetic easy axis of a nanostructure is determined by the direction of the effective anisotropy field in it. Due to the strong shape anisotropy in a nanostructure, magnetic easy axis have been usually parallel to its length. But in an array of closely arranged nanostructures, strong magnetostatic interaction is developed because of the close proximity of neighbouring nanostructure, resulting the direction of easy axis perpendicular to its length which is undesirable in most of the magnetic storage applications [87]. Therefore, nanostructures of transition metals have attracted a great deal of interest in modern research for their manifold applications in everyday life. Specially, nanostructures of nickel (Ni), iron (Fe), cobalt (Co) and their mixed alloys (FeNi, CoNi, etc.) have found special attention due to their unique, fascinating size and structure dependent properties and also for their nontoxic nature and easy synthesis techniques. In addition, the magnetic properties of these ordered nanostructures can also be tuned by some irradiation process.

On the other hand, transition metal based oxides such as NiO, $Co_3O_4$, $Fe_2O_3$, etc. have gained tremendous application towards the development of clean and sustainable energy. Transforming natural energy, such as wind, tide, and solar energies can generate large amounts of clean and sustainable energy. The development of energy storage devices is extremely important to store the harvested energy for wide applications. Supercapacitors, batteries, and conventional capacitors are commonly used energy storage devices. Among these energy storage devices, supercapacitors have attracted rapidly growing attention due to their unique features, such as high power density, long cycle life, and small size. Specially transition metal oxide based supercapacitors are attractive because of their variable oxidation states, with finely controlled and tunable redox potentials [3, 4]. To develop high-performance supercapacitors, a couple of fundamental issues, such as low energy density, must be addressed. The energy density of commercial supercapacitors based on carbon electrodes is generally less than 10 Wh/kg, much lower than that of batteries. While metal oxides are available for high-energy-density supercapacitors, they suffer from poor rate capability and poor cycling stability.

There is an urgent demand to improve the electrochemical performance of metal oxides. In addition, organic electrolytes and ionic liquids with broad operating potential windows offer relatively higher energy density. However, organic electrolytes with poor electrical conductivity are not environmentally friendly while ionic liquids are cost-ineffective, leading to both types of electrolytes being undesirable in practical applications. In view of environmental concerns and cost, aqueous electrolytes are desirable by configuring smart supercapacitors with appropriate electrode materials. Thus, to exploit advanced electrode materials is the key to develop high-performance supercapacitors.

In this backdrop the main objectives of this work are summarized as follows:

- We have developed the anodized alumina oxide (AAO) templates by two steps anodization technique. We have standardized the anodization process with pores of different sizes of AAO templates by varying the anodization voltage and the concentration of the electrolyte solution.
- Further, these AAO templates have used as a host for the fabrication of transition metals (Ni, FeNi and CoNi) based various nanostructures (nanowires, nanotubes, nanoblocks).
- We have studied the effect of alpha particle irradiation on the magnetic properties of Ni nanowires. We observed that alpha particle irradiation is a useful tool to change the magnetic properties of the nanowires as per need.
- We have studied the aspect ratio dependent magnetic properties of FeNi nanowires and CoNi nanotubes.
- We have also prepared some transition metal oxide based core/shell hybrid nanostructures (Ni/NiO core/shell nano-heterostructures and NiO-nanoblocks) by controlled oxidation of as-prepared transition metal based nanostructures (Ni nanowires and nanoblocks) for supercapacitor electrodes, which shows very high quality electrochemical performance.

- Further, electrical conductivity of supercapacitor electrode material (NiO) improved by hydrogenation process and introducing impurities via doping of one metal oxide material with other metal oxide material. The resultant products (H-Ni/NiO, Fe-Ni/$Fe_2O_3$-NiO and Co-Ni/$Co_3O_4$-NiO core/shell nano-heterostructures) exhibit enhanced electrochemical performance as a supercapacitor electrode material.

## 1.8. Organization of the Thesis

The entire thesis has been divided into six different chapters. A brief sketch of the chapters is given below.

***Chapter 1*** gives an introduction about transition metal based different nanostructures and their potential applications in magnetic and energy storage devices. Followed by their detail literature review. The motivation of the thesis has been justified with the outline of the work described in this thesis.

***Chapter 2*** describes the synthesis techniques for fabrication of different nanostructures and also various characterization techniques of these nanostructures.

***Chapter 3*** is about the synthesis of highly ordered porous anodized alumina oxide (AAO) membranes by two step anodization technique. We have standardized the anodization process with pores of different sizes of AAO templates by varying the anodization voltage and the concentration of the electrolyte solution. Further, we have studied their structural, morphological, optical and magnetic properties in detail.

***Chapter 4*** describes the fabrication of transition metal based ordered nanostructures (Ni nanowires, FeNi nanowires & CoNi nanotubes) prepared by AAO template assisted electrodeposition technique. We have studied their structural, morphological, and magnetic properties in detail. We have also studied the effect of alpha particle irradiation on the magnetic properties of Ni nanowires. We observed

that alpha particle irradiation is a useful tool to change the magnetic properties of the nanowires as per need. In addition, we have studied the aspect ratio and temperature dependent magnetic properties of FeNi nanowires and CoNi nanotubes.

***Chapter 5*** describes the fabrication of transition metal oxide based core/shell hybrid nanostructures (Ni/NiO core/shell nano-heterostructures and NiO-nanoblocks) by controlled oxidation of as-prepared transition metal based nanostructures (Ni nanowires and nanoblocks). Their structural, morphological and electrochemical properties have studied in details for their energy storage applications. In addition, the electrical conductivity of supercapacitor electrode material (NiO) improved by hydrogenation process and introducing impurities via doping of one metal oxide material with other metal oxide material. The resultant products (H-Ni/NiO, Fe-Ni/$Fe_2O_3$-NiO and Co-Ni/$Co_3O_4$-NiO core/shell nano-heterostructures) have shown enhanced electrochemical performance as a supercapacitor electrode materials.

***Chapter 6*** concludes the thesis with an idea about the scope for future work in this direction.

# Bibliography


[1] D. Appell, *Nature (London)* **419**, 553 (2002)

[2] R. P. Cowburn, *Nature (London)* **448**, 544 (2007)

[3] J. R. Miller and P. Simon, *Science*, **321**, 651 (2008)

[4] P. Simon and Y. Gogotsi, *Nat. Mater.*, **7**, 845 (2008)

[5] J. I. Martin, J. Nogues, K. Liu, J. L. Vicent, I. K. Schuller, *J. Magn. Magn. Mater.*, **256**, 449 (2003)

[6] E. Rabani, D. R. Reichman, P. L. Geissler, and L. E. Brus, *Nature (London)* **426**, 271 (2003)

[7] S. Sun, *Adv. Mater.,* **18**, 393 (2006)

[8] Z. L. Wang, *Adv. Mater.*, **12**, 1295 (2000)

[9] F. Cerrina and C. Marrian, *MRS Bull.*, **December**, 56 (1996)

[10] Y. Xia, J. A. Rogers, K. E. Paul and G. M. Whitesides, *Chem. Rev.*, **99**, 1823 (1999)

[11] H. Masuda, and K. Fukuda, *Science*, **268**, 1466 (1995)

[12] A. Fert and L. Piraux, *J. Magn. Magn. Mater.*, **200**, 338 (1999)

[13] M. Lindeberg and K. Hjort, *Sens. Actuators A Phys.*, **105**, 150 (2003)

[14] S. L. Tung, W. Chen, M. Lu, S. G. Yang, F. M. Zhang and Y. W. Du, *Chem. Phys. Lett.*, **384**, 1 (2004)

[15] A. Hultgren, M. Tanase, C. S. Chen and D. H. Reich, *IEEE Trans. Magn.*, **40**, 2988 (2004)

[16] W. O. Rosa, L.G. Vivas, K.R. Pirota, A. Asenjo and M. Vazquez, *J. Magn. Magn. Mater.,* **324**, 3679 (2012)

[17] X. W. Wang, G. T. Fei, B. Wu, L. Chen and Z. Q. Chu, *Phys. Lett. A,* **359**, 220 (2006)

[18] H. Pan, B.H. Liu, J.B. Yi, C.K. Poh, S.H. Lim, J. Ding, Y.P. Feng, C.H.A. Huan and J.Y. Lin, *J. Phys. Chem. B,* **109**, 3094 (2005)

[19] S. Thongmee, H.L. Pang, J.B. Yi, J. Ding, J.Y. Lin and L.H. Van, *Acta Mater.,* **57**, 2482 (2009)

[20] L.D.L.S. Valladares, L.L. Felix, A.B. Dominguez, T. Mitrelias, F. Sfigakis, S.I. Khondaker, C.H.W. Barnes and Y. Majima, *Nanotechnology,* **21**, 445304 (2010)

[21] V. Vega, T. Bohnert, S. Martens, M. Waleczek, J.M. Montero-Moreno, D. Gorlitz, V.M. Prida and K. Nielsch, *Nanotechnology*, **23**, 465709 (2012)

[22] M. Yan, A. Kakay, S. Gliga, and R. Hertel, *Phys. Rev. Lett.,* **104**, 057201 (2010)

[23] C. T. Boone, J.A. Katine, M. Carey, J. R. Childress, X. Cheng, and I.N. Krivorotov, *Phys. Rev. Lett.,* **104**, 097203 (2010)

[24] O.A. Tretiakov, Y. Liu, and Ar. Abanov, *Phys. Rev. Lett.,* **105**, 217203 (2010)

[25] Z. Z. Sun and J. Schliemann, *Phys. Rev. Lett.*, **104**, 037206 (2010)
[26] J.I. Martin, J. Nogues, K. Liu, J.L. Vicent, I. K. Schuller, *J. Magn. Magn. Mater.*, **256**, 449 (2003)
[27] R. Agarwal, *Small*, **4**, 1872 (2008)
[28] M. Law, J. Goldberger and P. D. Yang, *Annu. Rev. Mater. Res.,* **34**, 83 (2004)
[29] H. Pan and Y. P. Feng, *ACS Nano,* **2**, 2410 (2008)
[30] M. Ben-Ishai and F. A Patolsky, *Adv. Mater.*, **22**, 902 (2010)
[31] J. A. Goebl, R. W. Black, J. Puthussery, J. Giblin, T. H. Kosel and M. J. Kuno, *Am. Chem. Soc.*, **130**, 14822 (2008)
[32] L. J. Lauhon, M. S. Gudiksen, C. L. Wang and C. M. Lieber, *Nature*, **420**, 57 (2002)
[33] Y. B. He, G. R. Li, Z. L. Wang, C. Y. Su and Y. X. Tong, *Energy Environ. Sci.*, **4**, 1288 (2011)
[34] J. P. Liu, J. Jiang, C. W. Cheng, H. X. Li, J. X. Zhang, H. Gong and H. J. Fan, *Adv. Mater.*, **23**, 2076 (2011)
[35] H. Bethe, *Ann. Physik*, **3**, 133 (1929)
[36] L. Neel, *J. Phys. Radium*, **15**, 225 (1954)
[37] R. Skomski and J. M. D. Coey, *Permanent Magnetism*, 2nd ed. (Institute of Physics, Bristol, 1999)
[38] E. H. Frei, S. Shtrikman, and D. Treves, *Phys. Rev.,* **106**, 446 (1957)
[39] P. Bryant and H. Suhl, *Appl. Phys. Lett.*, **54** (1) 78 (1988)
[40] A. Aharoni, *J. Appl. Phys.,* **68** (6) 2892 (1990)
[41] C. A. Ross, M. Farhoud, M. Hwang, I. H. Smith, M. Redjdal, and F. B. Humphrey, *J. Appl. Phys.*, **89**, 1310 (2001)
[42] C.A. Ross, M. Hwang, M. Shima, H. I. Smith, M. Farhoud, T.A. Savas, W. Schwarzacher, J. Parrochond, W. Escoffier, H. Neal Bertram, F.B. Humphrey and M. Redjdal, *J. Magn. Magn. Mater.,* **249,** 200 (2002)
[43] C. A. Ross, S. Haratani, F. J. Castan, Y. Hao, M. Hwang, M. Shima, J. Y. Cheng, B. Vogeli, M. Farhoud, M. Walsh, and H. I. Smith, *J. App. Phys.*, **91**(10), 6848 (2002)
[44] A. N. Bogdanov, U. K. Robler and K. H. Muller, *J. Magn. Magn. Mater.,* **242**, 594 (2002)
[45] A. Aharoni, *J. Appl. Phys.* , **82**, 1281 (1997)
[46] J. D. Jackson, Classical Electrodynamics, *John Wiley & Sons, Inc.* (1999)
[47] M. Grimsditch, Y. Jaccard and I.K. Schuller, *Phys. Rev. B,* **58**, 11539 (1998)
[48] J. Rivas, A. Kazadi, M. Bantu, G. Zaragoza, M.C. Blanco, M.A. Lopez-Quintela, *J. Magn. Magn. Mater.*, **249,** 220 (2002)
[49] A. Encinas-Oropesa, M. Demand, L. Piraux, I. Huynen and U. Ebels, *Phys. Rev. B,* **63**, 104415 (2001)

[50] V. Raposo, J.M. Garcia, J.M. Gonzalez and M. Vazquez, *J. Magn. Magn. Mater.*, **222,** 227 (2000)
[51] L. Clime, P. Ciureanu, and A. Yelon, *J. Magn. Magn. Mater.*, **297,** 60 (2006)
[52] S. Gangopadhyay, G. C. Hadjipanayis, B. Dale, C. M. Sorensen, K. J. Klabunde, V. Papaefthymiou and A. Kostikas, *Phys. Rev. B,* **45**, 9778 (1992)
[53] F. T. Parker, and A. E. Berkowitz, *Phys. Rev. B,* **44**, 7437 (1991)
[54] P. Novak, K. Muller, K. S. V. Santanam and O. Hass., *Chem. Rev.,* **97**, 207 (1997)
[55] D. R. Rolison, and L. F. Nazar., *MRS Bulletin*, **36**(07), 486 (2011)
[56] M. Winter and R.J. Brodd, *Chem Rev.*, **104**(10), 4245 (2004)
[57] A.G. Pandolfo and A.F. Hollenkamp, *J. Power Sources,* **157**, 11 (2006)
[58] A. Burke, *J. Power Sources,* **91**, 37 (2000)
[59] Zhang, L. L. and X. S. Zhao. *Chem. Soc. Rev.,* **38**, 2520 (2009)
[60] P. Jampani, A. Manivannan and P. N. Kumta, *Electrochem. Soc. Interface* **19**, 57 (2010)
[61] N. L. Wu, *Mater. Chem. Phys.*, **75**, 6 (2002)
[62] T. Brousse, M. Toupin, and D. Belanger, *J. Electrochem. Soc.,* **153**, A2171 (2006)
[63] R. B. Rakhi, Wei Chen, Dongkyu Cha, and H. N. Alshareef, *Nano Lett.*, **12**, 2559 (2012)
[64] L. Piraux, S. Dubois, J. L. Duvail, K. Ounadjela and A. Fert, *J. Magn. Magn. Mater.*, **175**, 127 (1997)
[65] D.J. Sellmyer, M. Zheng and R. Skomski, *J. Phys. Cond. Mat.*, **13**, R433 (2001)
[66] H. Zhu, S. Yang, G. Ni, D. Yu and Y. Du, *Scripta Materialia*, **44**, 2291 (2001)
[67] H. Zhu, S. Yang, G. Ni, D. Yu and Y. Du, *J. Magn. Magn. Mater.*, **234**, 454 (2001)
[68] J.B. Wang, Q.F. Liu, D.S Xue, Y. Peng, X.Z Cao and F.S. Li, *J. Phys. D: Appl. Phys.*, **34**, 3442 (2001)
[69] J. P. Zheng, P. J. Cygan and T. R. Jow, *J. Electrochem. Soc.,* **142**, 2699 (1995)
[70] S. Xiong, C. Yuan, X. Zhang, B. Xi and Y. Qian, *Chem. Euro. J.*, **15**, 5320 (2009)
[71] S. C. Pang, M. A. Anderson and T. W. Chapman, *J. Electrochem. Soc.*, **147**, 444 (2000)
[72] K. C. Liu and M. A. Anderson, *J. Electrochem. Soc.*, **143**, 124 (1996)
[73] R. N. Reddy and R. G. Reddy, *J. Power Sources*, **156**, 700 (2006)
[74] C. C. Hu, W. C. Chen and K. H. Chang, *J. Electrochem. Soc.*, **151**, A281 (2004)
[75] M.W. Xu, D.D. Zhao, S.J. Bao and H.L. Li, *J. Solid State Electrochem.*, **11**, 1101 (2007)
[76] M. Xu, L. Kong, W. Zhou and H. Li, *J. Phys. Chem. C*, **111**, 19141 (2007)
[77] C. Yuan, X. Zhang, L. Su, B. Gao and L. Shen, *J. Mater. Chem.*, **19**, 5772 (2009)
[78] L.B. Kong, J.W. Lang, M. Liu, Y.C. Luo and L. Kang, *J. Power Sources*, **194**, 1194 (2009)

[79] T.Y. Wei, C.H. Chen, K.H. Chang, S.Y. Lu and C.C. Hu, *Chem. Mater.*, **21**, 3228 (2009)
[80] W.J. Zhou, J. Zhang, T. Xue, D.D. Zhao and H.L. Li, *J. Mater. Chem.*, **18**, 905 (2008)
[81] P. Griunberg, R. Schreiber, Y. Pang, M.B. Brodsky and H. Sowers, *Phys. Rev. Lett.*, **57**, 2442 (1986)
[82] P.M. Levy, S. Zhang and A. Fert, *Phys. Rev. Lett.*, **65**, 1643 (1990)
[83] A.E. Berkowitz, J.R. Mitchell, M.J. Carey, A.P. Young, S. Zhang, F.E. Spada, F.T. Parker, A. Hutten and G. Thomas, *Phys. Rev. Lett.*, **68**, 3745 (1992)
[84] A. Fert and L. Piraux, *J. Magn. Magn. Mater.*, **165**, 1083 (1996)
[85] G. Che, B.B. Lakshmi, E.R. Fisher, C.R. Martin, *Nature*, **393**, 346 (1998)
[86] Z. Miao, D. Xu, J. Ouyang, G. Guo, X. Zhao, Y. Tang, *Nano Lett.*, **2**, 717 (2002)
[87] B. Das, K. Mandal, P. Sen, A. Bakshi, P. Das, *Physica B*, **407**, 3767 (2012)

# Chapter 2 | Experimental Details

This chapter describes different synthesis methods of nanostructures and also various techniques to characterize them.

## 2.1. Preamble

In this chapter we will present an overview about various experimental techniques that have been applied to synthesize unique nanostructures of various materials along with their characterization processes employed to investigate different properties of these nanostructured materials. We develop homemade setups to synthesize the porous alumina membranes. While the nanowires (NWs), nanotubes (NTs), core/shell nano-heterostructures are synthesized using a commercial electrochemical cell (potentiostat AutoLab-30). Thermal evaporation and RF (radio frequency) sputtering techniques to prepare gold thin films on alumina membranes is described in detail. For high temperature annealing of the samples commercial furnace systems have been used.

The structure, morphology and phase of the synthesized nanostructures are studied using X-Ray Diffraction (XRD), Scanning Electron Microscope (SEM), Field Emission Scanning Electron Microscope (FESEM), Transmission Electron Microscope (TEM), High Resolution Transmission Electron Microscope (HRTEM), Energy Dispersive X-Ray Analysis (EDAX), and Selected Area Electron Diffraction (SAED). The chemical analysis on the electronic structure of the nanostructures is conducted by employing X-ray photoelectron spectroscopy (XPS). Photoluminescence analyses is carried out using spectrofluorometer. The magnetic characterizations are carried out employing Vibrating Sample Magnetometer (VSM). The electrochemical properties of the samples were investigated by cyclic voltammetry (CV), galvanostatic (GV) charge/discharge and electrochemical impedance spectroscopy (EIS) tests by using a software controlled conventional three-electrode electrochemical cell (potentiostat AutoLab-30).

## 2.2. Approach for designing of nanomaterials

There are two approaches for synthesis of nanomaterials and the fabrication of nanostructures. Top down approach refers to slicing or successive cutting of a bulk material to get nanosized structures. Bottom up approach refers to the buildup of a material from the bottom: atom by atom, molecule by molecule or cluster by

cluster. Both approaches play very important role in modern industry and most likely in nanotechnology as well. There are advantages and disadvantages in both approaches. Attrition or Milling is a typical top down method in making nanoparticles, whereas the electrodeposition is a good example of bottom up approach in the synthesis of nanowires.

The biggest problem with top down approach is the imperfection of surface structure and significant crystallographic damage to the processed patterns. These imperfections which in turn leads to extra challenges in the device design and fabrication. But this approach leads to the bulk production of nanomaterial. Regardless of the defects produced by top down approach, they will continue to play an important role in the synthesis of nanostructures. Though the bottom up approach often referred in nanotechnology, it is not a newer concept. All the living beings in nature, observe growth by this approach only and also it has been in industrial use for over a century. Examples include the production of salt and nitrate in the chemical industry. Although the bottom up approach is nothing new, it plays an important role in the fabrication and processing of nanostructures. There are several reasons for this and explained as below. When structures fall into a nanometer scale, there is a little chance for a top down approach. All the tools we have possessed are too big to deal with such tiny subjects. Bottom up approach also promises a better chance to obtain nanostructures with less defects, more homogeneous chemical composition. On the contrary, top down approach most likely introduces internal stress, in addition to surface defects and contaminations.

## 2.3. Synthesis Techniques

### 2.3.1. Electrochemical Anodization Technique

Electrochemical anodization is a simple and elegant way to synthesize porous oxide films on a conducting metal surface such as aluminum (Al) [1-3]. We engineer porous alumina membranes in our laboratory by two step anodization of pure aluminum using a homemade electrochemical cell set-up. The schematic diagram of

the set-up is shown in Fig. 2.1 (a). The experimental set-up that is developed in our laboratory is shown in Fig. 2.1 (b).

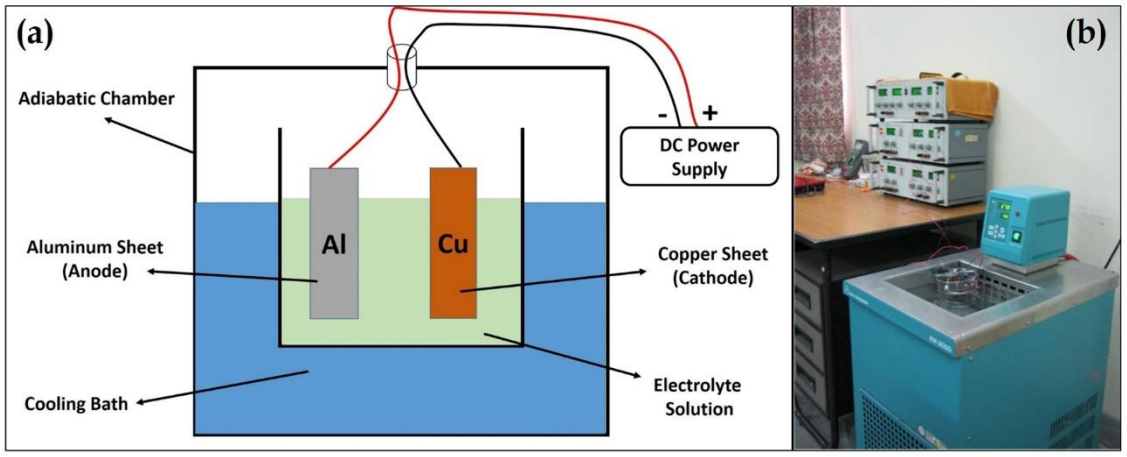


**Figure 2.1 (a)** Schematic diagram of the experimental set-up for anodization of thin aluminum sheet, (b) Experimental set-up of the anodization of thin aluminum sheet

The electrochemical cell consisted of two electrodes: *Cathode* - a thin (~ 1 mm thick) copper (Cu) sheet connected to the negative terminal of a DC power supply, *Anode* – a thin (~ 130 µm thick) aluminum (Al) sheet connected to the positive terminal of the DC power supply and electrolyte solution. The back side of the Al sheet is covered by conventional transparent tape to restrict the growth of oxide film only on the front side of Al sheet as shown in Fig. 2.1 (b). The whole electrochemical cell kept in an adiabatic chamber (cooling bath) and the temperature of the chamber kept constant around 11˚C with the use of a chiller as shown in Fig. 2.1 (b).

Under a suitable constant potential difference across the electrodes, thin porous oxide film starts to grow over the aluminum surface [4]. In our case we maintained a potential difference within the range of 60 V to 64 V to maintain a constant current density of ~ 2 mA / $cm^2$ across the electrodes. The voltage drops across the electrodes changes with the anodization time due to the growth of non-conducting oxide layer on the aluminum surface.

The growth mechanism and details of synthesized alumina membranes are described in *chapter 3*. The conversion of aluminum into an alumina film on the Al surface is an exothermic reaction. Depending upon suitable choice of electrolyte solution and under a typical potential difference, the porous type oxide film

develops during the anodization process. The porous oxide film growth with uniform pore distribution is attributed to the thermally assisted, field accelerated dissolution of oxide at the base of pores. This dissolution of oxide layer at pore bottom and formation of new oxide layer at metal/oxide interface to maintain a dynamic equilibrium [5]. In order to attain the equilibrium we maintain a constant temperature of 11 $^0$C by immersing the cell in a temperature bath.

## 2.3.2. Sputtering deposition technique

We have used this technique to deposit thin gold films on one side of the AAO template and also over the as grown nanowires (discussed in *Chapter 4*). The setup diagram of the sputtering system is shown in Fig. 2.2. In our case target, i.e. Au, and the substrate are placed inside a vacuum chamber where the pressure is maintained at ~$10^{-5}$ mbar during the sputtering process.

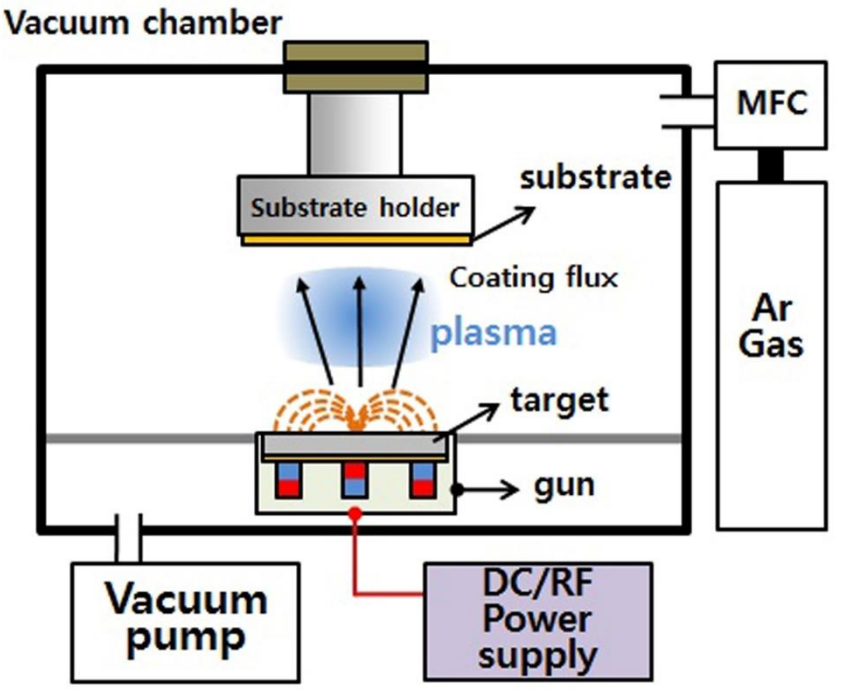


**Figure 2.2** Schematic diagram of DC sputtering deposition setup.

Once the vacuum is reached, argon gas is introduced in the chamber. This Ar gas is ionized and form plasma by a strong potential difference between anode (substrate) and cathode (Au) and these positive ions are accelerated to the target

(cathode). After impact with the target, a momentum transfer is happened and then the target atoms are released from the target, travel to the positive substrate where they form layers of atoms. For efficient momentum transfer to happen, atomic weight of the sputtering gas should be close to that of the target material. Actually, dc sputtering is used for conducting materials. However, for non-conducting materials there is positive charge buildup on the material which stops the sputtering. In such cases, RF sputtering is efficient where a magnet is used to increase the electron path length, therefore, enhancing the probability of electron collision with the Ar atoms and hence increases the ionization efficiency.

### 2.3.3. Thermal evaporation deposition technique

Thermal evaporation is a technique commonly used to deposit thin films of metals. The metal source is heated up to evaporate in a vacuum chamber that maintains a pressure of ~ $10^{-6}$ mbar. At an elevated temperature, the thermal energy of surface atoms of the metal becomes greater than the binding energy of the same and they become free from the metal surface. Under such high vacuum atmosphere the typical mean free paths of the evaporated particles are in the range of few meters. That large mean free path allows the particles (atoms/molecules) to travel to the target object (substrate) where they deposited. On the substrate, the deposited particles lower their energy through the dissipation of heat and make a thin film of the source material. Generally a diffusion pump is employed to achieve such high vacuum within the chamber to extract all unwanted gaseous particles within the chamber. However, hot objects within the chamber (e.g. heating filament, molybdenum boat in our case) produces unwanted vapors that limit the quality of the vacuum. A cooling system is employed to keep the chamber and the substrate holder temperature at normal. In case of metal oxide thin film deposition, the deposition is carried out in the presence of oxygen, so that the metal can react to produce theoxide film. Perhaps, the oxygen atoms can collide with the metallic particles within the chamber and reduce the amount of vapor that reaches the substrate.

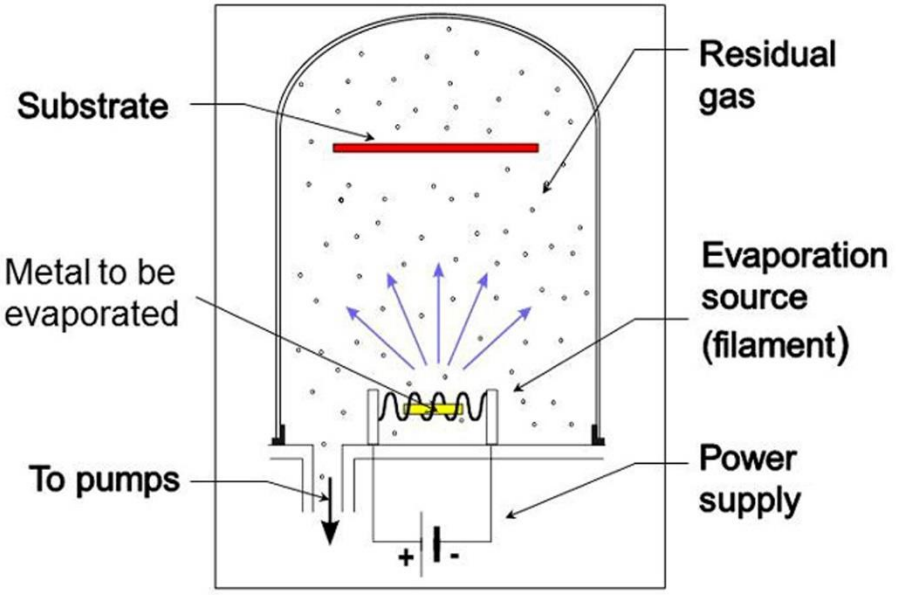


**Figure 2.3.** Schematic diagram of thermal evaporation.

The quality of the film (i.e. uniformity in thickness, contamination free) is mostly depending on the quality of vacuum within the chamber and the quality of the substrate on which the film is deposited. As the evaporated materials approach the substrate from a particular direction, the rough surface of the substrate thus leads a non-uniform deposition of thin film. A schematic diagram of the set-up is shown below in Fig. 2.3.

## 2.3.4. Electrodeposition Technique

Electrodeposition technique for fabrication of specially nanowires (NWs), nanotubes (NTs) etc. is a very cost effective and relatively simpler process as compared to the lithography processes, e.g. optical, electron beam, ion beam lithography etc. We have employed a commercial electrodeposition set-up (Autolab PGSTAT 302n) in order to prepare magnetic NWs within the nano pores of alumina (AAO) having average pore diameter of ~55 -200 nm with a thickness of ~50 mm and an average pore density of ~$10^9$ $cm^{-2}$.

The set-up consists of a software controlled conventional electrochemical cell and a power supply (Potentiostat AutoLab-30), as shown in Fig. 2.4 (a). The electrochemical cell, as shown in Fig. 2.4 (b), consists of three electrodes: working

electrode (WE), counter electrode (CE) and reference electrodes (RE). The working electrode is generally the template on which the desired electrochemical depositions are carried out.

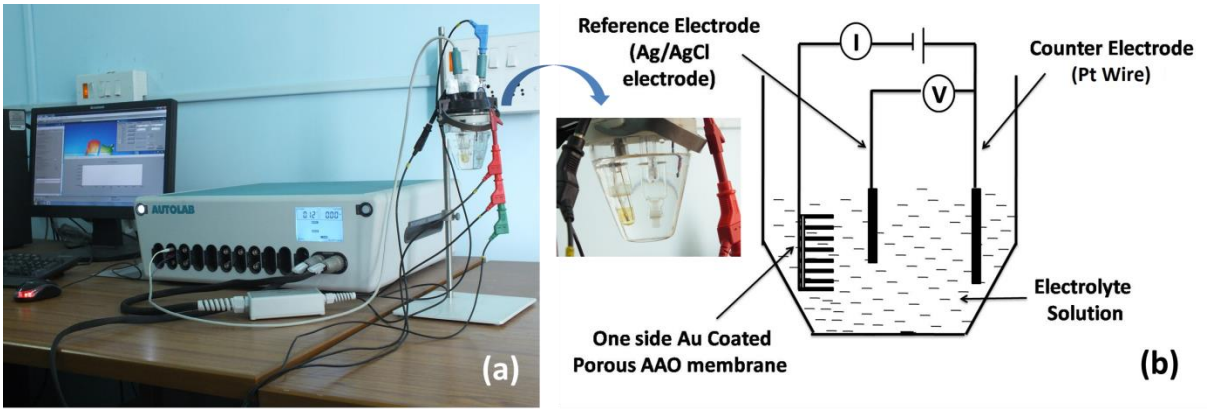


**Figure 2.4** (a) Electrodeposition setup for fabrication of metallic NWs; (b) Schematic diagram of the electrochemical cell with various operating electrodes.

To deposit the metal ions in the pores of AAO template in order to synthesize NWs, we use AAO membrane as working electrode. However first of all, one side of the AAO membranes is coated with a conductive gold (Au) layer of ~ 100 nm thicknesses either by thermal evaporation or by RF sputtering technique. For polycarbonate membranes, sputtering is necessary as the evaporation technique melts and burns the membranes at elevated temperature. For alumina membranes, both the techniques are applicable. In case of metal deposition from the aqueous solutions of their salts, the working electrode is connected to the negative terminal of the power supply, i.e. it is used as cathode. We have used a platinum wire as the counter electrode having the purity of ~ 99.99% commercially purchased from Sigma-Aldrich. The reference electrode is Ag/AgCl in saturated KCl solution, this electrode is used to measure the other electrode potentials with respect to it. The cell has the volume capacity of ~ 100 cc for the electrolyte solutions.

Nanowires and Nanotubes are deposited in the pores of alumina template by choosing a particular potential of corresponding depositions from linear sweep voltammetry (LSV) scan. The LSV scan gives a current vs. voltage profile for a particular electrolyte solution and for a particular choice of electrodes. LSV scanned between 0 V to – 1.5 V is presented in Fig. 2.5.

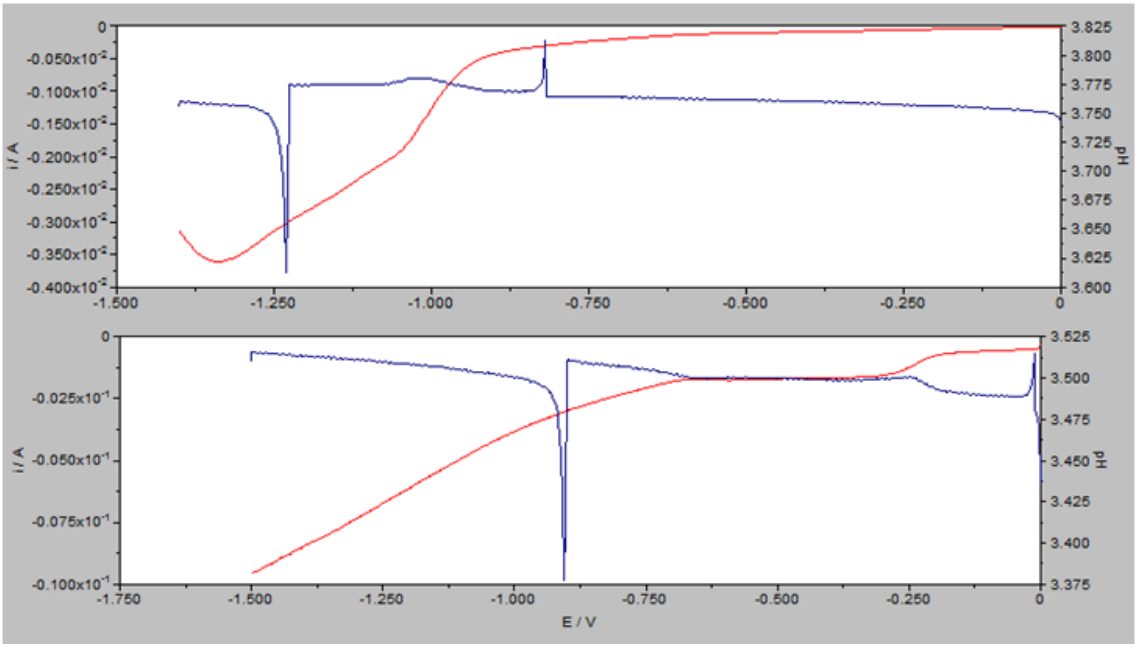


**Figure 2.5** LSV profile for a typical Ni (top), Co (bottom) nanowires deposition in porous template. LSV scans (curves in red solid lines) for scan of deposition voltage of nanowire in porous alumina template. Blue solid lines in the terminals represent corresponding pH changes of the electrolytes during the potential sweeps.

It shows, up to a certain value of the applied voltage, the current remain near zero value and with the increase in voltage, no deposition of cations at cathode is observed. After that, the current suddenly increases with further increase in voltage and attain a maximum value. The sudden increase in current indicates deposition of metal ion at cathode. Simultaneously, the pH value of the solution during the LSV scan is also recorded. The pH graph shows a spike near the potential where the sudden jump in current has started. We choose the potential of deposition just before the pH spike and very near to the start of the jump in current value. The working electrode i.e., the one sided Au coated (~100 nm thick) porous alumina membranes, is placed vertically within the electrolyte solution with the open end of the nano-pores facing towards counter electrode (Pt wire). Under a negative potential of the working electrode with respect to the counter, the positively charged metal ions move towards the working electrode membrane and enter to the nano channels through the open end. Inside the nano channels, formation of nanowires is the consequence of reduction of metal ions by capturing electron from gold thin film at the other end of the pores. Usually higher rate of ion deposition leads to formation of

nanowire whereas the lower rate leads to nanotube formation within the nano channels. We have prepared various transition metal based nanowires and nanotubes, which will be described elaborately in *Chapter 4* of this thesis.

## 2.4. Phase and Morphology Characterization Techniques

### 2.4.1. X-ray diffractometer

X-ray crystallography is a method of determining atomic and molecular structure of a crystalline material in which the atomic planes of the material diffract x-rays in different specific directions depending on their orientation. By measuring the angle and intensity of the diffracted beams, a three dimensional idea of the density of electrons within the specified crystal can be obtained. From this density of electrons, mean position of the atoms in the crystal can be determined.

In a practical setup as shown in Fig. 2.6 (a), a monochromatic beam of x-rays (Cu $K_\alpha$, λ~1.54 Å) is made to fall on a crystalline sample. These x-rays are scattered elastically by the electrons within the crystal planes and form outgoing spherical waves. Now, these scattered waves will interfere constructively in few specific directions that can be determined by Bragg's law given as:

$$2d \sin\theta = n\lambda \tag{2.1}$$

where, $d$ is the crystal plane spacing, $\theta$ is the diffraction angle and $n$ is an integer. These diffracted X-rays are then detected, processed and counted. By scanning the sample through a range of 2θ angles, all possible diffraction directions of the lattice should be attained due to the random orientation of the powdered material. Conversion of the diffraction peaks to d-spacings allows identification of the elements/compound present in the sample because each element/compound has a set of unique d-spacings. Typically, this is achieved by comparison of d-spacings with standard reference patterns (ICSD). Powder diffractometers come in two basic varieties: θ-θ in which the X-ray tube and detector move simultaneously or a θ-2θ in which the X-ray tube is fixed, and the specimen moves at ½ the rate of the detector to maintain the θ-2θ geometry. Our X-ray Panalytical system is a θ-2θ

system. In both systems the geometry shown in the diagram in Fig.2.6 (a) is maintained during data collection. The angles and intensities of the diffracted beams are processed and recorded electronically using a detector, electronics and specialized software resulting in Intensity vs. $2\theta$ plot for the specific sample, as shown in Fig. 2.6 (b) for Ni nanowires sample.

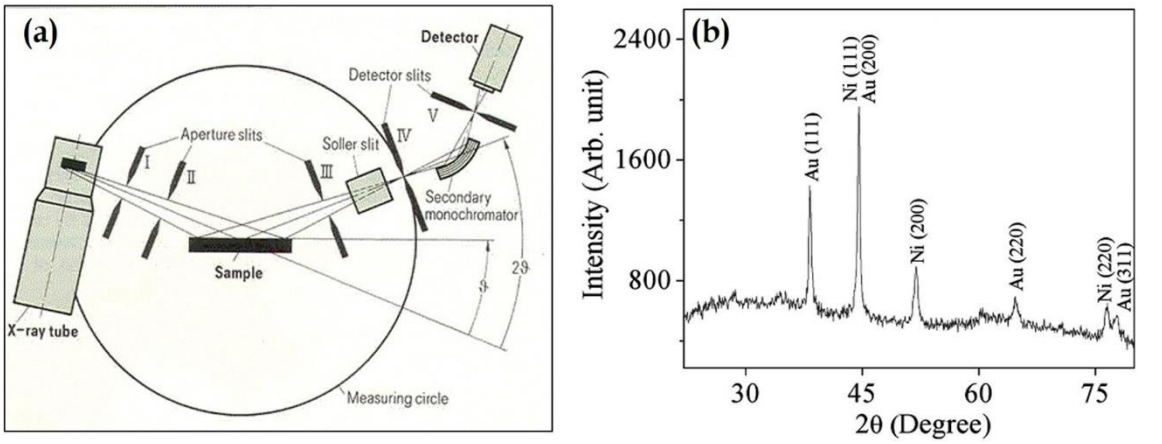


**Figure 2.6** (a) Schematic diagram of X-ray diffractometer in $\theta$-$2\theta$ mode, © chemwiki.ucdavis.edu. (b) XRD pattern of Ni nanowire of 100 nm diameter.

The grain size ($d$) of the sample can be calculated by observing the width of the diffraction peaks and using the relation as given by Debye-Scherrer:

$$d = 0.9\lambda / (\beta \cos\theta) \tag{2.2}$$

where, $\beta$ is the full width at the half maximum of the diffraction peak at a diffraction angle of $2\theta$ [6].

## 2.4.2. Electron Microscopes

Electron Microscopes are microscopic instruments that use a beam of highly energetic electrons to examine objects on a very fine scale of submicron length [7]. This examination can yield information about the topography (surface features of an object), morphology (shape and size of the particles making up the object), composition (the elements and compounds that the object is composed of and the relative amounts of them) and crystallographic information (how the atoms are arranged in the object). Electron microscopes function exactly as their optical

counterparts except that they use a focused beam of electrons instead of light to "image" the specimen and gain information as to its structure and composition. The Transmission Electron Microscope (TEM) was the first type of EM to be developed first in 1931 and is used to "see through" the specimen [8]. However, the Scanning Electron Microscope (SEM) debuted in 1935 with the first commercial instruments around 1965 [9, 10]. Its late development was due to the electronics involved in "scanning" the beam of electrons across the sample.

#### 2.4.2.1. Scanning Electron Microscope (SEM)

The basic steps involved in all electron microscopes are the following: A stream of electrons is formed in high vacuum (by electron guns). This stream is accelerated towards the specimen (with a positive electrical potential) while is confined and focused using metal apertures and magnetic lenses into a thin, focused, monochromatic beam. The sample is irradiated by the beam and interactions occur inside the irradiated sample, affecting the electron beam. These interactions and effects are detected and transformed into an image. The above steps are carried out in all electron microscopes regardless of type.

In SEM (Fig. 2.7), the electron beam is thermionically emitted from an electron gun fitted with a tungsten filament cathode and focused in vacuum into a fine probe that is rastered over the surface of the specimen. The electron beam passes through scan coils and objective lens that deflect horizontally and vertically so that the beam scans the surface of the sample. SEM works on a voltage between 2 to 50 kV. Other types of electron emitters include lanthanum hexaboride ($LaB_6$) cathodes and field emission guns (FEG) [11], which may be of the cold-cathode type using tungsten single crystal emitters or the thermally-assisted Schottky type, using emitters of zirconium oxide. When the primary electron beam interacts with the sample, the energy exchange between the electron beam and the sample results deceleration of incident electrons through the energy dissipation and produces a variety of signals. These signals include secondary electrons, backscattered electrons, diffracted backscattered electrons, characteristic X-rays, visible light (cathodo-luminescence) and heat. Secondary and backscattered electrons are conventionally separated

according to their energies [12]. Detectors of each type of electrons are placed in the microscope in proper positions to collect them.

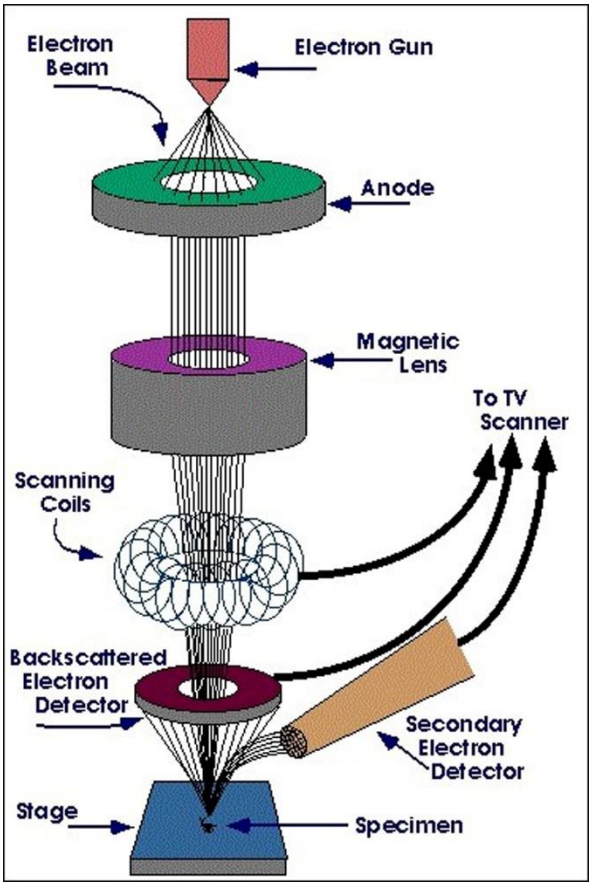


**Figure 2.7** Schematic diagram of Scanning electron microscope.

Emission of secondary electrons by inelastic scattering of incident electrons produces the SEM micrograph of the sample. Due to the very narrow electron beam, SEM micrographs have a large depth of field yielding a characteristic three-dimensional appearance useful for understanding the surface structure of a sample. Whereas, characteristic X-rays produced by inelastic collisions of the incident electrons with electrons in discrete orbitals (shells) of atoms in the sample are used for elemental analysis. The process is known as energy dispersive analysis of X-ray (EDAX). A field-emission cathode in the electron gun of a SEM (FESEM) provides narrower probing beams at low as well as high electron energy, resulting in both improved spatial resolution and minimized sample charging and damage. The sample preparation includes a thin gold coating on the sample (mainly for electrically non conducting samples) to avoid static charge accumulation during

SEM imaging. The FESEM and EDAX image of NiO nanowires is shown in Fig. 2.8 (a) & (b), respectively.

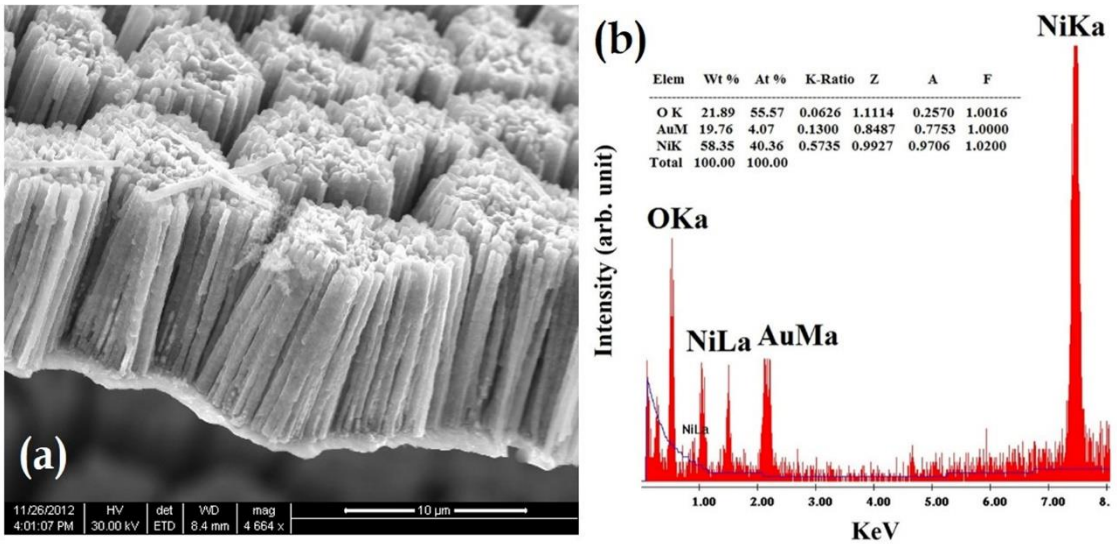


**Figure 2.8 (a)** SEM image of NiO nanowires, (b) EDAX spectra obtained from NiO nanowires.

### 2.4.2.2. Transmission Electron Microscope (TEM)

In TEM, mainly two different types of interactions between the electron beam and specimen have been used to construct an image; these are unscattered electrons (transmitted beam) and elastically scattered electrons (diffracted beam). Schematic diagram of a TEM is shown in Fig. 2.9 (a) & (b). In this process, incident electrons are transmitted through the thin specimen without any interaction occurring inside the specimen. The transmission of unscattered electrons is inversely proportional to the specimen thickness. Areas of the specimen that are thicker will have fewer transmitted unscattered electrons and so will appear darker, conversely the thinner areas will have more transmitted and thus will appear lighter. This mode of operation to create contrast in image is known as bright field imaging mode. TEM image of Ni/NiO core/shell nano-heterostructures is shown in Fig. 2.9 (c). Another important mode of TEM imaging is electron diffraction. In case of crystalline sample the electron beam undergoes Bragg scattering in accordance with the Bragg's law as given by Eq. (2.1). All incident electrons have the same energy (thus wavelength) and enter the specimen normal to its surface. Now, the electrons that are scattered by the same set of parallel planes can be collated using magnetic lenses to form a

pattern of spots; each spot corresponding to a specific atomic spacing (or crystalline plane). This pattern can then yield information about the orientation, atomic arrangements and phases present in the area being examined. Diffraction pattern image of Ni/NiO core/shell nano-heterostructures is shown in Fig. 2.9 (d).

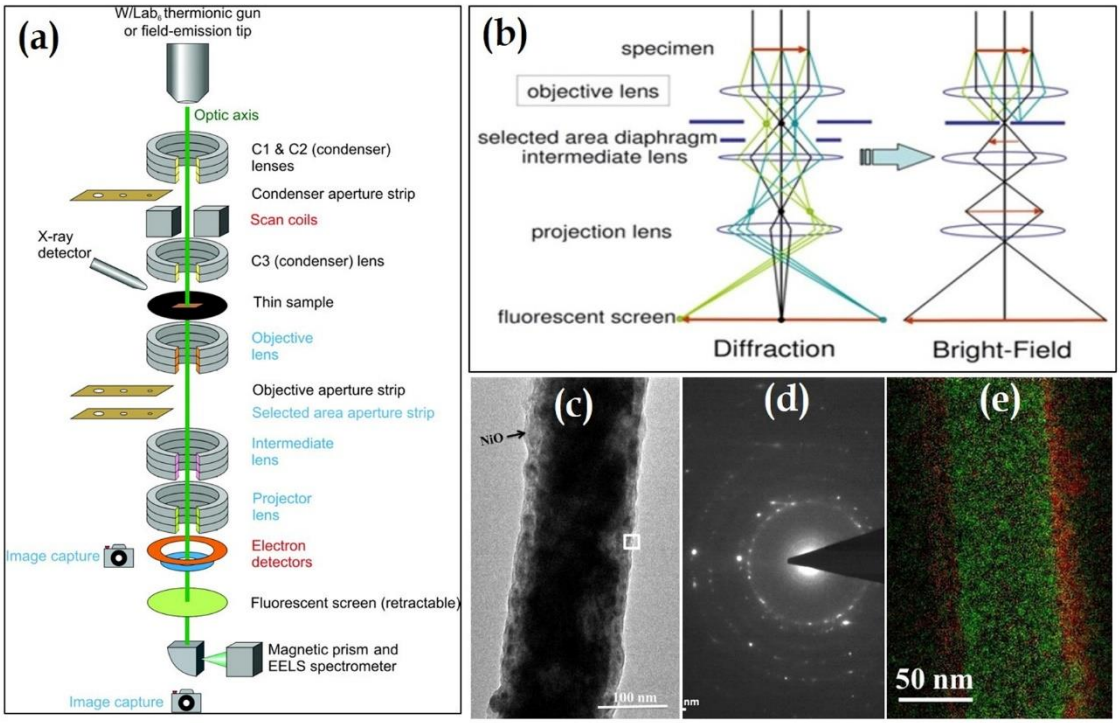


**Figure 2.9** (a) & (b) Schematic diagram of TEM image forming by electron beam; (c), (d) and (e) are the TEM image, selected area electron diffraction (SAED) pattern and EFTEM image, respectively, of Ni/NiO core/shell nano-heterostructures.

In case of high resolution TEM (HRTEM) mode, we can achieve a resolution as much as 0.2 nm which is very efficient in observing the lattice fringes of the specimen under observation. Energy filtered transmission electron microscopy (EFTEM) is a technique used in TEM, where electrons of particular energies are used to form an image or diffraction pattern. This technique provides information about the elemental composition of the material under observation. EFTEM image of Ni/NiO core/shell nano-heterostructures is shown in Fig. 2.9 (e).

Another technique that is performed in TEM is electron energy loss spectroscopy (EELS) where a material is illuminated with electrons having known narrow range of kinetic energy. These electrons undergo inelastic scattering with

some energy loss. The amount of energy loss is measured with an electron spectrometer and represented in terms of what caused the energy loss.

### 2.4.3. X-ray Photoelectron Spectroscopy (XPS)

XPS is a quantitative spectroscopic technique to measure the elemental composition, chemical formula, chemical state and electronic state of elements that exist within the material under observation. XPS spectra is obtained by illuminating the sample by x-rays and simultaneously measuring the kinetic energies and the number of electrons that escape from the top 1-10 nm of the substance being analyzed. As the energy of the irradiating x-ray photon ($E_{Photon}$) is known, the binding energy ($E_{Binding}$) of each electron emitted from the surface of the material can be calculated using the Ernest Rutherford equation as given below.

$$E_{Binding} = E_{Photon} - (E_{Kinetic} + \Phi) \tag{2.3}$$

where, $E_{Kinetic}$ is the kinetic energy of the emitted electron and Φ is the work function of the spectrometer.

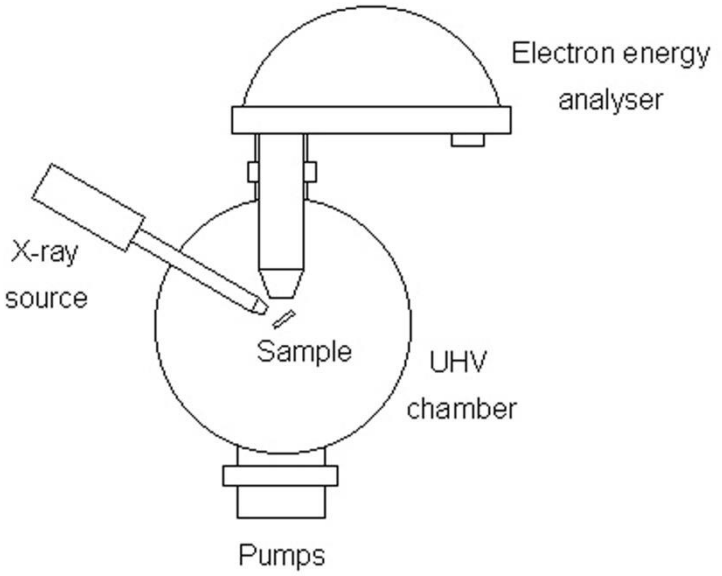


**Figure 2.10** Schematic diagram of an XPS spectrometer.

XPS spectrum is a plot of the number of electrons detected (Y-axis) with the binding energy of that electrons (X-axis). Each material produces its characteristics XPS peaks that correspond to the electronic configuration of the electrons in different

orbitals such as 1s, 2s, 2p etc. and the number of electrons detected is directly proportional to the amount of that element present in the irradiated portion of the sample. As the electron counting detector in XPS instruments is typically 1 m away from the x-ray irradiated sample, so, XPS must be performed in ultra-high vacuum (UHV) condition. The schematic diagram of the XPS system is shown in Fig. 2.10.

## 2.5. Magnetic Characterization Techniques

### 2.5.1. Vibrating Sample Magnetometer (VSM)

Vibrating sample magnetometer (VSM) is based on Faraday's law that states, an emf (electromotive force) will be generated in a coil if there is a change in flux linking the coil. The induced emf in a coil with 'n' turns with a cross-sectional area of 'a' can be written as,

$$V = -na\frac{dB}{dt} \tag{2.4}$$

When the coil is positioned in a constant magnetic field,

$$\mathbf{B} = \mu_0\mathbf{H} \tag{2.5}$$

Now if we place a magnetic sample having magnetization '**M**' near the coil, then

$$\mathbf{B} = \mu_0 (\mathbf{H} + \mathbf{M}) \tag{2.6}$$

The corresponding flux change can be written as

$$\Delta\mathbf{B} = \mu_0\mathbf{M} \tag{2.7}$$

The induced emf in pick-up coils expressed at the beginning thus can be rewritten as

$$Vdt = -na\mu_0 M \tag{2.8}$$

The above equation implies that the output signal of the coil is proportional to the magnetization M but independent of the magnetic field in which the magnitude of **M** is to be determined.

Schematic diagram of a VSM is shown in Fig. 2.11. In a VSM, the sample is subjected to a sinusoidal motion (of frequency ν) and the corresponding voltage is induced in suitably located stationary pickup coils.

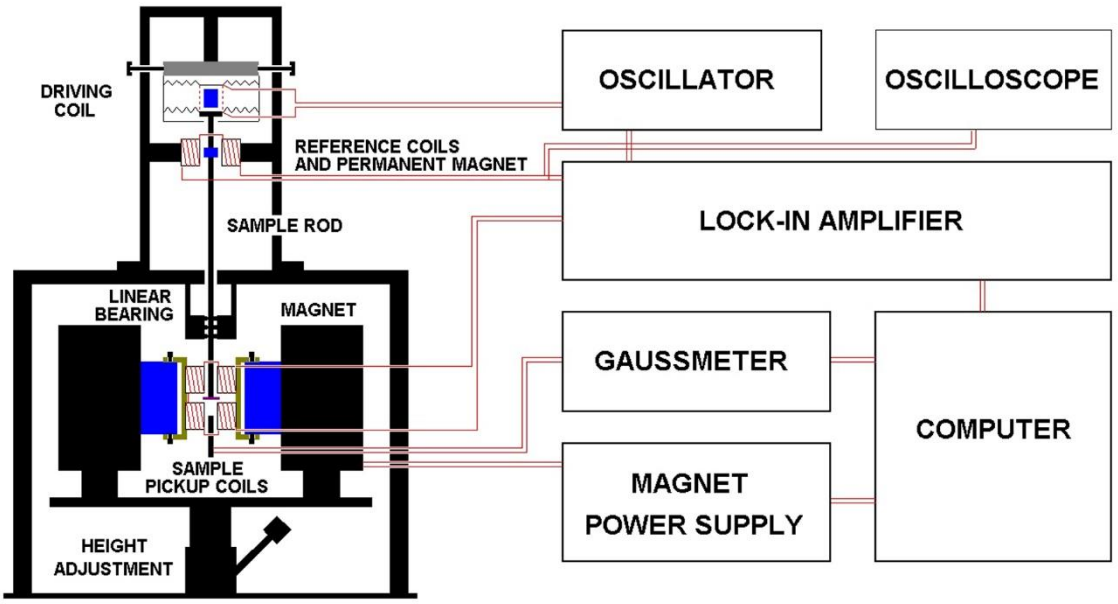


**Figure 2.11** Schematic diagram of Vibrating sample Magnetometer.

The electrical output signals of these latter coil has the same frequency (ν). Its intensity of proportional to the magnetic moment of the sample, the vibration amplitude and the frequency (ν). The schematic diagram of the set-up is shown in fig f below. The sample to be measured is centered in the region between the poles of a electromagnet which can generate a uniform magnetic field $\boldsymbol{H}_0$. A thin vertical non-magnetic sample rod (made of plastic/quartz) connects the sample holder with a transducer assembly located above the magnet. The transducer converts a sinusoidal as drive signal (generated by an oscillator/amplifier circuit) into a sinusoidal vertical vibration of the sample rod. The sample is thus subjected to a sinusoidal motion in the magnetic field $\boldsymbol{H_0}$.

Pickup coils made of copper and mounted on the poles of the magnet pick up the signal resulting from the motion of the sample. However, though the pick-up coil signal at the vibration frequency (ν) is proportional to the magnitude of the moment of the sample, it is also proportional to the vibration amplitude and frequency. Thus the moment readings taken simply by measuring the amplitude of the signal are subject to errors due to variation in amplitude and frequency of vibration. In order to

avoid this difficulty, a nulling technique is introduced employing a vibrating capacitor for generating a reference signal that varies with moment, vibration amplitude and frequency in the same manner as the signal from the pickup coils. When these two signals are processed in an appropriate manner, it is possible to eliminate the effects of vibration amplitude and frequency shifts. In that case, one obtains readings that vary only with the moment of the sample.

In case of NWs, we measured the corresponding hysteresis loops at two different orientations of the samples as shown in Fig. 2.12. The NWs are placed either parallel to the external uniform magnetic field $H_0$ named as out-of-plane (OP) configuration or perpendicular to $H_0$ named as in-plane (IP) configuration. The words out-of-plane (OP) and in-plane (IP) are coined from the orientation of the flat planes of alumina or polycarbonate membranes within which the NWs are deposited.

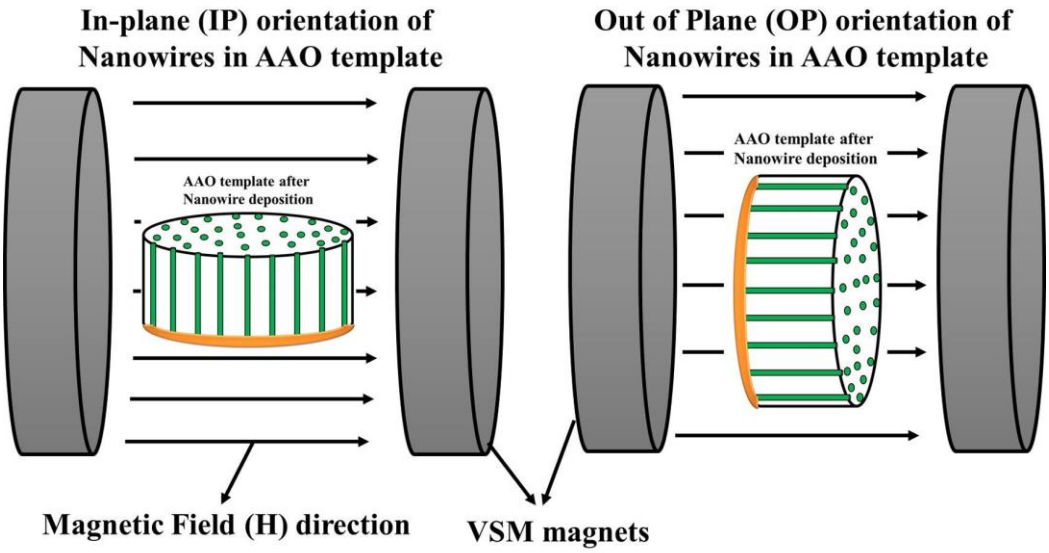


**Figure 2.12.** Placement of NW samples between the pole pieces of VSM magnet.

The VSM in our laboratory (Lakeshore made) has a maximum magnetic field generating capability of 2.1 T without cryogenic system and 1.76 T can be achieved with $LN_2$/LHe dewar between the coils. The moment versus temperature or temperature dependent hysteresis loops can be measured using a cryogenic system (Liq. $N_2$) that can operate within a temperature range of 80 to 400 K with temperature stability of ±0.2 K and temperature resolution of 0.001 K. Noise level of

1.25 μemu (RMS value) in moment measurement can be achieved using the system [13].

### 2.5.2. Magnetic Barkhausen Noise (MBN) measurement technique

Barkhausen technique has his importance because of his capability to characterize material properties accurately, easily, quickly and without damaging tested materials. Magnetic Barkhausen Noise (MBN) is considered as an important technique for micro structural and mechanical characterization of ferromagnetic materials like steels. The main advantages of this method are that this technique has non-destructive character and it offers the possibility to evaluate samples of various shapes and sizes. MBN is sensitive to various parameters which affect the magnetic domains configuration and domain-wall, pinning sites, which are strongly influenced by grain size, composition, different phases, surface conditions, hardness, residual stress, fatigue and damage, magnetic field strength and applied stress.

The Magnetic Barkhausen Noise technique is based on the concept that the ferromagnetic materials consist of domains which are magnetized along a certain crystallographic easy direction of magnetization. Domains are separated from one another by boundaries (domain walls). Application of a magnetic field causes the domain wall movement: the domain on one side of the wall has to increase in size while the domain on the opposite side of the wall shrinks. The result is a change in the overall magnetization of the sample. If a coil of conducting wire is placed near the sample during the domain wall movement, the resulting change in magnetization will induce an electrical pulse in the coil. In 1919 professor Barkhausen proved that the magnetization process (hysteresis loop) is not continuous but is built from small steps caused when the magnetic domains move under an applied magnetic field as shown in Fig. 2.13. When the electrical pulses produced by all domain movements are added together, a noise-like signal called Barkhausen noise is generated. Barkhausen noise spectrum starts at the magnetizing frequency and extends beyond 2 MHz in most ferromagnetic materials. The signal is exponentially damped as a function of the travelled distance inside the material.

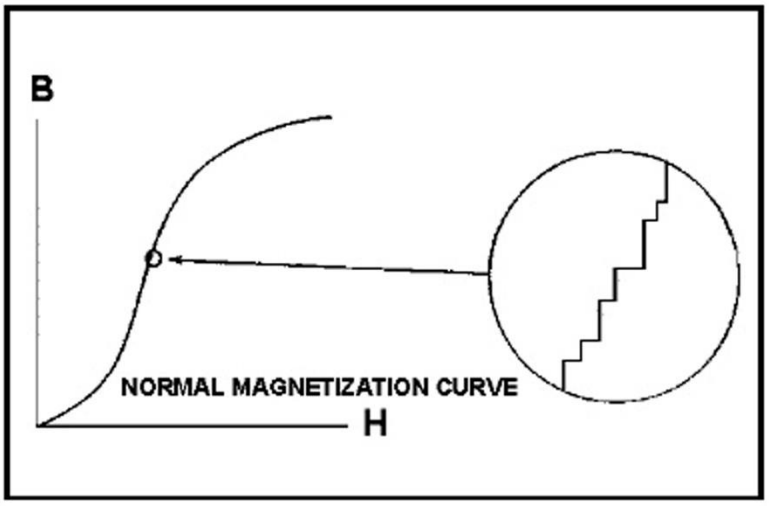


**Figure 2.13:** Magnetic Barkhausen Noise (MBN) in the hysteresis loop.

Magnetic Barkhausen Noise is characterized by several different parameters. The parameter is not limited to a particular aspect of the Barkhausen signal, but simply a generic parameter that is calculated from a complete cycle of the Barkhausen emission. Some of the parameters that are frequently used for MBN analysis will be discussed in this. Usually, only voltage above and below a certain threshold are considered in order to maintain the integrity of the analysis. MBN energy ($E_{MBN}$): $E_{MBN}$ is calculated by integrating the square of these voltages with respect to time i.e.

$$E_{MBN} = \sum_{i=1}^{n} \int V_i^2 dt \tag{2.9}$$

where the time integral is over each event and the summation is taken over all n measured events.

Schematic diagram of Magnetic Barkahusen Noise set-up is shown in Fig. 2.14 (a). Generation detection and analysis of Barkhausen noise were accomplished using a home fabricated Barkhausen Noise experimental setup as shown in Fig. 2.14 (b). The instrument consists of a Helmholtz coil for applying a time varying magnetic field to the sample to generate Barkhausen Noise. The signal to the Helmholtz coil produced by a 15 MHz Function/Arbitrary waveform Generator (Agilent -33120A) and amplified by a bipolar power supply /Amplifier (Kepco, BOP 72-3M). The sweep field frequency was set at various frequencies from the waveform generator (4 Hz and 12 Hz).

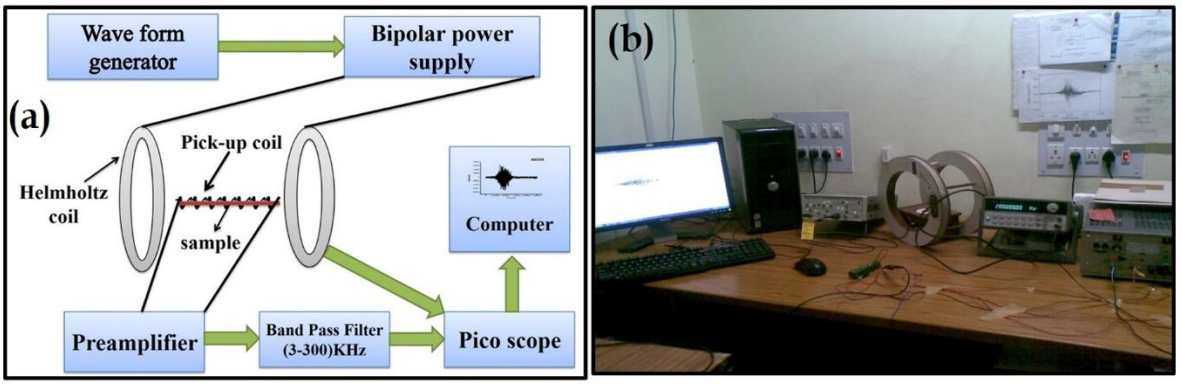


**Figure 2.14 (**a) Schematic and (b) Experimental setup **of** Magnetic Barkhausen Noise (MBN measurement.

Barkhausen Noise was detected using a pick –up coil wound around the sample located at the center of the Helmholtz coil, with the sample aligned parallel to the direction of the magnetic field. The signal from the pick-up coil was amplified by the low noise Preamplifier (Stanford research systems, Model SR560), passed through the band pass filter and then collected to a personal computer using Pico scope Software, as shown the photograph of the experimental setup for measuring MBN.

## 2.6. Optical Characterization Techniques

### 2.6.1. Photoluminescence (PL) Spectroscopy

PL is a process in which a specimen absorbs photons (electromagnetic radiation) of particular energy and then re-radiates photons with different energies. Quantum mechanically, this can be described as excitation of an electron to a higher energy state by absorbing photons and then a return to a lower energy state with the emission of photons. The period between absorption and emission is very short, in the order of 10 nanoseconds. Steady state PL measurements of our samples were done in Horiba Jobin Yvon Fluorolog 3 spectrofluorimeter. Schematic diagram of the PL spectrometer is shown in Fig. 2.15.

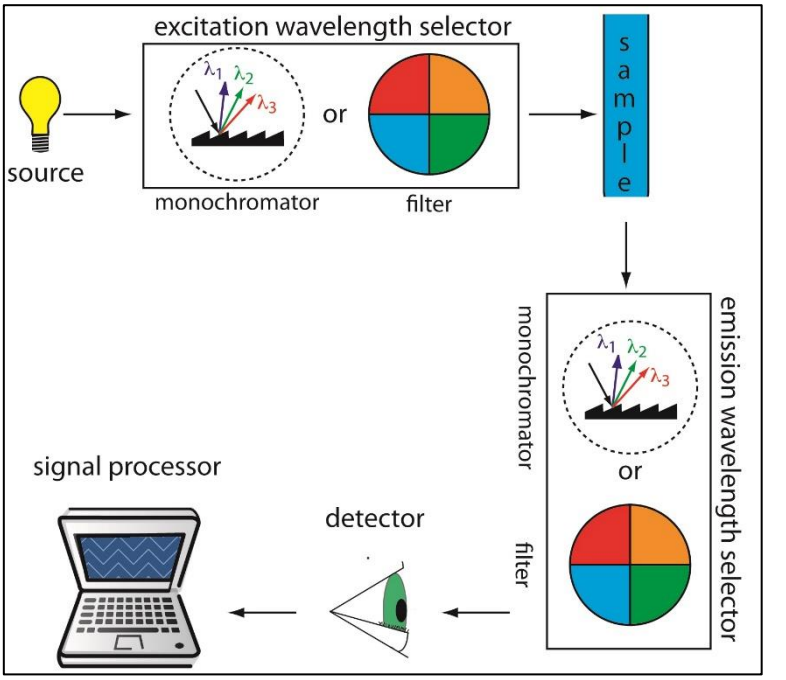


**Figure 2.15** Schematic diagram of photoluminescence spectrometer.

## 2.7. Electrochemical Characterization Techniques

The electrochemical properties of the samples were investigated by cyclic voltammetry (CV), galvanostatic (GV) charge/discharge and electrochemical impedance spectroscopy (EIS) tests by using a software controlled conventional three-electrode electrochemical cell (potentiostat AutoLab-30) consisted of the as-prepared samples as the working electrode, saturated Ag/AgCl as the reference electrode, the Pt wire as the counter electrode and 1M KOH solution as electrolyte, at room temperature.

### 2.7.1. Cyclic Voltammetry

A cyclic voltammogram is obtained by measuring the current at the working electrode during the potential scans. Fig. 2.17 shows a cyclic voltammogram resulting from a single electron reduction and oxidation. Consider the following reversible reaction:

$$M^{+} + e^{-} \rightleftharpoons M \tag{2.10}$$

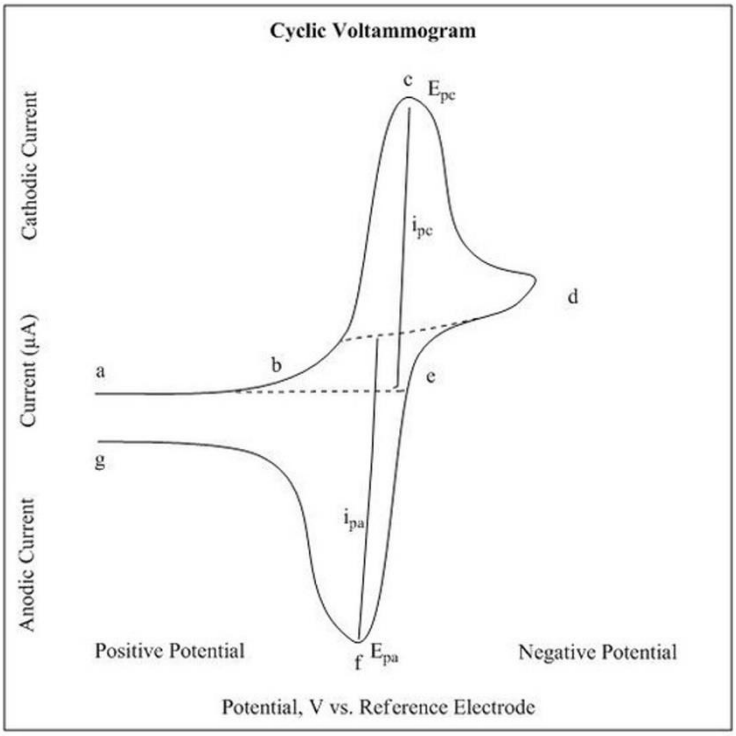


**Figure 2.16** Voltammogram of a Single electron oxidation-reduction.

In Fig. 2.16, the reduction process occurs from (a) the initial potential to (d) the switching potential. In this region the potential is scanned negatively to cause a reduction. The resulting current is called cathodic current ($i_{pc}$). The corresponding peak potential occurs at (c), and is called the cathodic peak potential ($E_{pc}$). The Epc is reached when all of the substrate at the surface of the electrode has been reduced. After the switching potential has been reached (d), the potential scans positively from (d) to (g). This results in anodic current ($I_{pa}$) and oxidation to occur. The peak potential at (f) is called the anodic peak potential ($E_{pa}$), and is reached when all of the substrate at the surface of the electrode has been oxidized.

A CV curve generally has a rectangular shape when the capacitance merely originates from the EDL and there are no Faradaic reactions between the active materials and the eletrolyte. The specific capacitance is estimated from the current at the middle point of potential range (*I*) and scan rate(*f*) according to the equation $C_{sp} = I/mf$ [14], where *m* is the mass of active material. With respect to pseudocapacitors, the pesucocapacitive behaviors usually lead to the presence of redox peaks with a derivation from the rectangle shape. Thus, the average specific capacitance is

calculated using the voltammetric charge integrated from the CV curve according to the following equation [15, 16]:

$$C_{sp}(F/g) = \frac{Q}{2mV} = \frac{I}{2mVf}\int_{V_c}^{V_a} I(V)dV \qquad (2.11)$$

where Q is the total charge obtained by the integration of positive and negative scans in a CV curve, *m* is the mass of the active material in two electrodes, *f*, the scan rate, ($V=Va - Vc$) represents the potential window.

## 2.7.2. Galvanostatic Charge-discharge

The typical galvanostatic charge/discharge (GCD) curves are shown in Fig. 2.17. For the GCD technique, the potential of a supercapacitor is linear, or almost linear with respect to the charge/discharge time ($dV/dt$ = constant) during a constant current operation, so that the state-of-charge (SOC) can be exactly pinpointed. In contrast, most batteries exhibit a relatively constant operating voltage because of the thermodynamics of battery reactants. As a result, their SOC could not be measured precisely [17, 18]. From a GCD curve, the specific capacitance of a supercapacitor cell ($C_{sp}$) can be calculated according to (Equation (2.12)):

$$C_{sp} = \frac{I}{m(dV/dt)} \qquad (2.12)$$

in which *I* (in A) is the discharge current, *m* (in g) is the total mass of active materials in two electrodes, *t* (in s) is the discharge time, *V* (in V) is the potential during the discharge process after IR drop. Hence, $dV/dt$ is the slope of discharge curve. It is recommended that the specific capacitance should be calculated by using two datum points from the discharge curve with $dV/dt = (V_{max} - ½V_{max})/(t2-t1)$, especially in the case of the nonlinear response between potential and time resulting from pseudocapacitive reactions [19]. Here, *t2* and *t1* (in s) are the discharge times at the points of maximum potential ($V_{max}$) and half of the voltage ($½V_{max}$).

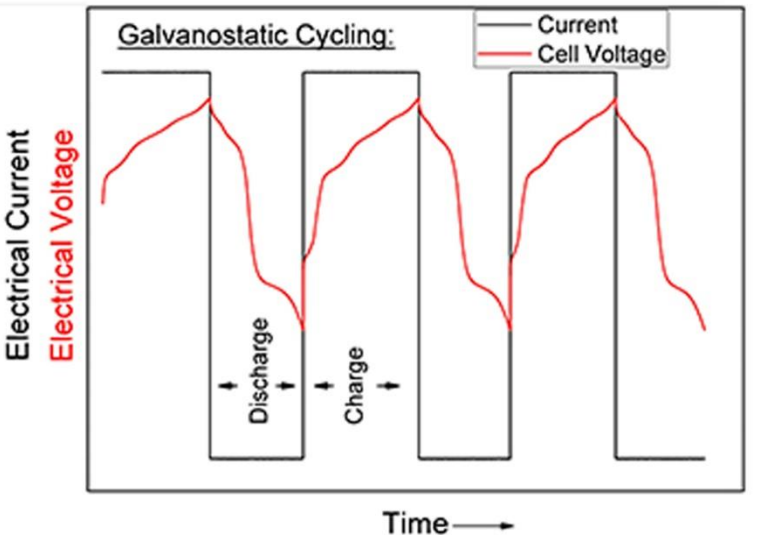


**Figure 2.17** Typical galvanostatic charge/discharge cycles of standard sample.

Energy density and power density are two important parameters to evaluate the capacitive performance of a supercapacitor cell. The energy density is the capacity to perform work, whereas the power density exhibits how fast the energy is delivered. The standard approach to obtaining the energy and power densities is based on the specific capacitance ($C_{sp}$) of a two-electrode system. The maximum energy stored ($E_{max}$, *Wh/kg*) and power delivered ($P_{max}$, *W/kg*) for a supercapacitor cell is respectively given in equations (2.13) and (2.14) [19, 20].

$$E_{\max} = 0.5 C_{sp} V^2 \tag{2.13}$$

$$P_{\max} = \frac{V^2}{4R_s} \tag{2.14}$$

in which $V$ is the cell voltage (in $V$). The cell voltage is determined by the thermodynamic stability of the electrolyte solution. The specific capacitance of the cell depends extensively on the electrode materials. Hence, a broad operating cell voltage, a large capacitance, and minimum ESR are essential for a supercapacitor with good performance. In the fundamental research, the transformed equations below are usually used to calculate the maximum energy density and power density [21].

$$E_{\max} = \frac{0.5 C_{sp} V^2}{3.6} \tag{2.15}$$

$$P_{\max} = \frac{E_{\max} 3600}{t} \tag{2.16}$$

## 2.7.3. Electrochemical Impedance Spectroscopy

Electrochemical impedance spectroscopy (EIS) is a powerful tool to evaluate the supercapacitor frequency behavior and electrochemical series resistance (ESR). Normally, EIS is conducted at the open circuit voltage (OCV) by applying a small amplitude of alternative potential (5 ~ 10 mV) in a range of frequency (generally 0.01 to 100Hz). The resistance ($Z$) is defined as, $Z = Z' + jZ''$, where $Z'$ and $Z''$ are the real part and the imaginary part of impedance, respectively. The specific capacitance is calculated from the imaginary part ($Z''$) of the collected EIS data according to

$$C = \frac{-1}{2\pi v Z'' m} \tag{2.17}$$

where, $v$ (in Hz) is the frequency, and $m$ is the mass of electrode materials.

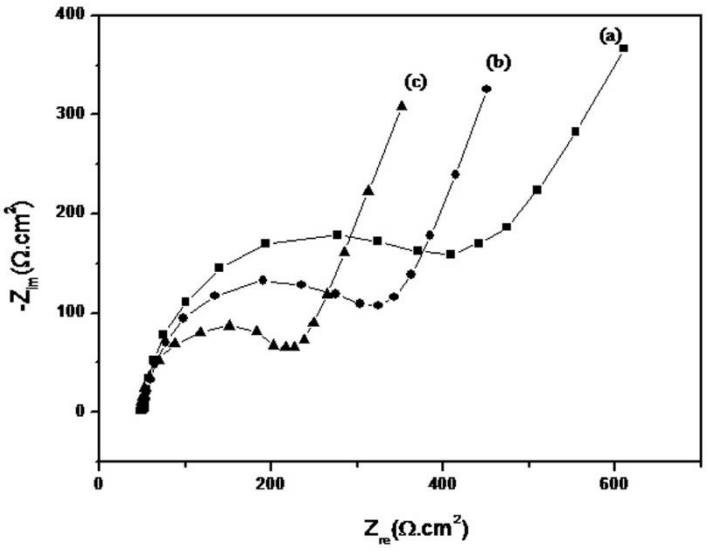


**Figure 2.18** Typical Nyquist plot of standard sample.

The other important form for EIS is to plot $Z'$ against $Z''$ to obtain a so-called Nyquist plot. A typical Nyquist plot impedance curve exhibits a semicircle over the

high frequency range, followed by a linear part in the low frequency region, as shown in Fig. 2.18. It is noteworthy that a large semicircle observed from a Nyquist plot is an indicative of high charge-transfer resistance, contributing to the poor electrical conductivity of materials, whereas a more vertical the line is more closing to an ideal capacitor [22]. The ESR values are determined from a linear fit to the IR drop values (*IR drop*) obtained from GCD curves at different current densities according to [23, 24]:

$$IR_{drop} = a + bI \tag{2.18}$$

where *a* represents the difference between the applied potential and the charged potential of the capacitor, *b* is two times of the value of ESR (Rs), and *I* is the discharge current. Therefore, the maximum power density follows:

$$P_{\max} = \frac{V^2}{4R_s} = \frac{(4-a)^2}{2b} \tag{2.19}$$

# Bibliography


[1] H. Asoh, K. Nishio, M. Nakao, T. Tamamura and H. Masuda, *J. Electrochem. Soc.*, **148**, B152 (2001)

[2] F. Brown and W.D. Mackintosh, *J. Electrochem. Soc.*, **120,** 1096 (1973)

[3] K. Kobayashi, K. Shimizu, G.E. Thompson, and G.C. Wood, *J. Appl. Electrochem.*, **15,** 781 (1985)

[4] H. Wang and H. W. Wang, *Mater. Chem. Phys.*, **97**, 213 (2006)

[5] J. P. OSullivan and G. C. Wood, *Proc. Roy. Soc. Lond. A*, **317**, 511 (1970)

[6] B. D. Cullity and S. R. Stock, Elements of X-ray Diffraction, 3rd Edition**,** Prentice Hall (2001)

[7] R. Erni, M. D. Rossell, C. Kisielowski and U. Dahmen, *Phys. Rev. Lett.*, **102** (9), 096101(2009)

[8] E. Ruska, Nobel Foundation. Retrieved 2010-01-31 (1986)

[9] M. Knoll, *Zeitschrift für technische Physik* **16**, 467 (1935)

[10] Cambridge Scientific Instrument Company, USA.

[11] T.R. Groves, H.C. Pfeiffer, T.H. Newman and F.J. Hohn, *J. Vac. Sci. Technol. B*, **6**(6), 2028 (1988)

[12] C.R. Brundle, C.A. Evans Jr., S. Wilson, Encyclopedia of materials characterization, Butterworth-Heinemann publications, 1992

[13] Lake Shore Cryotronics, Inc., USA

[14] P. Simon and Y. Gogotsi, *Nat. Mater.*, **7**, 845 (2008)

[15] A. Burke, *J. Power Sources,* **91**, 37 (2000)

[16] L. Piraux, S. Dubois, J. L. Duvail, K. Ounadjela and A. Fert, *J. Magn. Magn. Mater.*, **175**, 127 (1997)

[17] J. R. Miller and P. Simon, *Science*, **321**, 651 (2008)

[18] D.J. Sellmyer, M. Zheng and R. Skomski, *J. Phys. Cond. Mat.*, **13**, R433 (2001)

[19] H. Zhu, S. Yang, G. Ni, D. Yu and Y. Du, *Scripta Materialia*, **44**, 2291 (2001)

[20] Zhang, L. L. and X. S. Zhao. *Chem. Soc. Rev.,* **38**, 2520 (2009)

[21] D. Hulicova-Jurcakova, A. M. Puziy, O. I. Poddubnaya, F. Sualrez-Garcca, J. M. D. Tascoln and G. Q. Lu, *J. Am. Chem. Soc.*, **131**, 5026 (2009)

[22] P. L. Taberna, P. Simon and J. F. Fauvarque, *J. Electrochem. Soc.*, **150**, A292 (2003)

[23] Y. R. Nian and H. Teng, *J. Electrochem. Soc.,* **149**, A1008 (2002)

[24] A. Izadi-Najafabadi, S. Yasuda, K. Kobashi, T. Yamada, D. N. Futaba, H. Hatori, M. Yumura, S. Iijima and K. Hata, *Adv. Mater.*, **22**, E235 (2010)

# Chapter 3

# Porous Anodic Aluminum Oxide: Synthesis and Characterization

This chapter describes the synthesis of highly ordered porous anodized alumina oxide (AAO) membranes, standardization of anodization process with pores of different sizes of AAO templates and study of their structural, morphological optical and magnetic properties in detail.

## 3.1. Preamble

Recently, one-dimensional (1-D) nanostructures such as nanowires, nanorods, nanobelts, and nanotubes have also become the focus of intensive research owing to their unique application in the mesoscopic physics and fabrication of nanoscale devices [1], it is generally accepted that 1D nanostructures provide a good system to investigate dependence of electrical, magnetic and mechanical etc. properties on dimensionality and size reduction (or quantum confinement). They are also expected to play an important role as both interconnects and functional units in fabricating electronics, magnetic, optoelectronics and electrochemical devices with nanoscale dimensions. In comparison with quantum well and dots, the advancement of 1D nanostructures have been slow until very recently, as hindered by the difficulties associated with the synthesis and fabrication of these nanostructures with well-controlled dimension, morphology, phase purity and chemical composition. Although 1D nanostructures can now be fabricated using a number of advanced nanolithography techniques [2], such as electron-beam or focused ion beam writing, X-ray or UV lithography, further development of these techniques into practical routes to large quantities of 1D nanostructures from a diversified range of materials, rapidly, and at reasonably low costs, still requires great ingenuity. In contrast, unconventional methods based on chemical synthesis might provide an alternative and the intriguing strategy for generating 1D nanostructures in terms of material diversity, cost, throughout, and the potential for high volume production [3].

In 1857, Buff first found that aluminum can be electrochemically oxidized in an aqueous solution to form an oxide layer that is thicker than the native one [4]. This phenomenon has been called "anodization" because the aluminum part to be processed constitutes the anode in an electrolytic cell. In the early 1920s, the phenomenon observed by Buff was exploited for industrial scale applications, for example, protection of seaplane parts from corrosive seawater [5]. Many desirable engineering properties such as excellent hardness, corrosion, and abrasion resistance can be obtained by anodizing aluminum metals in acid electrolytes [6].

Recently, this nearly century-old industrial process has been drawing increasing attention from scientists in the field of nanotechnology. Template

synthesis in nanometer scale, however, proved now another elegant, inexpensive and technologically simple approach for the fabrication of various nanoscale sophisticated materials (e.g. arrays of nanowires, nanotubes) [7, 8]. The templates can be synthesize by electrochemical anodization of thin metal sheet (thickness of micrometer length scale) of aluminum, tin or zinc. Porous AAO film grown on aluminum is composed of a thin barrier oxide layer in conformal contact with aluminum, and an overlying, relatively thick, porous oxide film containing mutually parallel nanopores extending from the barrier oxide layer to the film surface [9]. Each cylindrical nanopore and its surrounding oxide region constitute a hexagonal cell aligned normal to the metal surface. Under specific electrochemical conditions, the oxide cells self-organize into the hexagonal close packed arrangement, forming a honeycomb-like structure [9-11]. Pore diameter and density of self-ordered porous AAOs are tunable in wide ranges by properly choosing anodization conditions: pore diameter = 10−400 nm and pore density = $10^{8}$−$10^{10}$ pores $cm^{-2}$. We synthesize highly ordered porous alumina templates by electrochemical process. In this chapter, we discuss the synthesis procedure of the templates and their structural magnetic and optical properties. Further, this novel and tunable structural features of porous AAOs will be used for synthesizing a diverse range of nanostructured materials in the forms of nanowires, and nanotubes, and also for developing functional nanodevices.

## 3.2. Experimental Details

In order to prepare alumina membrane in a more simple way, we took an aluminum sheet with the purity of ~ 99.998% and purchased from Sigma Aldrich with the thickness of ~ 150 nm and area of ~ (5 × 10) mm. One side of the sheets is covered by a transparent tape, so that only the other side of aluminum comes to the contact of electrolyte solution. Then a two-step anodizing method was employed to obtain the AAO template. The detail of the experimental set-up is discussed earlier in *chapter 2*. By varying the experimental parameters like concentration of electrolyte and applied anodization voltage, we prepared various AAO templates. The two-step electrochemical anodization of the aluminium foils was carried out in various acid

electrolyte solution (3-20 wt% of oxalic, sulfuric and phosphoric) by varying the D.C. anodization voltage, and current density. The voltage was maintained at a constant value of ~ 40 to 80 V to achieve a current density of 200-500 $Am^{-2}$. The anodization was carried out at $11^0$ C to dissipate the heat generated during the exothermic reaction of conversion of aluminum in to alumina. The first anodization was carried out for 15 minutes. The thin porous alumina layer grown on the aluminium foil surface after the first-stage of anodization was removed by chemical etching using a mixture of 60 wt% phosphoric ($H_3PO_4$), 28 wt% sulphuric ($H_2SO_4$) and 12 wt% nitric ($HNO_3$) acid solution. The etched Al foil was re-anodized for 3 hours for the second time keeping all the anodization parameters the same as that in the first-stage to obtain more uniform porous structure. Finally the hexagonally arranged nanoporous structure was detached from the base aluminum using mercury chloride ($HgCl_2$) solution. The as prepared AAO template was dipped inside the 10 wt% phosphoric acid ($H_3PO_4$) solution for 15 min for pore widening and pore rounding of the self-organized nanoporous template. Consequently, AAO templates with regular pore arrangement were obtained.

The crystallographic nature of the as-prepared AAO template has been analyzed by X-ray diffraction (XRD, Panalytical X'Pert Pro diffractometer), and the composition of the AAO template has been determined by energy dispersive X-ray (EDAX) analysis. The morphology and the structure of the arrays of AAO template studied by scanning electron microscope (SEM, FEI Quanta-200 Mark-2) and transmission electron microscope (TEM, FEI TECNAI G2 TF20ST). The crystalline structure of the AAO template has been further investigated by the high-resolution TEM (HRTEM). The PL measurements of the AAO template has been conducted using a spectrofluorometer (Horiba JobinYvon, Fluorolog-3) under a Xe lamp source. RT magnetic measurements of the AAO template has been performed using a vibrating sample magnetometer (VSM, Lakeshore, model 7144) by placing the axis of the sample along the direction of the applied magnetic field to get the maximum coupling of the flux.

## 3.3. Results and Discussions

### 3.3.1. Ionic Conduction in Anodic Aluminum Oxide

The current density passing across the oxide film can be written as:

$$j = j_a + j_c + j_e \tag{3.1}$$

Where, $j_a$, $j_c$ and $j_e$ are the anion-contributing, cation-contributing and electron-contributing current density, respectively. Since the electronic conductivity in the aluminum oxide is very low, the ionic current density ($ji = ja + jc$) is the predominant mode to transport the charges. The relationship between the ionic current, $ji$, and the electric field, $E$, can be expressed in terms of the Guntherschultze-Betz equation:

$$j_i = j_0 \exp(\beta E) \tag{3.2}$$

where both $j_0$ and $\beta$ are temperature- and metal-dependent parameters. For the aluminum oxide, he electric field $E$, $j_0$ and $\beta$ are in the range of $10^6$ to $10^7$ V/cm, $10^{-16}$ to $3 \times 10^{-2}$ mA/cm$^2$ and $1 \times 10^{-7}$ to $5.1 \times 10^{-6}$ cm/V, respectively . Based on the Guntherschultze-Betz equation, the rate-limiting steps of the film formation are determined by the ionic transport either at the metal/oxide interface, within the bulk oxide or at the oxide/electrolyte interface. Nowadays, it is generally accepted that the oxides simultaneously grow at both interfaces, e.g., at the metal/oxide interface by $Al^{3+}$ transport and at the oxide/electrolyte interface by oxygen ion transport.

### 3.3.2. Type of Anodic Aluminum Oxide

Anodization of aluminum in aqueous electrolytes forms anodic oxide films with two different morphologies, that is, the nonporous barrier-type oxide films and the porous-type oxide films. The chemical nature of the electrolytes mainly determines the morphology of AAOs [6, 9, 12]. A compact nonporous barrier-type AAO films can be formed in neutral electrolytes (pH 5−7), such as borate, oxalate, citrate, phosphate, adipate, tungstate solution, etc., in which the anodic oxide is practically insoluble. Meanwhile, porous-type AAOs are formed in acidic electrolytes, such as sulfuric, oxalic, phosphoric, chromic acid, etc., in which anodic

oxide is slightly soluble.

The two types of anodic oxides (i.e., barrier- vs porous-type AAO) differ in their oxide growth kinetics. In the case of barrier-type oxide formation under potentiostatic conditions (i.e., U = constant), current density (j) decreases exponentially with time (t). Correspondingly, the film growth rate decreases almost exponentially with time (t), which places a limit on the maximum film thickness obtainable for barrier-type AAO films (Figure 3.1). It has been experimentally verified that the thickness of barrier-type film is directly proportional to the applied potential (U). On the other hand, current density (j) in porous-type anodization under potentiostatic conditions remains almost constant within a certain range of values during the anodization process, due to the constant thickness of the barrier layer at the pore bottom. The thickness of the resulting porous oxide film is linearly proportional to the total amount of charge (i.e., anodization time, t) involved in the electrochemical reaction.

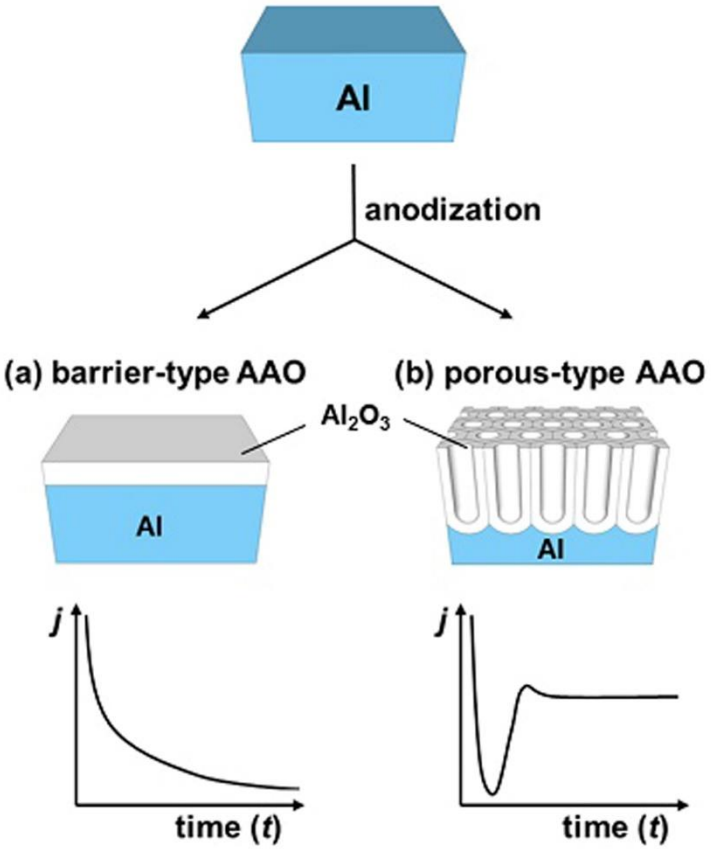


**Figure 3.1.** Two different types of anodic aluminum oxide (AAO) formed by (a) barrier-type and (b) porous-type anodizations, along with the respective current (j) - time (t) transients under potentiostatic conditions

Films of controlled morphology may be developed by appropriate selection of electrolyte and film-forming conditions. Thus, films grown at high current efficiency in largely near-neutral electrolytes at ambient temperatures are highly uniform in thickness and relatively compact; such films are termed as barrier films. It has seen that barrier films may develop at current efficiencies of film formation above approximately 60% [13, 14]. However, irrespective of the current density, the relatively high field developed across the alumina gives rise to $Al^{3+}$ egress and $O^{2-}$ or $OH^-$ ingress through the anodic film.

In acidic electrolytes, or selected alkaline electrolytes, the relatively compact barrier-type anodic films on aluminum no longer develop as a result of anodic polarization. Examination of the resultant film at appropriate magnification and resolution reveals a relatively regular porous oxide film [15]. The pores, of the cylindrical section, pass normally to the macroscopic aluminum surface, but are separated from it by a relatively compact barrier layer of scalloped appearance.

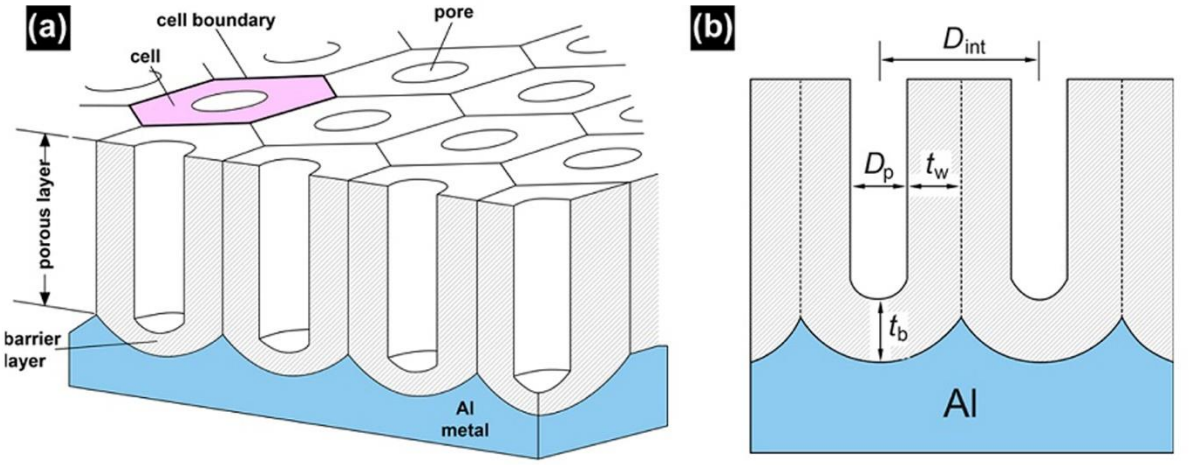


**Figure 3.2.** Schematic diagram of (a) idealized structure of te porous alumina template obtained from anodization of thin aluminum sheet and (b) a cross sectional view of the anodized layer.

In an alumina membrane, each hollow pore is surrounded by alumina wall and can be considered as a cell. Hence, the pore diameter is defined as the diameter of the pores, wall thickness is the thickness of the alumina wall separating two nearest neighbor pores and interpore distance is the centre to centre distance of two consecutive pores. Ideally, an alumina template will consist of closed packed arrays of hexagonally arranged cells and can be represented schematically as shown in Fig.

3.2 below. The alumina templates or membranes consist of nanopores are often characterized by given parameters such as pore diameter ($D_p$), wall thickness ($t_w$), barrier layer thickness ($t_b$) and interpore distance ($D_{int}$).

The pore diameters of the membranes can range from few nanometers to hundreds of nanometer by altering the anodization conditions. On the other hand, the depth of the fine parallel channels can even exceed 100 μm. The growth, morphology and composition of porous anodic films on aluminium have received widespread attention, with the various stages in their development observed and it is known that the major anodic film parameters (barrier layer thickness and pore and cell diameters) are directly dependent upon the steady-state voltage [16].

### 3.3.3. Growth Mechanism of Anodic Aluminum Oxide

The anodic growth of alumina both $Al^{3+}$ cations and oxygen-containing anions (e.g., $O^{2-}$ or $OH^-$) are mobile within the anodic oxide under high electric field (E). $Al^{3+}$ ions migrate outwardly toward the oxide/electrolyte interface, while $O^{2-}$ or $OH^-$ anions move inwardly toward the metal/ oxide interface. Therefore, one can consider both (i) the metal/ oxide and (ii) the oxide/electrolyte interfaces as the growth front of anodic oxide during anodization of a valve-metal. For anodizing aluminum, the following elementary reactions are considered to be possibly occurring at the interfaces (Figure 3.3).

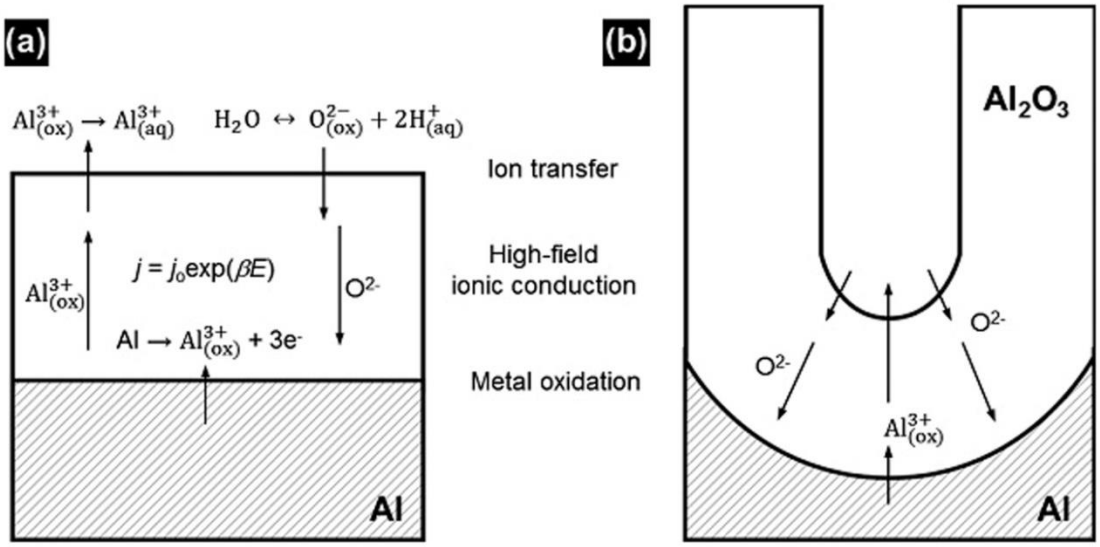


**Figure 3.3.** Schematic diagram showing elementary interfacial reactions for (a) barrier type, (b) porous type anodic aluminum oxide.

(i) At the metal/oxide interface:

$$Al \rightarrow Al^{3+}_{(ox)} + 3e^{-} \tag{3.3}$$

$$2Al^{3+}_{(ox)} + 3O^{2-}_{(ox)} \rightarrow Al_2O_3 \tag{3.4}$$

(ii) At the oxide/electrolyte interface:

$$2Al^{3+}_{(ox)} + 3O^{2-}_{(ox)} \rightarrow Al_2O_3 \tag{3.5}$$

$$Al_2O_3 + 6H^{+}_{(aq)} \rightarrow 2Al^{3+}_{(aq)} + 3H_2O_{(l)} \tag{3.6}$$

$$Al^{3+}_{(ox)} \rightarrow Al^{3+}_{(aq)} \tag{3.7}$$

$$2O^{2-}_{(ox)} \rightarrow O_{2(g)} + 4e^{-} \tag{3.8}$$

$$2H_2O_{(l)} \rightarrow O^{2-}_{(ox)} + OH^{-}_{(ox)} + 3H^{+}_{(aq)} \tag{3.9}$$

Reactions eq. (3.4) and (3.5) correspond to the formation of anodic oxide at the metal/oxide and oxide/electrolyte interfaces, respectively. Reaction eq. (3.6) describes dissolution of anodic alumina by Joule's heat induced oxide dissolution and/or field-induced oxide dissolution. On the other hand, reaction eq. (3.7) occurs through field-assisted direct ejection of $Al^{3+}$ ions from the metal/oxide interface through oxide into the electrolyte. Reactions eq. (3.6)–(3.8) decrease the net current efficiency ($\eta_j$) associated with the anodic oxide formation. Reaction eq. (3.9) describes the heterolytic dissociation of water molecules at the oxide/electrolyte interface, which supplies oxygen anions to the metal/oxide interface to form anodic oxide.

### 3.3.4. Structural Characterization of Anodic Aluminum Oxide

The two-step electrochemical anodization of the aluminium foils was carried out separately in 3 wt% oxalic, sulfuric and phosphoric acid electrolyte solution to fabricate AAO membranes. AAO membranes were prepared in oxalic acid solution by varying the D.C. anodization voltage in between 40 and 80 V is maintaining a constant current density of 200 A/m$^2$. For the AAO membranes synthesized using phosphoric and sulfuric acid electrolytes, D.C. anodization voltages were controlled between 40–45 and 25–30 V, respectively to maintain a constant current density of 200 A/m$^2$. AAO membranes prepared in oxalic, phosphoric and sulfuric acid

electrolytes for 2, 4 and 6 h of second stage anodization are denoted as AO2, AO4 and AO6; AP2, AP4 and AP6; AS2, AS4 and AS6, respectively. The details of the anodization process parameters are summarized in Table 3.1.

**Table 3.1.** Summary of anodization parameters

| Sample | 2nd–Stage anodization Time (h) | Electrolyte Solution | Anodization Voltage (V) | Current density (A/m²) |
|---|---|---|---|---|
| AO2 | 2 | Oxalic Acid (3 wt %) | 50-65 | 250 |
| AO4 | 4 | | | |
| AO6 | 6 | | | |
| AP2 | 2 | Phosphoric Acid (3 wt %) | 40-50 | 250 |
| AP4 | 4 | | | |
| AP6 | 6 | | | |
| AS2 | 2 | Sulfuric Acid (3 wt %) | 30-40 | 250 |
| AS4 | 4 | | | |
| AS6 | 6 | | | |

Figure 3.4 shows the SEM images of the as prepared porous top surface of the AAO template fabricated by using oxalic (AO2 and AO6), phosphoric (AP2 and AP6) and sulfuric acid (AS2 and AS6) electrolyte solution. It is evident from Fig. 3.4 (a) and (b) that the average pore diameter of the AAO template prepared by using oxalic acid solution is nearly 70 and 75 nm. The AAO template AP2 has an average pore diameter of 60-65 nm (Fig. 3.4(c)), whereas, the template AP6 contains pores of dimension of about 70-75 nm (Fig. 3.4(d)). On the other hand, AS2 and AS6 have pore sizes of 50 and 60 nm, respectively (Fig. 3.4(e) and (f)). The pore diameter of the templates prepared in oxalic acid electrolyte is smaller than that prepared in phosphoric and sulfuric acid solution. In case of the AAO templates prepared by using phosphoric and sulfuric acid the pore diameter increases with the increase of the anodization time. It is evident from Fig. 3.4 that the pores of the as prepared AAO templates are not all well open and round in shape. Here, it is to be noticed that the variation in the pore diameter and pore morphology of the AAO templates strongly depends upon the electrolyte solutions. The acid solutions used in this work have different dissociation constants and hence, the concentrations of the $O^{-2}$ /$OH^-$ ions in the electrolytes are also different. Generally, the growth of the AAO template through electrochemical anodization of aluminium is controlled by the concentration

of the available $O^{-2}$ /$OH^{-}$ ions in the acid solutions.

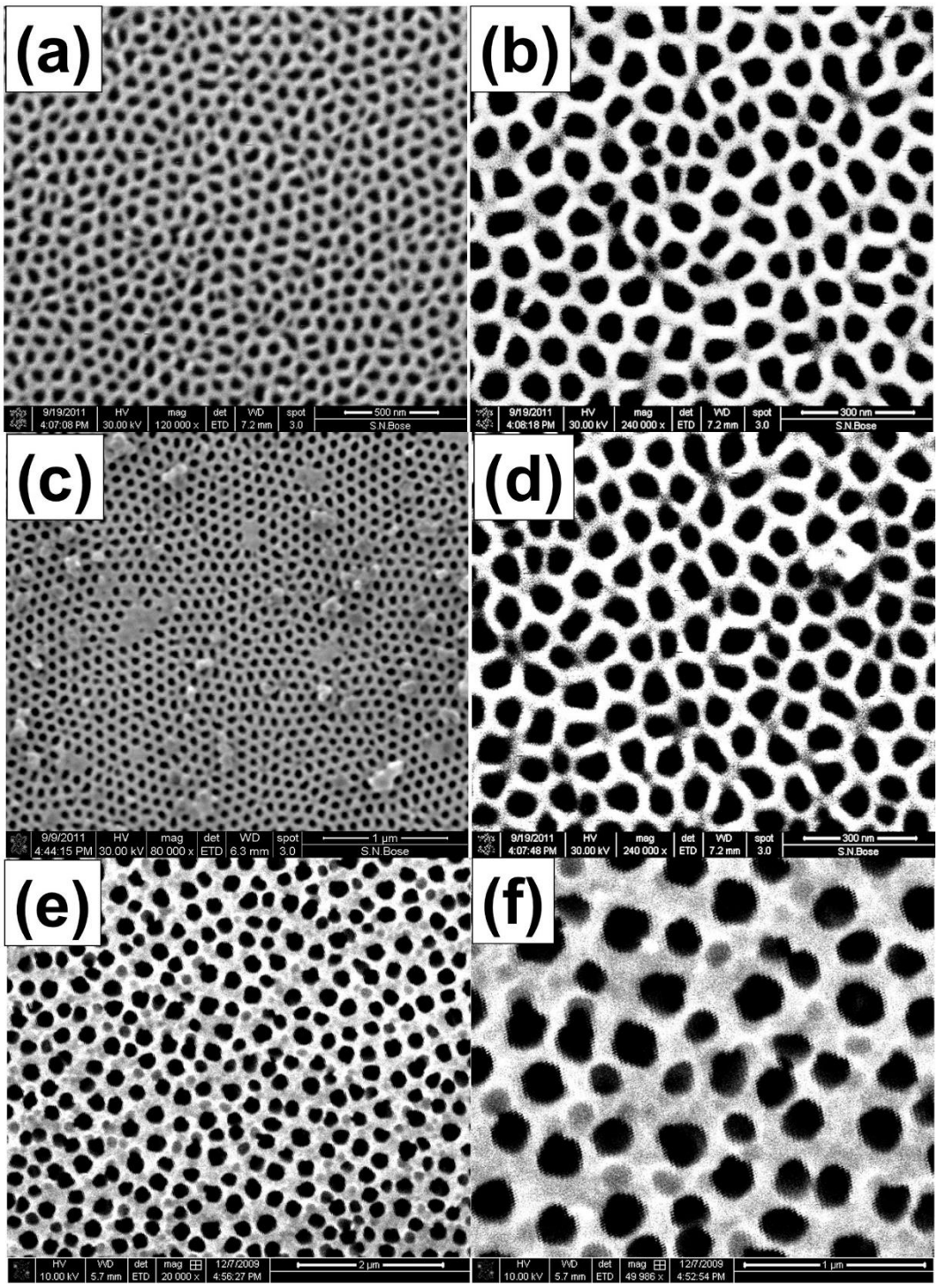


**Figure 3.4**. SEM images (top view) of AAO templates (a) AO2, (b) AO6, (c) AP2, (d) AP6, (e) AS2 and (f) AS6.

Therefore, the variation of pore diameter and pore morphology of AAO with the change of the electrolytes is quite obvious. The mechanism of pore growth and reactions are detailed in section 3.3.3 of this thesis. Furthermore, the anodization of

aluminium is an exothermic reaction. Therefore, the bath temperature was maintained at 11°C so that the huge morphological change of AAO can not take place due to the heat generated during the anodization reaction.

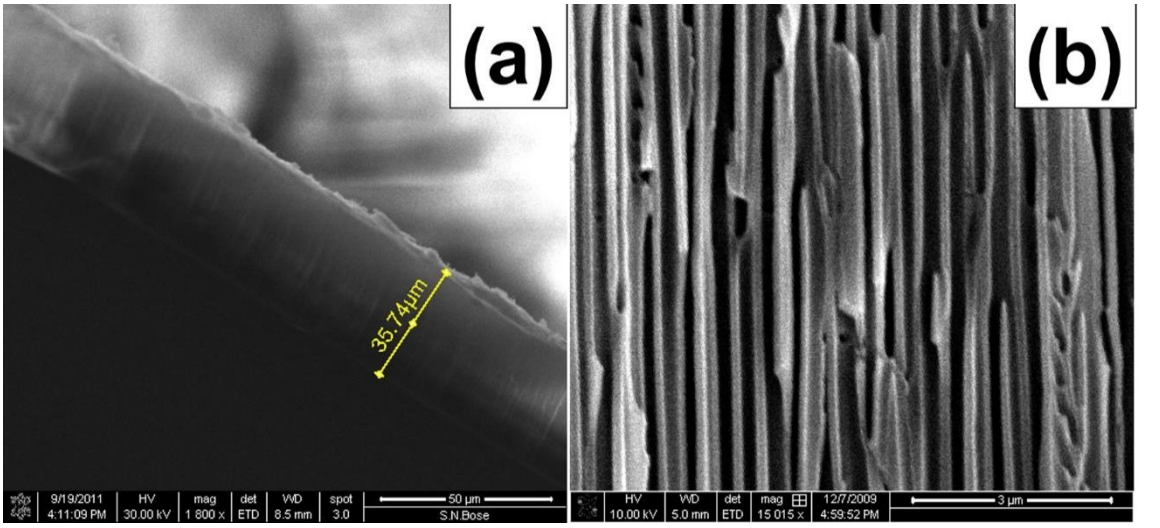


**Figure 3.5**. (a) The cross sectional SEM images of the thick porous AAO template (AO6) grown on aluminium foil and (b) high magnification images showing the pore channels.

Figure 3.5 (a) and (b) shows the cross sectional SEM images of the as prepared porous AAO template (AO6) grown on the aluminium foil substrate. It is evident from Fig. 3.5 (a) that the thickness of the porous alumina template is nearly 35 μm. Here, it is worth mentioning that the thickness of this porous template increases with the increase of the anodization time. Figure 3.5 (b) shows the high magnification cross sectional SEM image of the porous AAO template. The pore channels can be seen clearly in Fig. 3.5(b). It is also evident from Fig. 3.5(b) that all the pores grow vertically with respect to the aluminium foil surface and the pores have high aspect ratios. The pore diameter is about 70 nm and the average inter pore distance is 100 nm.

The account of the elemental composition of the AAO templates synthesized in different electrolyte solutions, has been investigated by EDS and Figure 3.6 shows the representative EDS spectra of the AAO templates (AO6, AP6 and AS6) prepared by using oxalic, phosphoric and sulfuric acid electrolyte solutions. It is evident from the EDS spectra that the AAO templates contain Al and O only, whereas the presence of the negligibly small amount of C, P and S appear because of the acidic inclusions from the electrolyte solution. Here, it would be worthwhile to mention

that the templates prepared by using different electrolyte solution for different time durations show similar type of EDS spectra.

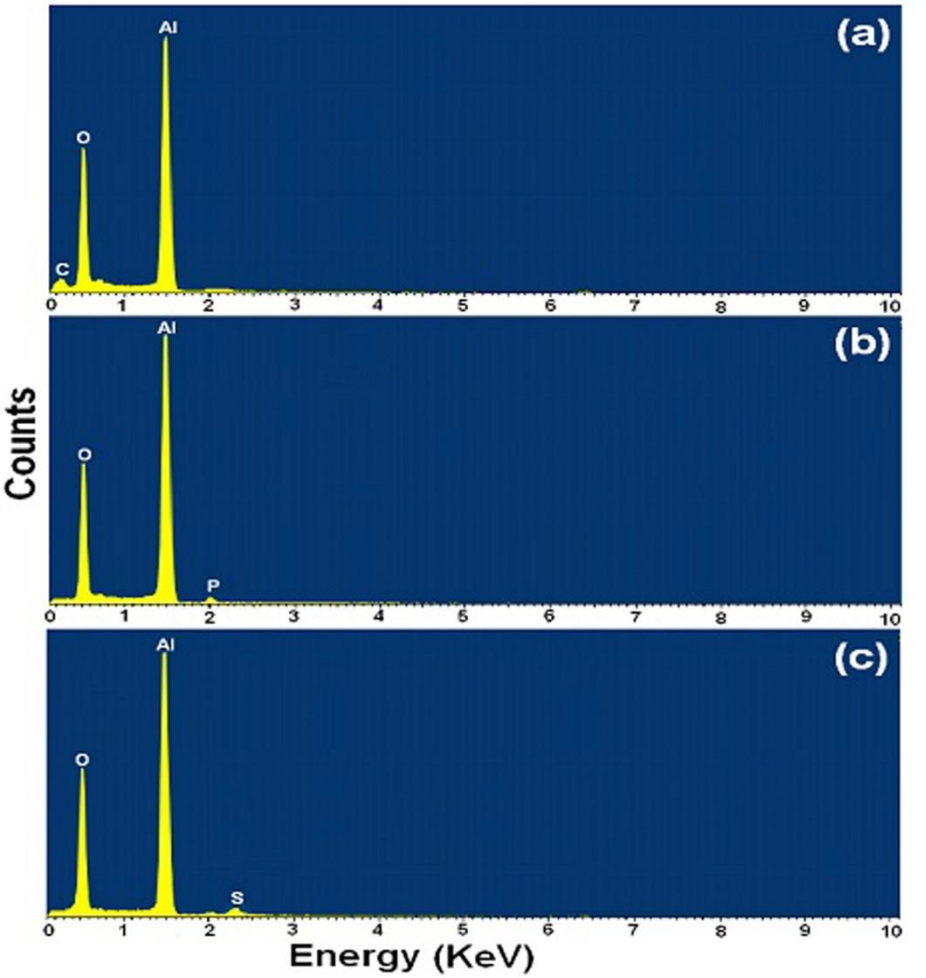


**Figure 3.6**. EDS spectra of the AAO templates (a) AO6, (b) AP6 and (c) AS6.

Figure 3.7 shows the representative XRD patterns of the as prepared thick porous AAO templates synthesized by using oxalic, phosphoric and sulfuric acid electrolyte after 6 h of second stage anodization. Here, it is to be noted that all the templates prepared in different electrolyte solution for different anodization times exhibit a similar type of XRD patterns. However, in the XRD patterns (see Fig. 3.7) no characteristics diffraction peaks are observed from any particular crystallographic plane of the porous alumina template. Therefore, it can be inferred that the AAO templates are noncrystalline in nature.

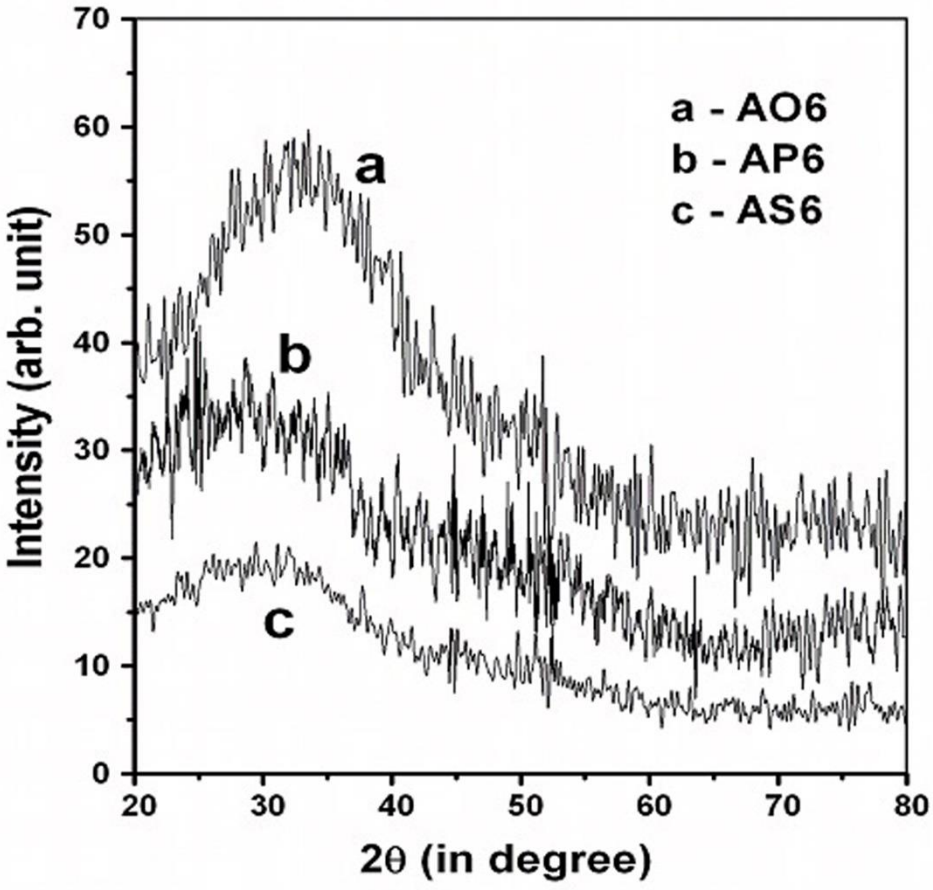


**Figure 3.7**. XRD patterns of the AAO templates: (a) AO6, (b) AP6 and (c) AS6.

The detailed information about the structure and crystallographic nature of the AAO membranes can be obtained by TEM and selected area electron diffraction (SAED) pattern characterization. Fig. 3.8 (a) shows the representative TEM image of the AAO membrane containing the nanopores fabricated using oxalic acid electrolyte.

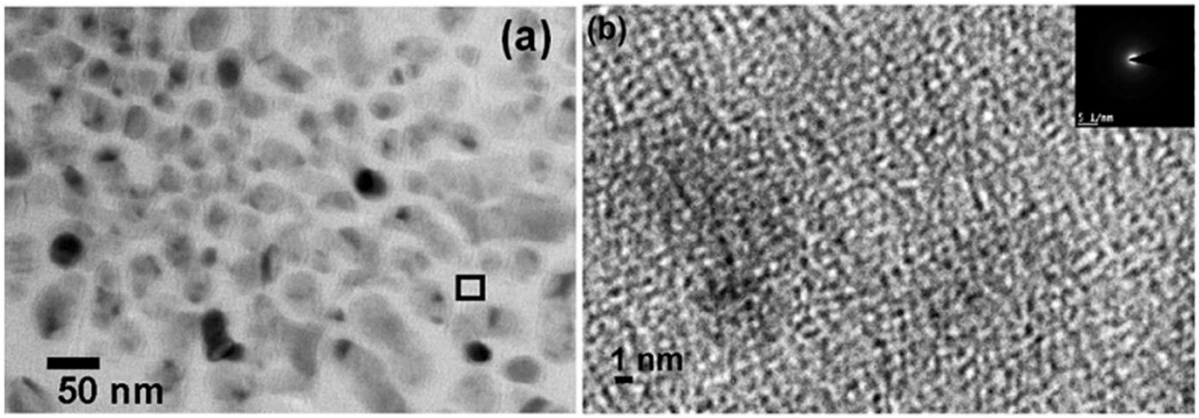


**Figure 3.8**. TEM image of the as prepared AAO membrane: (a) and (b) HRTEM image of the marked part (rectangular box in (a)) of the alumina layer. Inset of (b) shows the SAED pattern of the AAO.

The dark spots in the TEM images represent the pores of the AAO membrane and the bright region corresponds to the alumina layer in between the pores. It is evident (Fig. 3.8 (a)) that the average pore size is in the range of 50 nm. Fig. 3.8 (b) shows the HRTEM micrograph of the alumina layer (from the marked region of Fig. 3.8 (a)) of the AAO membrane with the corresponding SEAD pattern in the inset. The amorphous nature of the AAO membrane is evident from Fig. 3.8 (b), where the as grown alumina layer has no specific lattice order and the atoms are oriented in a random fashion. The HRTEM studies on the AAO membranes vividly indicate the presence of large concentration of structural defects in the noncrystalline membranes. Furthermore, the diffused SAED pattern of the AAO (inset of Fig. 3.8 (b)) clearly indicates the amorphous nature of the AAO membrane. It is found that all the AAO membranes grown on aluminium substrates by using different electrolyte solutions are amorphous in nature and they contain large concentrations of structural defects.

### 3.3.5. Optical Characterization of Anodic Aluminum Oxide

Figure 3.9 shows the room temperature PL spectra of the AAO templates prepared by using oxalic, phosphoric and sulfuric acid electrolyte solution after three different second-stage anodization time. The PL investigation was carried out under the excitation of the 315 nm line of Xe lamp. Fig. 3.9 (a) shows that the AAO templates AO2, AO4 and AO6 exhibit a strong and broad PL emission band around 434 nm. Here, it is worth mentioning that the PL spectrum of AO2 can be de-convoluted into another two different bands at 475 and 525 nm, respectively. In the PL spectrum of AO4, another low intensity band at 525 nm is observed, which is not present in AO6. However, in case of the AAO templates fabricated by using phosphoric acid (AP2, AP4 and AP6) and sulfuric acid (AS2, AS4 and AS6) electrolyte, nearly similar trends in PL emission spectra is observed. For AP2 the prominent PL emission band appears at 380 nm. On the other hand, AP4 and AP6 exhibit PL band around 409 nm. The PL emission band of AS2 is situated around 430 nm and the same for AS4 and AS6 is centered on 440 nm. Figure 3.9(d) shows the PL emission spectra of the AO6, AP6 and AS6 together for a comparative study.

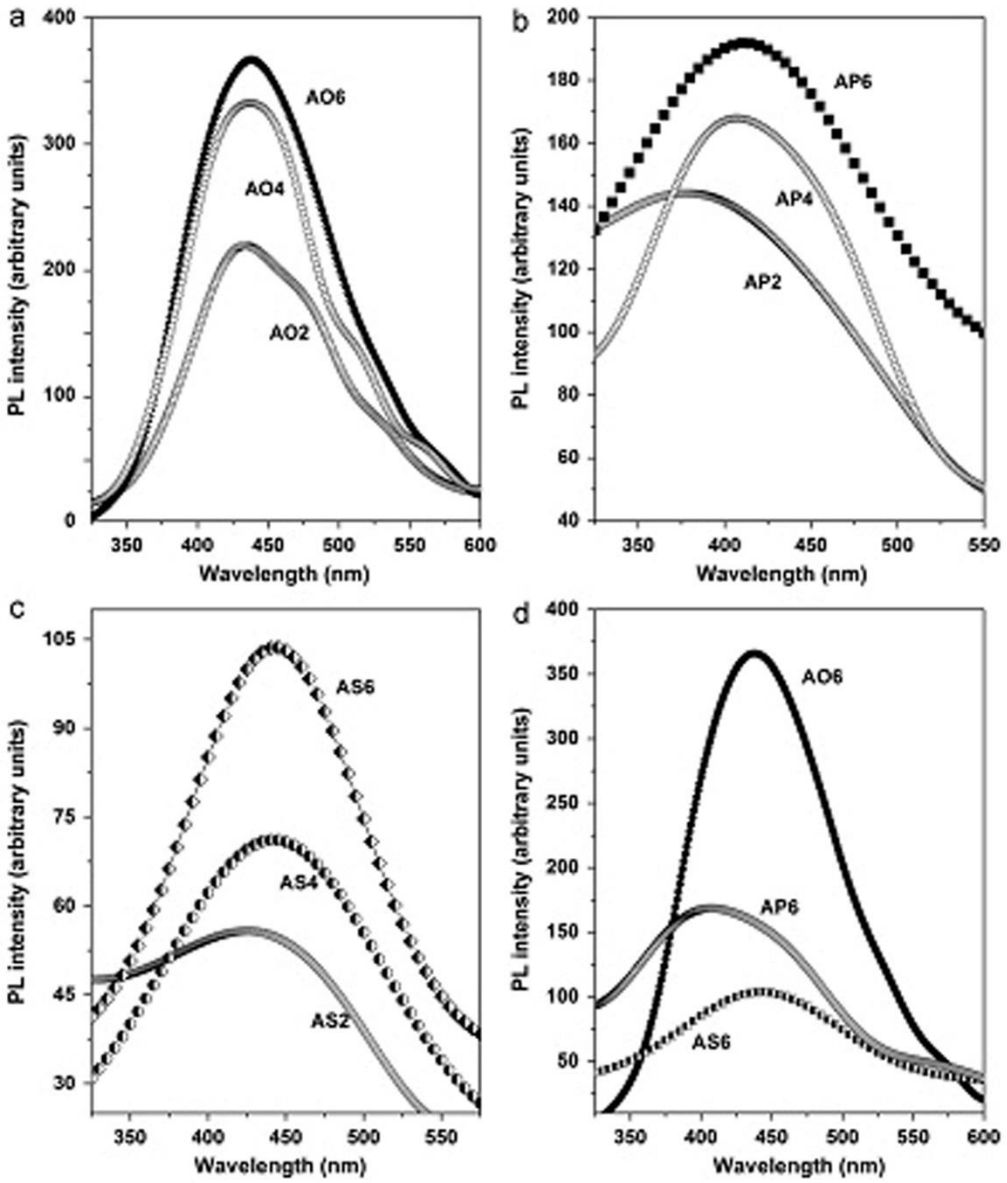


**Figure 3.9**. PL spectra of the as prepared AAO membranes: (a) AO2, AO4 and AO6; (b) AP2, AP4 and AP6; (c) AS2, AS4 and AS6 and (d) AO6, AP6 and AS6 together.

It is evident from Figure 3.9(d) that the intensity of room temperature PL spectra of AO6 is higher than AP6 and AS6, whereas, the PL intensity of AS6 is weakest. It is also seen that for all the cases the PL emission intensity increases gradually with the increase in the anodization time.

The light emission characteristics of the AAO templates have been demonstrated by different researchers based on their experiment, but their results are not free from ambiguities. Therefore, the true luminescence mechanism of AAO templates is still indistinct. In general, the proposed PL emission mechanism of the AAO has been broadly discussed under two major headings (i) the luminescent

centers created from the acidic impurities and (ii) the oxygen vacancy related defect centers present in the templates. The PL centers created in the AAO template from the oxalic and sulphuric acid impurities have been reported to be the main reason behind the light emission behaviour of the AAOs, by some researchers [17, 18]. On the other hand, major research communities have explained the luminescence behaviour of AAO templates on the basis of oxygen vacancy related defect centers (F+ and F centers) grown in the template during anodization [19, 20, 21, 22]. Thus, the true PL mechanism of the AAOs appears to have become more complicated. However, it would be worthwhile to mention that during the growth of the AAO template on aluminium substrates through electrochemical anodization, compressive stresses of large magnitude is generated at the aluminium/alumina interface due to the volume expansion caused by the conversion of aluminium to alumina [23]. Moreover, anodization of aluminium is an exothermic electrochemical reaction, which generates a huge amount of heat during the growth of the AAO template. Therefore, the compressive stress coupled with thermal energy lead to the formation of a large proportion of structural defects in the AAO template during its growth through anodization. Large numbers of oxygen vacancies are also generated spontaneously in the AAO templates when the oxygen ($O^{2-}$) ions, which are generated from $OH^{-}$ ions of the electrolyte, migrate through the alumina layer towards the aluminium/alumina interface because of the applied electric field. Additionally, the $C_2O_4^{2-}$, $PO_2^{-4}$ and $SO_2^{-4}$ ions from the electrolyte can also get directly incorporated in the templates as impurities or by replacing few $O^{2-}$ ions from AAO template [18]. However, the EDS study of the AAO templates has shown that there are very little acidic inclusions in the templates to cause luminescence.

In general, there are three types of oxygen vacancies namely, oxygen vacancies without electron (F++centers), singly ionized oxygen vacancies (F+ centers) and doubly ionized oxygen vacancies (F centers). Here, the presence of F++ centers in AAO can be ruled out because of its instability [24]. Therefore, F+ and F centers are the main oxygen vacancies present in AAO template, where the F+ centers can transform to F centers by taking electrons from the migrating electron rich ions during long term anodization [25]. In this regard, the singly ionized oxygen

vacancies (F+) generated during anodization process introduce defect states in the electronic structure of AAO template and they are expected to take the main responsibility behind the luminescence characteristics of AAOs [19, 20]. The PL band observed in this experiment in the blue wavelength region can be attributed to the F+ centers present in the alumina templates. It is important to note that the previous EDS studies have shown that the templates contain very less amount of acidic impurities in them. The acidic impurities incorporated in the AAO templates can also be transformed into the luminescent centers and can contribute in light emission. Therefore, the transformed acidic impurities may also have a role in the light emission characteristics of the templates. The PL emission bands appears at the high wavelength region for the samples prepared in oxalic acid solution, can be attributed to the luminescent centers transformed from carboxylic impurities. Figure 3.9 shows that the PL emission spectra of the AAO templates are quite broad. Therefore, it can be inferred from the broad nature of the PL emission spectra of the AAO templates that both the F+ centers and the acidic impurity related luminescent centers contribute in the light emission. Although, the intensity of the light emissions from the luminescent centers created by the acidic impurities should be low as the numbers of such luminescent centers are less in the AAO template. Moreover, the light emissions from the acidic impurity related PL centers can overlap with that of the F+ centers and may remain eclipsed under the high intensity PL emission peak of the F+ centers. Therefore, the experimental evidences indicate that the blue emission from the AAO templates can be attributed to the F+ centers, where, the contribution of the acidic impurity related luminescent centers in the PL emission spectra is negligible. The increase of the intensity of PL band with the increase of the anodization time is caused by the increase in the number of the F+ centers during anodization. Figure 3.9(d) shows that the PL intensity of AO6 template is much higher than the AP6 and AS6 templates. The explanation of this phenomenon is that the concentration of the oxygen vacancy related defects in AO6 template is much higher than that of the AS6 and AP6.

### 3.3.6. Magnetic Characterization of Anodic Aluminum Oxide

It is well known that, pure aluminum is paramagnetic in nature at room temperature. During the anodization of aluminum, the conversion of aluminum to alumina oxide started to form on the surface of aluminum. The magnetic state of alumina membrane after being taken out from the aluminum base has been studied by VSM. Magnetization loop of the representative AAO sample (AO6) membrane measured at room temperature indicates diamagnetic phase as shown in Fig. 3.10.

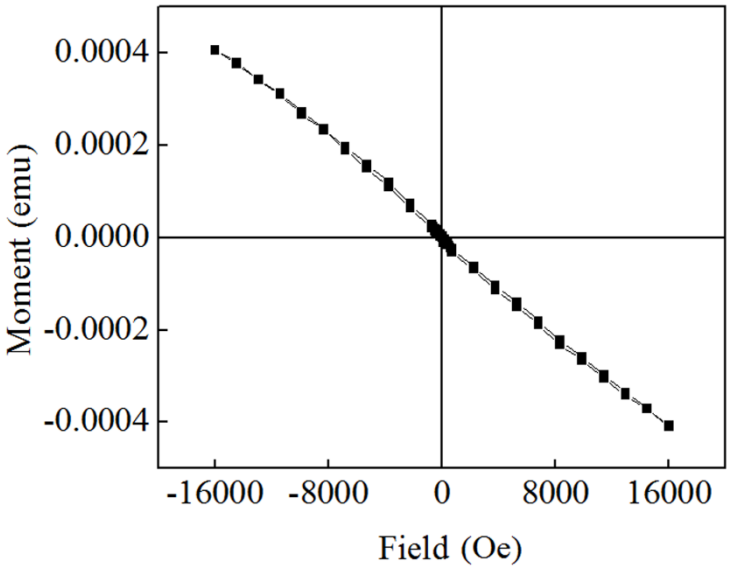


**Figure 3.10**. Experimental MH loops of AAO membrane (AO6) taken by vibrational sample magnetometer

From the curve it is observed that the membrane has a week diamagnetic property. The Al and O are both paramagnetic in nature but while they form the amorphous $Al_2O_3$, it becomes diamagnetic because of the covalent bond form between them.

## 3.4. Conclusion

In summary, the AAO templates have been successfully fabricated through the controlled electrochemical anodization of aluminium foil by using oxalic, phosphoric and sulfuric acid electrolyte solution. The morphology of the templates has been investigated by SEM. The crystallographic analysis shows that the AAO templates are non-crystalline in nature. The in-depth structural information of the templates has been obtained by the TEM study. It has been found that all the AAO

templates exhibit PL emission in the visible blue wavelength region. Herein, the luminescence mechanism of the template synthesized by using oxalic, phosphoric and sulfuric acid electrolyte for different anodization time duration has been explained based on their structural characteristics obtained by the XRD and TEM studies. The studies show that the noncrystalline AAO templates contain large proportion of structural defects. The in depth PL investigation has shown that the singly ionized oxygen vacancy related defect centers (F+ centers) take the major responsibility behind the light emission characteristics of the AAO templates, whereas, the luminescent centers transformed from acidic impurities have little contribution to the PL emission spectra. From magnetic measurements it is observed that the AAO membrane has a week diamagnetic property.

## Bibliography


[1] Z. L. Wang, *Adv. Mater.*, **12**, 1295 (2000)

[2] F. Cerrina and C. Marrian, *MRS Bull.*, **December**, 56 (1996)

[3] Y. Xia, J. A. Rogers, K. E. Paul and G. M. Whitesides, *Chem. Rev.*, **99**, 1823 (1999)

[4] Buff, H. Liebigs, *Ann. Chem.*, **3**, 265 (1857)

[5] Bengough, G. D.; Stuart, J. M. Improved process of protecting surfaces of aluminium of aluminium alloys. U.K. Patent **223**, 994, August 2, (1923)

[6] J. W. Diggle, T. C. Downie, C. W. Goulding, *Chem. Rev.*, **69**, 365 (1969)

[7] A. P. Malozemo, and J. C. Slonczewski, Magnetic Domain Walls in Bubble Material, Academic Press, New York (1979)

[8] J. C. Slonczewski, *J. Appl. Phys.* **44**, 1759 (1973)

[9] F. Keller, M. S. Hunter, D. L. Robinson, *J. Electrochem. Soc.*, **100**, 411 (1953)

[10] H. Masuda, K. Fukuda, *Science*, **268**, 1466 (1995)

[11] H. Masuda, M. Satoh, *Jpn. J. Appl. Phys.*, **35**, L126 (1996)

[12] A. R.Despic,́ *J. Electroanal. Chem.*, **191**, 417 (1985)

[13] J. M. Kape, *Electroplat. Met. Finish.*, **14**, 407 (1961)

[14] R. C. Furneaux, W. R. Rigby, A. P. Davidson, *Nature*, **337**, 147 (1989)

[15] G. E. Thompson, G. C. Wood, *Nature*, **290**, 230 (1981)

[16] J. M. Kape, *Metallugia*, **60**, 181 (1959)

[17] T. Gao, G. Meng and L. Zhang, *J. Phys.: Condens. Matter,* **15**, 2071 (2003)

[18] Y. Li, C. W. Wang, L. R. Zhao and W. M. Liu, *J. Phys. D: Appl. Phys.,* **42**, 045407 (2009)

[19] Z. Li and K. Huang, *J. Phys.: Condens. Matter,* **19**, 216203 (2007)

[20] Y. Du, W. L. Cai, C. M. Mo, J. Chen, L. D. Zhang and X. G. Zhu, *Appl. Phys. Lett.,* **74,** 2951 (1999)

[21] J. H. Chen, C. P. Huang, C. G. Chao and T. M. Chen, *Appl. Phys. A*, **84**, 297 (2006)

[22] G. S. Huang, X. L. Wu, Y. F. Mei, X. F. Shao and G. G. Siu, *Appl, Phys. Lett.*, **93** 582 (2003)

[23] A. P. Li, F. Müller, A. Birner, K. Nielsch and U. Gösele, *J. Appl. Phys.*, **84,** 6023 (1998)

[24] J. H. Wu , X. L. Wu, N. Tang, Y. F. Mei and X. M. Bao, *Appl. Phys. A*, **72** 735 (2001)

[25] Y. F. Mei, G. G. Siu, G. S. Huang and X. L. Wu, *Applied Surface Science,* **230**, 393 (2004)

# Chapter 4

# Transition metals based magnetic nanowires and nanotubes

This chapter describes the fabrication of transition metal based ordered nanostructures (Ni nanowires, FeNi nanowires & CoNi nanotubes) prepared by AAO template assisted electrodeposition technique and study of their structural, morphological, and magnetic properties in detail. It also includes the study of the effect of alpha particle irradiation on the magnetic properties of Ni nanowires and the aspect ratio and temperature dependent magnetic properties of FeNi nanowires and CoNi nanotubes.

# 4.1. Effect of α-particle irradiation on the magnetic properties of Ni nanowires

## 4.1.1. Preamble

Irradiation induced damage in materials has been a long cited topic in research. It is a well-established fact that a dose of irradiation has considerable effects on both the living and non-living systems. The majority of irradiation effect analysis is connected with irradiation-induced effects in crystal bulk. Detailed studies on the nature of irradiation damage in a bulk Al [1], Cu [1–3], molybdenum [3], Fe [3,4], Cr [5], Ni [1, 4, 6], amorphous & crystalline magnetic alloys [7-12], permalloy [13], permanent magnets [14,15], $Fe_2O_3$ [4,16] has been made in literature and found to depend on the dose of irradiation. In the last two decades, science of nano-materials dominates in the field of materials science due to the unique desirable features of nanometric scale and availability of characterization tools. One-dimensional nanostructures are of huge importance in the realization of future data storage devices and till date Ni remains the best chosen material for nano magnetic storage devices or switching devices as far as its availability, cost and magnetic property are concerned. But to maintain or increase the magnetic properties of nanowires as compared to their bulk counterparts is one of the most critical steps in the magnetic properties of nanowires.

Magnetic properties of a nanowire (NW) are governed by various anisotropy energies such as shape, magnetocrystalline and surface anisotropies [17, 18]. However the magnetic behavior of the arrays of nanowires is determined by the magnetic nature of individual nanowires as well as by the interactions among them. The direction of the magnetic easy axis of a NW is determined by the direction of the effective anisotropy field in it. Due to the strong shape anisotropy in a NW, magnetic easy axis is usually parallel to its length. But in an array of closely arranged NWs, strong magnetostatic interaction is developed because of close proximity of neighbouring NWs, resulting the direction of easy axis perpendicular to its length which is undesirable in most of the applications [19, 20]. In this regard, efforts have been made to study magnetic properties of magnetic nanowires. Either through

simulation models or through experiments, but a small part of the effort is devoted to analysis of the magnetic properties of nanostructures after irradiation. Lack of understanding of the irradiation effect on the magnetic properties of nanowires may lead to the evolution of magnetic storage devices and switching devices. To obtain deeper physical insights into the irradiation effect here we report the influence of α-particle irradiation on structural and magnetic properties of Ni NWs with the fast α-particle fluences of $2x10^{15}$ and $2x10^{16}$ α/cm$^2$. In the present work, we observed that alpha particle irradiation could be a useful tool to change the magnetic properties of the NWs as per need. By generating pinning centres within the NWs, their coercivity could be increased. On the other hand, it could reduce the magnetocrystalline anisotropy by damaging the crystal structure to various extents and hence could change the resultant anisotropy and the direction of the magnetic easy axis within the NWs.

### 4.1.2. Experimental

High-density arrays of Ni NWs were fabricated within alumina membranes by the electrodeposition method. The thickness of an alumina membrane was approximately 50 μm with nanosized pores of an average diameter of ~100 nm and a pore density of $10^9$ per square cm. Highly ordered self-organized nanoporous anodic aluminum oxide (AAO) template fabricated by the controlled two-stage electrochemical anodization of high-purity aluminum foil, as described in the previous chapter and elsewhere [21-23] has been used as the host to prepare the Ni NWs. The AAO template with one side coated with a conductive gold (Au) layer of 0.1 μm thickness grown by thermal evaporation technique has been used as a working electrode in the electrodeposition process to fabricate the highly ordered arrays of Ni NWs, as describes elsewhere [24-27]. Arrays of Ni NWs have been electrodeposited in the pores of AAO using the aqueous solution of 0.57 M of $NiSO_4$ and 0.32 M of $H_3BO_3$ as electrolyte at room temperature (RT). The boric acid has been used as a buffer. The electrochemical deposition has been conducted by using the dc voltage of −0.9 V, following linear sweep voltametry results, maintaining the pH of the electrolyte at 3.5. The electrodeposition was carried out for 18 min to

prepare the Ni NWs of ~12 μm long. Three samples of the arrays of Ni NWs prepared in the same condition. For further measurements and characterization of nanowires, the alumina membranes were dissolved in 2 M of NaOH solution at room temperature. One sample, we call it un-irradiated sample and another two will be irradiated with alpha particles.

Irradiation was done with a beam of 40 MeV α particles obtained from the Variable Energy Cyclotron in Kolkata. The beam current was 100 nA. Electrical insulation of the target holder from the beam tube was ensured by the perspax flange and teflon bush in the screws connecting the target holder and the beam line. The samples attached to the aluminium target holder were cooled by flowing compressed air [28, 29]. Samples were subjected to dose of $2x10^{15}$ and $2x10^{16}$ $\alpha/cm^2$. We had three samples for the characterization sample-1 (unirradiated sample), sample-2 (irradiated with $2x10^{15}\alpha/cm^2$) and sample-3 (irradiated with $2x10^{16}\alpha/cm^2$). Scanning electron microscope (FEI Quanta-200 Mark-2) and Transmission electron microscope (FEI TECNAI TF20ST) were used to observe the NWs, their surface morphology and to determine their length and diameter. The crystalline structures of Ni NWs were investigated by transmission electron microscopy. The phase of the samples was confirmed by x-ray diffraction (X'Pert Pro, Panalytical) and the composition of the NWs was determined using energy dispersive analysis by x-ray (EDAX). Magnetic properties were studied using a vibrating sample magnetometer (Lakeshore, model 7144).

### 4.1.3. Results and Discussions

Fig. 4.1 (a) & (b) shows the SEM micrograph of the sample-1 and sample-3 which indicates the uniformity in length and diameter of the NWs. The inset of Fig. 4.1 (a) shows smoothness on the surface of Ni NWs compared to sample-3 shown in the inset of the Fig. 4.1 (b). To check the composition of the NWs, we performed EDAX measurement shown in Fig. 4.1 (c) which confirms the presence of Ni in the samples as well as the absence of sulphur and boron contamination.

Fig. 4.2 (a) is a TEM micrograph of the individual NW of sample-3 liberated from the AAO template; the diameter of the NWs is about ~100 nm. Black spots are

also visible on the surface of the NWs after irradiation. Each NW is polycrystalline; Fig. 4.2 (b) shows the selected-area electron diffraction pattern of the NWs, revealing reflections corresponding to the face-centered-cubic (fcc) structure of nickel. Fig. 4.2 (c) is a high-resolution TEM image of a sample-3. The lattice spacing in the image is about 0.2 nm, indicating a (111) fcc plane of Ni. As [111] direction is the magnetocrystalline easy axis in Ni, this anisotropy will try to align the magnetic easy axis of a NW in a direction perpendicular to its length. From high resolution micrographs we found that there is no change in the crystalline structures of the NWs after the irradiation of the sample by α particle.

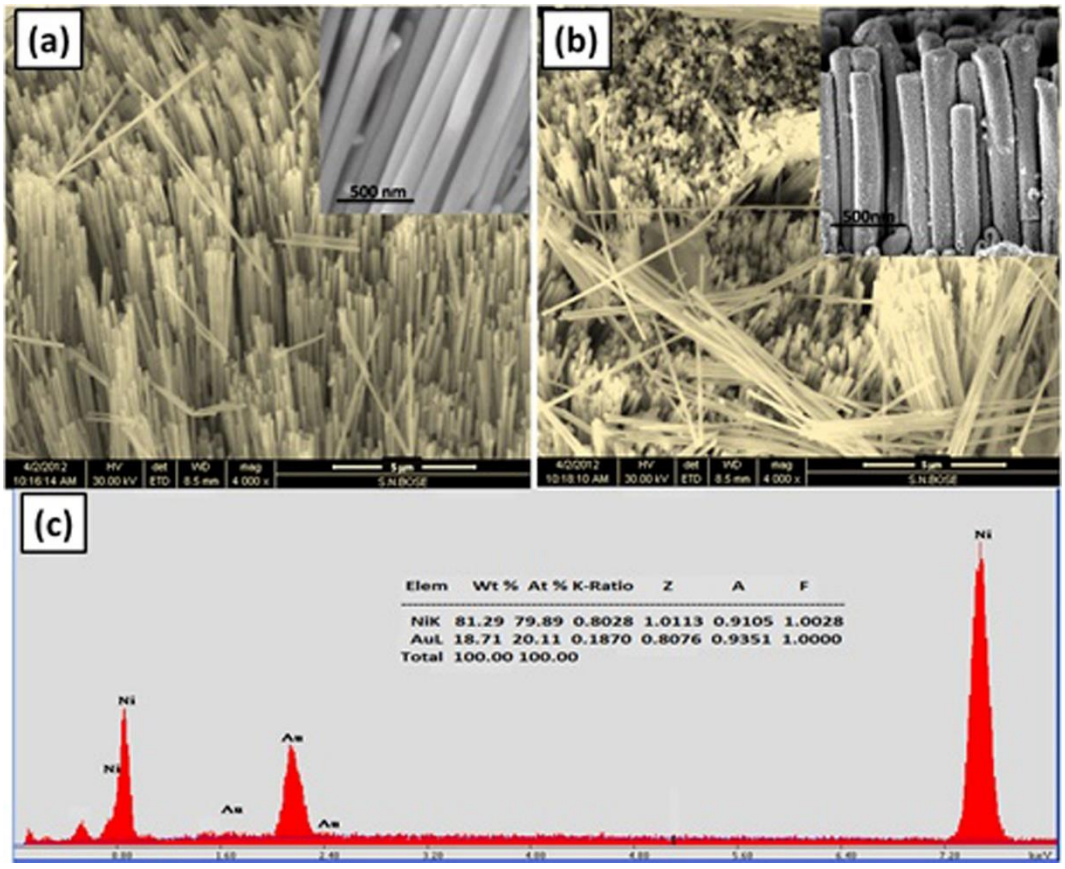


**Figure 4.1. (a)** & **(b)** SEM micrograph of sample-1& sample-2 respectively and **(c)** EDAX pattern of sample-3.

Fig. 4.2 (d) indicates that no variation in the relative "2 theta" position has been observed in XRD spectra when spectra of irradiated cases are compared with the unirradiated case. As "2 theta" position in a XRD pattern is the outcome of the shape and size of unit cell, this means that no changes are there in the shape and size

of unit cell after irradiation. Atomic positions in the lattice after irradiation would not be the same, and it is evident from relative intensity pattern in pre and post-irradiation XRD spectra, which are different. All of them show prominent peaks of Ni and one peak (220) of Au as gold was deposited on one side of the template for Ni deposition. The XRD study confirms that the crystal geometry does not change on irradiation. However, decrease in XRD peak intensities and increase in peak broadness on increasing irradiation dose indicates the deterioration of crystal structure to some extent after irradiation [30].

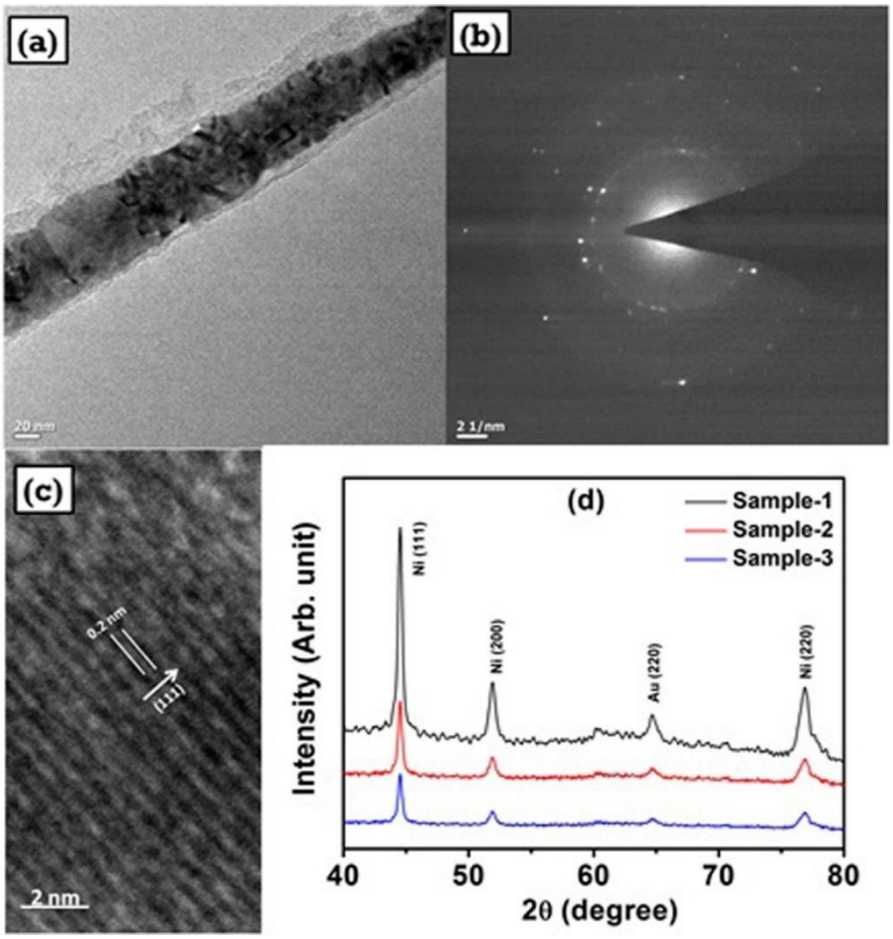


**Figure 4.2 (a)** TEM micrograph of the single NW of sample-3, **(b)** selected area electron diffraction (SAED) pattern of sample-3, **(c)** High resolution TEM micrograph sample-3 and **(d)** XRD spectrum of sample-1, sample-2 and sample-3.

Intensity of the peaks is decreasing with the increase of irradiation doses. The observed XRD spectra also provide information about polycrystalline nature of Ni nanowires of fcc lattice geometry. The induced point defects can directly impair the structure sensitive magnetic properties or indirectly affect the intrinsic magnetic

properties by causing some changes in the arrangement of atoms. From above structural analysis we concluded there were point defects induced in the NWs after irradiation.

From Fig. 4.3 (a) & (b) we observed coercivity ($H_c$) increases with the increase alpha particle irradiation doses and considerable shape change towards squareness**.**

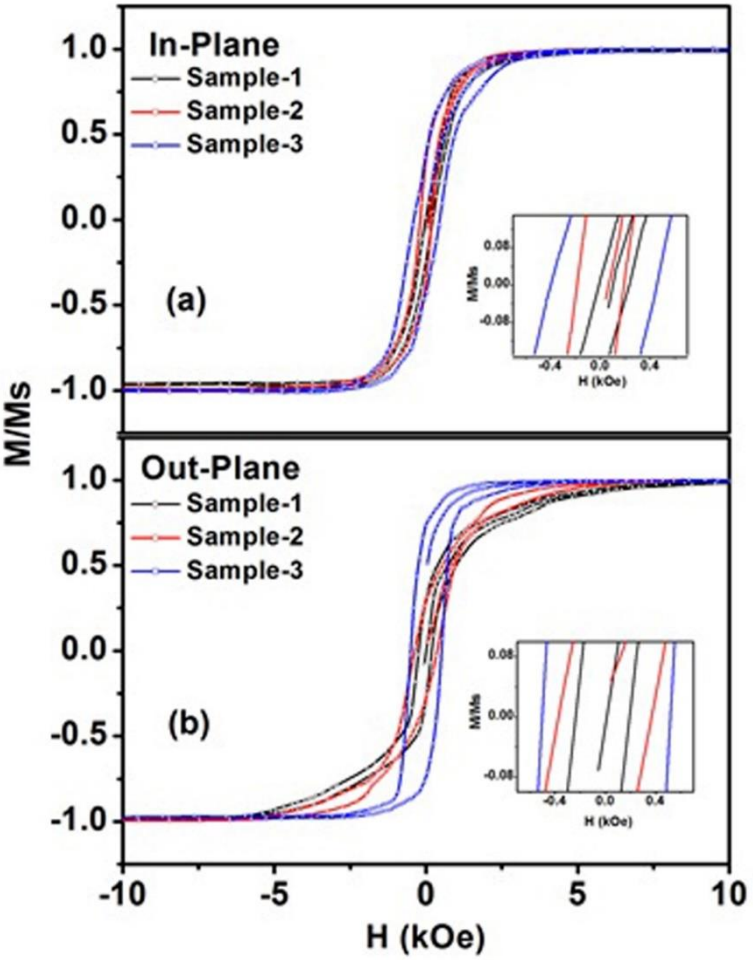


**Figure 4.3 (a)** M-H loop of sample-1,2&3 when applied magnetic field was perpendicular (IP) to NWs axis and **(b)** M-H loop of sample-1,2&3 when applied magnetic field was parallel (OP) to NWs axis at room temperature.

Fig.4.4 shows the In-plane (IP, along the surface of the template and perpendicular to the wire axis) and out-of-plane (OP, perpendicular to the template surface and parallel to the wire axis) magnetic hysteresis loops of (a) sample-1 (b) sample-2 and (c) sample-3. In case of sample-1 (unirradiated), IP hysteresis loop shows higher increase in magnetisation with magnetic field compared to its OP counterpart which suggests that the magnetic easy axis in this sample is in the IP direction. Similar trend is also observed in the sample-2 (irradiated with lower dose)

though the difference in IP and OP behaviour reduces. However the sample-3 (irradiated with higher dose) shows the opposite trend in magnetic behaviour which is an indication of OP magnetic easy axis in this sample.

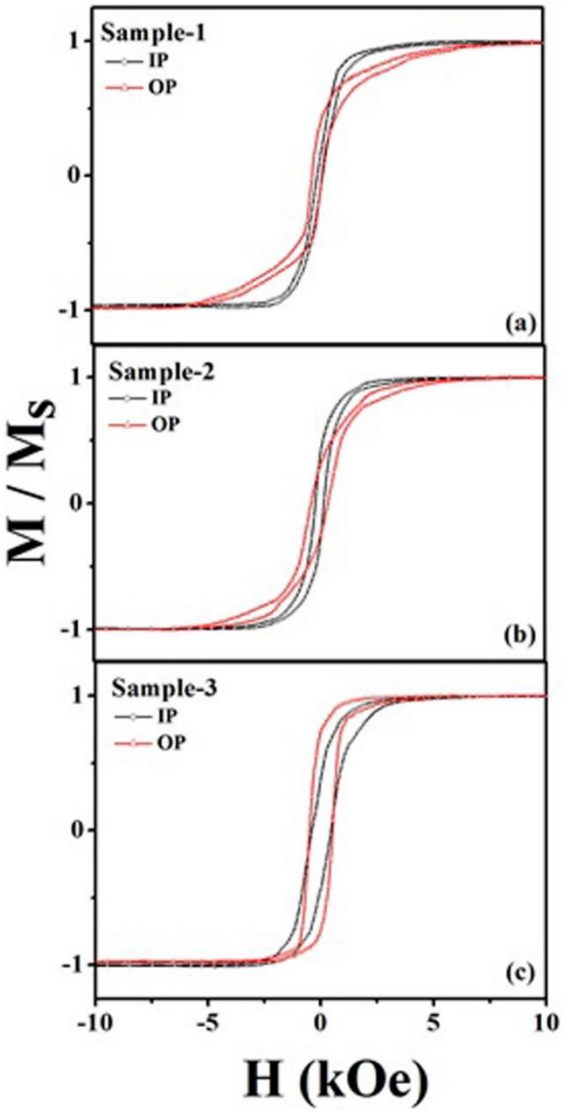


**Figure 4.** Comparison of M-H loops between In-plane (IP) and out-plane (OP) direction of applied magnetic field for **(a)** sample-1, **(b)** sample-2 and **(c)** sample-3.

In the case of an array of closely spaced nanowires, magnetostatic interactions between the nanowires play an important role in governing their magnetic properties as it opposes the shape anisotropy of the individual nanowires. [18, 27] After the irradiation of the sample there are some pinning centre's generated in the NWs that generates obstacle in the motion of the domain walls. Because of this obstacles there are some changes arising in the magnetic properties of the NWs. Before irradiation of the samples magnetocrystalline anisotropy dominates over the

shape anisotropy. In contrast, shape anisotropy dominating compare to other anisotropy after the irradiation of the samples with high doses of the α-particle. Magnetostatic interaction between the NWs decreases with high dose of irradiation on the sample due to this the magnetic easy axis of the sample-3 changes along the direction of the NWs axis.

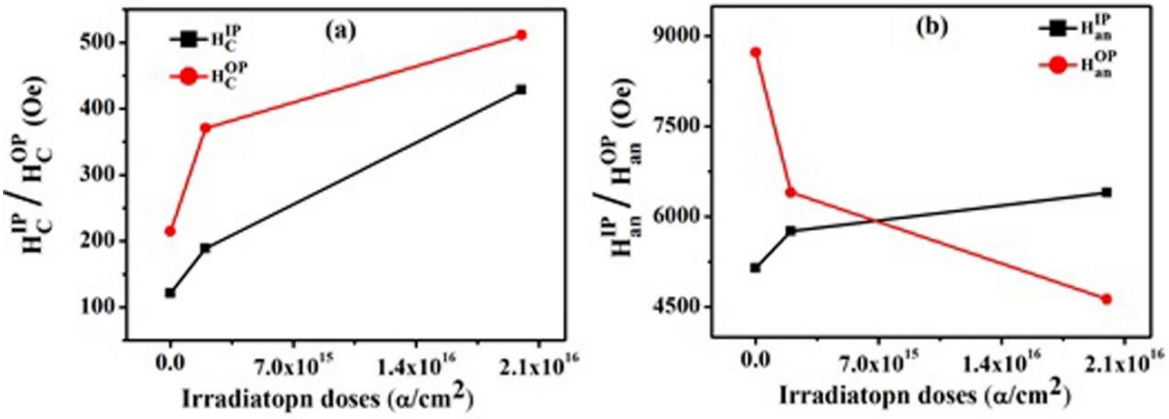


**Figure 4.5.** Comparisons of magnetic properties **(a)** coercivity ($H_c$) and **(b)** anisotropy field ($H_k$) for both the cases IP and OP direction of applied magnetic field in sample-1, sample-2 and sample-3

Both IP and OP coercivity, $H_c^{IP}$ and $H_c^{OP}$ respectively, are found to increase on increasing irradiation dose, as shown in Fig. 4.5 (a), due to the increase in pinning centres within the NWs. These pinning centres hinder the domain wall motions resulting higher $H_c$. Remanence also enhances significantly in both directions on irradiation. However, the estimated magnetic anisotropy field, $H_{an}$ does not follow the same trend as shown in Fig. 4.5 (b). For the unirradiated sample-1, OP $H_{an}$ ($H_{an}^{OP}$) is much higher than the IP $H_{an}$ ($H_{an}^{IP}$). Sample-2 also shows the similar behaviour but with much less difference between them. On the other hand, sample-3 with maximum irradiation dose shows the opposite trend. In this case, $H_{an}^{IP}$ is higher than $H_{an}^{OP}$.

For an array NWs, preferential direction of magnetization is determined by the competition among dipole-dipole interaction, magnetocrytalline and shape anisotropy. Assuming the array of NWs as a two dimensional infinite array of magnetic dipoles, the total field acting on one NW along OP direction, $F_{OP}$ is the sum of the dipole fields and the field due to shape anisotropy ($F_{sh}$) and can be written as [19, 20]:

$$F_{OP} = -4.2\frac{M_S V}{D^3} + F_{Sh} \tag{4.1}$$

When all the moments are aligned perpendicular to the wires the total field acting on one wire is the sum of the dipole fields and the field due to magnetocystalline anisotropy ($F_k$) and can be written as [19, 20]:

$$F_{IP} = 2.1\frac{M_S V}{D^3} + F_K \tag{4.2}$$

Where V is the volume of a NW and D is the inter-wire distance. The first terms in Eq.(4.1) and (4.2) are the magnetostatic interaction field when the external magnetic field is applied along OP and IP directions respectively and they are estimated to be $2.83\text{x}10^4$ and $1.41\text{x}10^4$ Oe respectively [20]. The negative sign in Eq.(4.1) is used to indicate the interaction field produced by surrounding NWs on the test NW is opposite to its magnetization. In other word, interaction in OP direction is anti-ferromagnetic (AFM) in nature while that in IP direction is ferromagnetic (FM), i.e. supports the magnetization of the test NWs. $F_{sh}$ and $F_k$ are found to be 8930 Oe and 7032 Oe respectively [20].

The above model explains the crossover of resultant anisotropy fields (Fig. 4.5 (b)) which leads to a directional change of easy axis from IP to OP with the change in magnetocrystalline anisotropy field due to irradiation. From the HRTEM micrograph, it is observed that the magnetic easy axis of Ni, [111] direction is perpendicular to the wire axis, i.e., in the IP direction. Therefore in the unirradiated sample, $F_{IP}$ (~$2.12\text{x}10^4$ Oe) is higher than $F_{OP}$ (~$1.93\text{x}10^4$). As a result $H_{an}^{IP}$ is lower than the $H_{an}^{OP}$ and the magnetic easy axis is along the IP direction. From the XRD studies (Fig. 4.2(d)) we observe that the crystalline structure of the NWs deteriorated due to irradiation thereby reducing $F_k$. In sample-3, because of much reduction in $F_k$, $F_{IP}$ is less than $F_{OP}$ resulting the crossover of $H_{an}$ (Fig. 4.5 (b)) as well as change in the direction of magnetic easy axis from IP to OP.

We perform magnetic Barkhausen noise (MBN) measurements to justify the increase in pinning centre on α-particle irradiation. MBN increases with the increase of the irradiation doses as more pinning centers develop within the sample and domain wall motion is hindered. Fig. 4.6 shows that the MBN [31, 32] of sample-3 is

higher in OP direction compare to sample-1 and sample-2, which suggests the increment of pinning centre in Ni NWs on α-particle irradiation.

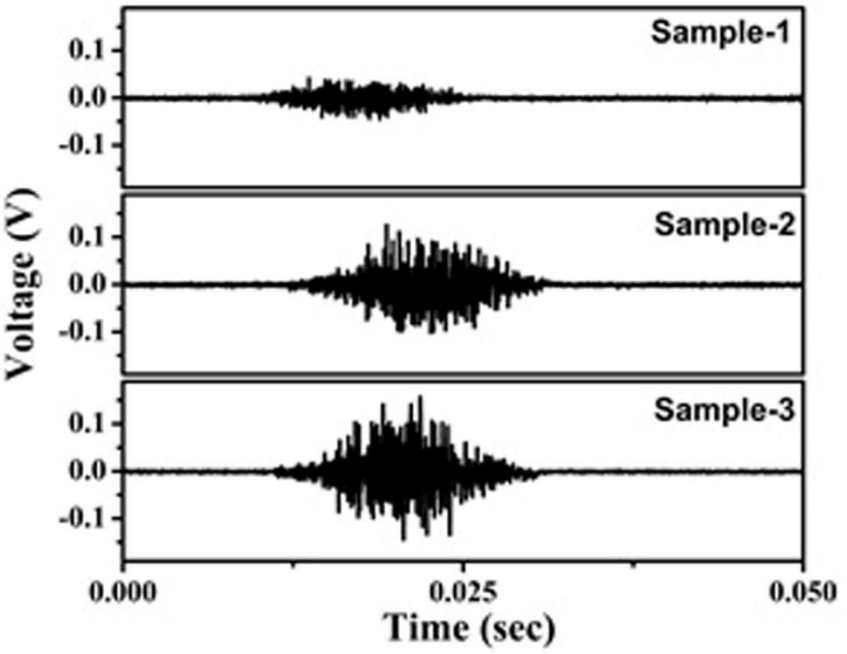


**Figure 4.6**. Magnetic Barkhausen Noise for sample 1, 2 and 3.

## 4.1.4 Conclusion

In conclusions, arrays of Ni NWs, each NW with diameter~100nm and prepared by electrodeposition technique, were irradiated with different doses of α-particles. Irradiation produces pinning centres within the NWs and results in increase in coercivity. Irradiation also reduces crystallinity of the NWs and hence magnetocrystalline anisotropy. As a result magnetic easy axis changes from IP to OP direction.

## 4.2. Effect of aspect ratio and temperature on magnetic properties of Permalloy nanowires

### 4.2.1. Preamble

Magnetic nanowires (NWs) have recently attracted tremendous attention because of their potential applications in various fields, particularly in high density perpendicular magnetic storage [33-36]. Highly ordered arrays of such nanowires show novel and interesting magnetic properties different from those of bulk and thin films and sensitively depend on their sizes, shapes, and the interactions among them [17,27,37]. Among the various methods for preparing nanowires, electrodeposition is widely used because of its simplicity and low cost. In this method, various magnetic materials such as Fe, Co, Ni, and their alloys were embedded into the nanopores of silica, alumina, or polycarbonate membranes by the electrodeposition technique [25, 38,39]. Magnetic properties of a NW are governed by various anisotropy energies such as shape, magnetocrystalline and surface anisotropies [17, 18]. However the magnetic behavior of the arrays of nanowires is determined by the magnetic nature of individual nanowires as well as by the interactions among them. The direction of magnetic easy axis of a NW is determined by the direction of effective anisotropy field in it. Due to the strong shape anisotropy in a NW, magnetic easy axis is usually parallel to its length. But in an array of closely arranged NWs, strong magnetostatic interaction is developed because of close proximity of neighbouring NWs, resulting the direction of easy axis perpendicular to its length which is undesirable in most of the applications [19, 20]. Since last decade many magnetic properties studies have been done on the permalloy nanostructures (nanowire, nanotube, nanoparticle etc.) [40-47]. Still aspect ratio and temperature dependent magnetic properties of permalloy NWs has not done yet. It is still not studied that how magnetic easy axis of permalloy nanowires depends upon the temperature and the aspect ratio.

In this back drop, here we study the structural and magnetic properties of the arrays of permalloy NWs with average NW diameter of ~200 nm were prepared in AAO membrane by the electrodeposition method. The aspect ratio of the nanowires was varied from 7.5 to 37.5 by varying the deposition timing and keeping the

diameter constant ~200nm. Magnetic properties of the samples such as hysteresis loop, coercivity ($H_C$), and squareness ($M_r/M_s$) ratio were studied at various temperatures between 80 and 300 K with above mentioned different aspect ratio. The experimental result confirms the direction of magnetic easy axis of the NWs along the axis of the NWs.

## 4.2.2. Experimental

High-density arrays of permalloy NWs have been fabricated by the synthesized template assisted electrochemical route (see Fig.4.7). A self-organized nanoporous anodic aluminium oxide (AAO) template fabricated by the controlled two-stage electrochemical anodization of high purity Al foil, as described in previous chapter and elsewhere [21-23], was used as the host to prepare the permalloy NWs. A through the pore AAO template with an average pore diameter of ~200 mm with a thickness of ~ 50 μm and an average pore density of ~ $10^9$ $cm^{-2}$ was prepared for this work. A layer of Au sputtered onto one side of the through pore AAO template was used as the working electrode in the electrodeposition process. The software controlled typical conventional three electrode electrochemical cell and a power supply (potentiostat AutoLab-30) was employed for the electrochemical deposition of permalloy NWs by using the gold-coated AAO template as the working electrode (cathode). A high purity Pt wire and an Ag/AgCl calomel electrode were used as the counter and reference electrode, respectively. Permalloy NWs have been electrodeposited in the pores of AAO using an aqueous solution of 100 $gL^{-1}$ $NiSO_4.7H_2O$, 20 g $L^{-1}$ $FeSO_4.7H_2O$ and 45 g $L^{-1}$ $H_3BO_3$ as the electrolyte at room temperature (RT). Here, the boric acid plays the role of the buffer. The pH of the electrolyte was maintained at 3.5 and the electrodeposition was conducted by using a dc voltage of -1.03 V following linear sweep voltammetry results. The electrodeposition was carried out for 5, 15, 30 and 45 minutes in order to prepare permalloy NWs of ~1.5, 3.2, 5.4 and 7.5 μm length respectively. Afterwards, the template containing the permalloy NWs was dipped in a 2 M NaOH solution at RT for a day to release the permalloy NWs by dissolving the template.

The crystal structure study of the permalloy NWs were analyzed by x-ray diffraction (XRD,Panalytical X'Pert Pro diffractometer). The account of the chemical

composition and elemental composition of the NW was investigated by energy dispersive x-ray (EDAX). The morphology and the structure of the NWs were studied by scanning electronmicroscope (SEM, FEIQuanta-200 Mark-2), transmission electron microscope (TEM, FEITECNAI G2 TF20ST) and scanning transmission electron microscopy (STEM). The crystalline structure of the NW was further investigated by the high-resolution TEM (HRTEM). Magnetic measurements of the permalloy NWs have been performed using a vibrating sample magnetometer (VSM, Lakeshore, model 7144) by placing the axis of the arrays of NWs sample along the direction of the applied magnetic field (OP – out of plane, H ∥ wire axis) and perpendicular to the direction of the applied magnetic field (IP – in plane, H ⊥ wire axis) within the temperature range of 80–300 K.

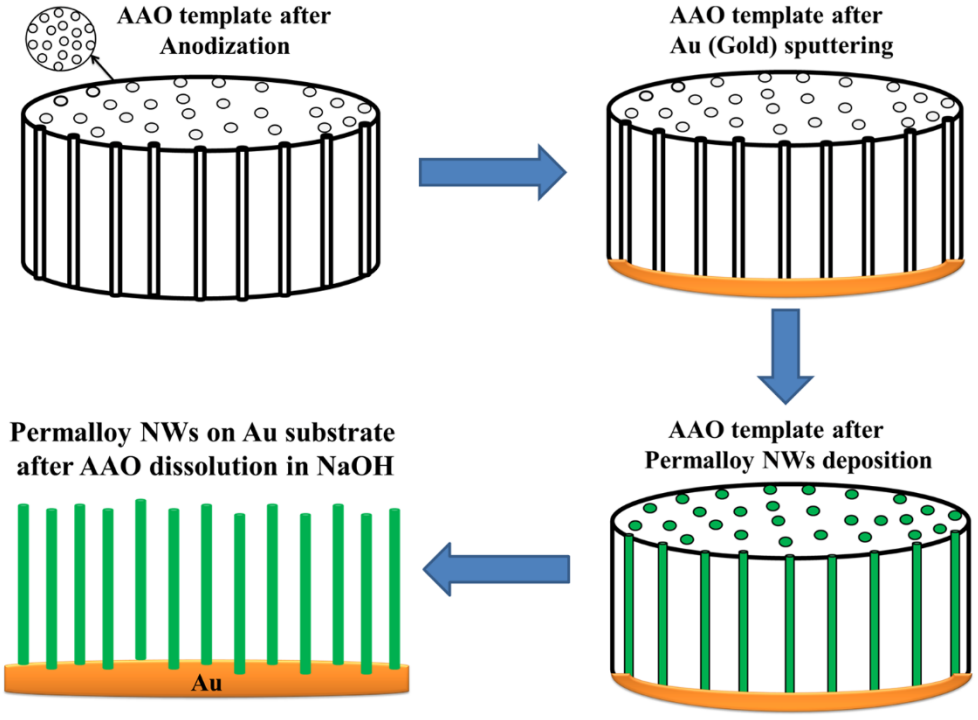


**Figure 4.7**. Illustration of the mechanism for the formation of permalloy nanowires.

## 4.2.3 Results and Discussions

### 4.2.3.1. Morphology, Crystallography and Chemical composition

From SEM micrograph (Fig. 4.8(a)) we observed that the pores of Anodized alumina oxide (AAO) template obtained after two step anodization technique have uniform pore diameters with an average pore diameter of ~200 mm with a thickness

of ~ 50 μm and an average pore density of ~ $10^9$ $cm^{-2}$. The crystallographic nature of the arrays of permalloy NWs investigated by XRD (Fig. 4.8 (b)) indicates that the as grown permalloy NWs are crystalline in nature. The diffraction peaks in the XRD pattern appear from the pure $FeNi_3$ face centered cubic (fcc) and the metallic Au layer underneath the NWs.

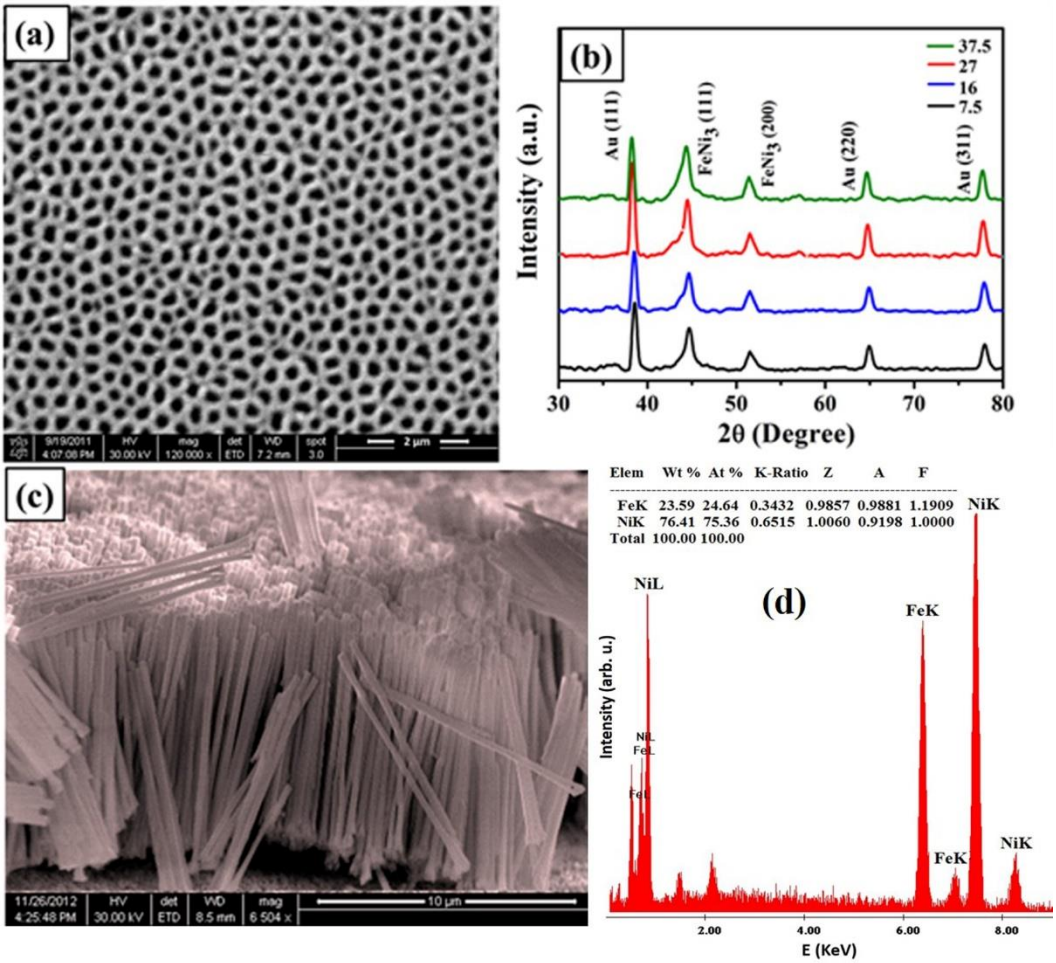


**Figure 4.8**. (a) SEM micrograph of the top view of the AAO template. (b) XRD Pattern of the as-prepared permalloy NWs with different aspect ratio. (c) SEM micrograph of the permalloy nanowires for aspect ratio 37.5. (d) EDAX micrograph of the permalloy nanowires.

The characteristic peaks of $FeNi_3$ at 44.3 (111) and 51.4 (200) were observed in the XRD patterns after electrodeposition. No iron and nickel oxides, hydroxides or other impurity phases are detected. Fig. 4.8(c) shows the scanning electron microscopy (SEM) image of as-prepared permalloy NWs grown perpendicular to the supporting Au substrate. It is evident from Fig. 4.8(c) that the length and the diameter of the NWs are uniform in nature as well as the surface of the nanowires is smooth. The local elemental composition of the as-prepared permalloy NWs was

studied by EDAX microanalysis at the single NW level, shown in Fig. 4.8(d). It confirms that the permalloy NW are composed of Fe and Ni elements. The elemental composition of Fe:Ni is 1:3 respectively, in atomic and weight percentage.

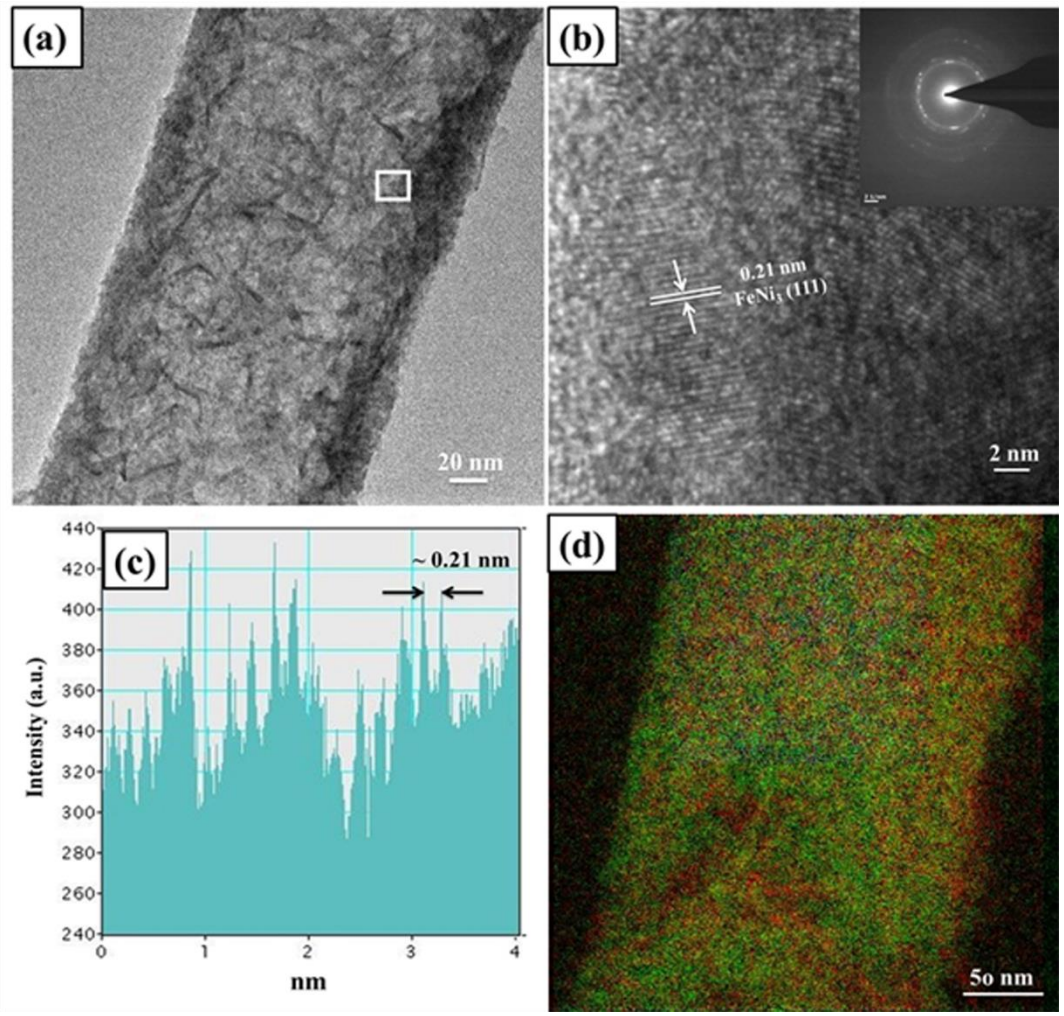


**Figure 4.9**. (a) TEM micrograph of permalloy nanowire for AR 37.5. (b) Typical HRTEM image and (inset of (b)) SAED pattern indicating the polycrystalline nature of the NW. (c) Corresponding intensity profile for the line across the lattice fringes. (d) STEM micrograph (colour mapping) of the as-prepared permalloy nanowires.

The transmission electron microscope (TEM) and the high resolution transmission electron microscope (HRTEM) micrographs of as-prepared permalloy NWs shown in Fig. 4.9(a)&(b), respectively, clearly shows the formation of permalloy NW ~ 200 nm diameter. It is also evident from Fig. 4.9 (a) &(b) that the formation of NW is uniform in nature. The inset image of the Fig. 4.9 (b) shows the selected area electron diffraction (SAED) pattern of the permalloy NW which indicates the polycrystalline nature of the NW. Figure 4.9 (b) shows a HRTEM image at the selected edge of an individual permalloy NW from Fig. 4.9 (a). As shown in

Fig. 4.9 (c), a typical intensity profile covers the line scan (labelled by a line in figure 4.9(b) across the lattice fringes. The periodic fringe spacing of 0.21 nm agrees well with interplanar spacing between the (111) planes of the permalloy NW. Figure 4.9 (d) show the typical STEM-EDX elemental colour mapping images of an individual permalloy NW. The results confirm the existence of Fe and Ni elements, which are distributed homogeneously over the entire permalloy NW.

### 4.2.3.2 Magnetic properties

Figure 4.10 shows the OP (H ∥ wire-axis) and IP (H ⊥ wire axis) hysteresis loops of the four samples at room temperature. For all samples, the change in magnetization with the magnetic field in the IP hysteresis loops is much less than that in the corresponding OP hysteresis loops. Remanence in the IP direction is also much smaller compared to the OP counterpart. Along the OP direction, magnetization saturates at a lower field compared to the IP direction. In the absence of an external magnetic field, the exchange interaction and different anisotropy fields e.g., shape, magneto crystalline, surface anisotropy fields [48], determine the equilibrium magnetization of a ferromagnetic nanostructure.

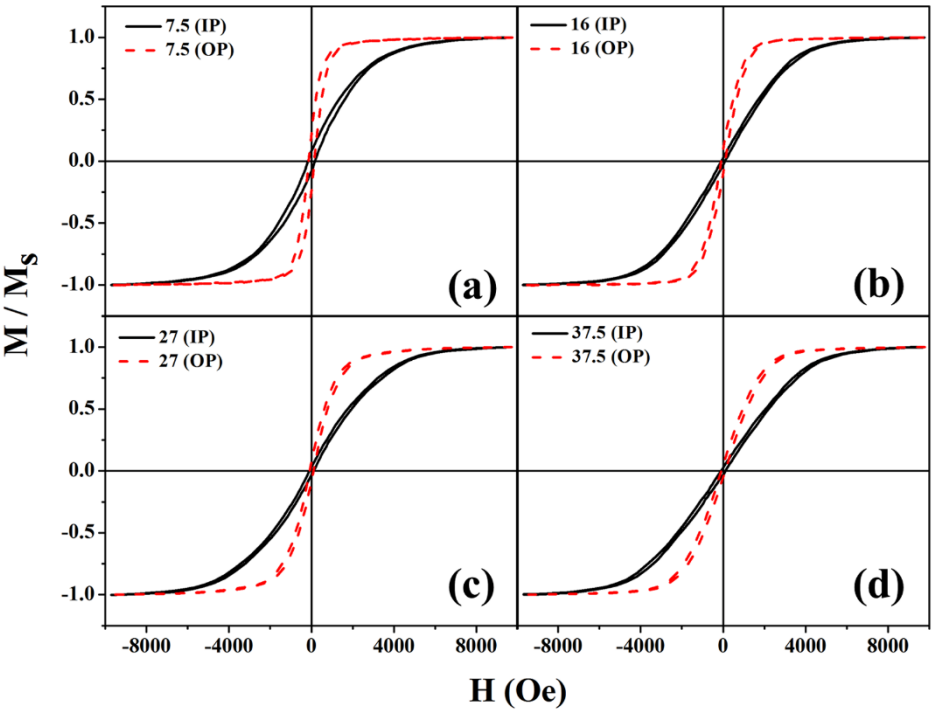


**Figure 4.10**. In-plane and out-of-plane magnetic hysteresis loops of arrays of nickel nanowires having an aspect ratio of (a) 7.5, (b) 16.0, (c) 27.0 and (d) 37.5.

At remanence, the arrangement of spins in a ferromagnetic cylinder can give rise to a flower or vortex state depending on the diameter of it [49-55]. In flower state, the spins are parallel to each other and are oriented along the NW axis. It follows a coherent magnetization reversal and produces square shaped hysteresis loop. Whereas in the vortex state, the magnetic spins are tilted in the circumferential direction and make a certain angle to each other. In this state, curling type of reversal takes place giving rise to a tilted hysteresis loop with much low remanence and high coercivity as observed in the Fig. 4.10 Here, the experimental data pointing towards the remanent state of our NWs is to be the flower state. All these characteristics indicate the direction of the domain magnetization parallel to the wire axis or the magnetic field. Which means the magnetic easy axis on the NWs are along the axis of the NWs.

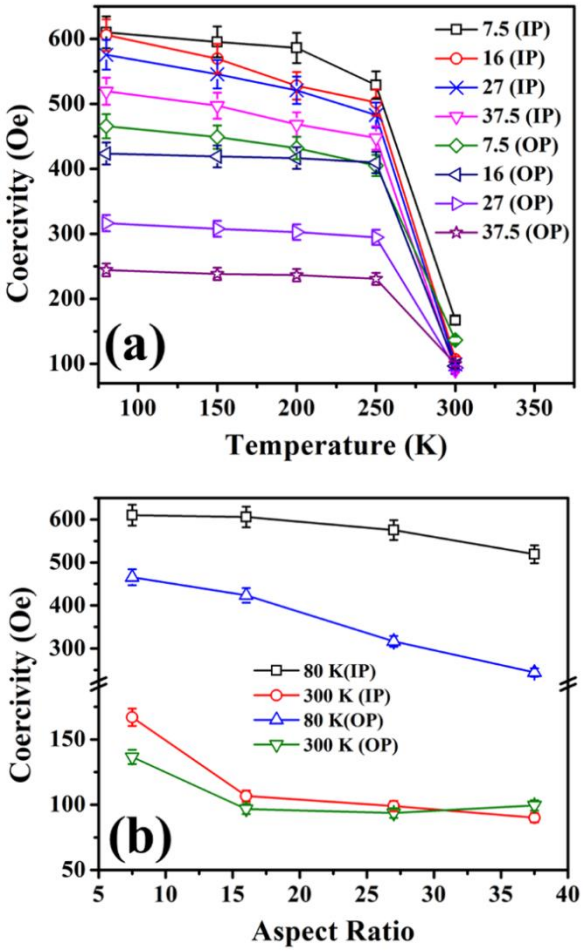


**Figure 4.11**. (a) Temperature dependence of in-plane and out-of-plane coercivity of arrays of permalloy nanowires having an aspect ratio of 7.5, 16.0, 27.0, and 37.5. (b) Variation of in-plane and out-of-plane coercivity of arrays of permalloy nanowires with the aspect ratio at temperatures 80 and 300 K. Error bars for the measurements are shown in the graph.

Temperature dependence (80–300 K) of OP coercivity ($H_C^{OP}$) and IP coercivity ($H_C^{IP}$) of the four samples is shown in Fig. 4.11(a). $H_C^{OP}$ and $H_C^{IP}$ of the four samples decrease with the increase in temperature. One of the possible reasons for this effect may be due to the reduction in magnetocrytalline anisotropy energy with the increase in temperature as observed in most of the ferromagnetic materials. Figure 4.11 (b) shows the variation of $H_C^{OP}$ and $H_C^{IP}$ with the aspect ratio at 80 and 300 K. At 300 K, $H_C^{OP}$ changes from 137 to 99 Oe and $H_C^{IP}$ changes from 167 to 90 Oe due the change in the aspect ratio from 7.5 to 37.5. At 80 K, $H_C^{OP}$ changes from 466 to 245 Oe and $H_C^{IP}$ changes from 610 to 519 Oe due to the same change in the aspect ratio. $H_C^{IP}$ is higher than $H_C^{OP}$ for all aspect ratios used in the present study .

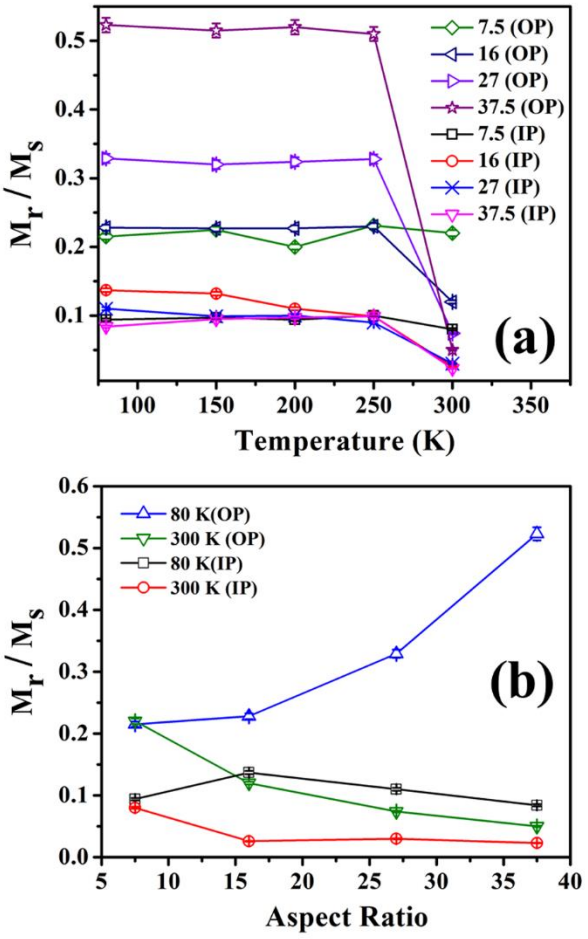


**Figure 4.12**. (a) Temperature dependence of in-plane and out-of-plane squareness ratio ($M_r/M_s$) of arrays of permalloy nanowires having an aspect ratio of 7.5, 16.0, 27.0, and 37.5. (b) Variation of in-plane and out-of-plane squareness ratio ($M_r/M_s$) of arrays of permalloy nanowires with an aspect ratio at 80 and 300 K. Error bars for the measurements are shown in the graph.

In-plane squareness ratios, $(M_r/M_s)^{IP}$, of all the samples are very small (Fig. 4.12 (a)) and remain almost constant with temperature. On the other hand, out-of-plane squareness ratios, $(M_r/M_s)^{OP}$, are remain almost constant below room temperature and shows significant sudden decrease with the increase in temperature from 80 to 300 K. The variation of squareness on the aspect ratio is shown in Fig. 4.12 (b) at 80 and 300 K. $(M_r/M_s)^{OP}$ increases with increase of aspect ratio for 80 K and vice versa observed for 300K. $(M_r/M_s)^{IP}$ have an initial increase at lower values of the aspect ratio then started decreasing for 80K and vice versa observed for 300K.

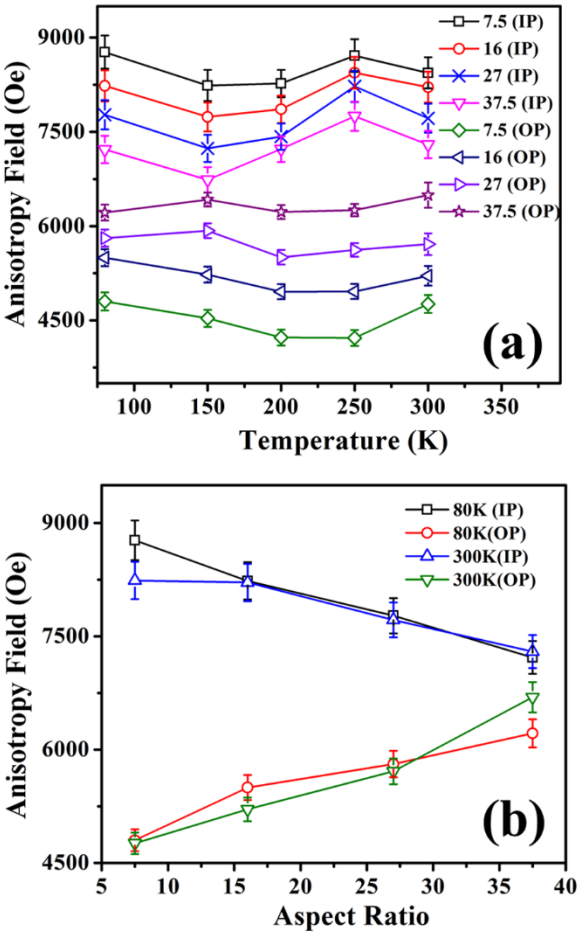


**Figure 4.13**. (a) Temperature dependence of in-plane and out-of-plane anisotropy field ($H_k$) of arrays of permalloy nanowires having an aspect ratio of 7.5, 16.0, 27.0, and 37.5. (b) Variation of in-plane and out-of-plane anisotropy field ($H_k$) of arrays of permalloy nanowires with an aspect ratio at 80 and 300 K. Error bars for the measurements are shown in the graph.

Temperature dependence (80–300 K) of OP anisotropy field ($H_{an}^{OP}$) and IP coercivity ($H_{an}^{IP}$) of the four samples is shown in Fig. 4.13 (a), we calculated from their hysteresis loops. $H_{an}^{OP}$ of the four samples shows variation increase and

decrease with the increase in temperature from 80 to 300 K. $H_{an}^{IP}$ of the four samples follow the reverse trend of $H_{an}^{OP}$ with the increase in temperature from 80 to 300 K. Figure 4.13 (b) shows the variation of $H_{an}^{OP}$ and $H_{an}^{IP}$ with the aspect ratio at 80 and 300 K. At 300 K, $H_{an}^{OP}$ changes from 4761 to 6694 Oe and $H_{an}^{IP}$ changes from 8239 to 7298 Oe due the change in the aspect ratio from 7.5 to 37.5. Which indicates that $H_{an}^{OP}$ increases with the increase of aspect ratio and $H_{an}^{IP}$ shows the reverse trend. At 80 K, $H_{an}^{OP}$ changes from 4802 to 6216 Oe and $H_{an}^{IP}$ changes from 8770 to 7220 Oe due to the same change in the aspect ratio. $H_{an}^{IP}$ is higher than $H_{an}^{OP}$ for all aspect ratios used in the present study. Above studies clearly indicate that the magnetic easy axis direction of the permalloy NWs are in the axial direction of the NWs.

$H_{an}^{IP}$ and $H_{an}^{OP}$ includes all the anisotropies that are present in the NWs in that direction. Anisotropies arise from geometrical shape, crystallinity of the NWs and magnetostatic interaction among the NWs are believed to be the most prominent contributions of $H_{an}$. Shape anisotropy of a NW originates from the self-demagnetization field of the NW. Numerical calculations of demagnetization fields [56], of the NWs used in our study show that, the shape anisotropy ($H_{sh}$) always tries to make the OP as easy direction. We calculated the shape anisotropy ($H_{sh}$) (~ $2\pi M_S$ = 5407 Oe, considering $M_S$ = 861 emu/cc) [57], for aspect ratio 37.5.

On the other hand, the magnetocrystalline anisotropy ($H_k$) remains constant for a particular wire diameter irrespective of its aspect ratio and depends only on the crystallinity of the NW. Here the NWs have fcc crystalline phase for NW with ~200 nm diameter. In case of single crystalline ~50 nm NWs, $H_k \sim \frac{2K_1}{M_S}$ = 1324 Oe (assuming anisotropy as uniaxial and neglecting higher order terms), where $K_1$ is the first order anisotropy constant and is equal to $5.7 \times 10^5$ erg/cc for fcc phase [45]. $H_k$ is much lesser in 200 nm NWs as they consist of textured fcc as well as polycrystalline phase. From the above discussions it is clear that, $H_{sh}$ is always greater than $H_k$ for all the NWs we studied and the resultant of these two tries to make the OP as the easy direction of magnetization.

### 4.2.4 Conclusion

In summary, permalloy nanowires with an average diameter of ~ 200 nm have been successfully fabricated in the pores of the self-engineered anodized aluminium oxide (AAO) templates by electrodeposition technique. By varying the length from 1.5 to 7.5 μm, got corresponding changes in aspect ratio from 7.5 to 37.5. Structural and magnetic studies of these nanowires have been done in details. Temperature and aspect ratio dependent in-plane and out-of-plane magnetic measurements of the permalloy nanowires indicate the magnetic easy axis of the nanowires along their axial direction, which is very desirable in magnetic recording device applications.

## 4.3. Angular dependent magnetic properties of 1D Permalloy nanowires using self-developed AAO templates

### 4.3.1. Preamble

In the past few years, one dimensional (1D) Permalloy nanostructured materials such as nanowires (NWs), nanochains and nanotubes have attracted significant attention due to their novel properties and potential applications in microelectronics and magnetic nanodevices [58-60]. Permalloy refers to an alloy of Ni and Fe with 80 and 20 at% composition respectively [61]. There are various techniques to fabricate magnetic NWs. Among those methods, electro deposition technique (EDT) is a low cost competitive technique for the controlled preparation of high-quality 1D nanostructures [59-61].

Porous anodic aluminum oxide template (AAO) is one of the most widely used templates utilized to fabricate various 1D nanomaterials [62, 63]. AAO has been used in the fields of electronics, magnetic [60, 64], energy storage [65], and biosensors [66]. Anodic aluminium oxide (AAO) templates show remarkable properties such as uniform pore diameter and length paralleling each other.

1D Permalloy NWs are particularly attractive due to their high permeability, low coercivity, near zero magnetostriction and high anisotropic magnetoresistance. Because of low magnetostriction of Permalloy, shape anisotropy plays a very important role in governing their magnetic properties. As a result, the NWs show unidirectional anisotropy along their length. Because of this property, they can be used in many applications such as recording head sensors, magnetic storage devices etc.

In this work, we report a simple and low-cost approach to fabricate large area highly ordered nanoporous anodized alumina oxide (AAO) templates by two-step anodization process. 1D Permalloy nanowire arrays were fabricated into the nanometer scaled pores of AAO template using electro deposition technique (EDT). We studied the growth, structural and angular dependence of magnetic properties of NWs.

## 4.3.2. Experimental

Highly ordered and self-organized nanoporous anodic aluminium oxide (AAO) templates were fabricated by the controlled two-stage electrochemical anodization of high purity Al foil, as described in previous chapter and elsewhere [21-23], was used as the host to prepare the permalloy NWs. Table 4.1 shows the anodizing conditions for preparing AAO templates. AAO templates with different pore size distribution were obtained by changing the anodizing voltage.

To use it as an electrode, one side of it was coated with a conductive gold layer of 0.1 μm thickness by the thermal evaporation technique. All electrochemical deposition of NWs was carried out using an AUTOLAB-30 potentiostat and a conventional three-electrode cell (20 $cm^3$ capacity). Electrolyte solution used for the Permalloy NW deposition consists of 100 g/L $NiSO_4$, 20 g/L $FeSO_4$, 20 g/L ascorbic acid and 30 g/L $H_3BO_3$. The pH of the solution is maintained at 3.5. Permalloy NWs were electrodeposited at room temperature. The electrodeposition time was 30 minutes. The length of the NWs obtained was ~14μm. For structural characterization of NWs, the electrodeposited AAO templates were dissolved in 2M of NaOH solution at room temperature.

**Table. 4.1**: Anodizing conditions and morphologic properties of AAO templates.

| Samples | Anodizing Voltage (V) | First Anodization Time (min.) | Second Anodization Time (hr.) | Average pore diameter (nm) |
|---|---|---|---|---|
| AAO#1 | 50 | 15 | 3 | 40 |
| AAO#2 | 55 | 15 | 3 | 58 |
| AAO#3 | 60 | 15 | 3 | 73 |
| AAO#4 | 65 | 15 | 3 | 95 |

Scanning electron microscope (FEI Quanta-200 Mark-2) and Transmission electron microscope (FEI TECNAI TF20ST) were used to observe the NWs, their surface morphology and to determine their length and diameter. The crystalline structures of FeNi NWs were investigated by transmission electron microscopy. The phase of the samples was confirmed by x-ray diffraction (X'Pert Pro, Panalytical) and

the composition of the NWs was determined using energy dispersive analysis by x-ray (EDAX). Magnetic properties were studied using a vibrating sample magnetometer (Lakeshore, model 7144) while the angle θ between the NWs and applied field changed from 0 to 90°.

### 4.3.3. Results and Discussions

We grew Permalloy NWs with average diameter of about 40 & 70 nm respectively and the average length of about 14 μm. Fig. 4.14(a) shows the SEM image of the Permalloy NWs with 40 nm diameter prepared within AAO templates by electrodeposition technique. This figure also indicates the uniformity in length and diameter of the NWs. To check the composition of the NWs, we performed EDAX measurement shown in Fig. 4.14(b) and found that Fe and Ni was 20:80 in at%.

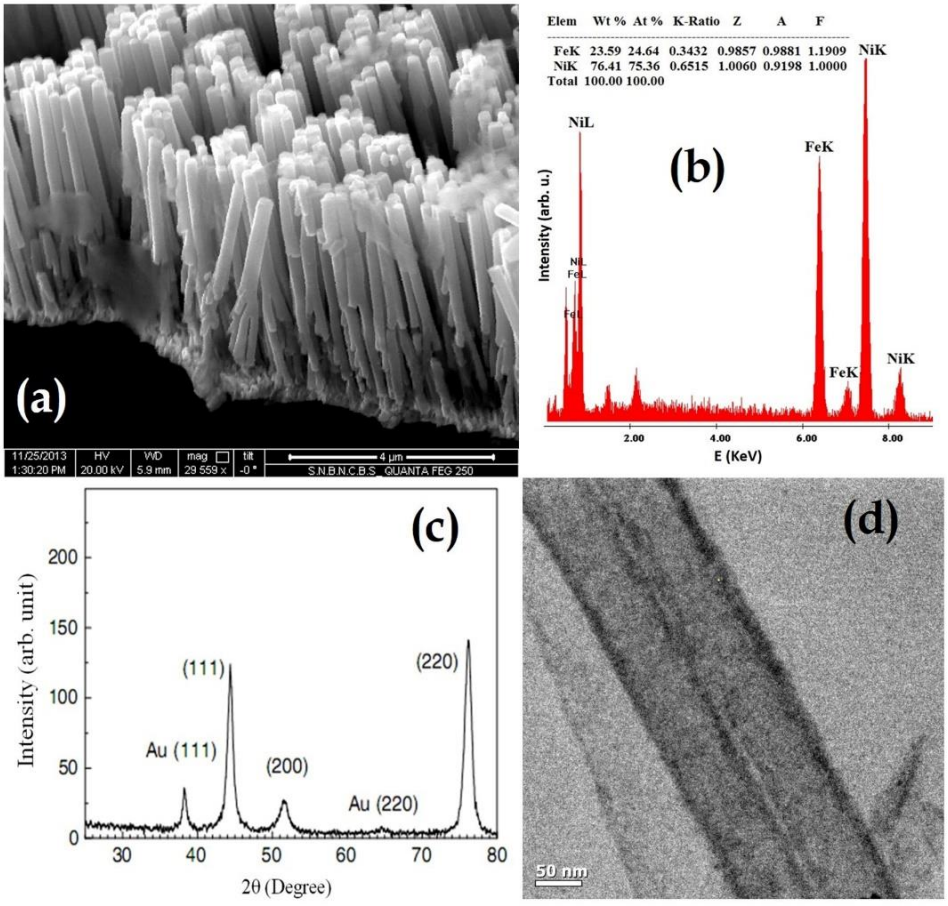


**Figure 4.14.** (a) SEM micrographs of NiFe NWs with 40 nm diameter, (b) EDAX spectra with elemental quantification of the sample shows the Ni:Fe = 80:20 in at%, (c) TEM image of the Permalloy nanowire with the diameter of 70 nm, (d) XRD pattern of NiFe NWs.

Figure 4.14 (c) shows the XRD pattern of the 70 nm sample. From the XRD pattern, it is observed that the permalloy NWs consists of face centered cubic (fcc) crystal structure. Gold (Au) peaks are also present in the pattern as one side of AAO template was coated with it to make the template conducting. TEM micrograph of NW with diameter 70 nm, shown in Fig. 4.14(d), indicates its uniform diameter throughout its length.

The magnetic hysteresis loops as a function of θ, the angle between the applied magnetic field and the NWs axis, are shown in Fig. 4.15(a) &(b) for 40 and 70 nm NWs respectively. The magnetic properties, such as coercivities ($H_c$) and remnant magnetization ($M_r/M_s$) are shown in Fig. 4.15 (a) (40nm) and 4.15 (b) (70nm). In case of 40nm NWs, coercivity $H_c$ decreases from 1307 Oe to 258 Oe on changing θ from 0° to 90°. Similar trend was also observed in the case of 70 nm NWs as well. We also observed that in case of 40nm NWs, remnant magnetization ($M_r/M_s$) decreases from 0.75 to 0.05 on changing θ from 0° to 90°. 70 nm NWs also shows similar change in remnant magnetization ($M_r/M_s$) with θ.

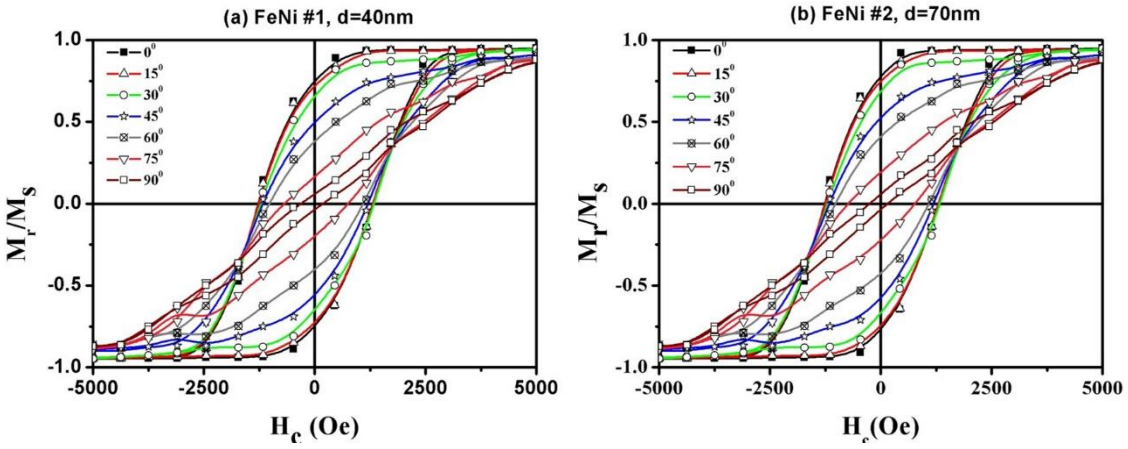


**Figure 4.15**. Angular dependence of Hysteresis loops of the Permalloy NWs arrays with diameter (a) 40 nm and (b) 70 nm.

$H_c$ for Permalloy NWs of 40 nm are higher than those for the NWs of 70 nm because the larger aspect ratio. In the case of an array of closely spaced nanowires magnetostatic interactions between the nanowires play an important role in governing their magnetic properties as it opposes the shape anisotropy of the individual nanowires [18]. Magnetostatic interaction due to dipolar coupling can be

taken into account by including additional anisotropy fields and the net magnetostatic field can be written as following equation:

$$H_{MF} = 2\pi M_S - 2\pi M_S\gamma - 4\pi M_S\gamma\,, \tag{4.3}$$

where the filling factor $\gamma=3.67(d/D)^2$, $(d/D)$ being the ratio of the nanowire diameter to the interwire distance. In Eq. (4.3), besides the self-demagnetizing field $2\pi M_S$, two additional contributions come into play. The first one is $2\pi M_S\gamma$ due to charges on the cylindrical wire surfaces producing a dipolar field and the second one is $4\pi M_S\gamma$ developed by the charges at the top and bottom ends. Combining all contributions, Eq. (4.3) can be written as:

$$H_{MF} = 2\pi M_S(1-3\gamma) \tag{4.4}$$

Eq. (4.4) determines how the $H_c$ and $M_r/M_s$ for NWs depend upon the aspect ratio. We also calculated the magnetic anisotropy field ($H_K$) as a function of θ for 40nm and 70nm NWs and they are shown in the inset of Fig. 4.16 (a) and (b). In case of 40nm NWs, $H_K$ increases from 1165Oe to 4995 Oe on changing θ from 0° to 90°. Similar change was also observed in 70 nm NWs.

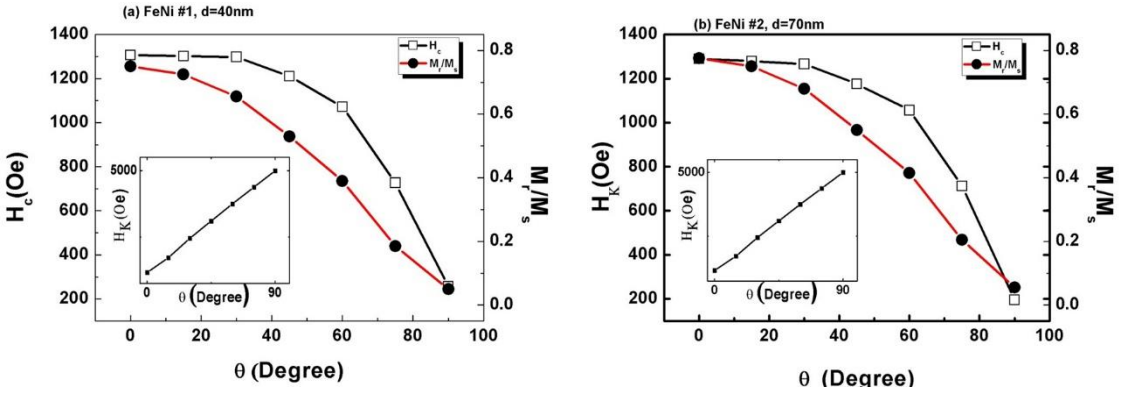


**Figure 4.16**. Angular dependence of $H_c$ and $M_r/M_s$ of the Permalloy NWs with diameters (a) 40 nm and (b) 70nm. Inset: angular dependence of magnetic anisotropy field ($H_K$) of the respective NWs.

The change of the magnetic properties with the direction of applied magnetic field demonstrated that the permalloy NWs prepared in this work showed strong shape anisotropy and the easy axis was parallel to the NWs. As magnetocrystalline

as well as magnetostrictive anisotropy were much less in permalloy, shape anisotropy played the most important role in governing their magnetic properties.

### 4.3.4. Conclusion

In summary, The AAO templates prepared by two-step anodizing method have highly ordered and high density pore arrangement, which is proper for the fabrication of 1D nanowire arrays. Permalloy NWs arrays were fabricated into the AAO templates and their morphologic and magnetic properties were characterized. Permalloy NWs arrays showed strong shape anisotropy with the easy axis parallel to the NWs.

# 4.4. Study of aspect ratio and temperature dependent magnetic properties of CoNi nanotube arrays

## 4.4.1. Preamble

Since last few years, the arrays of ordered nanotubes have attracted researchers' interest due to its broad application in various fields such as medicine, electronics, etc. Especially, magnetic nanotubes are more attractive due to their potential applications in the field of high density magnetic recording devices and magnetic sensor [67-70], where they have an edge over non-magnetic nanotubes because they can be manipulated according to the requirement by applying an external magnetic field [71]. So far, there are various techniques known for the fabrication of the arrays of ordered nanotubes, among them template assisted electrodeposition technique is very famous because of its simplicity, low cost and controllability over the parameters [72-74]. By using this electrodeposition method, various metallic and alloy nanotubes have been embedded into the pores of anodized aluminum oxide (AAO) template and studied their magnetic properties extensively [75-78]. Although, very few reports on the magnetic properties of CoNi nanotubes have been reported.

It is very well known fact that the magnetic properties of a single nanotube depend upon various anisotropy energies, such as orientation of crystal axis, texture, and geometrical characteristics, shape, magnetocrystalline and surface anisotropies. The direction of the effect anisotropy field inside the nanotube denotes the direction of the magnetic easy axis inside the nanotube. However, In case of the closely packed arrays of nanotubes, the magnetostatic interaction among the nanotubes plays an important role to define the magnetic properties of the nanotubes, compare to other anisotropies. [79, 80]. The magnetostatic interaction term depends upon the aspect ratio of the nanotubes. [18, 79]**.** Temperature is also an important parameter which affects the magnetic properties of the nanostructures.

So far there is no report found which explains the aspect ratio and temperature dependence magnetic properties of the arrays of CoNi nanotubes. In this paper, we focused on the impact of electrodeposition parameter on the aspect

ratio of the CoNi nanotubes. At the same time, we also studied the effect of aspect ratio and temperature on the magnetic properties of the produced CoNi nanotubes.

## 4.4.2. Experimental

The template assisted electrodeposition technique was performed for the fabrication of high-density arrays of CoNi nanotubes. We fabricated anodic aluminium oxide (AAO) template by the controlled two-stage electrochemical anodization procedure of high purity (99.999%) Al foil, as described in previous chapter. As a result, we got AAO templates with an average pore diameter about 100 nm, with a thickness of about 50 μm. Such fabricated AAO templates were used as the host to prepare the CoNi NTs.

A very uniform thin layer (~500 nm) of conductive Au sputtered onto one side of the AAO template. Such Au sputtered AAO template was used as the working electrode in the electrodeposition process. The software controlled conventional three electrode electrochemical cell and a power supply (potentiostat AutoLab-30) was used for the electrochemical deposition of CoNi NTs. A high purity Pt wire and an Ag/AgCl electrode were used as the counter and reference electrode, respectively. The arrays of CoNi NTs have been electrodeposited in the pores of AAO using an aqueous solution of 55 g $L^{-1}$ $NiSO_4.7H_2O$, 45 g $L^{-1}$ $CoSO_4.7H_2O$, 40 g $L^{-1}$ $H_3BO_3$ and 10 g $L^{-1}$ $NH_4OH$ as the electrolyte at room temperature. Here, $H_3BO_3$ and $NH_4OH$ play the role of the buffer. The electrodeposition of CoNi was conducted by using a dc voltage of -1.55 V vs. Ag/AgCl following linear sweep voltammetry results and the pH of the electrolyte was maintained at 3.5 during electrodeposition process. The electrodeposition was carried out for 5, 30 and 60 minutes in order to prepare three samples of CoNi NTs (sample-1, sample-2 and sample-3) of ~1.5, 6.5 and 12 μm lengths respectively. Afterwards, the template containing the CoNi NTs was dissolved in a 2 M NaOH solution at room temperature for a day to get the arrays of CoNi NTs on Au substrate.

The crystallographic structure of the CoNi NTs were examined by x-ray diffraction (XRD,Panalytical X'Pert Pro diffractometer). Field emission scanning

electron microscope (FESEM, FEI Quanta-200 Mark-2) and Transmission electron microscope (TEM, FEI TECNAI G2 TF20ST) were used to study the morphology and the structure of the arrays of CoNi NTs. X-ray (EDAX) and X-ray photoelectron spectroscopy (XPS) were used to analyze the crystal structures, chemical composition and elemental composition, respectively, of the as prepared CoNi NTs. Magnetic measurements of the CoNi NTs have been performed using a vibrating sample magnetometer (VSM, Lakeshore, model 7144) by placing the axis of the arrays of CoNi nanotubes sample along the direction of the applied magnetic field (OP – out of plane, H parallel to the wire axis) and perpendicular to the direction of the applied magnetic field (IP – in plane, H perpendicular to the wire axis) within the temperature range of 80–350 K.

### 4.4.3. Results and Discussions

From FESEM micrograph (Fig. 4.17(a)) we observed that the pores of Anodized alumina oxide (AAO) template obtained after two step anodization technique have uniform pore diameters with an average pore diameter of ~100 nm and an average distance among pores ~ 55 nm. Fig. 4.17 (b) shows the Field emission scanning electron microscopy (FESEM) image of as-prepared arrays of CoNi nanotubes grown perpendicular to the supporting Au substrate. It is evident from Fig. 4.17 (b) that the length and the diameter of the nanotubes are uniform in nature as well as the surface of the nanotubes is smooth. The local elemental composition of the as-prepared CoNi NTs was studied by EDAX microanalysis at the single NW level, shown in Fig. 4.17 (c). It confirms that the CoNi NTs are composed of Fe and Ni elements. The elemental composition of Co:Ni is 1:1 respectively, in atomic percentage, whereas, whereas the peak for Au due to the presence of Au substrate. The crystallographic nature of the arrays of CoNi NTs investigated by XRD (Fig. 4.17 (d)) indicates that the as grown CoNi NTs are crystalline in nature. The diffraction peaks in the XRD pattern appear from the hcp phase of CoNi and the metallic Au layer underneath the nanotubes. The characteristic peaks of CoNi at 44.4, 51.7 and 76.2 were observed in the XRD patterns for the corresponding planes of (111), (200)

and (220), respectively, after electrodeposition. No other oxides, hydroxides or other impurity phases of cobalt and nickel are detected.

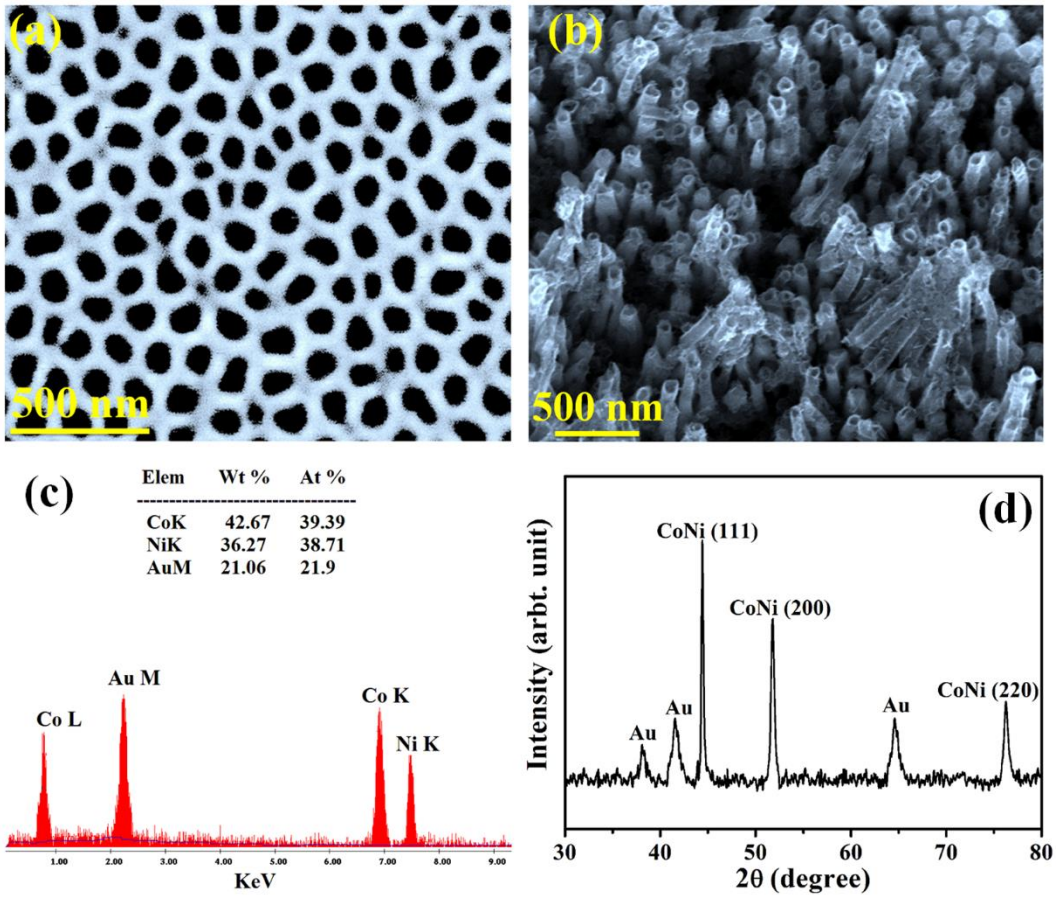


**Figure 4.17.** (a) SEM micrograph of the top view of the AAO template. (b) SEM micrograph (c) EDAX micrograph and (d) XRD Pattern of the as- prepared CoNi nanotubes.

The transmission electron microscope (TEM) and the high resolution transmission electron microscope (HRTEM) micrographs of as-prepared CoNi NTs shown in Fig. 4.18(a) and 4.18 (b), respectively, clearly shows the formation of CoNi NTs ~ 200 nm diameter. It is also evident from Fig. 4.18 (a) and 4.18 (b) that the formation of NW is uniform in nature. The inset image of the Fig. 4.18 (b) shows the selected area electron diffraction (SAED) pattern of the CoNi NTs which indicates the polycrystalline nature of the NW. Figure 4.18 (b) shows a HRTEM image at the selected edge of an individual CoNi NTs from Fig. 4.18 (a). As shown in Fig. 4.18 (c), a typical intensity profile covers the line scan (labelled by a line in figure 4.18(b)) across the lattice fringes. The periodic fringe spacing of 0.21 nm agrees well with interplanar spacing between the (111) planes of the CoNi NTs. Figure 4.18 (d) show

the typical STEM-EDX elemental colour mapping images of an individual CoNi NTs. The results confirm the existence of Fe and Ni elements, which are distributed homogeneously over the entire CoNi NTs.

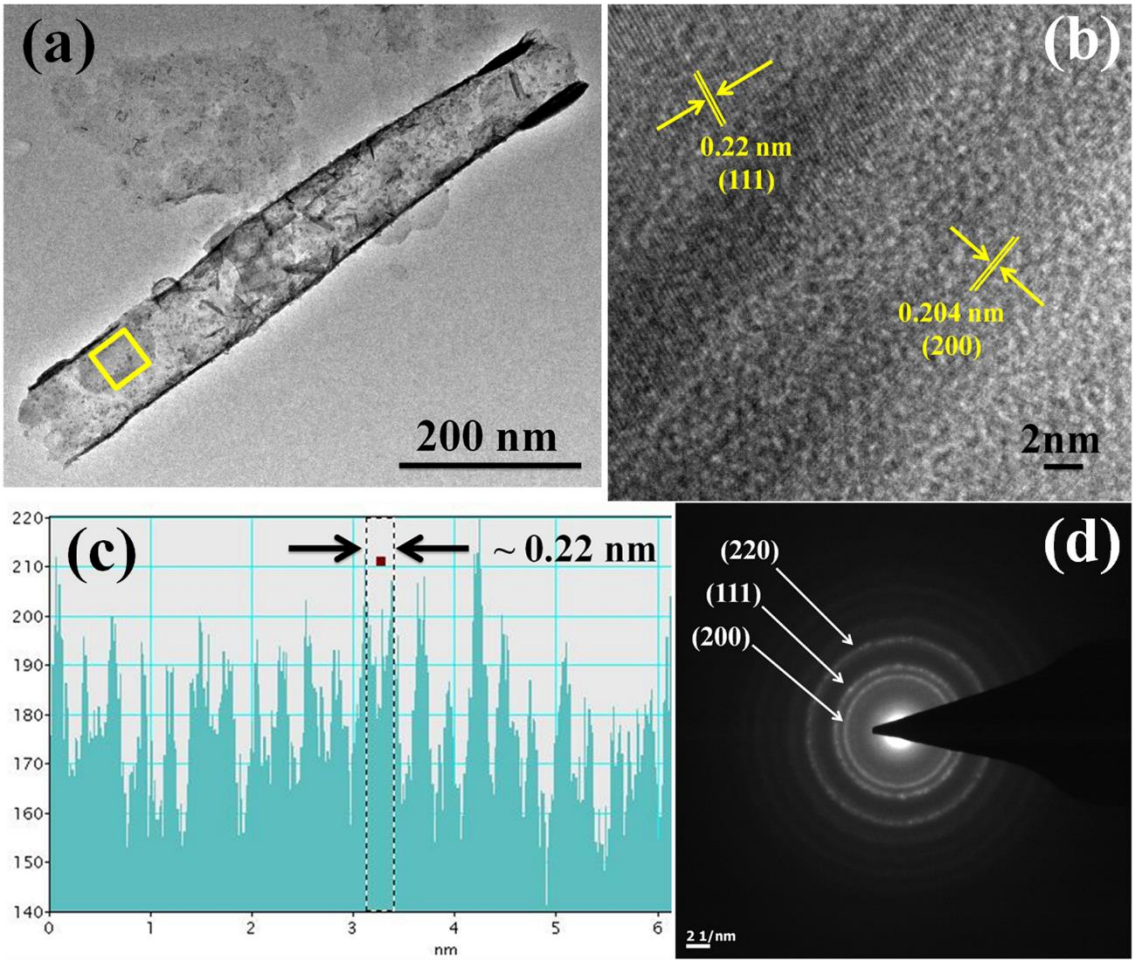


**Figure 4.18.** (a) TEM micrograph, (b) Typical HRTEM image, (c) Corresponding intensity profile for the line across the lattice fringes. (d) SAED pattern of the as-prepared CoNi nanotubes.

Figure 4.19 shows the in-plane (IP, along the surface of the template and perpendicular to the wires axis) and out-of-plane (OP, perpendicular to the template surface and parallel to the wire axis) magnetic hysteresis loops of the three sample (with aspect ratio: 15, 65 and 120) at room temperature. In case of sample 1 (with aspect ratio 15), IP magnetic hysteresis loop shows a higher increase in the magnetization with magnetic field compared to its OP counterpart, which suggests that the magnetic easy axis in the nanotubes in the IP direction (perpendicular to the nanotubes long axis). However, in case of sample 2 (with aspect ratio 65) both IP & OP hysteresis loops are showing the same kind of change with the increase of magnetic field. On contrary of the two previous results, OP hysteresis loop changes

much compare to IP hysteresis loop for sample 3 (with aspect ratio 120). These results clearly suggest that the magnetic easy axis of the arrays of nanotubes are changing from IP to OP direction with the increase in the aspect ratio from 15 to 120.

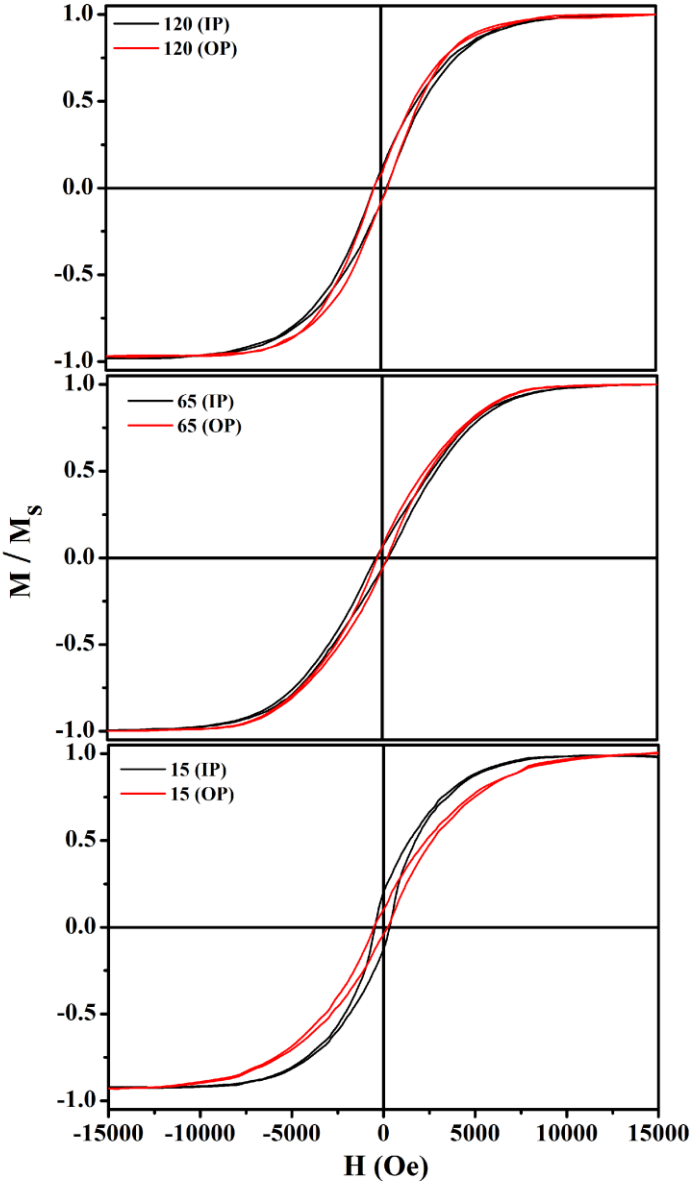


**Figure 4.19**. In-plane and out-of-plane magnetic hysteresis loops of arrays of CoNi nanotubes having an aspect ratio of 15, 65 and 120.

The coercivity change with temperature mainly depends on the saturation magnetization and magnetocrystalline anisotropy at low temperature. Because of the high aspect ratio of the nanotube, when the external field is applied, the demagnetization energy in the direction along the tube axis is much smaller than perpendicular to the tube axis, and the sample could be magnetized more easily

along the tube axis. The magnetic moments in the nanotubes are aligned mainly in the plane of tube walls, and the distributions of the magnetic moment in the plane are isotropic.

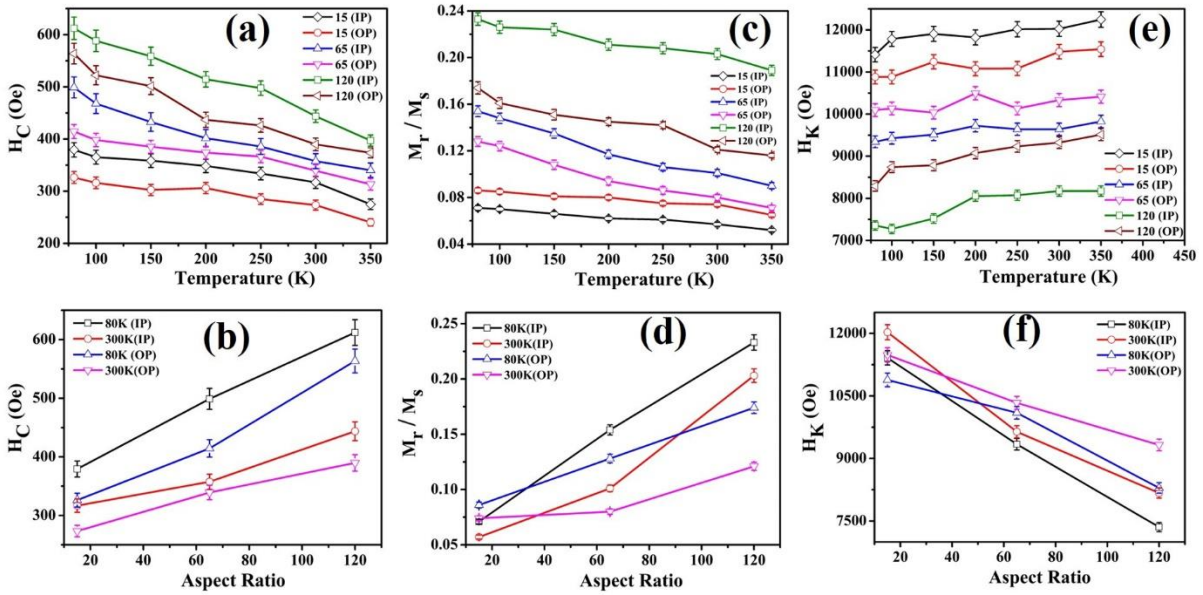


**Figure 4.20**. Temperature dependence of in-plane and out-of-plane (a) coercivity ($H_c$), (c) squareness ratio ($M_r/M_s$), (e) anisotropy field ($H_k$) of arrays of CoNi nanotubes having an aspect ratio of 15, 65, 120; Variation of in-plane and out-of-plane (b) coercivity ($H_c$), (d) squareness ratio ($M_r/M_s$), (f) anisotropy field ($H_k$) of arrays of CoNi nanotubes with the aspect ratio at temperatures 80 and 300 K.

Temperature dependence (80–350 K) of OP coercivity ($H_C^{OP}$) and IP coercivity ($H_C^{IP}$) of the three samples is shown in Fig. 4.20(a). $H_C^{OP}$ and $H_C^{IP}$ of the three samples decrease with the increase in temperature. One of the possible reasons for this effect may be due to the reduction in magnetocrytalline anisotropy energy with the increase in temperature as observed in most of the ferromagnetic materials. Figure 4.20 (b) shows the variation of $H_C^{OP}$ and $H_C^{IP}$ with the aspect ratio at 80 and 300 K. $H_C^{IP}$ is higher than $H_C^{OP}$ for all aspect ratios used in the present study.

In-plane squareness ratios, $(M_r/M_s)^{IP}$, of all the samples are small compare to their out-of-plane counterpart (Fig. 4.20 (c)). On the other hand, In-plane squareness ratios, $(M_r/M_s)^{IP}$ and out-of-plane squareness ratios, $(M_r/M_s)^{OP}$, are decreasing with the increase in temperature from 80 to 350 K. The variation of squareness on the aspect ratio is shown in Fig. 4.20 (d) at 80 and 350 K. $(M_r/M_s)^{IP}$ and $(M_r/M_s)^{OP}$ increases with increase of aspect ratio for 80 K and 300K.

Temperature dependence (80–350 K) of OP anisotropy field ($H_{an}^{OP}$) and IP anisotropy field ($H_{an}^{IP}$) of the three samples is shown in Fig. 4.20 (e), we calculated from their hysteresis loops. $H_{an}^{IP}$ and $H_{an}^{OP}$ of the three samples shows variation increase with the increase in temperature from 80 to 350 K. But $H_{an}^{OP}$ is higher than $H_{an}^{IP}$ for aspect ratio 15 and 65 but reverse trend observed for aspect ratio 120 for temperature range from 80 to 350 K, which is suggesting that the magnetic easy axis is changing from IP direction to OP direction with the increase in aspect ratio. Figure 4.20 (f) shows the variation of $H_{an}^{OP}$ and $H_{an}^{IP}$ with the aspect ratio at 80 and 300 K. At 300 K, both $H_{an}^{IP}$ and $H_{an}^{OP}$ decreases with the increase in aspect ratio. But there is a cross over in both $H_{an}^{IP}$ and $H_{an}^{OP}$, which indicates that magnetic easy axis changing from IP direction to OP direction with the increase in aspect ratio.

### 4.4.4. Conclusion

In summary, The AAO templates prepared by two-step anodizing method have highly ordered and high density pore arrangement, which is proper for the fabrication of 1D CoNi nanotube arrays. CoNi nanotube arrays were fabricated into the AAO templates and their morphologic and magnetic properties were characterized. The CoNi nanotube arrays showed that their magnetic easy axis direction changes from perpendicular direction to axial direction of nanotubes with the increase in aspect ratio from 15 to 120.

## Bibliography


[1] S.A. Fabritsive and A.S. Pokrovsky, *J. Nucl. Mater.* **417**, 940 (2011).

[2] A. Iwase, S. Ishino, *J. Nucl. Mater.* **276**, 178 (2000).

[3] C.A. English, *J. Nucl. Mater.* **108**, 104 (1982).

[4] R. C. Hall, W. S. Byrnes, and R. G. Crawford, *J. Appl. Phys.* **30**, S288 (1959).

[5] R. Nagar, B.R. Mehta, J.P. Singh, D. Jain, V. Ganesan, S.V. Kesapragada, D. Gall, *J. Vac. Sci. Technol., A, Vac. Surf. Films* **26**(4), 887 (2008).

[6] H.G.F. Wilsdorf, *Phys. Rev. Lett.* **3**(4), 172 (1959).

[7] R. D. Brown, J. R. Cost, and J. T. Stanley, *J. Appl. Phys.* **55**, 1754 (1984).

[8] Y. S. Kim, M. H. Phan, S. C. Yu, K. S. Kim, H. B. Lee, B. G. Kim, and Y. H. Kang, *Physica B* **327**, 311 (2003).

[9] L. R. Aronin, *J. Appl. Phys.* **25**, 344 (1954).

[10] A. I. Schindler, E. I. Salkovitz, and G. S. Ansell, *J. Appl. Phys.* **30**, S282 (1959).

[11] H. Morita, Y. Tanji, H. Hiroyoshi and Y. Nakagawa, *J. Magn. Magn. Mater.* **31-34**, 107 (1983).

[12] C.G. Kim, H.C. Kim, S.S. Yoon, D.G. Park, J.H. Hong, *J. Magn. Magn. Mater.* **203**, 217 (1999).

[13] A. I. Schindler and C. M. Williams, *J. Appl. Phys.* **35**, 877 (1964).

[14] E.W. Blackmore, *IEEE Transactions on Nuclear Science*, **32**, 5 (1985).

[15] J. R. Cost, R. D. Brown, A. L. Giorgi and J. T. Stanley, *IEEE Transactions on Magnetics*, **24**, 3 (1988).

[16] W. E. Henry and E. I. Salkovitz, *J. Appl. Phys.* **30**, S286 (1959).

[17] M. Vázquez, M. Hernández-Vélez, K. Pirota, A. Asenjo, D. Navas, J. Vélezquez, P. Vargas, and C. Ramos, *Eur. Phys. J. B*, **40**, 489 (2004).

[18] A. Encinas-Oropesa, M. Demand, L. Piraux, I. Huynen, and U. Ebels, *Phys. Rev. B* **63**, 104415 (2001).

[19] G.J. Strijkers, J.H.J. Dalderop, M.A.A. Broeksteeg, H.J.M. Swagten, W.J.M. de Jonge, *J. Appl. Phys.* **86**, 5141 (1999).

[20] B. Das, K. Mandal, P. Sen, A. Bakshi, P. Das, *Physica B* **407**, 3767 (2012).

[21] G. G. Khan, N. Mukherjee, A. Mondal, N. R. Bandyopadhyay, A. Basumallick, *Mater. Chem. Phys.* **122**, 60 (2010).

[22] J. Sarkar, G. G. Khan, A. Basumallick, *Bull. Mater. Sci.* **30**, 271 (2007).

[23] G. G. Khan, A. K. Singh and K. Mandal, *Journal of Luminescence* **134,** 772 (2013).

[24] M. Vázquez, K. Pirota, J. Torrejón, D. Navas, and M. Hernández-Vélez, *J. Magn. Magn. Mater.* **294**, 174 (2005).

[25] N. B. Chaure, P. Stamenov, F. M. F. Rhen, and J. M. D. Coey, *J. Magn. Magn. Mater.* **290–291**, 1210 (2005).

[26] C.L. Xu, H. Li, G.-Y. Zhao, and H.-L. Li, *J. Magn. Magn. Mater.* **253**, 1399 (2006).

[27] B. Das, Pintu Sen, S. K. Bandopadhya and K. Mandal, *J. Appl. Phys.* **103**, 013908 (2008).
[28] S.K. Bandyopadhyay, P. Barat, P. Sen, U. De, A. De, P. K. Mukhopadhaya, S. K. Kar and C. K. Majumdar, *Physica C* **228**, 109 (1994).
[29] S.K. Bandyopadhyay, P. Sen, P. Barat, U. De, K. Mandal, S. K. Kar and C. K. Majumdar, *Physica C* **267**, 303 (1996).
[30] U. De, K. Mandal, D. Sanyal and C.K. Majumdar, *Physica C*, **339**, 113 (2000).
[31] K. Mandal, M.E. Loukas, A. Corey, and D.L. Atherton, *J. Magn. Magn. Mater.*, **175**, 255 (1997).
[32] K. Mandal, Th. Cramer, D.L.Artherton, *J. Magn. Magn. Mater.*, **212**, 231 (2000).
[33] D. Appell, *Nature London* **419**, 553 (2002).
[34] R. P. Cowburn, *Nature London* **448**, 544 (2007).
[35] C. A. Ross, M. Hwang, M. Shima, J. Y. Cheng, M. Farhoud, T. A. Savas, Henry I. Smith, W. Schwarzacher, F. M. Ross, M. Redjdal, and F. B. Humphrey, *Phys. Rev. B* **65**, 144417 (2002).
[36] M. P. Proenca, J. Ventura, C. T. Sousa, M. Vazquez, and J. P. Araujo, *Phys. Rev. B* **87**, 134404 (2013).
[37] R. Ferre, K. Ounadjela, J. M. George, L. Piraux, and S. Dubois, *Phys. Rev. B* **56**, 14066 (1997).
[38] H. Masuda and K. Fukuda, *Science* **268**, 1466 (1995).
[39] M. S. Sultan, B. Das, K. Mandal, and D. Atkinson, *J. Appl. Phys.* **112**, 013910 (2012).
[40] J. Wang, Q. F. Liu, D. S. Xue1, Y. Peng, X. Z. Cao, and F. S. Li, *J. Phys. D: Appl. Phys.* **34**, 3442 (2001).
[41] C. Rousse and P. Fricoteaux, *J Mater. Sci.* **46**, 6046 (2011).
[42] B. L. Cushing, V. O. Golub, M. Henry, B. L. Oliva, E. Cook, C. W. Holmes, and C. J. O. Connor, *Nanotechnology* **16**, 1701 (2005).
[43] S. Xue, M. Li, Y. Wang, and X. Xu, *Thin Solid Films* **517**, 5922 (2009).
[44] X. Kou, X. Fan, H. Zhu, and J. Q. Xiao, *Appl. Phy. Lett.* **94**, 112509 (2009).
[45] X. Zhang, H. Zhang, T. Wu, Z. Li, Z. Zhang, and H. Sun, *J. Magn. Magn. Mater.* **331**, 162 (2013).
[46] Q. F. Liu, C. X. Gao, J. J. Xiao, and D. S. Xue, *J. Magn. Magn. Mater.* **260**, 151 (2003).
[47] P. Tibertoa, L. Boarinoa, F. Celegatoa, G. Barreraa, N. D. Leoa, M. Coissona, F. Vinaia, and P. Alliaa, *Appl. Surf. Sci.* **259**, 44 (2012).
[48] A. Aharoni, Introduction to the Theory of Ferromagnetism, 2nd edn., Oxford University Press Inc., New York, US (2000).
[49] E. H. Frei, S. Shtrikman, and D. Treves, *Phys. Rev.* **106**, 446 (1957).
[50] P. Bryant and H. Suhl, *Appl. Phys. Lett.* **54**, 78 (1988).
[51] A. Aharoni, *J. Appl. Phys.* **68**, 2892 (1990).

[52] C. A. Ross, M. Farhoud, M. Hwang, I. H. Smith, M. Redjdal, and F. B. Humphrey, *J. Appl. Phys.* **89**, 1310 (2001).

[53] C. A. Ross, S. Haratani, F. J. Castan, Y. Hao, M. Hwang, M. Shima, J. Y. Cheng, B. Vogeli, M. Farhoud, M. Walsh, and H. I. Smith, *J. App. Phys.* **91**, 6848 (2002).

[54] A. N. Bogdanov, U. K. Rler, and K.-H. Muller, *J. Magn. Magn. Mater.* **594**, 242 (2002).

[55] A. Aharoni, *J. Appl. Phys.* **82**, 1281 (1997).

[56] A. N. Bogdanov, U. K. Rler, and K. H. Muller, *IEEE Trans. Magn.* **38**, 2586 (2002).

[57] B. D. Cullity and C. D. Graham, Introduction to Magnetic Materials, John Wiley & Sons, Inc., Hoboken, New Jersey (2009).

[58] J. Shen, R. Skomski, M. Klaua, H. Jenniches, S.S. Manoharan, J. Kirschner, *Physical Review B*, **56**, 2340 (2004).

[59] W. Wernsdorfer, B. Doudin, D. Mailly, K. Hasselbach, A. Benoit, J. Meier, J.P Ansermet, B. Barbara, *Physical Review Letter*, **77**, 1873 (1996).

[60] T. M. Whitney, J. S. Jiang, P. C. Searson, C. L. Chien, *Science*, **261**, 1316 (1993).

[61] J. E. Wegrowe, D. Kelly, A. Fromck, S. E. Gitbert, J. P. Ansermet, *Physical Review Letter*, **82**, 3681 (1999).

[62] A. Yamaguchi, F. Uejo, T. Yoda, T. Uchida, *Nature Materials*, **3**, 337 (2004).

[63] W. Wang, Q. Huang, F. Jia, J. Zhu, *Journal of Applied Physics*, **96**, 615 (2004).

[64] K. Nielsch, F. Müller, A. P. Li, U. Gösele, *Advanced Materials*, **12**, 582 (2000).

[65] G. L. Che, B. B. Lakshmi, E. R. Fisher, C. R. Martin, *Nature*, **393**, 346 (1998).

[66] F. Matsumoto, K. Nishio, H. Masuda, *Advanced Materials*, **16**, 2105 (2004).

[67] S. Iijima, *Nature* **354,** 56 (1991).

[68] S.S. Parkin, M. Hayashi, L. Thomas, *Science* **320,** 190 (2008).

[69] A. Yamaguchi, T. Ono, S. Nasu, K. Miyake, K. Mibu, T. Shinjo, *Physical Review Letters* **92**, 077205 (2004).

[70] Z.K. Wang, M.H. Kuok, S.C. Ng, D.J. Lockwood, M.G. Cottam, K. Nielsch, R.B. Wehrspohn, U. Gosele, *Physical Review Letters* **89**, 027201 (2002).

[71] P. Landeros, S. Allende, J. Escrig, E. Salcedo, D. Altbir, E.E. Vogel, *Applied Physics Letters* **90**, 102501 (2007).

[72] N. Ahmad, J.Y. Chen, J. Iqbal, W.X. Wang, W.P. Zhou, X.F. Han, *Journal of Applied Physics* **109**, 07A331 (2011).

[73] F. Tao, M. Guan, Y. Jiang, J. Zhu, Z. Xu, Z. Xue, *Advanced Materials* **18**, 2161 (2006).

[74] C. Rath, S. Anand, R.P. Das, K.K. Sahu, S.D. Kulkarni, S.K. Date, N.C. Mishra, *Journal of Applied Physics* **91** 2211 (2002).

[75] X.W. Wang, Z.H. Yuan, S.Q. Sun, Y.Q. Duan, L.J. Bie, *Materials Chemistry and Physics* **112,** 329 (2008).

[76] D. Li, R.S. Thompson, G. Bergmann, J.G. Lu, *Advanced Materials* **20,** 4575 (2008).

[77] D. Zhou, M.G. Zhu, M.G. Zhou, Z.H. Guo, W. Li, *Journal of Applied Physics* **109**, 07B720 (2011).

[78] Xiu-Feng Han, Shahzadi Shamaila, Rehana Sharif, Jun-Yang Chen, Hai-Rui Liu, Dong-Ping Liu, *Advanced Materials* **21** 4619 (2009).

[79] D. Zhou, T. Wang, M.G. Guao, W. Li and F. S. Li, *J. Magn.* **16.** 413 (2011).

[80] M. P. Proenca, C. T. Sousa, J. Escrig, J. Ventura, J. Vazquez and J. P. Araujo, *J. Appl. Phys.* **113,** 093907 (2013).

# Chapter 5

# Transition metals based hybrid nanostructures for energy storage application

This chapter describes the fabrication of transition metal based core/shell hybrid nanostructures (Ni/NiO core/shell nano-heterostructures and NiO-nanoblocks) by controlled oxidation of as-prepared transition metal based nanostructures (Ni nanowires and nanoblocks). Their structural, morphological and electrochemical properties have studied in details for their energy storage applications. In addition, the electrical conductivity of supercapacitor electrode material (NiO) improved by hydrogenation process and introducing impurities via doping of one metal oxide material with other metal oxide material. The resultant products (H-Ni/NiO, Fe-Ni/$Fe_2O_3$-NiO and Co-Ni/$Co_3O_4$-NiO core/shell nano-heterostructures) have shown enhanced electrochemical performance as supercapacitor electrode materials.

## 5.1. Preamble

Since last decade, energy crisis is one of the vital problems in the society due to the excessive use of fossil-fuel resources and environmental pollution. Therefore, the development of very light weight and environment friendly proficient energy storage devices has become the priority of the researchers and scientists for satisfying the demand of modern consumer's hybrid electric and portable electronics devices [1-4]. In this progression, researchers have developed new type of energy storage devices offer to satisfy the demand of energy crises called supercapacitors, also known as electrochemical capacitors which consist high power density, high rate capability, superb cycle stability and high energy density compare to conventional battery and capacitors [5-8]. The supercapacitors are classified in two groups, based on their charge storage method. First group called pseudocapacitors which involve the redox reactions of the electrode materials at the surface of electrode and electrolyte interface, second group known as electric double layer capacitors which hold charge separation at the surfaces of electrode and electrolyte interface [9,10]. By changing the morphology of the electrode materials, one can manipulate the performance of a supercapacitor. The performance and quality of the supercapacitors are very much dependent on the materials and morphology used in the preparation of their electrodes. Recently, many metal oxide based materials (like $RuO_2$, NiO, $Fe_2O_3$, $MnO_2$, $Co_3O_4$, $TiO_2$, etc.) have been used for the fabrication of pseudocapacitor electodes, among them NiO, $Co_3O_4$ and $Fe_2O_3$ have been widely used as redox active materials for the fabrication of supercapacitor electrodes of different morphologies. The reasons behind the extensive use of NiO, $Co_3O_4$ and $Fe_2O_3$ as supercapacitor electrode materials are: they are very stable in nature, they are non-toxic as well as environment friendly and they are very cheap and easily available. After having so much of supportive properties for being used as electrode materials in supercapacitors, still their reported specific capacitance values are very low compared to their own theoretical specific capacitance value and other metal oxide based electrodes. The only problem restricts them to be used as an electrode material for high performance supercapaitor is their bad electrical conductivity and we all are aware of the fact that electrode material must have high electrical conductivity for high performance supercapacitor.

In the recent development process of supercapacitor performance, it has been found that the electrical conductivity could be improved by introducing impurities via doping of one metal oxide material with other metal oxide material. This doping process enhances the charge movement which affect the reactions at the interface of electrode and electrolyte [11, 12]. Since then many mixed component transition metal oxides (binary and ternary) hybrid nanostructures have been demonstrated as the promising supercapacitor electrodes. Among various hybrid nanostructures based on transition metal oxides; the hybrid core/shell nanostructure on conductive substrate have attracted significant interest since they offer innovative prospects for the growth of nobel compound materials with enhanced properties and can be very useful for energy storage devices [13-19]. It has been demonstrated that these hybrid core/shell nanostructure are exceptionally useful during electron-charge transfer reactions and the diffusion of ions due to their unique structures. One more significant advantage of this core/shell structure on conductive substrate is that during fabrication of electrode it doesn't require any binder, which redeem it from extra binder weight.

Keeping all the above research facts in the mind, still there are plenty chance to enhance the electrochemical properties of NiO, Co3O4 and $Fe_2O_3$ based electrodes remarkably. In this backdrop, we report a simple fabrication technique and electrochemical properties of the electrode based on transition metal based core/shell hybrid nanostructures (core/shell nano-heterostructures and nanoblocks), for the first time, for its following technical and scientific advantages as supercapacitor electrode: (1) the 1D nano-heterostructures have high aspect ratio and thus have large surface area which serves as huge platform for ion intercalation/deintercalation in the electrolyte solution; (2) the as grown porous thin nanolayer of transition metal oxide on transition metal would serves as a short diffusion path for the ions and also the charge carriers. Moreover, the porous structure again increases their specific area which in turn enhances their electrochemical performance; (3) the thin surface layer of transition metal oxide has high redox activity, whereas the core consists of pure transition metal would serve as the fast path for electron transport channel to the current collector; (4) furthermore,

the hydrogenation will introduce the hydroxyl groups on the surface and subsurface regions of NiO that would enhance the electrochemical activity of the electrode; (5) introducing impurities via doping of one metal oxide material with other metal oxide material. The unique feature of this electrode fabrication technique is that it doesn't contain any extra binder material. As a result, there would be enhancement in the charge transfer kinetics. According to our anticipations, transition metal based hybrid nanostructure shows high quality supercapacitive performance in terms of specific capacitance, energy density, power density, cycling stability and rate capability; these profound results made it alternative for the next generation supercapacitor electrodes.

# 5.2. Hydrogenated Ni/NiO Core/Shell nano-heterostructures for high performance supercapacitor electrode.

## 5.2.1. Experimental

### 5.2.1.1. Reagents

Aluminum foil (99.99+% pure, 0.2 mm thick), Oxalic acid (99.99+% pure), Nickel sulphate hexahydrate ($NiSO_4.6H_2O$, 99.99+% pure), Boric acid ($H_3BO_3$, 99.9+% pure) and Sodium hydroxide (NaOH, 99.9+% pure) were purchased from SIGMA-ALDRICH. All chemicals were of analytical grade and were used without further purification.

### 5.2.1.2. Synthesis of the Ni/NiO and hydrogenated Ni/NiO (H-Ni/NiO) core/shell nano-heterostructure

The scheme of the preparation of the arrays of H–Ni/NiO core/shell NHs is shown in Fig. 5.1. The high-density arrays of Ni/NiO core/shell NHs were synthesized by the high-temperature oxidation of the metallic Ni NWs prepared by the template assisted electrochemical deposition route. Highly ordered self-organized nanoporous anodic aluminium oxide (AAO) templates were fabricated by the controlled two-stage electrochemical anodization of high-purity aluminum foil in oxalic acid solution as described elsewhere [20]. The 100 nm diameter porous AAO template with one side coated with a conductive gold (Au) layer grown by thermal evaporation technique was used as the working electrode to synthesize the highly ordered arrays of Ni NWs through electrodeposition. Software controlled three-electrode electrochemical cell and a power supply (potentiostat AutoLab-30) was used for the electrochemical deposition of Ni NWs. A high-purity Pt wire and an (Ag/AgCl) electrode were used as the counter and reference electrodes, respectively. The arrays of Ni NWs were grown in the pores of AAO using the aqueous solution of 0.57 M $NiSO_4.6H_2O$, 0.32 M $H_3BO_3$ and 0.15 M $NH_4OH$ as electrolyte at room temperature. Here, boric acid and ammonium hydroxide were used as a buffer to maintain the pH of the electrolyte around 3.5 and also to control the electrodeposition process. The deposition of the arrays of Ni NWs was conducted for 15 minutes by using a dc voltage of -1.03 V, following linear sweep voltammetry

results. After the growth of the Ni NWs the template was removed by dissolving it in 2 M of NaOH solution.

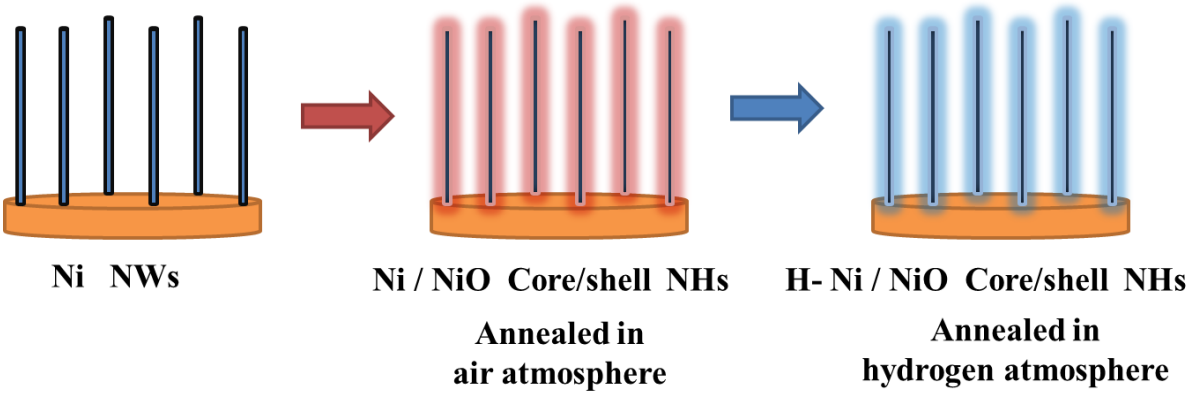


**Figure 5.1:** Scheme for the preparation of Ni/NiO and H-Ni/NiO core/shell NHs electrodes.

The open arrays of Ni NWs grown on the Au layer were finally oxidized to form Ni/NiO core/shell NHs by heating them at 450°C for 30 min. in oxygen atmosphere. The H–Ni/NiO core/shell NHs was obtained by annealing the Ni/NiO core/shell NHs in hydrogen atmosphere at temperature of 400°C for 20 minutes. The mass of the active electrode material was measured by using a microbalance having an accuracy of 0.1 μg. The mass of the active electrode materials was calculated by subtracting the mass of the equal area Au foil layer, on which the NHs were grown, from the total mass of the cathode (electrode material and the Au layer). The loading density of the Ni/NiO and H-Ni/NiO core-shell 1D nano-heterostructures electrode was found to be 0.30 and 0.346 mg/cm$^2$, respectively.

## 5.2.2. Results and Discussions

### 5.2.2.1. Morphology, Crystallography and Chemical composition

Figure 5.2(a) shows the FESEM micrograph of the as-prepared H-Ni/NiO core/shell NHs grown perpendicular to the supporting Au substrate. It is evident from Fig. 5.2(a) that the length (~12 μm) and the diameter of the 1D NHs are uniform in nature as well as the surface of the NHs is rough and porous (inset of Fig. 5.2(a)) as compared with the as grown Ni NWs (Fig. 5.3 (a)). The roughness and porosity in the H-Ni/NiO core/shell NHs arise during to the oxidation of the as grown Ni NWs surface to convert it into NiO. TEM micrograph of the H-Ni/NiO core/shell NHs,

depicted in Fig. 5.2(b), clearly shows the formation of a thin nanolayer of NiO over Ni NW core, thus forming the 1D core-shell type H-Ni/NiO NHs of about 150 nm diameter. It is also evident from figure that the thickness of the NiO shell nanolayer grown on Ni NW core is almost uniform (~ 20–25 nm).

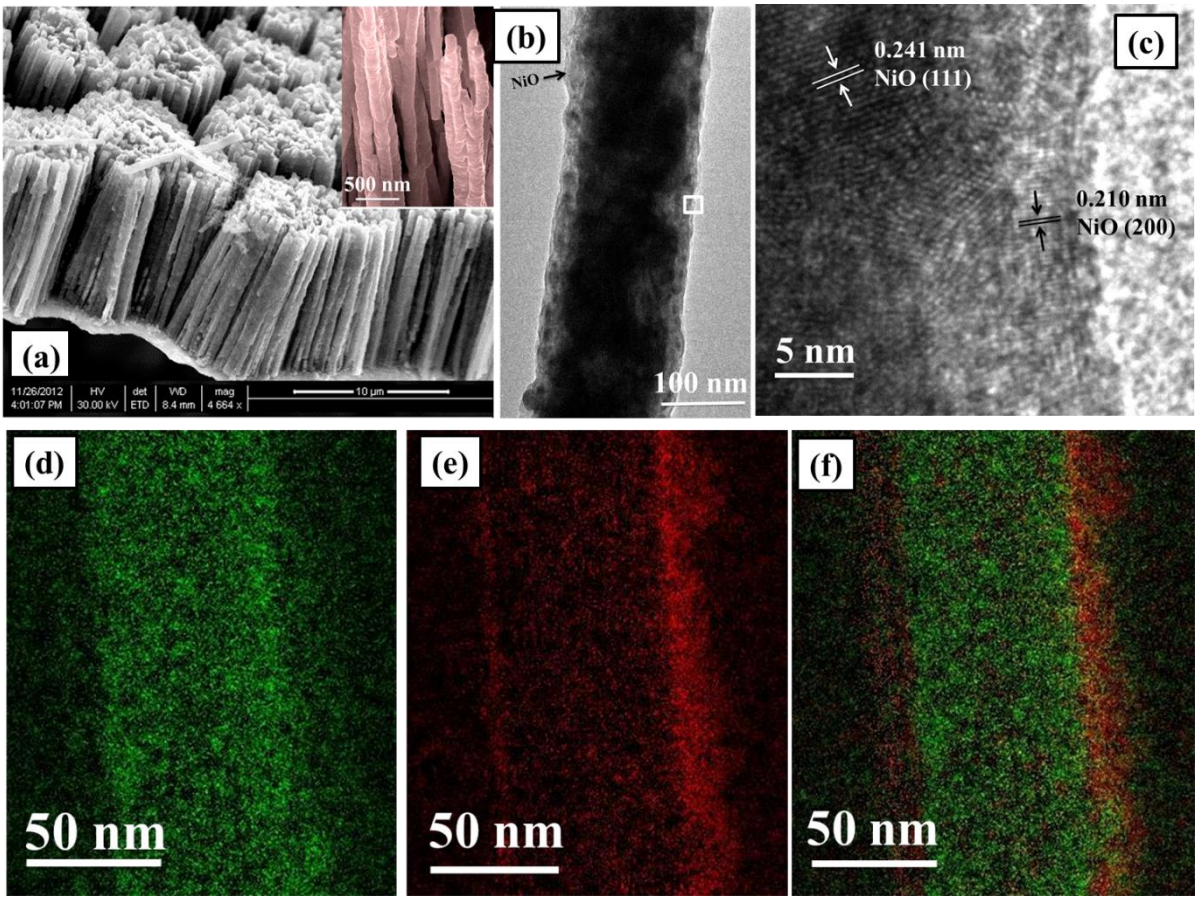


**Figure 5.2.** (a) FESEM, (b) TEM and (c) HRTEM micrographs of the as prepared H-Ni/NiO core/shell NHs; inset of figure (a) shows the magnified version of the core/shell NHs; (d), (e) and (f) represent the energy filtered TEM (EFTEM) images (color mapping) of Ni, O and the whole H-Ni/NiO core/shell NHs, respectively.

The formation of NiO shell can be further clarified from the HRTEM image of H-Ni/NiO core/shell NHs, as shown in Fig. 5.2(c). Two different sets of lattice fringes have been found having lattice spacing of about 0.241 and 0.21 nm that correspond to the (111) and (200) crystalline planes of cubic NiO, respectively, which indicates that the as grown NiO nano-layer is polycrystalline in nature. However, the uniformity in the chemical composition of H-Ni/NiO core/shell NHs can only be confirmed from the EFTEM images (Fig. 5.2(d), (e) & (f)). Fig. 5.2(d) and (e) show the color mapping of Ni (in green color) and O (in red color), respectively, whereas

their composite structure is shown in Fig. 5.2(f). From these images it is clear that the Ni concentration is very high at the center of the NHs as compared to the outer surface where oxygen concentration is dominant because of the formation of the NiO at the surface. This study again confirms the formation of a very good quality H-Ni/NiO core/shell nano-heterostructure with uniform chemical composition.

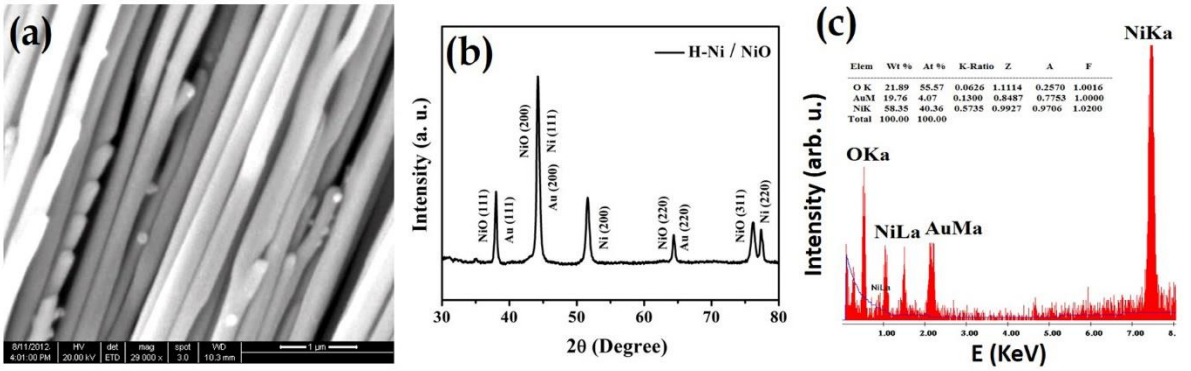


**Figure 5.3**. (a) FESEM micrograph of the as prepared Ni NWs, (b) The XRD pattern of the as-prepared H-Ni/NiO core/shell NHs, (c) The EDAX spectrum of the H-Ni/NiO core/shell NHs.

The crystallographic nature of the arrays of H-Ni/NiO core/shell NHs investigated by XRD (Fig. 5.3(b)) also indicates the polycrystalline in the nature of the NiO nanolayer grown on Ni NWs core. The diffraction pattern consists of peaks that correspond to the pure fcc Ni core, cubic NiO shell nanolayer and also the metallic Au layer underneath the NHs. The characteristic peaks at $2\theta$ = 37.5, 43.3 and 63.9 degrees in the XRD pattern represent the (111), (200) and (220) crystalline faces of NiO with cubic texture, respectively [21, 22]. The EDAX spectrum of the H-Ni/NiO core/shell NHs, shown in (Fig. 5.3(c)) clearly shows the presence of Ni and O in the NHs whereas the peak for Au appears because of the substrate.

The chemical composition and the valence state of the elements in the as-prepared Ni/NiO and the H-Ni/NiO core/shell NHs have been further investigated by the x-ray photoelectron spectroscopy. In Fig. 5.4(a), the peaks of Ni $2p_{3/2}$ and Ni $2p_{1/2}$ located at 855 and 873.9 eV, respectively, with an energy separation of 18.9 eV, are in good agreement with reported data of Ni $2p_{3/2}$ and Ni $2p_{1/2}$ in NiO, which confirms that Ni is in +2 oxidation state [21, 23]. Fig. 5.4(b) shows the O 1s core level spectra of Ni/NiO and H-Ni/NiO core/shell NHs. In the H-Ni/NiO core/shell NHs the O 1s peak becomes broader compared with that of the Ni/NiO core/shell NHs.

The core level O 1s band in the H-Ni/NiO core/shell NHs could be deconvoluted into two peaks located at 529.1 and 533.1eV (see Fig. 5.4(b)), whereas the Ni/NiO core/shell NHs exhibits a single peak located at 530.7 eV. The low energy peak (at 530.7 eV) can be ascribed to the formation of O–Ni bond [21, 24], whereas the additional shoulder peak at higher binding energy (at 533.1 eV) is attributed to the Ni-OH bond.[14, 31] Thus the XPS studies confirm the formation of hydroxyl group on NiO surface after the hydrogen treatment of the Ni/NiO core/shell NHs.

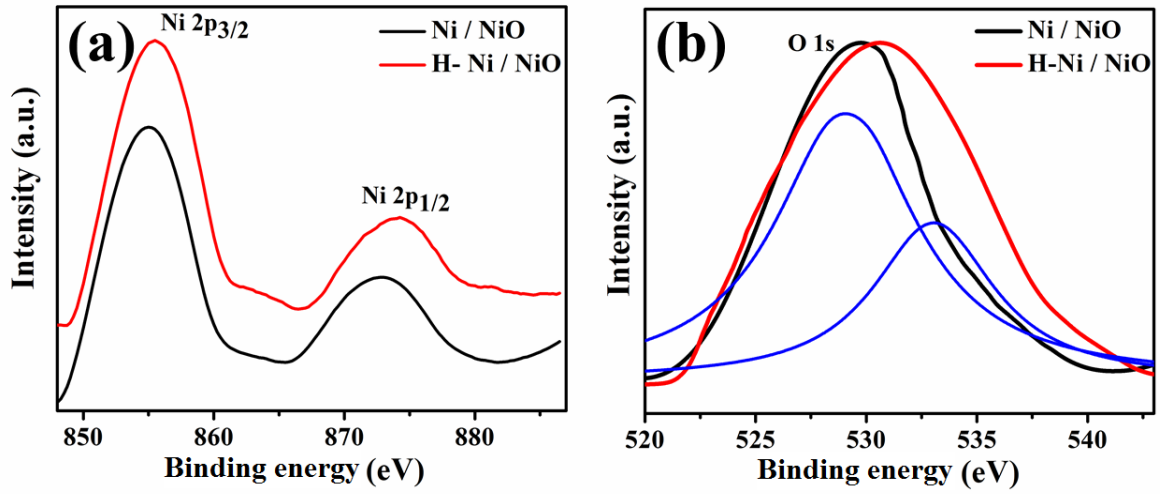


**Figure 5.4**. The XPS spectra for the (a) Ni 2p and (b) normalized O 1s core level of the as-prepared Ni/NiO and H-Ni/NiO core/shell NHs.

### 5.2.2.2. Electrochemical Analysis

Cyclic voltammetry (CV) is the method used for the determination of the electrochemical properties of Ni/NiO and H–Ni/NiO core/shell 1D NHs electrodes. Fig. 5.5 (a) and (b) show the CV curves of the Ni/NiO and H–Ni/NiO core/shell NHs, respectively, recorded at different scan rates of 2, 5, 10, 20, 30, 50, and 100 $mVs^{-1}$ within a voltage window of 0 – 0.6 V in 1 M KOH aqueous solution at room temperature. The shapes of the CV curves in the as grown NHs were different to those of the electric double layer capacitors, manifested by the two strong peaks that correspond to the superficial faradic oxidation/reduction reactions.[1] The oxidation peak is due to the conversion of NiO (or $Ni(OH)_2$) to NiOOH, whereas the reduction peak is simply because of the reverse reaction. Clearly, the redox peaks reveal its

Faradaic pseudocapacitive property based on the surface redox mechanism of $Ni^{2+}$ to $Ni^{3+}$. The faradic reaction can be described as [25]:

$$NiO + OH^- \leftrightarrow NiOOH + e^- \text{ and } Ni(OH)_2 + OH^- \leftrightarrow NiOOH + H_2O + e^- \quad (5.1)$$

Hence, the capacitance of the Ni/NiO and H- Ni/NiO core/shell NHs electrode is derived from a pseudocapacitive capacitance based on the apparent redox peaks. In case of Ni/NiO core/shell NHs, all the CV curves exhibit an obvious electrochemical oxidation process which is characterized by a current leap especially at the upper potential.

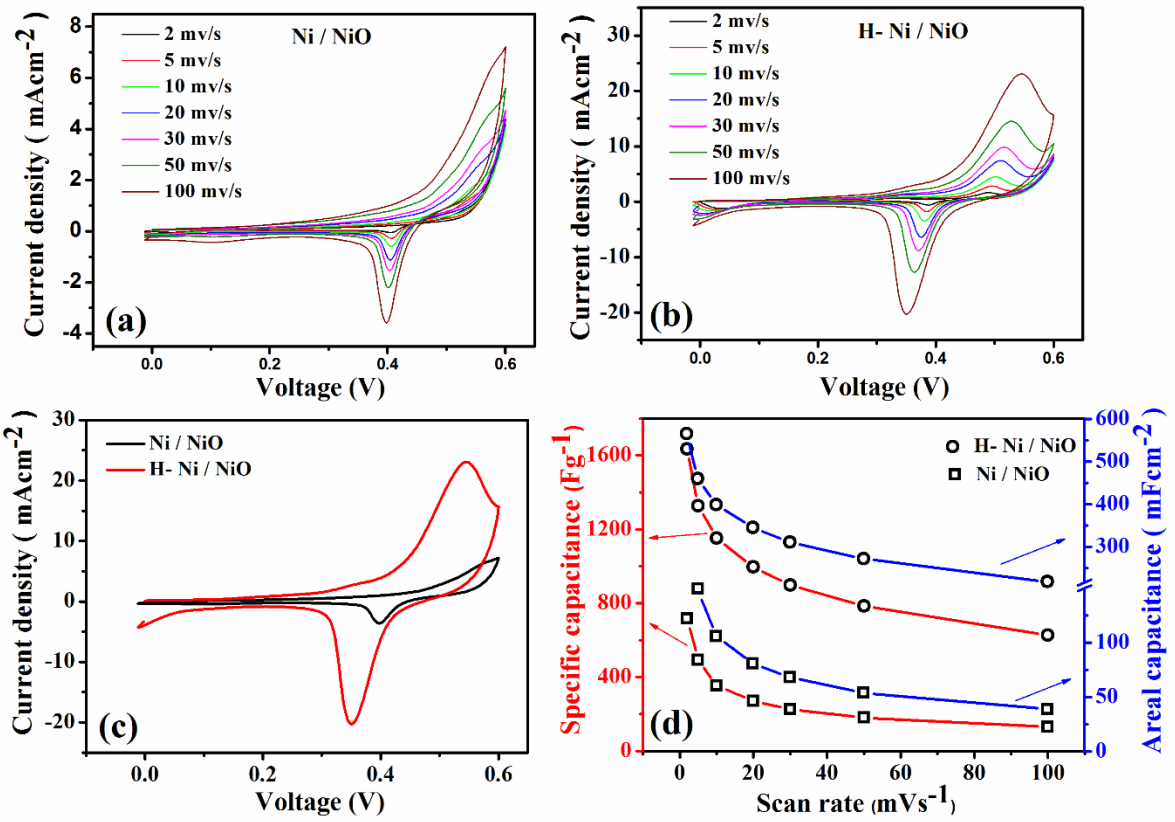


**Figure 5.5.** Cyclic voltammetry curves of the as prepared (a) Ni/NiO and (b) H−Ni/NiO core/shell NHs electrode at different scan rates in a 1 M KOH solution. (c) Comparison between the CV curves of Ni/NiO and H−Ni/NiO core/shell NHs electrode at scan rate of 100 $mVs^{-1}$. (d) Variation of specific capacitance (*Cs*) and areal capacitance (*Ca*) as a function of scan rate of Ni/NiO and H−Ni/NiO core/shell NHs electrode.

However, there is no obvious current leap at the upper potential limit of H-Ni/NiO core/shell NHs electrode sample has been observed which indicates that the electrochemical oxidation process was completed. The potential and the current

at the two peaks shifted more towards the positive and negative axes as the scan rate increases, which is because of the large rough surface area of the Ni/NiO and H-Ni/NiO core/shell NHs electrodes and the fast ionic/electronic diffusion rate during the faradic redox reaction [26]. In addition, the similar shape of oxidation and reduction peaks throughout the whole range of scan rates signifies good kinetic reversibility of both the electrodes [27, 28]. In comparison to the Ni/NiO core/shell NHs electrode, H−Ni/NiO core/shell NHs electrode delivers an obvious pseudocapacitive characteristic, which can be attributed to the oxidation/reduction of surface hydroxyl groups, as observed in other electrode materials for pseudocapacitors [29-32]. In electrochemical electrodes the interface/surface structure and the ionic/electronic diffusion play a vital role in improving the rate capability and specific capacitance of the supercapacitor [33]. Nearly six times enhancement in current density and the area under the CV curves in case of H-Ni/NiO core/shell NHs compare to Ni/NiO core/shell NHs observed at a scan rate of 100 $mVs^{-1}$ (Fig. 5.5(c)) indicates significant enhancement in capacitive performance of Ni/NiO core/shell NHs after hydrogenation.

Furthermore, quantitative study of the capacitive performance of the electrode materials has been done by calculating, the areal capacitance ($C_a$, $mFcm^{-2}$) and specific capacitance ($C_{sp}$, $Fg^{-1}$) of the Ni/NiO and H-Ni/NiO core/shell NHs electrodes according to the following equations [34, 35]:

$$C_a = \frac{I}{fA} \tag{5.2}$$

$$C_{sp} = \frac{I}{fm} \tag{5.3}$$

where, '$I$(A)' is the average cathodic current of the CV loop, '$f$ ($Vs^{-1}$)' is the scan rate, '$A$($cm^2$)' is the area of the working electrode and '$m$ (g)' is the mass of the redox active material. Calculated areal and specific capacitance of the Ni/NiO and H-Ni/NiO core/shell NHs electrodes as a function of scan rate are shown in Fig. 5.5(d). At scan rate of 2 $mVs^{-1}$, the $C_{sp}$ and $C_a$ values of the as prepared Ni/NiO core/shell NHs electrode were found to be nearly 717 $Fg^{-1}$ and 216 mF $cm^{-2}$, respectively.

However, significant enhancement has been found in the values $C_{sp}$ and $C_a$ (1635 $Fg^{-1}$ and 566 mF $cm^{-2}$, respectively) after the hydrogenation process of Ni/NiO core/shell NHs at a scan rate of 2 $mVs^{-1}$. This enhancement in the capacitive performance arises because the surface area, porosity of the outer surface and obviously the incorporation of the hydroxyl groups at the surface of the Ni/NiO core/shell NHs through hydrogenation. The value of $C_{sp}$ for this 1D H-Ni/NiO core/shell NHs is found to be remarkably higher than that of the other reported NiO based supercapacitors such as, thin films of NiO (~ 309 $Fg^{-1}$) [21], Mesoporous NiO Nanotubes (~409 $Fg^{-1}$) [22], nanoball-like NiOx (~951 $Fg^{-1}$) [27], NiO-$TiO_2$ Nanotube Arrays (~300 $Fg^{-1}$) [28], NiO Nanotubes (~266 $Fg^{-1}$) [36], NiO Nanocolumns (~ 390 $Fg^{-1}$) [37], hierarchical spherical porous NiO (~710 $Fg^{-1}$) [38], Ni–NiO core–shell (~128 & 149 $Fg^{-1}$) [39, 40], NiO/$Co_2O_3$ core/shell NWs (~835 $Fg^{-1}$) [41], Monolithic NiO/Ni Nanocomposites (~905 $Fg^{-1}$) [42]. However, we observed the specific and areal capacitance of the NHs electrodes are found to decrease with the increase of scan rates. The accessibility of ions inside every pores of electrode limits at higher scan rates because only the outermost portion of electrode has been utilized for the ion diffusion process. This is evident from the Fig. 5.5(d) that at higher scan rate of 100 mV/s the specific capacitance remains almost 627 $Fg^{-1}$ for H-Ni/NiO core/shell NHs electrode whereas it becomes 130 $Fg^{-1}$for the Ni/NiO core/shell NHs. The value of the specific capacitance rapidly decreases as the scan rate increases, due to the remarkable kinetic limitation in the reaction of NiOOH in the composite electrode [43].

The superior electrochemical performance of H-Ni/NiO core/shell 1D NHs can be attributed to two major improvements upon hydrogenation. Firstly, H-Ni/NiO core/shell NHs electrode exhibits improved electrical conductivity and enhanced electrochemical activity because of the incorporation of the hydroxyl groups on the NiO surface that facilitates the fast transport of charge carriers and improved pseudocapacitive performance, respectively [29-31]. Secondly, the Ni metallic core serves as the channel for the fast electron transport to the current collector (here Au) and thereby enhances the pseudocapacitance [35]. Moreover, the H-Ni/NiO core/shell NHs electrode shows good rate capacitance. The $C_{sp}$ and $C_a$ of

the H-Ni/NiO core/shell NHs electrode drop from 1635 to 627 F $g^{-1}$ and 566 to 217 mF $cm^{-2}$, respectively with a good retention of 38.4 and 34.6 % of the initial capacitance respectively, when the scan rate increases from 2 to 100 mV/s. In comparison, the Ni/NiO core/shell NHs electrode retains only 18.1 and 17.9% of the initial capacitance, respectively. The rate capability of the pseudocapacitors is related to the rate of ion diffusion (mass transport) in the electrode and the electrode conductivity. Here, it is expected that the Ni/NiO and H-Ni/NiO core/shell NHs electrodes should have similar ion diffusion rate because of their similar morphology. Therefore, the improved rate capacitance in H−Ni/NiO core/shell NHs is believed to be due to the enhanced electrical conductivity of the electrode (which is further confirmed by the electrochemical impedance spectroscopy studies). It is evident from Fig. 5.5 (a) and (b) that the shape of the CV curves for both of the Ni/NiO and H-Ni/NiO core/shell NHs electrodes remains almost unchanged with the change in the scan rate from 2 to 100 $mVs^{-1}$.

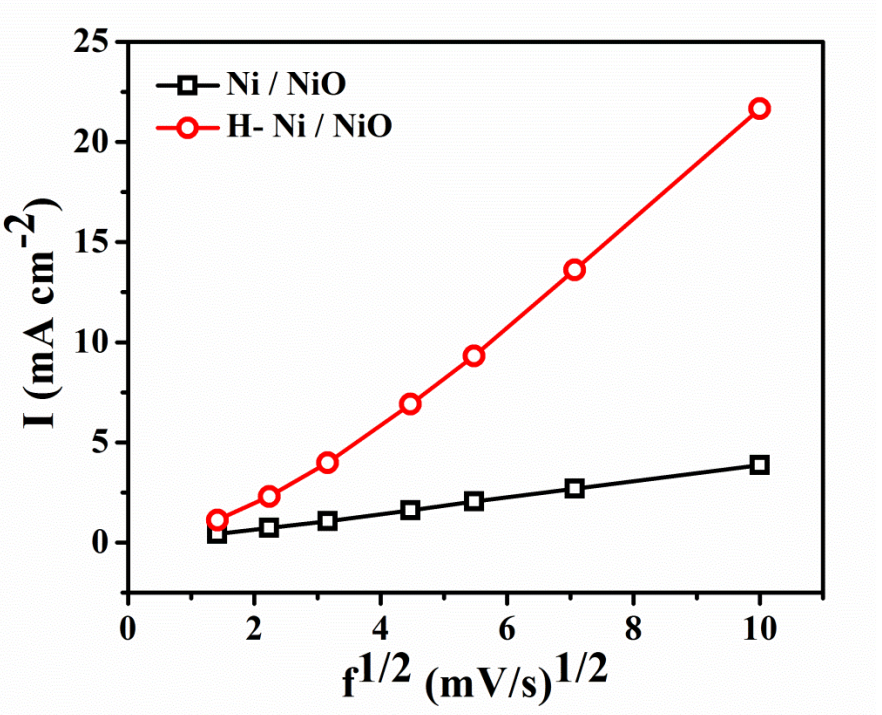


**Figure 5.6.** Peak current ($I$) vs. square root of scan rate ($f$) plot for both types of capacitors.

Furthermore, we observed a linear relation between the peak current ($I$) of CV loops at different scan rates with the square root of scan rate voltage ($f^{1/2}$) has been observed for both type of NHs electrodes (Fig. 5.6). This type of liner relation between current ($I$) and scan rate voltage ($f^{1/2}$) indicates a fast electron transfer rate

during the redox reactions and thus it is evident, these redox reactions are diffusion-controlled process rather than a kinetic process [44, 45].

In order to further understand the electrochemical performance of these supercapacitors, they have been investigated by galvanostatic (GV) charge/discharge method to confirm the improved supercapacitive performance. The charge/discharge curves of the Ni/NiO and H-Ni/NiO core/shell NHs electrodes in 1M KOH solution have been recorded at different current densities and stable potential window 0–0.6 V are shown in Fig. 5.7(a) and (b), respectively.

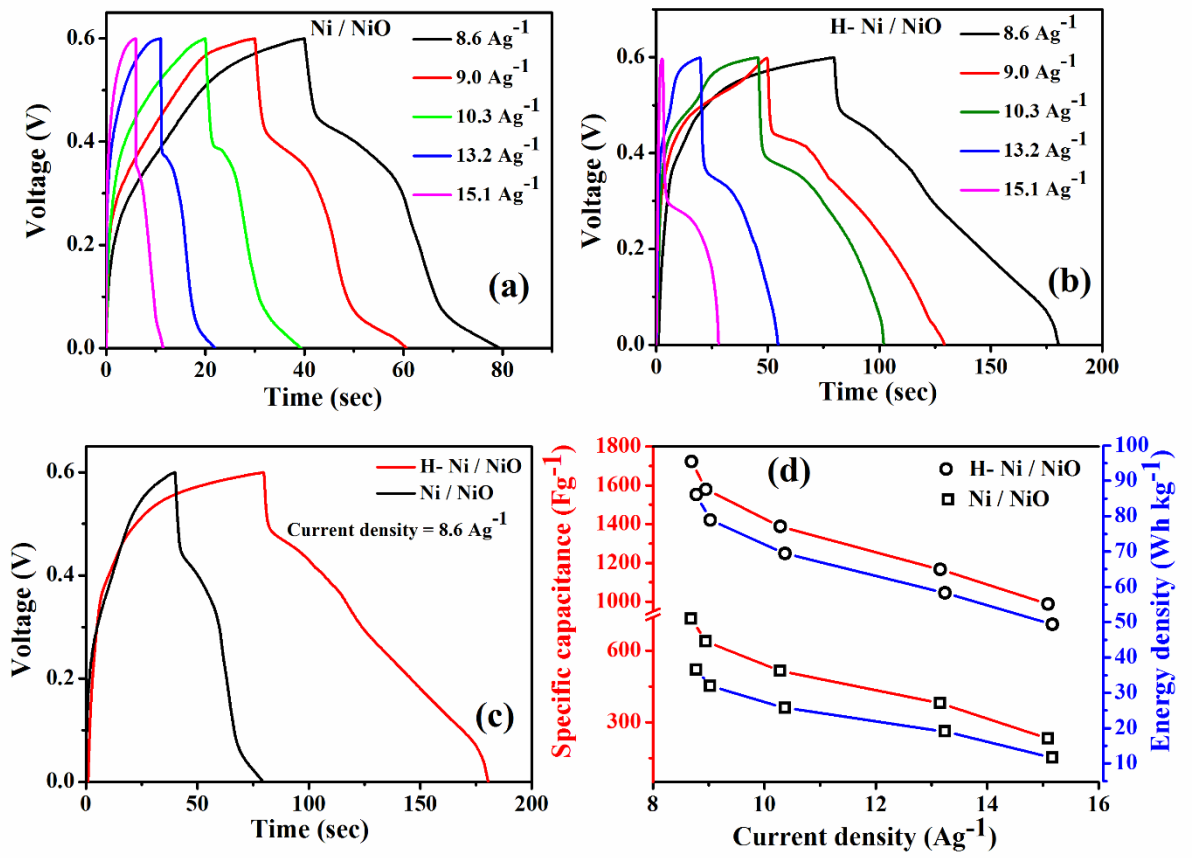


**Figure 5.7.** Constant current charge/discharge curves of the as-prepared (a) Ni/NiO and (b) H-Ni/NiO core/shell NHs electrodes at different current density. (c) Comparison between the charge/discharge curves of the Ni/NiO and H-Ni/NiO core/shell NHs electrodes at the current density of 8.6 $Ag^{-1}$. (d) Variation of specific capacitance and energy density of both types of NHs electrode as a function of current density.

Moreover, the potential-time profiles of Ni/NiO and H-Ni/NiO core/shell NHs exhibited symmetric charge/discharge features, even at a low current density of 8.6 $Ag^{-1}$, indicating good pseudocapacitive behavior and excellent reversible redox reaction [46]. Fig. 5.7(c) exhibits the potential-time curves of H-Ni/NiO core/shell

NHs electrodes indicating substantially prolonged over the Ni/NiO core/shell NHs electrode and the enhanced capacitive performance of the Ni/NiO core/shell NHs after hydrogenation. The discharging part of the potential-time profile of both the electrodes are divided into two stages at different current densities; a fast voltage drop followed by a slow discharge. Charging/discharging curves also exhibits that the fast voltage drop increases with the increase of current density for both the electrodes. The fast voltage drop is related to the internal resistance of the electrodes whereas the slow discharge with nonlinear slope represents that the faradic reactions occur on the surface of the H-Ni/NiO core/shell NHs electrode.

From the discharging curves, the specific capacitance of these supercapacitors electrodes was derived using following equation:

$$C_{sp} = \frac{I\Delta t}{m\Delta V} \tag{5.4}$$

where '$I$(A)' is the discharge current, '$\Delta t$ (s)' is the discharge time consumed in the potential range of '$\Delta V$(V)', '$m$(g)' is the mass of the active material (or mass of the electrode materials), $\Delta V$ is the potential window and ($I/m$) is the discharge current density. Fig. 5.7(d) shows the plot of specific capacitance ($C_{sp}$) as a function of current density for the Ni/NiO and H-Ni/NiO core/shell NHs electrodes. At current density of 8.6 $Ag^{-1}$, the $C_{sp}$ value of the as prepared Ni/NiO core/shell NHs electrode was found to be nearly 730.9 $Fg^{-1}$. However, significant enhancement has been found in the value $C_{sp}$ (1722 $Fg^{-1}$) after the hydrogenation process of Ni/NiO core/shell NHs at current density of 8.6 $Ag^{-1}$. A possible reason for this is that the ion and the electron have more time to diffuse through the interface/surface of the porous electrode during the faradic redox reaction. The values of $C_{sp}$ for Ni/NiO and H-Ni/NiO core/shell NHs electrode are consistent with the values calculated from the CV analysis. The specific capacitance decreases with the increase in current density for both the electrodes and tends to stabilize after current density of 10.3 $Ag^{-1}$ (Fig. 5.7(d)). Similar trend was observed in the case of increasing scan rate voltage (Fig. 5.5(d)) from CV curves calculation as well. At lower current density, ions can easily penetrate into the innermost portion of the electrode material through almost every available pores and channels resulting higher capacitive performance.

However, reverse trend occurs at higher current density. Surprisingly, in case of charging/discharging process the capacitance retention of the electrodes is found much higher than that observed from the CV analysis. Nearly 57% and 32% capacity retention have been observed for H-Ni/NiO and Ni/NiO core/shell NHs electrodes, respectively at a current density of 15.1 $Ag^{-1}$, demonstrating the relatively good high-rate capability of these electrodes. Energy density and power density are two important factors that influence the electrochemical performance of the supercapacitor electrode. A good electrochemical supercapacitor should possess a high energy density or high specific capacitance at higher current densities. Using the galvanostatic charge/discharge curves, the energy and power densities can be calculated using eq. (5.5) and (5.6) as follows,

$$E = \frac{1}{2} C_{sp} (\Delta V)^2 \tag{5.5}$$

$$P = \frac{E}{t} \tag{5.6}$$

where, '$E$ (Whkg$^{-1}$)', '$C_{sp}$ (F g$^{-1}$)', '$\Delta V$ (V)', '$\Delta t$ (s)' and '$P$ (kWkg$^{-1}$)' are the energy density, specific capacitance, potential window of discharge, time of discharge and power density, respectively.

Figure 5.7(d) shows the plot of Energy density (E) as a function of current density for the Ni/NiO and H-Ni/NiO core/shell NHs electrodes. Nearly 2.4 times enhancement of energy density has been observed for the H-Ni/NiO core/shell NHs electrode (86.1 Whkg$^{-1}$) compare to the Ni/NiO core/shell NHs electrode (36.5 Whkg$^{-1}$) at a current density of 8.6 $Ag^{-1}$. The energy density of H-Ni/NiO core/shell NHs electrode remains 49.35 Whkg$^{-1}$ at the current density 15.1 $Ag^{-1}$, which indicates good energy storage capability of these pseudocapacitors.

Furthermore, considering the real device application of these NHs, the Ragone plot (the energy density as a function of power density) of the fabricated all solid state SCs is shown in Fig. 5.8. The energy and power density are calculated based on the total mass of active materials of two electrodes. It is evident that the energy and power densities of the NHs SCs are much higher than those of a similar

system reported [22, 27, 28, 37, 39-41].

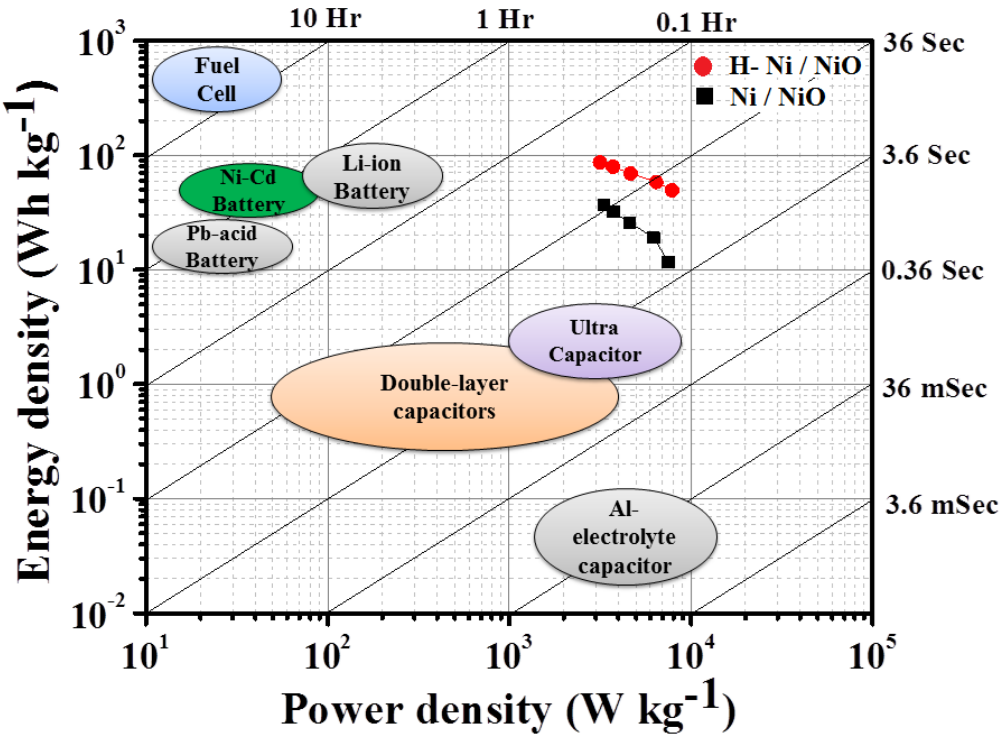


**Figure 5.8**: Ragone plot of the asymmetric supercapacitors consisting of Ni/NiO (■ black one) and H-Ni/NiO (● red one) core/shell NHs as cathode and Pt as anode in comparison with various electrical energy storage devices. Times shown are the time constants of the devices as obtained by dividing energy density by power.

In addition, for H-Ni/NiO and Ni/NiO core/shell NHs electrodes compared to the energy density that decreased from 30.66 $Whkg^{-1}$ to 8.49 $Whkg^{-1}$ and 11.73 $Whkg^{-1}$ to 2.19 $Whkg^{-1}$ respectively, the power density increased from 1126.42 $Wkg^{-1}$ to 1358.11 $Wkg^{-1}$ and 1069.42 $Wkg^{-1}$ to 1421.27 $Wkg^{-1}$ respectively, as the discharge current density increased from 4.6 $Ag^{-1}$ to 7.9 $Ag^{-1}$. Moreover, the energy density of H-Ni/NiO core/shell NHs electrodes reached was as high as 30.66 $Whkg^{-1}$ at a low power density of 1126.42 $Wkg^{-1}$, which shows its potential for application in electrochemical supercapacitors. More studies may be performed on porous NiO based electrochemical electrodes to optimize their energy and power densities and make them potential electrode materials for actual supercapacitors. More importantly, the power density and energy density of H-Ni/NiO and Ni/NiO core/shell NHs electrodes met the requirements of Li-ion, Ni-Cd and Pb-acid based batteries also.

Electrochemical impedance spectroscopy (EIS) has been used to investigate electrical conductivity and ion transfer of the supercapacitor electrodes. Fig. 5.9(a)

shows the experimental Nyquist impedance plot for the pseudocapacitor cells made of Ni/NiO and H-Ni/NiO core/shell NHs electrodes. The EIS spectra are composed of three distinct regions based on the order of decreasing frequencies. The intercept on the real axis in the high frequency range provides the equivalent series resistance (ESR), ($R_s$), which includes the inherent resistances of the electro active material, bulk resistance of electrolyte, and contact resistance at the interface between electrolyte and electrode [47].

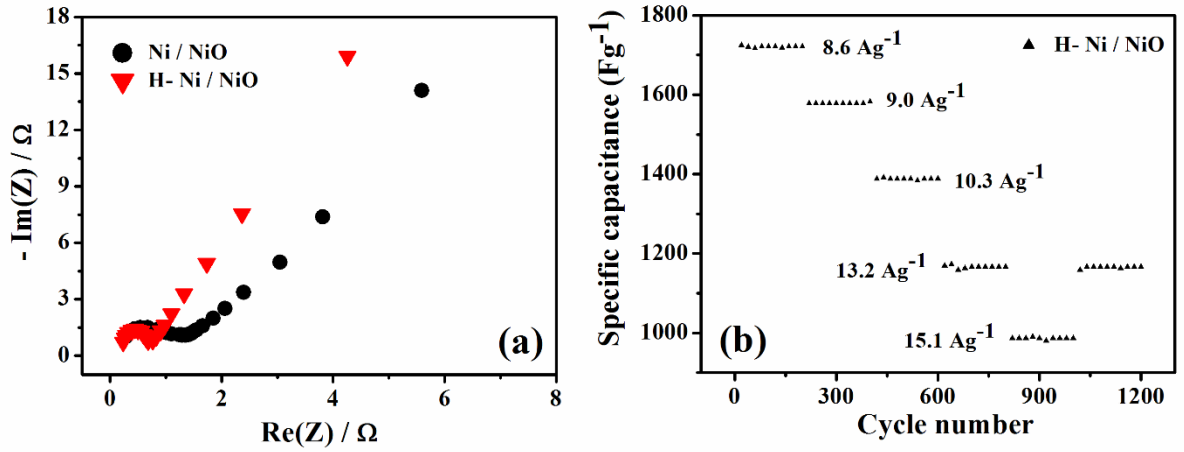


**Figure 5.9**. (a) Electrochemical impedance spectroscopy (Nyquist) plots for supercapacitors based on Ni/NiO and H-Ni/NiO core/shell NHs electrodes. (b) Capacitance retention of the H-Ni/NiO core/shell NHs electrodes at different current densities.

The magnitude of ESR obtained for Ni/NiO and H-Ni/NiO core/shell NHs electrodes are found to be 0.32 Ω and 0.235 Ω, respectively, which indicates higher electrical conductivity of H-Ni/NiO core/shell NHs compared with Ni/NiO core/shell NHs. The charge transfer resistance ($R_{ct}$) of the electrode material, resulting from the diffusion of electrons can be calculated from the diameter of semicircle in the high frequency range. The large diameter semicircle means larger charge-transfer resistance. Here, the $R_{ct}$ value for H-Ni/NiO core/shell NHs electrode (0.444 Ω) is smaller than that of the Ni/NiO core/shell NHs electrode (1.004 Ω), which indicates that H-Ni/NiO core/shell NHs are providing an ideal pathway for fast ion and electron transport. The Warburg resistance, which describes the diffusion of redox material in the electrolyte, can be reflected from the slope of the EIS curve in the low frequency range. The phase angle for the impedance plot of the Ni/NiO and H-Ni/NiO core/shell NHs electrode is found to be higher than 45°

in the low frequencies suggesting that the electrochemical capacitive behavior of the Ni/NiO and H-Ni/NiO core/shell NHs electrodes is controlled by diffusion process. The higher slope indicating the higher diffusion rate, describes the high diffusion of H-Ni/NiO core/shell NHs over the Ni/NiO core/shell NHs into the electrolyte [48]. These findings imply that the unique structure of the Ni/NiO and H-Ni/NiO core/shell NHs electrode can facilitate ionic motion in solid electrode.

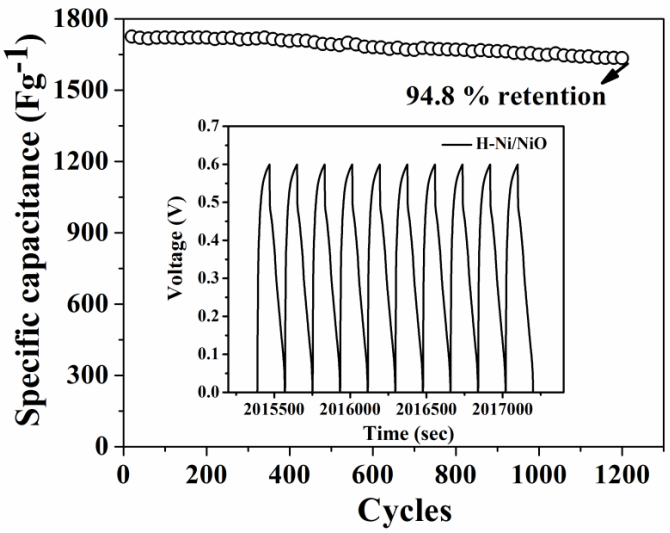


**Figure 5.10.** Cyclic performance of H-Ni/NiO core/shell NHs at a current density of 8.6 $Ag^{-1}$. The inset shows the charging/discharging curves for last 10 cycles of H-Ni/NiO core/shell NHs at a current density of 8.6 $Ag^{-1}$

Cyclic performance of the capacitors, which includes cycling life and capacitance retention, is another important characteristic of an electrochemical capacitor. Cycling life tests over 1200 cycles for the H-Ni/NiO core/shell NHs electrodes were carried out at 8.6 $Ag^{-1}$, and the results are shown in (Fig. 5.10). The sample exhibits good long term electrochemical stability. The capacitance loss after 1200 cycles is about 5.2%, which is better than that of the previously reported NiO based supercapacitors. The inset curves shown in (Fig. 5.10) are the last 10 cycles obtained from the cycling tests. The shapes were almost unchanged during the cycles. In continuation, we further performed cycling test of H-Ni/NiO core/shell NHs electrode over 1200 cycles as shown in Fig. 5.9(b), where the variation of the specific capacitance of H-Ni/NiO core/shell NHs electrode as a function of cycle number is plotted at different current densities from 8.6 to 15.1 $Ag^{-1}$. The H-Ni/NiO core/shell NHs electrode based supercapacitor exhibits good capacitance retention

after 1200 cycles and also high specific capacitance (over 1166 $Fg^{-1}$) was retained even at the large current density of 15.1 $Ag^{-1}$. Therefore, this study suggests that the H-Ni/NiO core/shell NHs electrode based supercapacitor is very stable during the long term cycle test.

### 5.2.3. Conclusion

In conclusion, the unique 1D Ni/NiO and H-Ni/NiO core/shell nano-heterostructures have been demonstrated with remarkable pseudocapacitive performance. The Ni/NiO core/shell NHs fabricated by controlled oxidation of Ni nanowires grown on the Au substrate via template assisted electrochemical route has been investigated as supercapacitor electrode. The electrochemical performance of the Ni/NiO core/shell NHs as pseudocapacitor has been found to improve significantly after the hydrogenation. The enhanced pseudocapacitance in H-Ni/NiO core/shell NHs is because of the improved conductivity and modified electrochemical activity of the NiO caused by the incorporation of hydroxyl groups at the surface through hydrogenation. Furthermore, in this unique 1D NHs, the highly porous nanolayer of H-NiO serves as the large platform for ion diffusion whereas the conductive Ni core provides the highway for fast transport of electrons to the current collector Au. The energy density and power density, measured at 15.1 A $g^{-1}$, are 49.35 $Whkg^{-1}$ and 7.9 $kWkg^{-1}$, respectively, demonstrating the superior performance of the electrode as pseudocapacitor. Nearly 57% capacitive retention after 1200 cycles at a current density of 15.1 $Ag^{-1}$ indicates the good rate capability of the NHs electrode. This study demonstrates an easy strategy to improve the electrochemical performance of the NiO based supercapacitors by making a unique 1D structure with improved ion/electron conductivity.

# 5.3. Co-Ni/$Co_3O_4$-NiO core/shell nano-heterostructure based electrodes for high-performance supercapacitors

## 5.3.1. Experimental

### 5.3.1.1. Reagents

Aluminium foil (99.99+% pure, 0.2 mm thick), Oxalic acid (99.9+% pure), Cobalt sulphate heptahydrate ($CoSO_4.7H_2O$, 99.95+% pure), Nickel sulphate hexahydrate ($NiSO_4.6H_2O$, 99.9+% pure), Boric acid ($H_3BO_3$, 99.9+% pure), Sodium hydroxide (NaOH, 99.9+% pure) and Potassium hydroxide (KOH, 99.9+% pure) were purchased from SIGMA-ALDRICH. All chemicals were of analytical grade and were used without further purification.

### 5.3.1.2. Synthesis of Co-Ni/$Co_3O_4$-NiO core/shell nano-heterostructures

Highly ordered nano-porous anodic aluminium oxide (AAO) templates were fabricated by the controlled two-stage electrochemical anodization of high-purity aluminium foil in oxalic acid solution as described elsewhere [1, 49, 50]. Fig. 5.11 schematically shows the two-step fabrication of the 1D Co-Ni/$Co_3O_4$-NiO core/shell nano-heterostructures: (1) electrodeposition of the arrays of Co-Ni NWs in AAO and (2) controlled high temperature oxidation of Co-Ni NWs in air atmosphere.

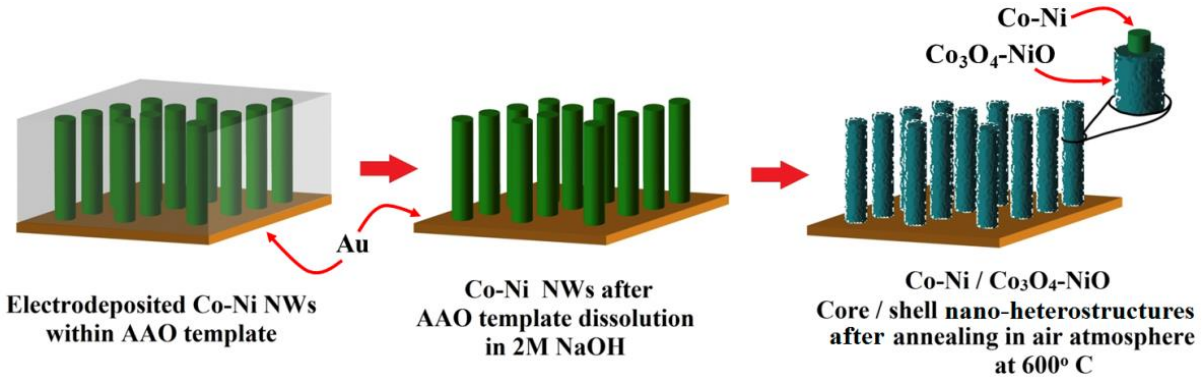


**Figure 5.11.** (Color online) Schematic overview of the preparation of Co-Ni/$Co_3O_4$-NiO core/shell nano-heterostructures.

The unique feature of this technique is that individual nano-heterostructure in the electrode has its own contact with the current collector (Au), which results the enhanced charge transfer kinetics. The software controlled three electrode electrodeposition unit (potentiostat AutoLab-30) equipped with power supply was

used to synthesise high density arrays of Co-Ni alloy NWs with the help of AAO template with one side coated with a conductive gold (Au) layer grown by the thermal evaporation technique. A high-purity Pt wire and an Ag/AgCl electrode were used as the counter and reference electrodes, respectively.

The arrays of Co-Ni alloy NWs were grown in the pores of AAO using the aqueous solution of 40 g $L^{-1}$ $CoSO_4.7H_2O$, 50 g $L^{-1}$ $NiSO_4.6H_2O$ and 30 g $L^{-1}$ $H_3BO_3$ as the electrolyte at room temperature. Here, boric acid and $NH_4OH$ were used as a buffer to maintain the pH of the electrolyte around 3.5 and also to control the electrodeposition process. The deposition of the arrays of Co-Ni alloy NWs was conducted for 30 minutes by using a dc voltage of -0.95 V, following the linear sweep voltammetry (LSV) results. After the growth of the Co-Ni alloy NWs the template was removed by dissolving it in 2 M NaOH aqueous solution. The open arrays of Co-Ni alloy NWs grown on Au layer were finally oxidized to form Co-Ni/$Co_3O_4$-NiO core/shell nano-heterostructure by annealing at 600°C for 10 min in air atmosphere. The mass of the active electrode material was measured by using a microbalance having an accuracy of 0.1 μg. The mass of the active electrode materials was calculated by subtracting the mass of the equal area Au foil layer, on which the nano-heterostructures were grown, from the total mass of the cathode (nano-heterostructures material and the Au layer). The loading density of the Co-Ni/$Co_3O_4$-NiO core/shell nano-heterostructures was found to be 0.376 mg $cm^{-2}$.

## 5.3.2. Results and Discussions

### 5.3.2.1. Morphology, Crystallography and Chemical composition

Figure 5.12(a) shows the field emission scanning electron microscopy (FESEM) image of the as-prepared Co-Ni/$Co_3O_4$-NiO core/shell nano-heterostructures having uniform diameter (~150 nm). Inset of Fig. 5.12(a) indicates that the surface of nano-heterostructures is very rough and porous compare to that of the Co-Ni NWs (Fig. 5.13(a)), which will further increase the active surface area of the electrode. The transmission electron microscopy (TEM) [Fig. 5.12(b)] and energy filtered TEM (EFTEM) [Fig. 5.12(d)] micrographs of the Co-Ni/$Co_3O_4$-NiO core/shell nano-heterostructures clearly show the formation the uniform nano-layer

(~ 25–30 nm) of $Co_3O_4$-NiO on Co-Ni metal alloy core. Formation of a good quality nano-heterostructures with uniform chemical composition is also evident from Fig. 5.12(d).

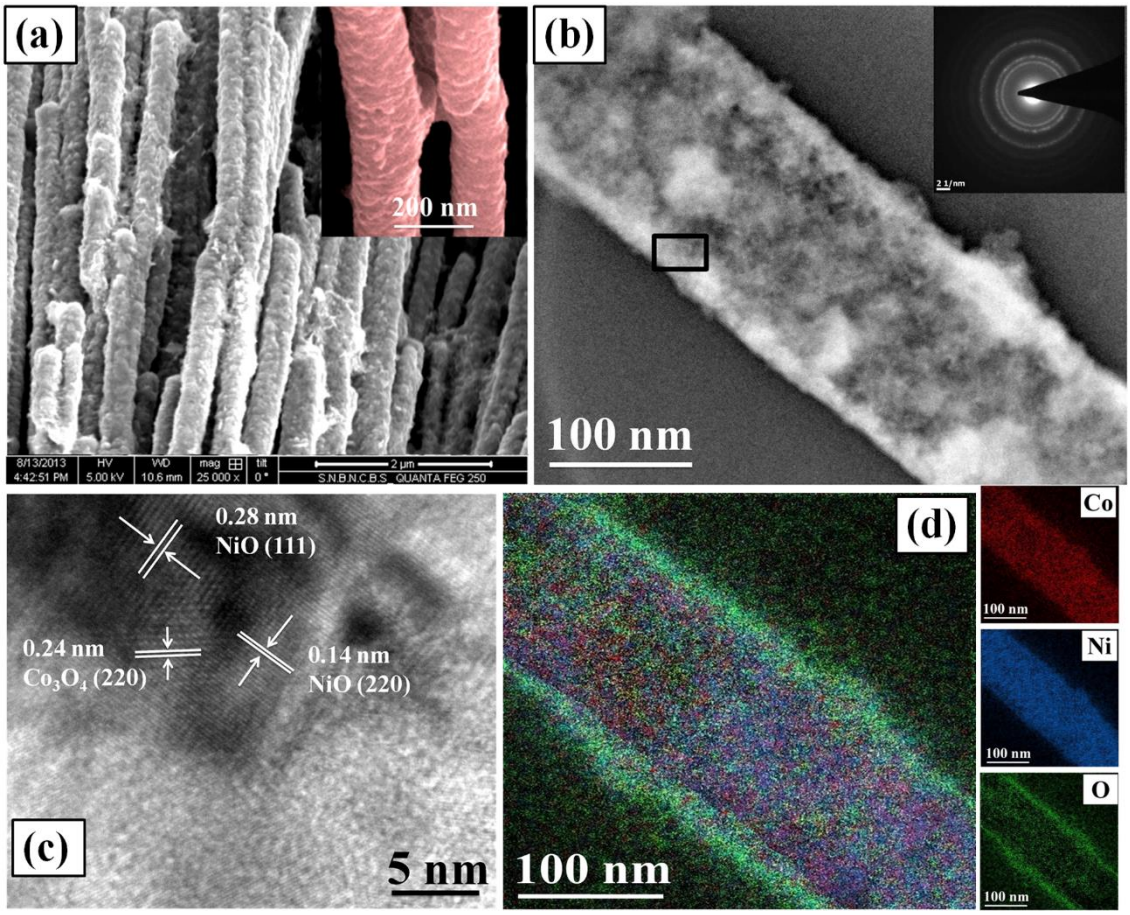


**Figure 5.12** (Color online) (a) and inset of (a): FESEM micrographs, (b) TEM and SAED pattern (inset of (b)), (c) HRTEM image and (d) EFTEM micrographs of the Co-Ni/$Co_3O_4$-NiO core/shell nano-heterostructures.

Single area electron diffraction (SAED) pattern [inset of Fig. 5.12(b)] and high resolution TEM (HRTEM) image [Fig. 5.12(c)] confirm the polycrystalline nature of the nano-heterostructures. The HRTEM micrograph with *d*-spacing of 0.28, 0.14 and 0.24 nm, correspond to the (111) NiO, (220) NiO and (220) $Co_3O_4$, respectively. The x-ray diffraction pattern of nano-heterostructures also shows its polycrystalline nature (Fig. 5.13(b)). The XRD pattern consists of peaks that correspond to the core containing Co and Ni and shell nanolayer which contains NiO and $Co_3O_4$ and also the metallic Au layer underneath the nano-heterostructures. The energy-dispersive x-ray spectroscopy (EDAX) spectrum confirms the presence of Co, Ni and O in the

nano-heterostructures, where the Co:Ni ratio is found to be 1.3:1 in $Co_3O_4$-NiO mixed oxides (Fig. 5.13(c)).

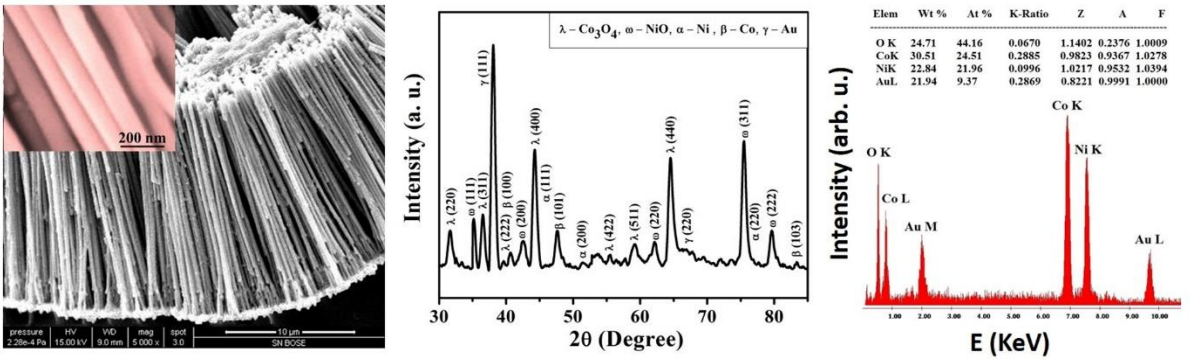


**Figure 5.13** (a) FESEM micrograph of the as prepared arrays of Co-Ni nanowires, (b) XRD pattern of the Co-Ni/$Co_3O_4$-NiO core/ shell nano-heterostructures, (c) EDAX spectrum of the Co-Ni/$Co_3O_4$-NiO core/ shell nano-heterostructures.

### 5.3.2.2. Electrochemical Analysis

Electrochemical properties of the Co-Ni/$Co_3O_4$-NiO core/shell nano-heterostructures electrode was studied by cyclic voltammetry (CV) and galvanostatic (GV) charge/discharge method by using a three-electrode system, where the nano-heterostructures as working electrode was dipped in 1 M KOH aqueous solution at room temperature. The Ag/AgCl and Pt were used as reference and counter electrodes, respectively. Fig. 5.14(a) shows the CV curves of the as-prepared nano-heterostructures, recorded at different scan rates (2-100 mV $s^{-1}$) within the voltage window of 0.1–0.5 V. Each CV loop characterized by oxidation and reduction peaks, demonstrate the pseudocapacitive behaviour of the nano-heterostructures, which is quite different from the rectangular CV loops owing to the formation of Helmholtz layer in electrical double layer capacitors (EDLCs). The redox peaks observed for all scan rates are associated with the surface or near surface based Faradic reactions as governed by the equations [34, 49]: $Co_3O_4 + H_2O + OH^- \leftrightarrow 3CoOOH + e^-$ and $NiO + OH^- \leftrightarrow NiOOH + e^-$. The charging process involves the oxidization of $Co^{2+}$ and $Ni^{2+}$ into $Co^{3+}$ and $Ni^{3+}$, respectively, with the movement of the corresponding electrons towards the current collector (Au) through the electrode; while discharging involves subsequent reduction of metal ions from +3 state to +2 state followed by the electron transport in reverse direction.

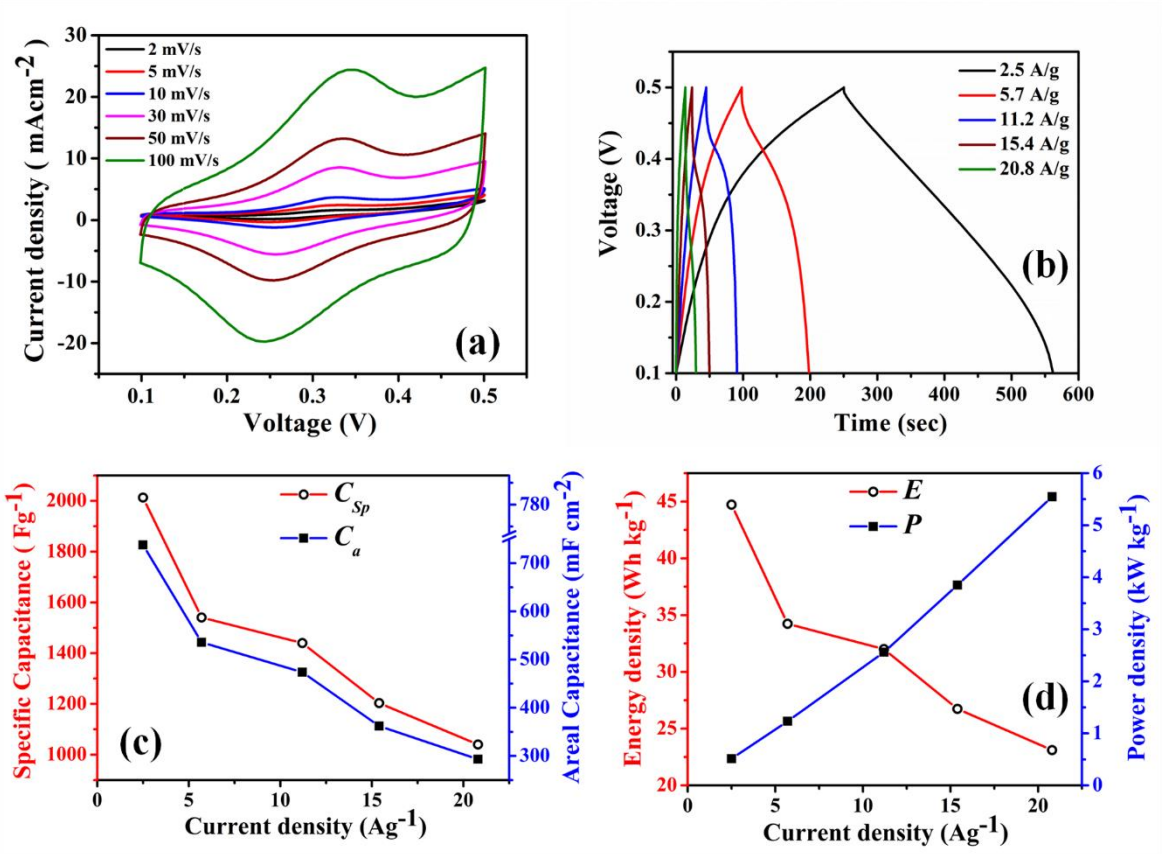


**Figure 5.14** (a) Cyclic voltammograms of the nano-heterostructures electrode recorded at different scan rates. (b) Galvanostatic charge/discharge curves of the nano-heterostructures electrode recorded at different constant current densities. (c) Areal capacitance and specific capacitance calculated from the charge/discharge curves as a function of current density. (d) Variation of power density and energy density of the nano-heterostructures as a function of current density.

Good kinetic reversibility characteristics of the electrode are confirmed from the highly symmetric nature of the redox peaks of the CV curves taken at different scan rates [27,28]. This observation also reveals the high cyclability of the electrode. The increase of current with increasing scan rate is quite obvious because during fast scanning diffusion layer cannot extend far from the electrode surface, thus facilitating higher electrolyte flux towards the electrode leading to higher value of current which is in contrary to the case at lower scan rates where the large width of the diffusion layer significantly reduces the electrolyte flux and hence the current. However, the linear relation between the peak current ($I$) of CV loops and the square root of scan rate ($f^{1/2}$) observed for nano-heterostructures at different scan rates (Fig. 5.15) demonstrates the fast electron transfer during redox reactions, indicating the superior performance of the nano-heterostructures as SC electrode [44]. This high rate performance can be attributed to the rough and porous structure of the

electrode materials which can store the electrolytic ions effectively to facilitate ion movement and also shortens the ion diffusion path to the interiors of the electrode even at higher scan rates.

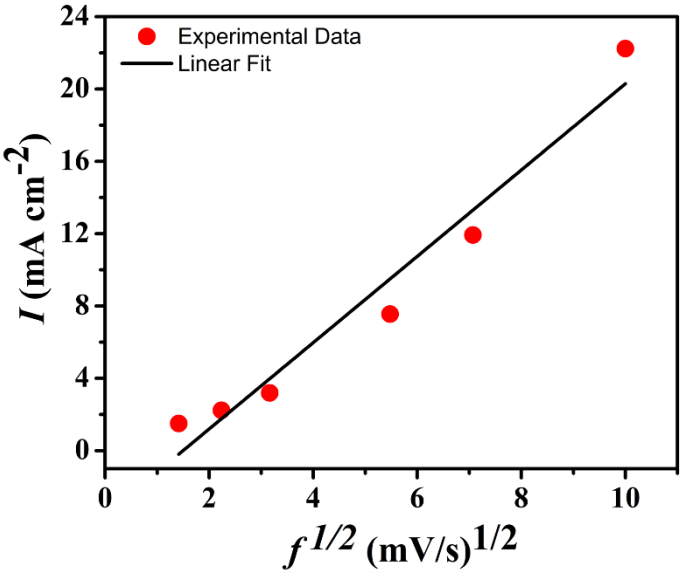


**Figure 5.15** Plotting of the peak current ($I$) of CV loops vs. the square root of scan rate ($f^{1/2}$) for the nano-heterostructures obtained at different scan rates.

Fig. 5.14(b) shows the typical constant current GV charge/discharge curves of the nano-heterostructures electrode at different current densities within the voltage window of 0.1–0.5 V. The symmetric nature of the curves suggests excellent electrochemical characteristics of the nano-heterostructures manifested by reversible redox reactions. All the charge/discharge curves of the nano-heterostructures exhibit low IR drop which can be attributed to the special core/shell designing of the electrode material and also due to the binder-free direct contact of nano-heterostructures with the current collector that significantly reduces the interfacial resistance. The symmetric nature of the cycling curves remains unaltered even when the current density reaches as high as 21 A $g^{-1}$, indicates very high rate stability of the electrode. From the discharging curves, the specific and areal capacitances are calculated by the formulas, $C_{sp} = I\Delta t/m\Delta V$ and $C_a = I\Delta t/a\Delta V$, respectively (where, $I$ is the discharge current, $\Delta t$ is the discharging time, $\Delta V$ is the potential window, $m$ is the mass of the active material (i.e., the total mass of the nano-heterostructures, here loading density of nano-heterostructures is 0.376 mg $cm^{-2}$) and $a$ is the surface area of working electrode) are shown in Fig. 5.14(c). The $C_{sp}$ of nano-heterostructures

electrode are found to be nearly 2013 F $g^{-1}$ at the current density of 2.5 A $g^{-1}$ and the $C_a$ of the nano-heterostructures electrode is 738 mF $cm^{-2}$ at an equivalent current density of 0.94 mA $cm^{-2}$. The capacitance of the Co-Ni mixed oxide is found comparable ($NiCo_2O_4$ nanosheet@carbon fabric [51], Ni-Co oxide NWs@$TiO_2$ [52]) and even much better than the values reported for other such Co/Ni based oxide composites, such as nanoporous NiO film [21], mesoporous $Co_2O_3$ NWs [34], spherical porous NiO [38], $NiCo_2O_4$ nanorods and nanosheets@carbon fibber [49], Ni-Co oxides [53], mesoporous NiO [54], $Co_3O_4$ NWs@carbon paper [55], $NiCo_2O_4$ nano-needle [56], $NiCo_2O_4$ NWs [57,58]. The $C_{sp}$ of the nano-heterostructures is 1040 F $g^{-1}$ even when the current density increases as high as 20.8 A $g^{-1}$, implying that it can retain ~ 51.67 % of its initial capacitance when the current density is increased by almost 8.5 times. This high specific capacitance with impressive rate capability, i.e. excellent capacitive performance of the nano-heterostructures is mainly due to the large surface area novel nano-architectural design of the electrode having good electrochemical utilization of two highly redox active materials together with high electrical conductivity provided by the metal alloy core. Here, the high surface area of the nano-heterostructure electrode (due to the presence of nano-porous oxide shell layer) provides significantly large platform for the fast charge intercalation/deintercalation within the electrode material during the faradic reactions whereas, the highly conductive core helps for faster electron transport that have been generated through redox reactions, to the current collector, thus promoted relatively high rate capability. Moreover, this thin porous oxide layer facilitates electrolytic ion and electron transport to the interiors of the electrode material, resulting higher electrochemical performance.

The energy and power densities calculated by the formulas, $E = \frac{1}{2}C_{sp}(\Delta V)^2$ and $P = E/\Delta t$, respectively (where, where, '$E$ (Wh $Kg^{-1}$)', '$C_{sp}$ (F $g^{-1}$)', '$\Delta V$ (V)', '$\Delta t$ (s)' and '$P$ (kW $kg^{-1}$)' are the energy density, specific capacitance, potential window of discharge, discharging time and power density, respectively.) from the charge−discharge curves at different current densities are plotted in Fig. 5.14(d). The energy density of the nano-heterostructures electrode decreases from 44.7 to 23 Wh $kg^{-1}$, when the power density for the same increases from 0.5 to 5.6 kW $kg^{-1}$, as the

discharge current density increased from 2.5 to 20.8 A $g^{-1}$. The nano-heterostructures SC maintains high power density without much reduction in energy density, which is found better than reported previously for: $NiO_x$ [59], $Ni(OH)_2$ [60], $CoO_x$ [61], $Co(OH)_2$ [62], based SC electrodes.

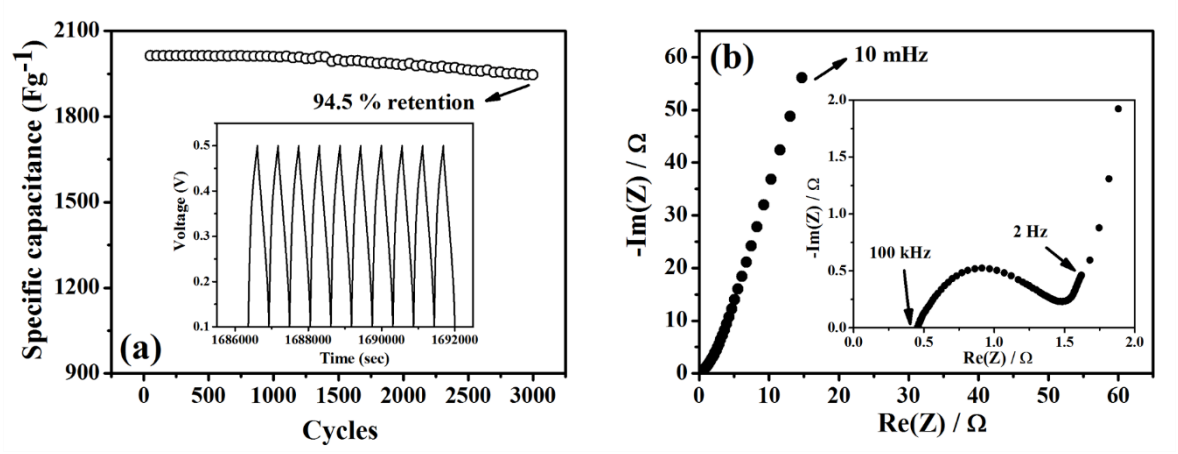


**Figure 5.15** (a) Cycling performance of nano-heterostructures elecrode (3000 charge/discharge cycles at a constant current density of 2.5 $Ag^{-1}$). Inset of (a): last 10 cycles of the charging/discharging curves. (b) Nyquist plot of the EIS data of the nano-heterostructures electrode over the frequency range from 10 mHz to 100 kHz.

The nano-heterostructures also exhibit excellent electrochemical cycling stability beyond 3000 cycles carried out at a current density of 2.5 $Ag^{-1}$, with a negligible decay (5.5 %) of its initial value of $C_{sp}$ [Fig. 5.15(a)]. From the last 10 charge/discharge cycles shown in Fig. 5.15(a) it can be seen that the symmetric triangular shape of the charging/discharging profiles remain almost unchanged during the long cycle test which again signifies stable electrochemical performance and efficient charge transport during the reactions. Such high stability of the electrode can be accounted for the higher mechanical integrity which can sustain significant structural distortion during repetitive charging/discharging process and also non-dissolution of active material within the electrolyte. However, small decrease in specific capacitance after 3000 cycles may be due to the swelling of the electrode material owing to the continuous ion insertion/deinsertion process during long cycle test.

The electrochemical impedance spectroscopy (EIS) measurements data of the nano-heterostructures analysed by using Nyquist plot is shown in Fig. 5.15(b). The finite slope of the impedance spectra ($\theta > 45^0$) at lower frequencies indicates diffusive

resistivity of the electrolyte within the pores of the nano-heterostructures. The intercept on the real axis in the high frequency region represents the equivalent series resistance ($R_s$), which includes bulk resistance of electrolyte, intrinsic resistance of active material, and contact resistance of electrode/electrolyte interface. The value of $R_s$ of the nano-heterostructure electrode is calculated as 0.452 Ω, indicates higher electrical conductivity of the electrode which can be attributed to the presence of Co-Ni alloy core within the nano-heterostructure. The diameter of the semicircle in the high frequency region provides the charge transfer resistance ($R_{ct}$) resulting from the diffusion of electrons. The $R_{ct}$ value of nano-heterostructures (1.033 Ω) represents its low faradic resistance due to high redox activity of the composite materials indicates easy charge transport across the electrode-electrolyte interface. Therefore, from the EIS analysis it can be understood that this unique core/shell combination of two redox active materials significantly reduces the inherent resistances of the whole electrochemical system leading to enhanced capacitive performance.

### 5.3.3. Conclusion

In conclusion, novel 1D Co-Ni/$Co_3O_4$-NiO core/shell nano-heterostructures with remarkable pseudocapacitance has been demonstrated. The nano-heterostructures are fabricated by combining simple electrochemical deposition of Co-Ni alloy Nanowires followed by controlled oxidation. The unique nano-architectural design of the nano-heterostructures electrode having large rough surface area coupled with the presence of two highly redox active materials with short ion diffusion path grown on the highly conducting metal alloy channel facilitating the faster charge transport helps to achieve enhanced electrochemical properties suitable for the supercapacitor applications.

# 5.4. High performance Supercapacitor Electrode based on Fe-Ni/$Fe_2O_3$-NiO Core/Shell Hybrid Nanostructures

## 5.4.1. Experimental

### 5.4.1.1. Reagents

Aluminium foil (99.99+% pure, 0.2 mm thick), Oxalic acid (99.9+% pure), iron sulphate heptahydrate ($FeSO_4.7H_2O$, 99.95+% pure), Nickel sulphate hexahydrate ($NiSO_4.6H_2O$, 99.9+% pure), Boric acid ($H_3BO_3$, 99.9+% pure), Sodium hydroxide (NaOH, 99.9+% pure) and Potassium hydroxide (KOH, 99.9+% pure) were purchased from SIGMA-ALDRICH. All chemicals were of analytical grade and were used without further purification.

### 5.4.1.2 Preparation of Fe-Ni/$Fe_2O_3$-NiO core/shell hybrid nanostructures

The common fabrication technique of Fe-Ni/$Fe_2O_3$-NiO core/shell hybrid nanostructure is schematically shown in Fig. 5.16. First of all highly porous anodic alumina oxide (AAO) templates which contains pore (diameter ~100 nm) were grown by two step anodization techniques as described in our previous report [63].

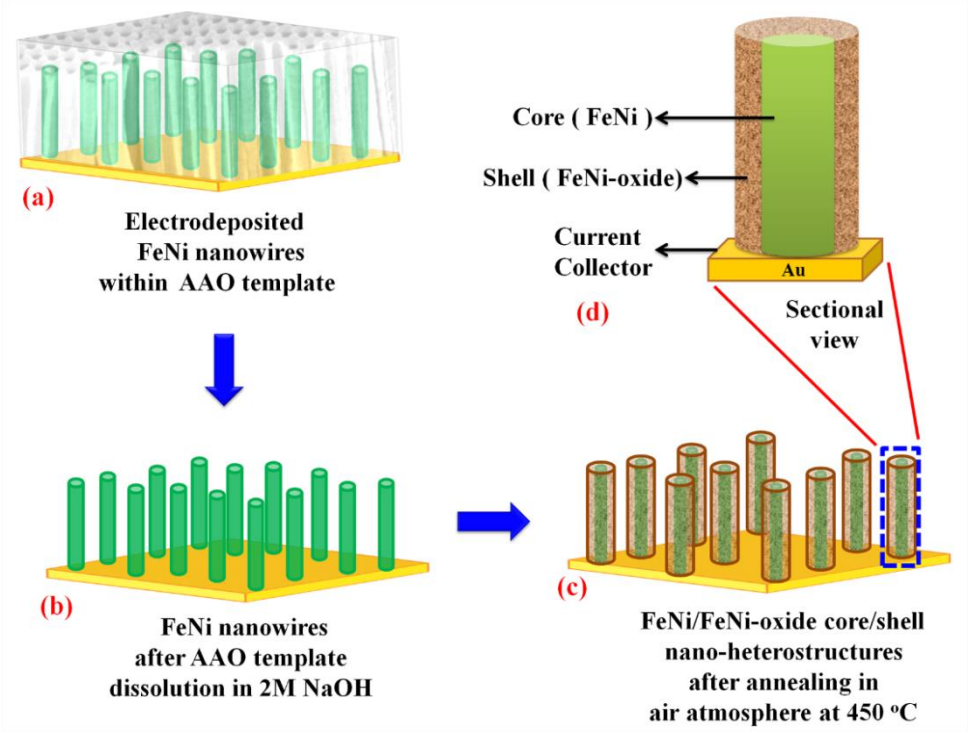


**Figure 5.16**. (a), (b) & (c) Schematic show the synthesis process of Fe-Ni/$Fe_2O_3$-NiO core/shell HNs on Au substrate. (d) Schematic diagram of the sectional view of single HNs.

After that thin gold layer was grown on one surface of the AAO template by DC sputtering technique. The arrays of FeNi nanowires (NWs) were grown inside the pores of self-developed AAO templates with the help of three electrode electrochemical cell and power supply (Autolab-30) by the electrodeposition technique as described in our previous report [64]. The aqueous solution of 80 g $L^{-1}$ $NiSO_4 \cdot 6H_2O$, 30 g $L^{-1}$ $FeSO_4 \cdot 7H_2O$, 15 g $L^{-1}$ $H_3BO_3$ and 10 g $L^{-1}$ $NH_4OH$ as electrolyte at room temperature. The deposition procedure was performed for 15 minutes at a voltage of 1.05 V vs. Ag/AgCl for growing FeNi NWs inside AAO templates. Then, the arrays of bare FeNi NWs were obtained from the electrodeposited AAO template by dissolving it in 2M NaOH solution. After that, the Fe-Ni/$Fe_2O_3$-NiO core/shell HNs were obtained by annealing the as prepared FeNi NWs at high temperature (450 °C) for a short period of time (15 minutes) in an oxygen atmosphere.

As-prepared Fe-Ni/$Fe_2O_3$-NiO core/shell HNs grown on the conductive current collector (Au) by above mentioned technique have been used for the fabrication of electrode. During fabrication of the electrode, the calculation of the loading mass density of the active electrode materials was done by micro balance with the precision of 0.1 microgram. The area of the electrode was estimated and found to be 0.15 $cm^2$. The resultant loading mass densities of the Fe-Ni/$Fe_2O_3$-NiO core/shell HNs electrode after subtracting the mass of the gold substrate layer from the entire mass of the electrode (redox active electrode stuff and the gold substrate layer) were calculated 0.387 mg $cm^{-2}$. Then, a conductive wire was connected at the back side of the electrode (Au exposed side). Further, the rest of the portion of Au exposed side of the electrode was covered with a non-conductive and non-reactive tape layer before inserting this electrode inside the cell.

## 5.4.2. Results and Discussions

### 5.4.2.1. Morphology, Crystallography and Chemical composition

A simple controlled oxidation technique was used to fabricate the Fe-Ni/$Fe_2O_3$-NiO core/shell hybrid nanostructures (HNs) and their structural and morphological studies were done by Field emission scanning electron microscope

(FESEM). The FESEM micrograph of the Fe-Ni/$Fe_2O_3$-NiO core/shell HNs on gold substrate is shown in Fig. 5.17(a). It is evident from Fig. 5.17(a) & (b), that the as-prepared 1D core/shell HNs are vertically aligned throughout the surface with uniform diameter and vertical length about 150 nm and 2 μm, respectively, for single core/shell HNs.

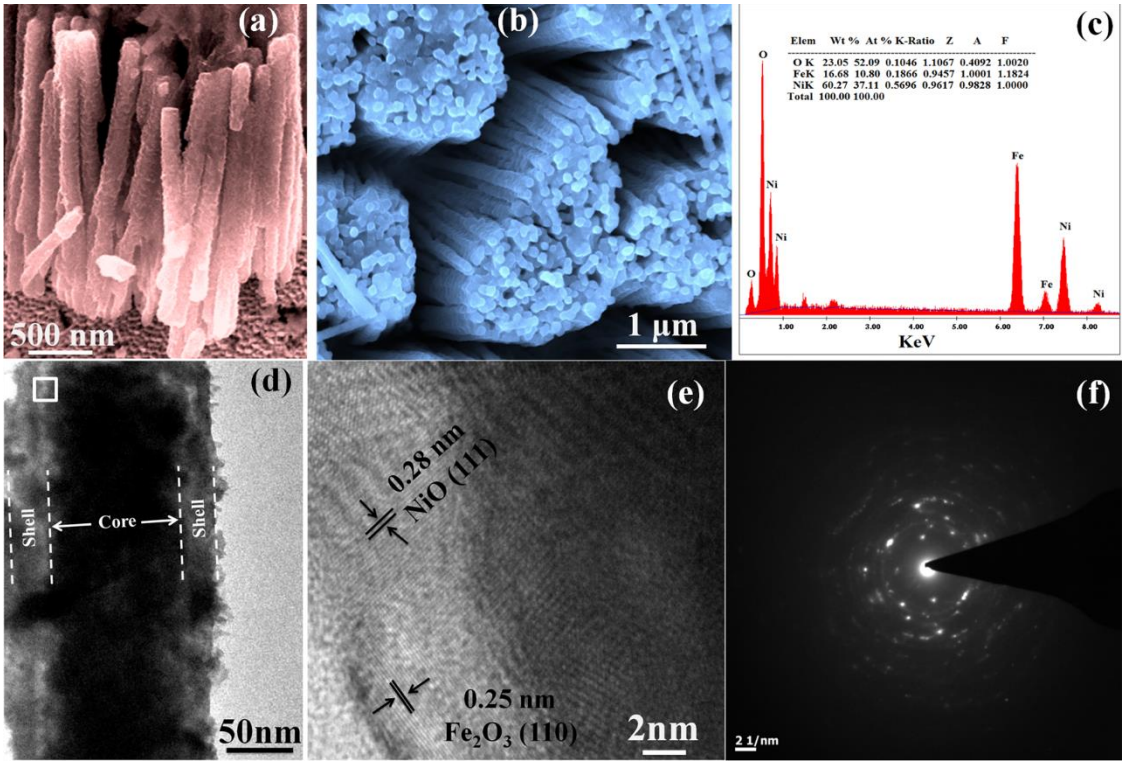


**Figure 5.17 (**a) & (b) FESEM micrograph (c) EDAX spectrum, (d) TEM mcicroghaph, (e) HRTEM micrograph, (f) SAED pattern of the Fe-Ni/$Fe_2O_3$-NiO core/shell HNs.

Moreover, the outer surface of Fe-Ni/$Fe_2O_3$-NiO core/shell HNs has become very rough and porous in comparison of FeNi nanowires. The rough and porous outer surface of Fe-Ni/$Fe_2O_3$-NiO core/shell HNs attributes in the enhancement of the surface area which will provide more surface area for redox reactions. Energy dispersive x-ray (EDAX) study was performed for finding out the elemental composition of the Fe-Ni/$Fe_2O_3$-NiO core/shell HNs. Fig. 5.17(c) shows the EDAX spectrum, which verifies the existence of Fe, Ni and O elemental composition in the core/shell HNs, where, the Au peak confirms the presence of gold layer as a current collector. In particular, the peak for oxygen in the EDAX spectrum confirms that, the growth of the oxide shell layer. Further, the detailed morphological and microstructural studies were carried out by Transmission electron microscope (TEM)

for a deeper understanding about the Fe-Ni/$Fe_2O_3$-NiO core/shell HNs. Fig. 5.17(d) shows the TEM micrograph of an individual Fe-Ni/$Fe_2O_3$-NiO core/shell HNs, which illustrate the formation of nearly 25 nm porous thin nanolayer of $Fe_2O_3$-NiO (shell) over FeNi nanowire with nearly 100 nm in diameter (core). Above TEM micrograph results confirm the formation of Fe-Ni/$Fe_2O_3$-NiO core/shell HNs (diameter ~ 150 nm). The enlarge High resolution TEM micrograph and selected area energy diffraction (SAED) of core-shell HNs traced from the area marked by the white square at the core and shell interface of Fe-Ni/$Fe_2O_3$-NiO core/shell HNs in Fig. 5.17(d). Fig. 5.17(e) & (f) show the HRTEM and SAED micrographs, which confirm the crystalline nature of the Fe-Ni/$Fe_2O_3$-NiO core/shell HNs. This crystalline nature is favourable for the improvement of the conductivity of the supercapacitor electrodes. The calculated lattice was found to be 0.28 nm and 0.25 nm corresponds to the inter-planer spacing of NiO (111) and $Fe_2O_3$ (110), respectively.

For a deeper understanding of microstructural and elemental composition of single Fe-Ni/$Fe_2O_3$-NiO core/shell HNs, scanning transmission electron microscope (STEM) study was performed. STEM micrograph of single Fe-Ni/$Fe_2O_3$-NiO core/shell HNs shows a thin shell layer of around 25 nm homogeneously envelops the surface of the core FeNi nanowire, which has a diameter of around 100 nm. To know about the elemental distribution (Ni, Fe and O) across core-shell HNs, energy-dispersive X-ray spectrometry (EDS) line scanning was performed across the HNs diameter (specified by an orange line in Fig. 5.18(a)). Fig. 5.18 (b)-(d) show, the EDS line scanning profile of Ni, Fe and O, respectively, where the Ni and Fe profile shows the higher intensity at the center of the profile, whereas, O shows the higher intensity at the outer edge of the spectrum profile due to the formation of NiO and $Fe_2O_3$. Investigation of these EDS line spectra reveals that the core-shell HNs have Ni and Fe at the core and O is concentrated on the outer surface as a thin shell layer. In addition, to confirm the previous elemental distribution (Ni, Fe and O) results across core-shell HNs, we performed an energy filtered transmission electron spectroscopy (EFTEM) study of same core-shell HNs sample, which is shown in the form of coloured elemental mapping of Ni (blue), Fe (red) and O (green), respectively

(shown in Fig. 5.18 (e)-(g), respectively). EFTEM micrographs of individual elements (Ni, Fe and O) clearly supports the results of the EDS scanning spectrum. These structural and morphological study evidences prove the formation of Fe-Ni/$Fe_2O_3$-NiO core/shell HNs.

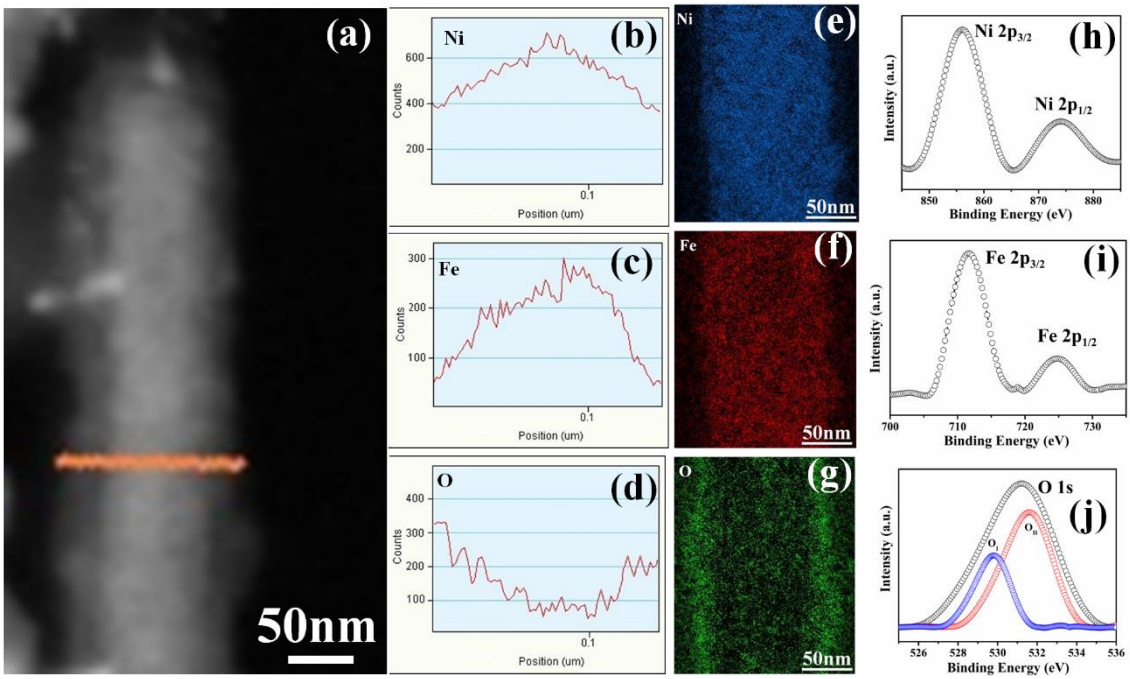


**Figure 5.18**. (a) STEM image of individual Fe-Ni/$Fe_2O_3$-NiO core/shell HNs**.** (b) – (d) EDS line scanning of Ni, Fe, and O, respectively, across the Fe-Ni/$Fe_2O_3$-NiO core/shell HNS indicated in (a). (e) – (g) EFTEM elemental mapping images of Ni (in blue color), Fe (in red color) and O (in green color), respectively, for the Fe-Ni/$Fe_2O_3$-NiO core/shell HNS indicated in (a). (h) – (j) The high resolution XPS spectrum of the Ni 2p, Fe 2p and O 1s core level, respectively, of Fe-Ni/$Fe_2O_3$-NiO core/shell HNs.

Furthermore, we have performed the X-ray photoelectron spectroscopy (XPS) studies of the Fe-Ni/$Fe_2O_3$-NiO core/shell HNs to the closer insight about the chemical compositions, metal oxidation states and about the outer surface of the electrode. The XPS spectrum of core-shell HNs confirms the presence of elemental components Ni, Fe and O. Fig. 5.18(h) shows the core level spectra of Ni 2p which consists two peaks of Ni $2p_{3/2}$ and Ni $2p_{1/2}$ obtained at the binding energy of 856 and 873.5 eV, respectively, which confirm the +2 oxidation ($Ni^{2+}$) state of Ni in the core-shell HNs sample. The core level XPS spectra of Fe 2p is shown in Fig. 5.18(i), which confirm the presence of two characteristic peaks Fe $2p_{3/2}$ and Fe $2p_{1/2}$ observed at the binding energy of 711.4 and 725 eV, respectively, corresponds to the trivalent (+3) state of Fe in Core-shell HNs [65]. The reason behind the splitting of 2p core levels of

Ni and Fe is spin−orbit coupling. The core level XPS spectra of O 1s is shown in Fig. 5.18(j), where the peak of core level O 1s obtained at 531.2 eV binding energy, which is deconvoluted into two peaks, centered on 529.8 eV ($O_I$) and 531.6 eV ($O_{II}$). The lower energy peak ($O_I$) confirm s the presence of oxygen in (-2) oxidation state due to the presence of NiO and $Fe_2O_3$ in core-shell HNs [66], whereas the higher energy peak ($O_{II}$) signify the presence of hydroxyl group in the core-shell HNs [66, 67].

**5.4.2.2. Electrochemical Analysis**

Cyclic voltammetry (CV) and galvanostatic charge/discharge (GCD) methods have been used to study the electrochemical properties of the Fe-Ni/$Fe_2O_3$-NiO core/shell HNs electrode in three electrode system electrochemical cell. Further, the CV measurements of the Fe-Ni/$Fe_2O_3$-NiO core/shell HNs were done in details. The CV measurements were done within a fixed voltage range (0 V to 0.55 V) by varying the scan rate (2, 10, 30, 50 and 100 mV $s^{-1}$), shown in Fig. 5.19 (a). The expected pseudocapacitive nature of the Fe-Ni/$Fe_2O_3$-NiO core/shell HNs electrode confirms from the behaviour of CV curves, which contains the oxidation and reduction peaks due to the faradic reactions occurred at the surface of as grown core-shell HNs. These faradic reactions implicate redox transitions of nickel oxide and iron oxide in the electrolyte, based on the equations: $Fe_2O_3 + M^+ + e^- \leftrightarrow Fe_2O_3M$, where, $M^+ = K^+$ or $H_3O^+$ and $NiO + OH^- \leftrightarrow NiOOH + e^-$. It is evident from Fig. 5.19 (a) that for Fe-Ni/$Fe_2O_3$-NiO core/shell HNs electrode there two oxidation peaks are detected at +0.3V and +0.35 V, which signifies to the oxidation of iron [$Fe^{2+}$ to $Fe^{3+}$] and nickel [$Ni^{2+}$ to $Ni^{3+}$] from the above redox equations, respectively, in the anodic process, whereas, only one reduction peak noticed at +0.1 V, which specify the reduction of iron [$Fe^{3+}$ to $Fe^{2+}$] and nickel [$Ni^{3+}$ to $Ni^{2+}$]. We observed from Fig. 5.19 (a) that the reduction peak is bigger than the oxidation peaks, which is reasonable because the reduction peak incorporates two reduction peaks of iron [$Fe^{3+}$ to $Fe^{2+}$] and nickel [$Ni^{3+}$ to $Ni^{2+}$] in the cathodic process. To reveal more information about redox reaction process during CV curve measurements, the average peak current density as a function of (scan rates)$^{1/2}$ plotted and found the linear relation curve (Fig. 5.20 (a)), which indicates a diffusion controlled mechanism of redox

reactions.[41,42] Moreover, the stability and kinetic reversibility of the core-shell HNs electrode confirmed from the analogous shape of the CV curves for all the scan rates (2, 10, 30, 50 and 100 mV $s^{-1}$) [68,69]. Interestingly, all the redox peaks are clearly visible even at a higher scan rate (100 mV $s^{-1}$) verifies that the core-shell HNs electrode possess rapid oxidation-reduction reactions at the interface of electrode and electrolyte [26, 28].

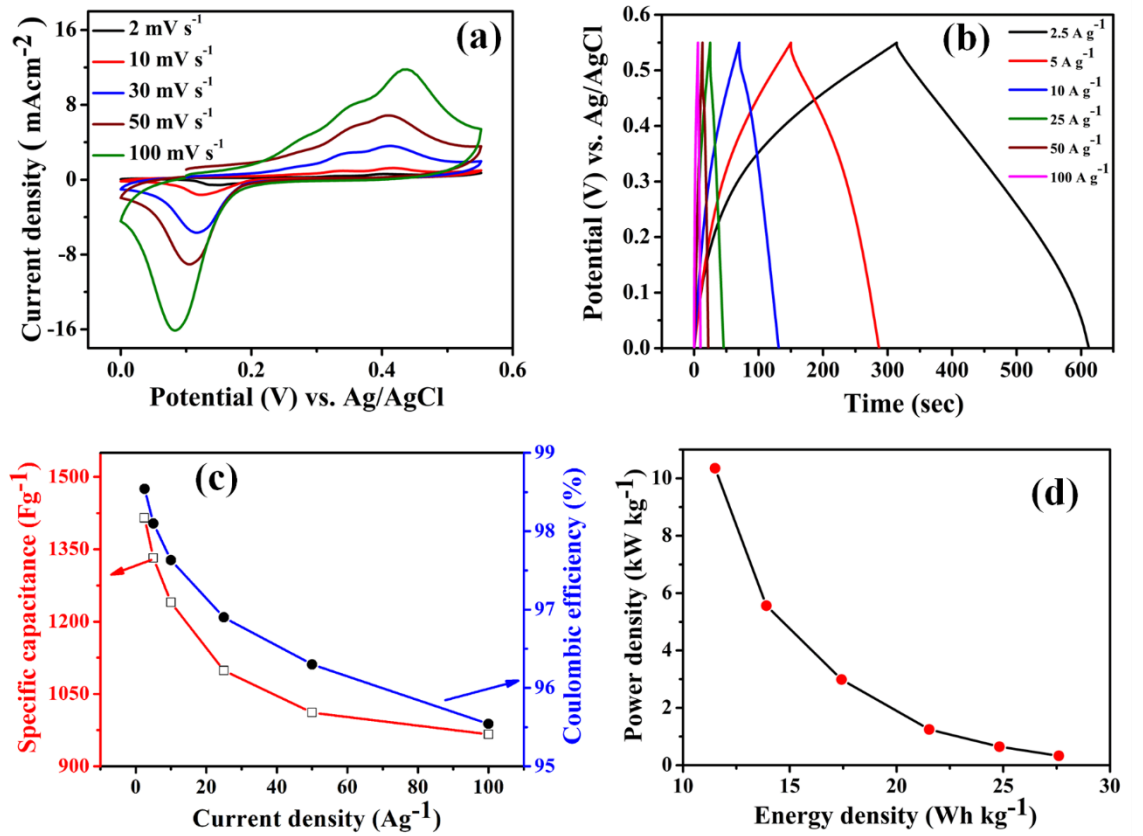


**Figure 5.19**. (a) Cyclic voltammetry curves, (b) Galvanostatic charge/discharge curves, (c) Specific capacitance and coulombic efficiency as a function of current densities, (d) power density vs. energy density plots, for Fe-Ni/$Fe_2O_3$-NiO core/shell HNs electrode.

The calculation of the areal capacitance of the Fe-Ni/$Fe_2O_3$-NiO core/shell HNs electrode has been done according to the reported formula, $C_a = I/(f\,A)$ [34, 70], where, $I$ denotes the peak current recorded from CV curves, $f$ represents the scan rate, $A$ is the nominal working electrode area. The behaviour of areal capacitance of the Fe-Ni/$Fe_2O_3$-NiO core/shell HNs has been observed with respect to the scan rate by varying the value of scan rate which is shown in Fig. 5.20 (b). The value of areal capacitance for core-shell HNs is found to be 291.5 mF $cm^{-2}$ for low scan rate value (2 mV $s^{-1}$ ) and areal capacitance value decreased upto 139.6 mF $cm^{-2}$ at very high scan

rate value (100 mV $s^{-1}$), which reveals high rate capability property of the Fe-Ni/$Fe_2O_3$-NiO core/shell HNs due to its unique architecture. The supercapacitive performance of as-prepared Fe-Ni/$Fe_2O_3$-NiO core/shell HNs has been revealed comparable performance to other transition metal based previously reported supercapacitors [28, 39, 71-73].

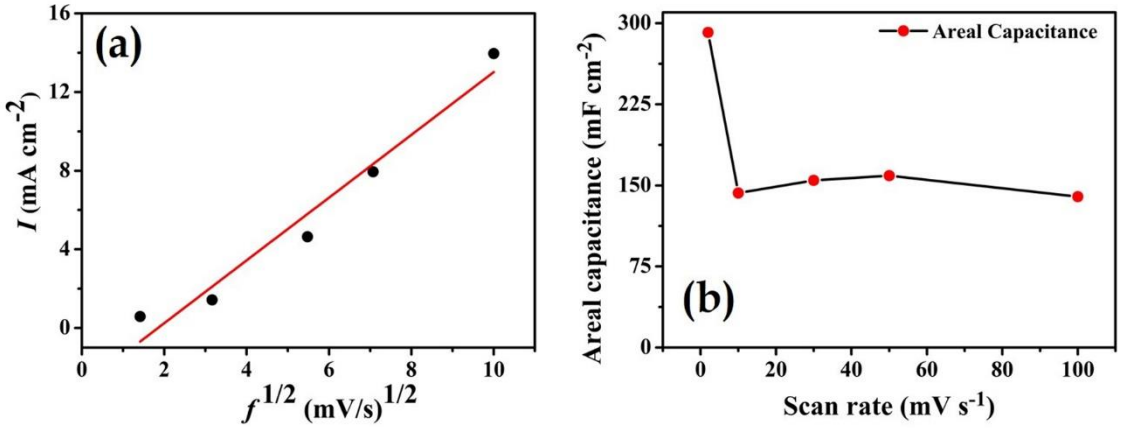


**Figure 5.20**. (a) Peak current (I ) vs. square root of scan rate ( f ) plot for as prepared Fe-Ni/Fe2O3-NiO core/shell HNs electrode, (b) Variation of areal capacitance as a function of scan rate of as prepared Fe-Ni/Fe2O3-NiO core/shell HNs electrode.

Further, electrochemical performance of Fe-Ni/$Fe_2O_3$-NiO core/shell HNs electrodes has been done using gavanostatic charge/discharge (GCD) method by varying the current density (2.5, 5, 10, 25 and 100 A $g^{-1}$). All GCD curves demonstrate nearly symmetric shapes in Fig. 5.19(b), indicating a good supercapacitive behaviour and excellent electrochemical reversibility of as-prepared Fe-Ni/$Fe_2O_3$-NiO core/shell HNs electrode [46]. According to the GCD curves, the calculation of the specific capacitance ($C_{sp}$) of as-prepared Fe-Ni/$Fe_2O_3$-NiO core/shell HNs electrode has been done by using the formula $C_{sp} = (I\,\Delta t)/(m\,\Delta V)$ [17, 34], where $I$ denotes the magnitude of discharge current, $\Delta t$ represents the discharging time, $\Delta V$ stands for the discharging potential window and $m$ indicates the redox active material mass. Fig. 5.19(c) shows the response of the specific capacitance ($C_{sp}$) while varying the value of current density for Fe-Ni/$Fe_2O_3$-NiO core/shell HNs. It is observed from Fig. 5.19 (c) that the maximum specific capacitance of the Fe-Ni/$Fe_2O_3$-NiO core/shell HNs acquired nearly 1415.09 F $g^{-1}$ at low current density (2.5 A $g^{-1}$) and gradually decreases to 966.18 F $g^{-1}$ with the

increase in current density upto 100 A $g^{-1}$ ,these results suggest that the Fe-Ni/$Fe_2O_3$-NiO core/shell HNs have very high rate capability and capacitive retention, which are very desirable properties for the high quality supercapacitors. In addition, Fig. 5.19 (c) also shows the variation of Coulombic efficiency (η =discharge time/charge time) as a function of current densities for Fe-Ni/$Fe_2O_3$-NiO core/shell HNs. It is clear from the Fig. 5.19 (c) that the Coulombic efficiency, decreasing with the increase of current density, which suggest that the ion/charge transfer rate decreases with the current density.

Further, the energy density and power density of the fabricated Fe-Ni/$Fe_2O_3$-NiO core/shell HNs electrode have been calculated according to the following known formulas, Energy density: $E = C_{sp}(\Delta V)^2/2$ and Power density: $P = E/(\Delta t)$, where, $C_{sp}$, $\Delta V$ and $\Delta t$ are denoting the specific capacitance, discharging potential window and total time of discharging, respectively, from their corresponding GDC curves. Fig. 5.19 (d) represents the variation of power density with respect to energy density, which shows the maximum power density (10.3 kW $kg^{-1}$) at lowest energy density (11.5 Wh $kg^{-1}$) of the device. Moreover, the device can have the maximum energy density limit is upto 27.6 Wh $kg^{-1}$ while retaining the lower power density limit (0.6 kW $kg^{-1}$) of the supercapacitor device. The electrochemical performance of as-prepared Fe-Ni/$Fe_2O_3$-NiO core/shell HNs is comparable with some previous reports of transition metal based nanostructure systems [27, 59, 74-79].

It is very important for good quality supercapacitors to posses long cycle life. Fig. 5.21 (a) depicts the long cycle performance test of as-prepared Fe-Ni/$Fe_2O_3$-NiO core/shell HNs electrode by the GCD method for successive 3000 cycles at different current densities (2.5 A $g^{-1}$ and 50 A $g^{-1}$). Nearly 95 % retention is observed after 3000 cycles, which suggest the high stability in long term application of Fe-Ni/$Fe_2O_3$-NiO core/shell HNs electrode. This small decrease in the capacitance after long continuous cycle due to increased internal resistance, which might be the result of the mechanical swelling/shrinking of the electrode during redox reactions. The inset of Fig. 5.21 (a) shows the shape of the last 10 charge/discharge cycle of the long cycle test (3000 cycles) remains almost unchanged (linear and symmetric) for both the

current densities (2.5 A $g^{-1}$ and 50 A $g^{-1}$). Such a good long cycle electrochemical stability of Fe-Ni/$Fe_2O_3$-NiO core/shell HNs electrode, made it a very strong candidate for long cycle supercapacitive applications.

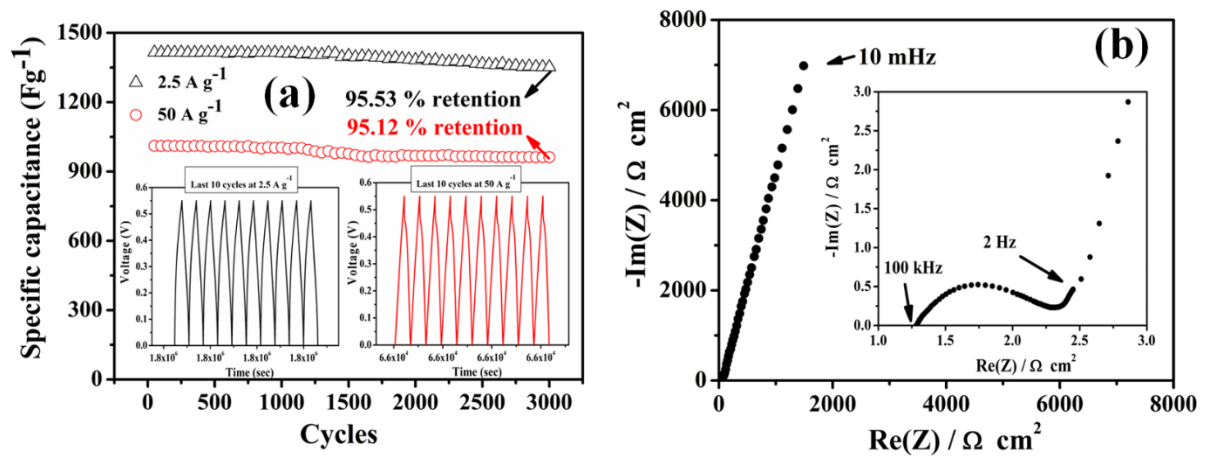


**Figure 5.21 (**a) The long cycle test of Fe-Ni/$Fe_2O_3$-NiO core/shell HNs for 3000 cycles by GCD method, whereas the last 10 GCD plot cycles for current densities 2.5 A $g^{-1}$ (in black ink) and 50 A $g^{-1}$ (in red ink) are shown in the inset (Fig. (a)). (b) the electrochemical impedance spectrum plots at the open circuit potential within ($10^{-2}$ Hz to $10^5$ Hz) frequency range, whereas the inset of (b) shows the magnified EIS spectra at high frequency range for Fe-Ni/$Fe_2O_3$-NiO core/shell HNs elctrodes.

Fig. 5.21 (b) shows the electrochemical impedance spectra of Fe-Ni/$Fe_2O_3$-NiO core/shell HNs electrode. The intercept of the curve in the high frequency region on the real axis and represent the equivalent series resistance ($R_s$) which include (ionic-electronic resistance, intrinsic resistance and contact resistance of the electrode), whereas the semicircle at high frequency range signify the charge transfer resistance ($R_{ct}$) of the electrode. The recoded value of $R_s$ (1.28 Ω $cm^2$) and $R_{ct}$ (1.07 Ω $cm^2$) are very low, which indicate the high electrical conductivity of electrode and rapid ion-charge transport during redox reactions at the contact of electrode-electrolyte. The straight line in the low frequency range denotes the Warburg resistance ($R_w$) which shows the high slope due to the high diffusion rate of ions within the porous surface of the electrode during redox reactions [48, 80, 81].

## 5.4.3. Conclusion

In conclusion, we have illustrated a simple fabrication technique of the Fe-Ni/$Fe_2O_3$-NiO core/shell hybrid nanostructures, which further realized as a high performance supercapacitor electode because of its advantageous structure. This

core-shell hybrid nanostructure consists highly porous shell nanolayer (NiO and $Fe_2O_3$) which provides huge redox active surface for faradaic reactions as well as reduces the distance for ion diffusion process, while the conductive FeNi core provide the highway to accelerate the transport of electrons to the current collector. Due to the advanced structure of this Fe-Ni/$Fe_2O_3$-NiO core/shell hybrid nanostructure electrode, it has provided high value of specific capacitance nearly 1415 F $g^{-1}$. Moreover, it exhibited a very long term cycling stability (which retain nearly 95% of its initial capacitance after successive 3000 charge/discharge cycles) and the low value of equivalent series resistance ($R_s$ = 1.28 Ω $cm^2$). These remarkable electrochemical performances suggest that the Fe-Ni/$Fe_2O_3$-NiO core/shell hybrid nanostructure could be the reliable and promising candidate for the fabrication of next generation supercapacitor electrodes for real life applications.

# 5.5. Hydrogenated NiO Nano-block Architecture for High Performance Supercapacitors

## 5.5.1. Experimental

### 5.5.1.1. Reagents

Copper foil (99.98 % pure, 0.1 mm thick), Nickel sulphate hexahydrate ($NiSO_4.6H_2O$, 99.99 % pure), Boric acid ($H_3BO_3$, 99.9 % pure), Potassium hydroxide (KOH, 99.9 % pure) and Sodium hydroxide (NaOH, 99.9 % pure) were purchased from Sigma-Aldrich. All chemicals were of analytical grade and were used without further purification.

### 5.5.1.2. Synthesis of NiO NBs and hydrogenated NiO (H-NiO) NBs

The high-density 3D architecture of NiO NBs were synthesized by the high-temperature oxidation of the highly rough metallic Ni thin film prepared by the metal substrate assisted electrochemical deposition technique. Software controlled three-electrode electrochemical cell and a power supply (potentiostat AutoLab-30) was used for the electrochemical deposition of Ni thin film. A high-purity Platinum wire and an Ag/AgCl electrode were used as the counter and reference electrodes, respectively. Ni thin film with rough surface was grown on the pure Cu substrate using the aqueous solution of 0.57 M $NiSO_4.6H_2O$, 0.32 M $H_3BO_3$ and 0.15 M $NH_4OH$ as electrolyte at room temperature. Here, boric acid and ammonium hydroxide were used as a buffer to maintain the pH of the electrolyte around 3.5 and also to control the electrodeposition process. The deposition of the Ni thin film was conducted for 30 minutes by using a DC voltage of -0.95 V, following linear sweep voltammetry (LSV) results. The Ni thin film grown on the Cu substrate was finally oxidized to form NiO NBs by heating them at 450°C for 30 minutes in oxygen atmosphere. The H–NiO NBs were obtained by annealing the NiO NBs in hydrogen atmosphere at temperature of 400°C for 20 minutes.

During this process, some portion of the other side of Cu substrate was also oxidized to form a thin layer (~ 12 µm) of CuO. After that, for making the electrical contact, the oxidized portion of Cu substrate was removed carefully by keeping the

other side of the Cu substrate (the side containing NiO NBs) untouched. The NiO and H-NiO film thickness was found to be ~3 μm. The mass of the active electrode material was measured by using a microbalance having an accuracy of 0.1 μg. The loading density of the NiO and H–NiO NBs electrodes were 0.327 and 0.314 mg/cm$^2$, respectively.

## 5.5.2. Results and Discussions

### 5.5.2.1. Morphology, Crystallography and Chemical composition

The scheme of the preparation of the arrays of H– NiO NBs is shown in Fig. 5.22. Deatils of the synthesis and fabrication of H-NiO NBs are given in the experimental section.

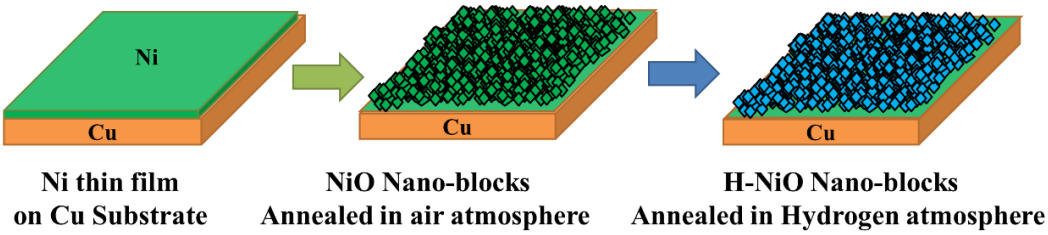


**Figure 5.22.** Schematic of the preparation of NiO and H–NiO NBs electrodes on Cu substrates.

Fig. 5.23 (a) shows the FESEM micrograph of the as-prepared 3D arrays of H–NiO NBs grown on Cu substrate. It is evident from this image that the surface of the as prepared nanostructure is very rough, which can also be seen from the magnified FESEM image (Fig. 5.23 (b)). It is found that the morphology of the as grown NiO NBs remains unchanged after hydrogenation. The 3D structure of the NiO NBs arises during the conversion of the as grown rough Ni thin film into NiO via high temperature oxidation. Fig. 5.23 (a) & (b) clearly demonstrates that the surface area of the as grown 3D NiO NBs is significantly higher. Though the shape and size of the grown NiO nanoblocks are irregular in nature, however, the average dimension of the single NiO nanoblock is found to be around 250 × 200 × 125 nm. The XRD pattern of the as-prepared H–NiO NBs, shown in Fig. 5.23 (c), indicates the polycrystalline nature of the as-grown NBs. The diffraction pattern consists of peaks that correspond to the pure fcc Ni, cubic NiO and also the metallic Cu substrate underneath. The characteristic peaks at 2θ = 37.5, 43.3 and 63.9 degrees in the XRD

pattern represent the (111), (200) and (220) crystalline faces of NiO with cubic texture, respectively [21, 22]. The presence of Ni (200) peak in the XRD pattern is due to the presence of some unoxidized Ni at the deepest portion of the Ni thin film. Fig. 5.23 (d) depicts the EDAX spectrum of the H– NiO NBs, which clearly shows the presence of Ni and O in the NiO, whereas the peak for Cu appears from the substrate.

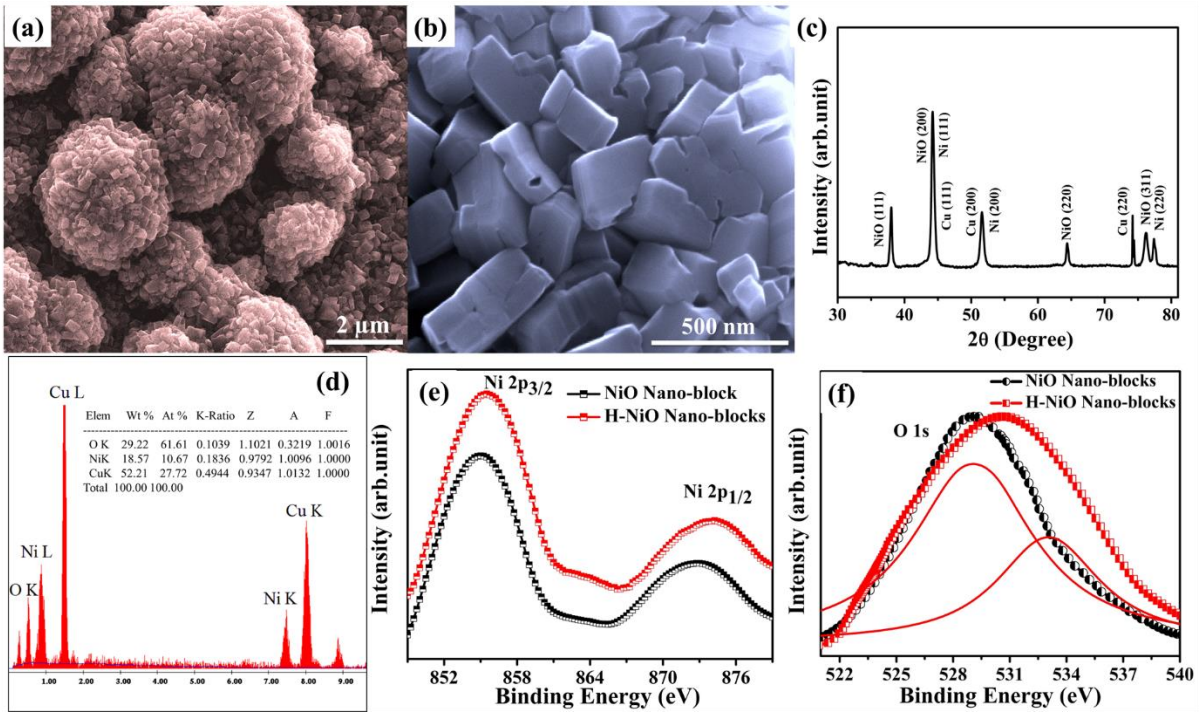


**Figure 5.23.** (a) and (b) FESEM micrographs of the as prepared H– NiO NBs. (c) XRD pattern of the as-prepared H–NiO NBs. (d) EDAX spectrum of the as-prepared H– NiO NBs. The XPS spectra for the (e) Ni 2p and (f) normalized O 1s core level of the as-prepared NiO and H– NiO NBs.

In Fig. 5.23 (e), the XPS core level peaks of H-NiO NBs shows the Ni $2p_{3/2}$ and Ni $2p_{1/2}$ located at 855 and 873.9 eV, respectively, with an energy separation of 18.9 eV, are in good agreement with reported data of Ni $2p_{3/2}$ and Ni $2p_{1/2}$ in NiO, which also confirms that Ni is in +2 oxidation state [21, 23]. Fig. 5.23 (f) shows the O 1s core level spectra of NiO and H– NiO NBs. The O 1s band for H–NiO NBs becomes broader compared with that of the pure NiO NBs. The O 1s band in the H–NiO NBs could be deconvoluted into two peaks located at 529.1 and 533.1eV (see Fig. 5.23 (f)), whereas the pure NiO NBs exhibits a single peak located at 530.7 eV. The low energy peak (at 530.7 eV) can be ascribed to the formation of O–Ni bond in NiO [21, 23], whereas the peak at higher binding energy (at 533.1 eV) is attributed to the Ni-

OH bond [21, 27]. XPS studies confirm the incorporation of hydroxyl groups on the surface and the subsurface region of the NiO NBs through hydrogenation.

#### 5.5.2.2. Electrochemical Analysis

Fig. 5.24 (a) and (b) show the CV measurement curves of the two electrodes at different scan rates ranging between 5 to 100 $mVs^{-1}$ within the voltage window of 0 to 0.6 V at room temperature. The shape of the CV curves of both the electrodes clearly reveals the pseudocapacitive behaviour of the electrodes which is totally different from the double layer capacitors. CV curves shows one strong redox peak (one oxidation and one reduction peaks) at every scan rates which are corresponding to the surface oxidation/reduction reactions as shown in the redox reaction given below [25]. The redox peaks show the Faradaic pseudocapacitive property based on the surface redox mechanism of $Ni^{2+}$ to $Ni^{3+}$, via following redox reaction: $NiO + OH^- \leftrightarrow NiOOH + e^-$ and $Ni(OH)_2 + OH^- \leftrightarrow NiOOH + H_2O + e^-$. In addition, because of the very high surface area and the fast ionic/electronic diffusion rate during the Faradic redox reaction at the surface, both the NiO and H– NiO NBs electrodes show very prominent electrochemical properties as supercapacitor [26, 33]. With the increase of scan rate, the potential and the current at the oxidation/reduction peaks shifted more towards the positive and negative axes, respectively due to an increase of the internal diffusion resistance within the pseudoactive material with an increase in scan rate [82, 83].

Furthermore, the oxidation and reduction peaks of the NiO NBs electrode are nearly symmetrical throughout the scan range 5–100 mV $s^{-1}$, indicating reversibility of redox reaction at the electrode surface [28]. But the redox peaks of H-NiO NBs electrode are asymmetric in nature; though it exhibits higher capacitive behaviour as evident from the higher area (Fig. 5.24 (c)) under their corresponding CV curves as compare to CV curves of NiO NBs electrodes. Fig. 5.24 (c) shows a 2.5 times enhancement in the current density in the CV curve of the H–NiO NBs electrode in comparison with the pure NiO NBs electrode at the scan rate of 100 mV $s^{-1}$. The calculated areal ($C_a$, mF $cm^{-2}$) and specific ($C_{sp}$, F $g^{-1}$) capacitance of both the electrodes as a function of scan rate are shown in Fig. 5.24 (d). The $C_a$ and $C_{sp}$ of the NiO NBs based electrodes are calculated using the equations (5.2) and (5.3). The

value of the $C_a$ and $C_{sp}$ for NiO NBs electrode are found to be 208.2 mF $cm^{-2}$ and 864.65 F $g^{-1}$, respectively at a scan rate of 5 $mVs^{-1}$. Whereas, the $C_a$ and $C_{sp}$ of H-NiO NBs electrode have been found to increase significantly to the values 371.8 mF $cm^{-2}$ and 1271.93 F $g^{-1}$, respectively at the scan rate of 5 mV $s^{-1}$, after the hydrogenation treatment.

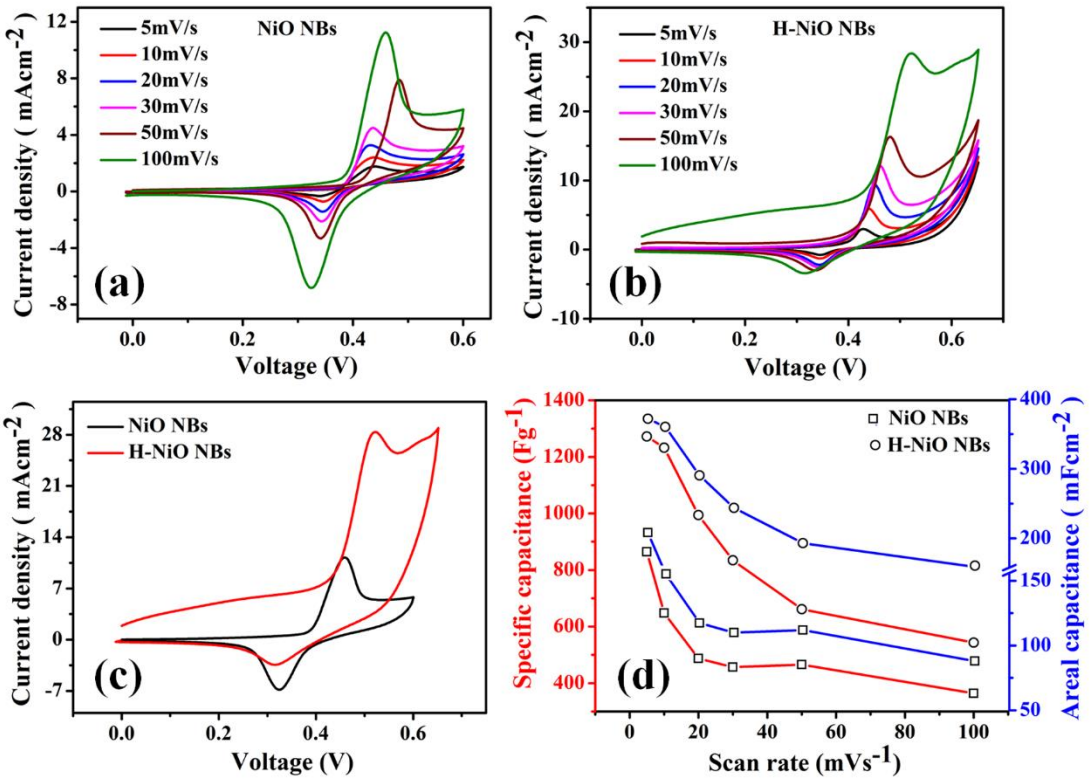


**Figure 5.24.** Cyclic voltammetry curves of the as-prepared (a) pure NiO and (b) H– NiO NBs electrode at different scan rates in a 1 M KOH solution at room temperature. (c) Comparison between the CV curves of pure NiO and H– NiO NBs at scan rate of 100 $mVs^{-1}$. (d) Variation of specific and areal capacitance as a function of scan rate of pure NiO and H–NiO NBs electrodes.

The noteworthy enhancement of the supercapacitive property of the H−NiO NBs electrode is due to the absorption of hydroxyl group on the surface of the NiO NBs having large surface area with high stability. Here, the value of specific capacitance for H-NiO NBs is found to be remarkably higher than that of the other reported NiO based supercapacitors like, thin films of NiO (~ 309 $Fg^{-1}$) [21], Mesoporous NiO Nanotubes (~409 $Fg^{-1}$) [22], nanoball-like NiOx (~951 $Fg^{-1}$) [27], NiO-$TiO_2$ Nanotube Arrays (~300 $Fg^{-1}$) [28], NiO Nanotubes (~266 $Fg^{-1}$) [36], NiO Nanocolumns (~ 390 $Fg^{-1}$) [37], hierarchical spherical porous NiO (~710 $Fg^{-1}$) [38], Ni–NiO core–shell (~128 & 149 $Fg^{-1}$) [39, 40], NiO/$Co_2O_3$ core/shell NWs (~835 $Fg^{-1}$)

[41], Monolithic NiO/Ni Nanocomposites (~905 $Fg^{-1}$) [42]. As shown in Fig. 5.24 (d), the values of $C_a$ and $C_{sp}$ decrease for both the electrodes with the increase of scan rate, this is because of the limitation of reaction kinetics at the electrodes [43]. The value of $C_{sp}$ of the H-NiO and NiO NBs drops from 1271.93 to 543.63 F $g^{-1}$ and 864.65 to 363.83 F $g^{-1}$, respectively with the increase of the scan rate. In addition, the value of $C_a$ also drops from 371.8 to 159 mF $cm^{-2}$ and 208.2 to 88 mF $cm^{-2}$ for H-NiO and NiO NBs, respectively when the scan rate increases from 5 to 100 mV $s^{-1}$.

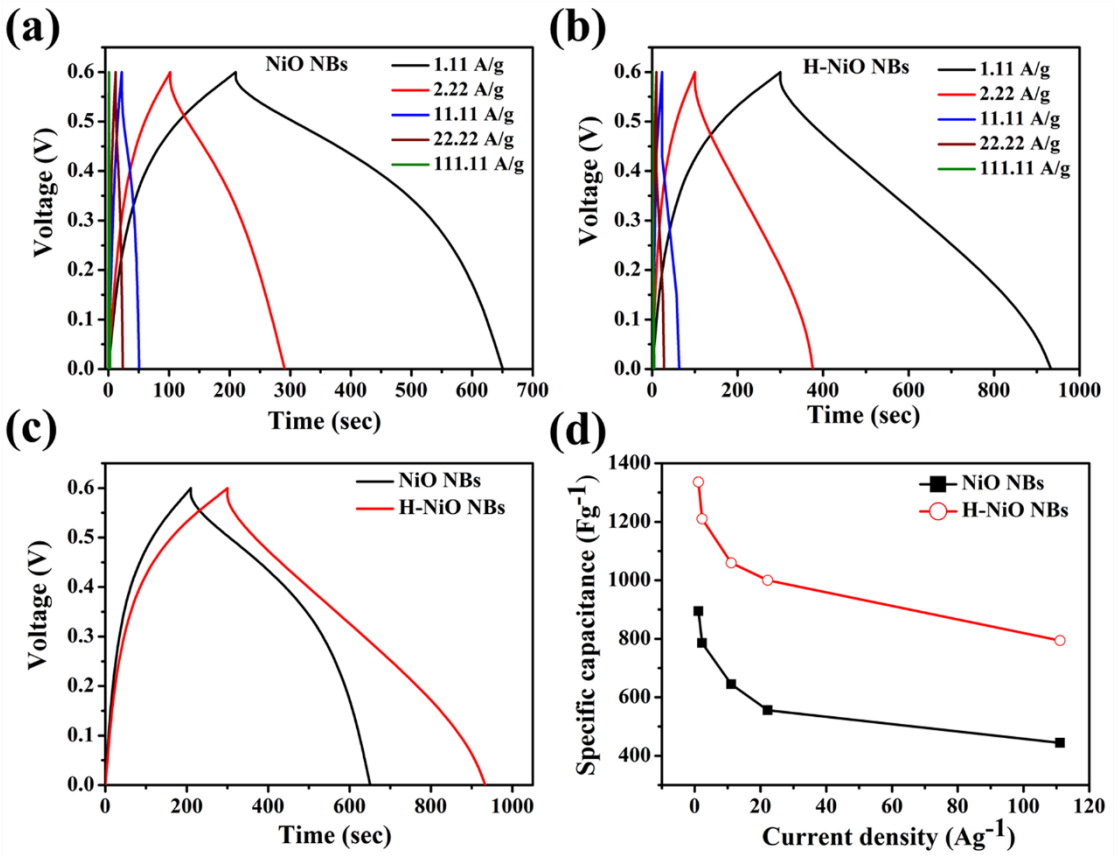


**Figure 5.25.** Constant current charge/discharge curves of the as-prepared (a) pure NiO and (b) H–NiO NBs electrodes at different current density. (c) Comparison between the charge/discharge curves of the pure NiO and H–NiO NBs electrodes at a current density of 1.11 A $g^{-1}$. (d) Variation of the specific capacitance of the electrodes as a function of current density.

The galvanostatic charge/discharge tests of the electrodes performed within a stable potential window of 0 – 0.6 V under different charge/discharge current densities ranging between 1.11 to 111.11 A $g^{-1}$ are shown in Fig. 5.25 (a) and (b), to demonstrate the improved supercapacitive performance of the electrodes. The potential-time plots exhibiting asymmetric charge/discharge profiles for both NiO and H-NiO NBs electrodes, characterized by slow discharging process as compare to

the charging, even at the high current density of 111.11 A $g^{-1}$. This slow rate of discharging exhibits higher coulombic efficiency (>100 %) for both type of electrodes, which can be explained by the redox reaction equation. In discharging process only a part of NiOOH gains electron and is reduced into NiO, while in charging process NiO loses electron and is completely oxidized into NiOOH. Since, NiOOH is partially converted into NiO during reduction, the unconverted NiOOH holds the electrons during discharging and thus the discharging takes longer time [84]. Fig. 5.25 (c) showing the enhancement in the discharging time of H–NiO NBs electrode over NiO NBs electrode at the current density of 1.11 A $g^{-1}$, indicates the enhanced pseudocapacitance behaviour of NiO NBs electrode after hydrogenation. The variation of $C_{sp}$ of both the electrodes is shown in Fig. 5.25 (d) as a function of current density. The values of $C_{sp}$ are calculated from the charging/discharging curves using the equation (5.4) [85].

The values of $C_{sp}$ are 1336.18 and 895.05 F $g^{-1}$ for H–NiO and NiO NBs electrodes, respectively at the low current density of 1.11 $Ag^{-1}$. There is decrement observed with the increase of current density in the specific capacitance although after certain current densities this decrement gets saturated at higher current densities. Nearly 61% and 49% specific capacity retention have been observed in H–NiO and NiO NBs electrode, respectively at a higher current density of 111.11 A $g^{-1}$. At lower current densities, ions can penetrate into the inner-structure of electrode materials, having access to almost all available pores of the electrode, but at higher current densities, an effective utilization of the material is limited only to the outer surface of the electrodes. This results in the reduction of the values of specific capacitance at higher current densities. At current densities above 2.22 A $g^{-1}$, specific capacitance tends to stabilize. This higher value of retention in the specific capacitance of the electrodes indicates the relatively good high-rate capability of these electrodes. Impressively, in case of charging/discharging process the capacitance retention of the electrodes is found much higher than that observed from the CV analysis. This is because of the fact that the ion and electron have more time to diffuse through the rough surface of the electrode during the redox reaction [86].

The energy ($E$) and the specific power ($P$) density of both the electrodes are calculated by using the equations (5.6) and (5.7). Fig. 5.26 (a) shows that the energy density of H–NiO and NiO NBs electrode decreases from 52.13 to 13.51 Wh $kg^{-1}$ and 37.56 to 12.49 Wh $kg^{-1}$, respectively, whereas the power density for the same increases from 0.28 to 19.44 kW $kg^{-1}$ and 0.31 to 24.4 kW $kg^{-1}$, respectively as the discharge current density increased from 1.11 A $g^{-1}$ to 111.11 A $g^{-1}$. This indicates the potential of the electrodes for application in electrochemical supercapacitors. The above mentioned values of energy and power density of both the electrodes are better than many other NiO based electrodes reported previously [22, 27, 28, 37, 39].

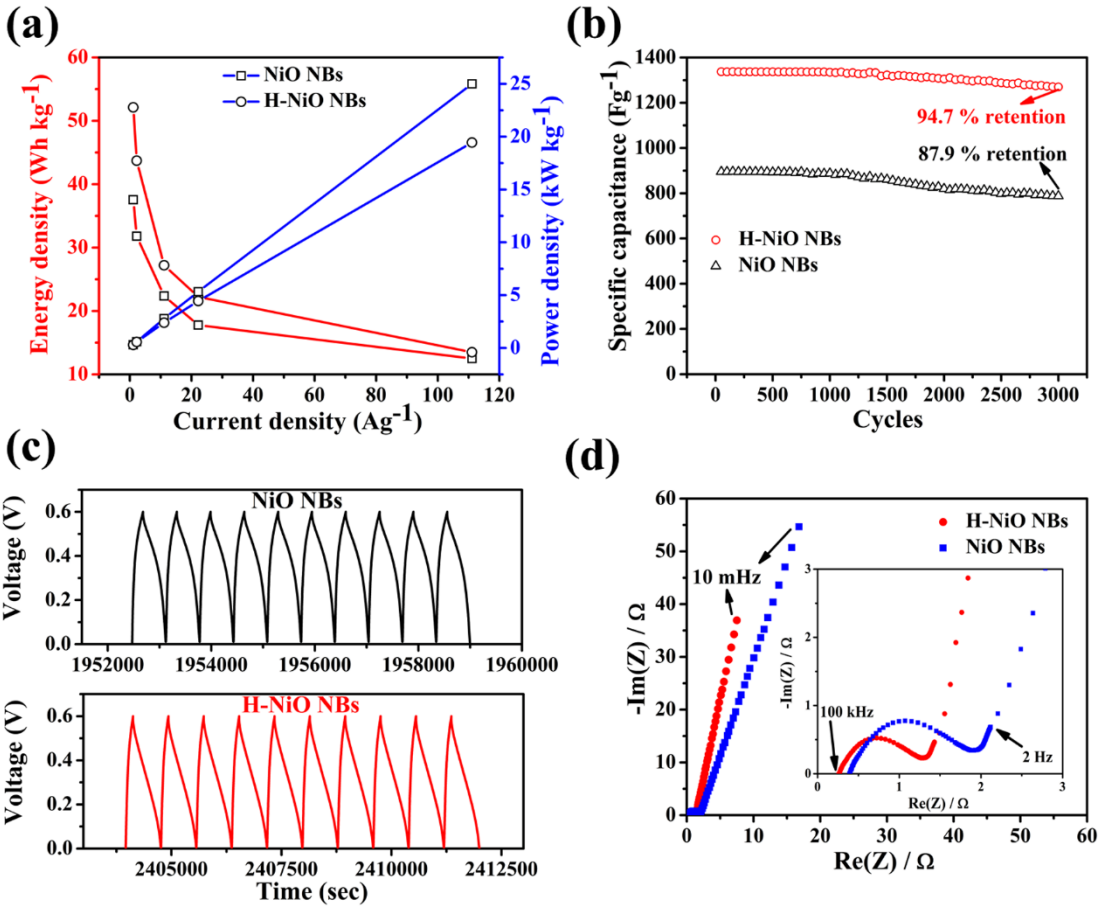


**Figure 5.26** (a) Variation of energy and power densities with charge/discharge current densities for NiO and H– NiO NBs electrodes. (b) The cycling performance of both NiO and H– NiO NBs electrodes showing the capacitance retention after 3000 cycles using a charge/discharge current density of 1.11 A $g^{-1}$. (c) The last 10 cycles of the galvanostatic charge/discharge curves of NiO and H– NiO NBs electrodes. (d) Electrochemical impedance spectroscopy (Nyquist) plots for the supercapacitors based on NiO and H–NiO NBs electrodes. The inset of (c) shows the Nyquist plot of both the electrodes at high frequency range.

The cyclic performance of both the NBs electrodes, which includes cycling life and specific capacitance retention of the supercapacitors are shown in Fig. 5.26 (b) tested over 3000 cycles, carried out at a current density of 1.11 A $g^{-1}$. The capacitance loss of H–NiO and NiO NBs electrodes after 3000 cycles is about 5.3 and 12.1 %, which are found to be better than that of the previously reported NiO based supercapacitors. Here, NiO NBs electrodes exhibit better cyclability compared with the H–NiO NBs. However, both the electrodes exhibit good long term electrochemical stability and high stable specific capacitance retention after a long cycle test in KOH solution, which are very important requirements for supercapacitors. Fig. 5.26 (c) shows the shapes of the last 10 cycles obtained from the cycling tests for both the electrodes remains almost unchanged during the cycles.

The electrical conductivity and ion transfer of the supercapacitor electrodes has been investigated by electrochemical impedance spectroscopy (EIS). Fig. 5.26 (d) shows the Nyquist impedance plots for the H–NiO and NiO NBs pseudocapacitors. EIS has been carried out in 1 M KOH solution within a frequency range of 0.1–$10^5$ Hz at amplitude of 10 mV versus the open circuit potential. The EIS spectra are divided into three distinct regions based on the order of decreasing frequencies. The slope of the EIS curve in the low frequency range reflects the Warburg resistance, which describes the diffusion rate of redox material in the electrolyte. The higher value of slope indicating the higher diffusion rate, describes the high diffusion of H–NiO over NiO NBs into the electrolyte [48]. The phase angle of the impedance plot of the H–NiO and NiO NBs electrodes found to be higher than 45° in the low frequencies suggests that the electrochemical capacitive behavior of both the electrodes is controlled by diffusion process. The shorter line at lower frequency correlates to the shorter variations in ion diffusion path and easier movement of the ions in the pores. The diameter of semicircle in the high frequency range represents the charge transfer resistance ($R_{ct}$) of the electrode material resulting from the diffusion of electrons. Here, the value of $R_{ct}$ for H–NiO electrode (1.02 Ω) is smaller than that of the NiO electrode (1.51 Ω), which indicates that H–NiO NBs are ideal for fast ion and electron transport, because the large diameter semicircle reflects larger charge-transfer resistance value. The intercept on the real axis in the high frequency range provides

the equivalent series resistance (ESR), which includes the bulk resistance of the electrolyte the inherent resistances of the electrode active material and the contact resistance at the interface between electrolyte and electrode [47]. The value of ESR calculated for H–NiO and NiO NBs electrodes are 0.263 and 0.389 Ω, respectively, which suggests higher electrical conductivity of H–NiO over NiO NBs electrode. These studies indicate that the H–NiO NBs electrode has low ion diffusion resistance, which can be attributed to the incorporation of hydroxyl groups on the surface of NiO NBs after hydroganetion.

### 5.5.3. Conclusion

In summary, large surface area electrodes made of 3D architecture of NiO and H–NiO nano-blocks have been successfully fabricated by the controlled electrodeposition followed by high temperature thermal treatment of the Ni thin film grown on the Cu substrate. Both the electrodes have been demonstrated based on their electrochemical performance as supercapacitor, where the H–NiO NBs exhibit remarkably superior pseudocapacitive performance. It has been found that the incorporation of hydroxyl groups on the surface/subsurface of NiO NBs through hydrogenation improving the electrochemical activity of the H–NiO NBs electrode as pseudocapacitor. In addition, H–NiO NBs serve as the ideal pathway for fast ion/electron diffusion, whereas the conductive Ni and Cu layer at the underneath work as the efficient current collector. The H–NiO NBs electrode exhibits high specific capacitance (1272 F $g^{-1}$), energy density (52.13 Wh $kg^{-1}$), power density (19.44 kW $kg^{-1}$) and excellent cycling stability (only 5.3% loss of its initial specific capacitance after 3000 cycles at current density of 1.1 A $g^{-1}$). H–NiO NBs electrode also exhibits excellent rate capability, where nearly 61% specific capacity retention has been found when the current density increases from 1.11 to 111.11 $Ag^{-1}$. Here, an easy and low cost fabrication technique of the surface modified unique nano-architecture has been demonstrated, which could remarkably improve the electrochemical performance of this type of transition metal oxide based electrodes for a new class of high-performance materials for pseudocapacitors.

## Bibliography


[1] P. Simon and Y. Gogotsi, *Nat. Mater.*, **7**, 845 (2008).

[2] J. R. Miller and P. Simon, *Science,* **321**, 651 (2008).

[3] Z. Chen, V. Augustyn, J. Wen, Y. Zhang, M. Shen, B. Dunn and Y. Lu, *Adv. Mat.,* **23**, 791 (2011).

[4] L. Bao, J. Zang and X. Li, *Nano Lett.* **11**, 1215 (2011).

[5] Z. Tang, C. H. Tang and H. Gong, *Adv. Funct. Mater.* **22**, 1272 (2012).

[6] Z. B. Lei, L. Lu and X. S. Zhao, *Energy Environ. Sci.* **5**, 6391 (2012).

[7] S. Chen, J. Zhu, X. Wu, Q. Han and X. Wang, *ACS Nano* **4**, 2822 (2010).

[8] C. Yuan, L. Yang, L. Hou, J. Li, Y. Sun, X. Zhang, L. Shen, X. Lu, S. Xiong and X. W. Lou, *Adv. Funct. Mater.* **22**, 2560 (2012).

[9] W. Chen, R. B. Rakhi, L. B. Hu, X. Xie, Y. Cui and H. N. Alshareef, *Nano Lett.* **11(12)**, 5165 (2011).

[10] R. B. Rakhi, W. Chen, D. Cha and H. N. Alshareef, *Adv. Energy Mater.* **2(3)**, 381 (2012).

[11] D. D. Zhao, W. J. Zhou and H. L. Li, *Chem. Mater.* **19**, 3882 (2007).

[12] G. W. Yang, C. L. Xu and H. L. Li, *Chem. Commun.* **48**, 6537 (2008).

[13] R. Li, X. Ren, F. Zhang, C. Du and J. Liu, *Chem. Commun.* **48**, 5010 (2012).

[14] T. Wei, C. Chen, H. Chien, S. Lu and C. Hu, *Adv. Mater.* **22**, 347 (2010).

[15] J. Liu, J. Jiang, C. Cheng, H. Li, J. Zhang, H. Gong and H. J. Fan, *Adv. Mater.* **23**, 2076 (2011).

[16] L. Yu, G. Zhang, C. Yuan and X. W. Lou, *Chem. Commun.* **49**, 137 (2013).

[17] D. Sarkar, G. G. Khan, A. K. Singh and K. Mandal, *J. Phys. Chem. C* **117**, 15523 (2013).

[18] Y. B. He, G. R. Li, Z. L. Wang, C. Y. Su and Y. X. Tong, *Energy Environ. Sci*. **4**, 1288 (2011).

[19] X. Xia, J. Tu, Y. Zhang, X. Wang, C. Gu, X. Zhao and H. J. Fan, *ACS Nano* **6 (6)**, 5531 (2012).

[20] J. Sarkar, G.G. Khan and A. Basumallick, *Bulletin of Materials Science*, **30**, 27 (2007).

[21] K. Liang, X. Tang and W. Hu, *J. Mater. Chem.*, **22**, 11062 (2012).

[22] S. Xiong, C. Yuan, X. Zhangb and Y. Qiana, *Cryst. Eng. Comm*, **13**, 626 (2011).

[23] C. D. Wager, W. M. Riggs, L. E. Davis, J. F. Moulder and G. E. Muilengerg, *Handbook of X-ray photoelectron spectroscopy*, Perkin-Elmer Corporation: Eden Prairie Minnesota, 1979.

[24] T. L. Barr, *J. Phys. Chem.*, **82**, 1801 (1978).

[25] S.R. Ovshinsky, M. A. Fetcenko and J. Ross, *Science*, **260**, 176 (1993).

[26] D. C. Wang, W. B. Ni, H. Pang, Q. Y. Lu, Z. J. Huang and J. W. Zhao, *Electrochim. Acta*, **55**, 6830 (2010).

[27] X. Tian, C. Cheng, L. Qian, B. Zheng, H. Yuan, S. Xie, D. Xiao and M. M. F. Choi, *J. Mater. Chem.*, **22**, 8029 (2012).
[28] J. H. Kim, K. Zhu, Y. Yan, C. L. Perkins and A. J. Frank, *Nano Lett.*, **10**, 4099 (2010).
[29] X. Lu, G. Wang, T. Zhai, M. Yu, J. Gan, Y. Tong and Y. Li, *Nano Lett.*, **12**, 1690 (2012).
[30] X. Z. Fan, Y. H. Lu, H. B. Xu, X. F. Kong and J. Wang, *J. Mater. Chem.*, **21**, 18753 (2011).
[31] H. Oda, A. Yamashita, S. Minoura, M. Okamotoa and T. Morimoto, *J. Power Sources*, **158**, 1510 (2006).
[32] D. Choi, G. E. Blomgren and P. N. Kumta, *Adv. Mater.*, **18**, 1178 (2006).
[33] C. Masarapu, H. F. Zeng, K. H. Hung and B. Q. Wei, *ACS Nano*, **3**, 2199 (2009).
[34] R. B. Rakhi, W. Chen, D. Cha and H. N. Alshareef, *Nano Lett.*, **12**, 2559 (2012).
[35] J. Yan, E. Khoo, A. Sumboja and P. S. Lee, *ACS Nano*, **4**, 4247 (2010).
[36] J. Xu, L. Gao, J. Cao, W. Wang and Z. Chen, *J Solid State Electrochem*, **15**, 2005 (2011).
[37] X. Zhang, W. Shi, J. Zhu, W. Zhao, J. Ma, S. Mhaisalkar, T. L. Maria, Y. Yang, H. Zhang, H. H. Hng and Q. Yan, *Nano Res.*, **3**, 643 (2010).
[38] C. Yuan, X. Zhang, L. Su, B. Gao and L. Shen, *J. Mater. Chem.*, **19**, 5772 (2009).
[39] J. H. Kim, S. H. Kang, K. Zhu, J. Y. Kim, N. R. Neale and A. J. Frank, *Chem. Commun.*, **47**, 5214 (2011).
[40] J. Y. Kim, S. H. Lee, Y. Yan, J. Oh and K. Zhu, *RSC Advances*, **2**, 8281 (2012).
[41] X. Xia, J. Tu, Y. Zhang, X. Wang, C. Gu, X. B. Zhao and H. J. Fan, *ACS Nano*, **6**, 5531 (2012).
[42] Q. Lu, M. W. Lattanzi, Y. Chen, X. Kou, W. Li, X. Fan, K. M. Unruh, J. G. Chen and J. Q. Xiao, *Angew. Chem. Int. Ed.*, **50**, 6847 (2011).
[43] K. W. Nam and K. B. Kim, *J. Electrochem. Soc.*, **149**, A346 (2002).
[44] C. Yuan, J. Li, L. Hou, X. Zhang, L. Shen and X. W. Lou, *Adv. Funct. Mater.*, **22**, 4592 (2012).
[45] D. Wang, Y. Li, Q. Wang and T. Wang, *J. Solid State Electrochem.*, **16**, 2095 (2012).
[46] J. Zhang, L. B. Kong, J. J. Cai, H. Li, Y. C. Luo and L. Kang, *Microporous Mesoporous Mater.*, **132**, 154 (2010).
[47] J.M. Luo, B. Gao and X.G. Zhang, *Mater. Res. Bull.*, **43**, 1119 (2008).
[48] L. Mai, H. Li, Y. Zhao, L. Xu, X. Xu, Y. Luo, Z. Zhang, W. Ke, C. Niu and Q. Zhang, *Sci. Rep.*, **3**, 1718 (2013).
[49] G. Zhang, and X. W. Lou, *Sci. Rep.* **3**, 1470 (2013).
[50] G. Guo, L. Huang, Q. Chang, L. Ji, Y. Liu, Y. Xie, W. Shi, and N. Jia, *Appl. Phys. Lett.* **99**, 083111 (2011).

[51] J. Du, G. Zhou, H. Zhang, C. Cheng, J. Ma, W. Wei, L. Chen, and T. Wang, *ACS Appl. Mater. Interfaces* **5**, 7405 (2013).

[52] F. Yang, J. Yao, F. Liu, H. He, M. Zhou, P. Xiao, and Y. Zhang, *J. Mater. Chem. A* **1**, 594 (2013).

[53] G. Hu, C. Tang, C. Li, H. Li, Y. Wang, and H Gong, *J. Electrochem. Soc.* **158**, A695 (2011).

[54] M. Yang, J. X. Li, H. H. Li, L.W. Su, J. P. Wei, and Z. Zhou, *Phys. Chem. Chem. Phys.* **14**, 11048 (2012).

[55] L. Yang, S. Cheng, Y. Ding, X. Zhu, Z. L. Wang, and M. Liu, *Nano Lett.* **12**, 321 (2012).

[56] G. Q. Zhang, H. B. Wu, H. E. Hoster, M. B. Chan-Park, and X. W. Lou, *Energy Environ. Sci.* **5**, 9453 (2012).

[57] H. Jiang, J. Mab, and C. Li, *Chem. Commun.* **48**, 4465 (2012).

[58] H. L. Wang, Q. M. Gao, and L. Jiang, *Small* **7**, 2454 (2011).

[59] B. Wang , J. S. Chen , Z. Wang , S. Madhavi, and X. W. Lou, *Adv. Energy Mater.* **2**, 1188 (2012).

[60] H. L. Wang, H. S. Casalongue, Y. Y. Liang, and H. J. Dai, *J. Am. Chem. Soc.* **132**, 7472 (2010).

[61] X. H. Xia, J. P. Tu, Y. J. Mai, X. L. Wang, and C. D. Gu, *J. Mater.Chem.* **21**, 9319 (2011).

[62] J. Jiang, J. P. Liu, R. M. Ding, J. H. Zhu, Y. Y. Li, A. Z. Hu, X. Li, and X. T. Huang, *ACS Appl. Mater. Interfaces* **3**, 99 (2011).

[63] G. G. Khan, A. K. Singh and K. Mandal, *J. Lumin.* **134**, 772 (2013).

[64] A. K. Singh, D. Sarkar, G. G. Khan and K. Mandal, *Appl. Phys. Lett.* **104**, 133904 (2014).

[65] D. Sarkar, G. G. Khan, A. K. Singh and K. Mandal, *J. Phys. Chem. C* **116**, 23540 (2012).

[66] C. R. Brundle, T. J. Chuang and D. W. Rice, *Surf. Sci.* **60**, 286 (1976).

[67] J. G. Kim, D. Pugmire, D. Battaglia and M. Langell, *Appl. Surf. Sci.* **165**,70 (2000).

[68] C. Yuan, J. Li, L. Hou, X. Zhang, L. Shen and X. W. Lou, *Adv. Funct. Mater.* **22**, 4592 (2012).

[69] D. Wang, Y. Li, Q. Wang and T. Wang, *J. Solid State Electrochem.* **16**, 2095 (2012).

[70] J. Yan, E. Khoo, A. Sumboja and P. S. Lee, *ACS Nano* **4**, 4247 (2010).

[71] M. Salari, S. H. Aboutalebi, K. Konstantinov and H. K. Liu, *Phys. Chem. Chem. Phys.* **13**, 5038 (2011).

[72] W. Xiao, H. Xia, J. Y. H. Fuh and L. Lu, *J. Electrochem. Soc.* **156**, A627 (2009).

[73] J. Liu, J. Jiang, M. Bosman and H. J. Fan, *J. Mater. Chem.* **22**, 2419 (2012).

[74] K. Xie, J. Li, Y. Lai, W. Lu, Z. Zhang, Y. Liu, L. Zhou and H. Huang, *Electrochem. Commun.* **13**, 657 (2011).

[75] P.M. Kulal, D.P. Dubal, C.D. Lokhande and V. J. Fulari, *J. Alloys Compd.* **509**, 2567 (2011).

[76] G. Binitha, M. S. Soumya, A. A. Madhavan, P. Praveen, A. Balakrishnan, K. R. V. Subramanian, M. V. Reddy, S. V. Nair, A. S. Nair and N**.** Sivakumar, *J. Mater. Chem. A* **1,** 11698 (2013).

[77] S. Shivakumara, T. R. Penki and N. Munichandraiah, *J Solid State Electrochem.* **18**, 1057 (2014).

[78] S. Kim, J. Lee, H. Ahn, H. Song and J. Jang, *ACS Appl. Mater. Interfaces,* **5**, 1596 (2013).

[79] S. Vijayakumar, S. Nagamuthu and G. Muralidharan, *ACS Appl. Mater. Interfaces,* **5**, 2188 (2013).

[80] J. P. Liu, J. Jiang, C. W. Cheng, H. X. Li, J. X. Zhang, H. Gong and H. J. Fan, *Adv. Mater.* **23**, 2076 (2011).

[81] A. K. Singh, D. Sarkar, G. G. Khan and K. Mandal, *ACS Appl. Mater. Interfaces* **6**, 4684 (2014).

[82] U. M. Patil, K. V. Gurav, V. J. Fulari, C. D. Lokhande and O. S. Joo, *J. Power Sources*, **188**, 338 (2009).

[83] Q. D. Wu, X. P. Gao, G. R. Li, G. L. Pan, T. Y. Yan and H. Y. Zhu, *J. Phys. Chem. C* **111**, 17082 (2007).

[84] C. Zhao, W. Zheng, X. Wang, H. Zhang, X. Cui and H. Wang, *Sci. Rep.* **3**, 2986 (2013).

[85] S. K. Meher, P. Justin and G. R. Rao, *ACS Appl. Mater. Interfaces* **3**, 2063 (2011).

[86] R. K. Selvan, C. O. Augustin, L. J. Berchmans and R. Saraswathi, *Mater. Res. Bull.* **38**, 41 (2003).

# Chapter 6 Conclusion and Scope of Future Work

In this chapter, the conclusion of whole thesis work and the scope of future work has pointed out.

## 6.1. Conclusion

This thesis contains the details about the fabrication of anodic aluminum oxide (AAO) templates by two-step anodization technique and transition metal based ordered nanostructures (nanowires, nanotubes, core-shell heterostructures) by the electrodeposition technique with the help of self-engineered anodic aluminum oxide (AAO) template. Further, their structural, morphological, magnetic and electrochemical properties have been studied in details.

We have been successfully fabricated the AAO templates through the controlled electrochemical anodization of aluminium foil by using oxalic, phosphoric and sulfuric acid electrolyte solution. We have standardized the pore size distribution and inter-pore distance of AAO templates with anodizing voltage. The morphology of the templates has been investigated by SEM. The crystallographic analysis shows that the AAO templates are non-crystalline in nature. The in-depth structural information of the templates has been obtained by the TEM study. It has been found that all the AAO templates exhibit PL emission in the visible blue wavelength region. Herein, the luminescence mechanism of the template synthesized by using oxalic, phosphoric and sulfuric acid electrolyte for different anodization time duration has been explained based on their structural characteristics obtained by the XRD and TEM studies. The studies show that the noncrystalline AAO templates contain a large proportion of structural defects. The in depth PL investigation has shown that the singly ionized oxygen vacancy related defect centers (F+ centers) take the major responsibility behind the light emission characteristics of the AAO templates, whereas, the luminescent centers transformed from acidic impurities have little contribution to the PL emission spectra. From magnetic measurements it is observed that the AAO membrane has a week diamagnetic property. Further, these AAO templates have been used as a host for the fabrication of transition metal based ordered nanostructures (nanowires, nanotubes, and core-shell heterostructures) by electrodeposition technique.

We have prepared the arrays of Ni nanowires by electrodeposition technique, each nanowire with diameter~100nm, were irradiated with different doses of α-particles. We have studied their structural, morphological and crystalline properties.

Irradiation produces pinning centres within the nanowires and results in increase in coercivity. Irradiation also reduces crystallinity of the nanowires and hence magnetocrystalline anisotropy. As a result, magnetic easy axis changes from perpendicular (in-plane) direction to the parallel (out-of-plane) direction with respect to the axial direction of nanowires. We observed that alpha particle irradiation is a useful tool to change the magnetic properties of the nanowires as per need. We have also prepared permalloy ($Fe_{20}Ni_{80}$) nanowires with an average diameter of ~200 nm in the pores of the self-engineered anodized aluminium oxide (AAO) templates by electrodeposition technique. By varying the length from 1.5 to 7.5 μm, got corresponding changes in aspect ratio from 7.5 to 37.5. Structural and magnetic studies of these nanowires have been done in details. Temperature and aspect ratio dependent in-plane and out-of-plane magnetic measurements of the permalloy nanowires indicate the magnetic easy axis of the nanowires along their axial direction, which is very desirable in magnetic recording device applications. Similarly, we have prepared arrays of $Co_{50}Ni_{50}$ alloy nanotubes with the diameter of ~100 nm by electrodeposition technique. By varying the length, we got corresponding changes in aspect ratio from 15 to 120. We have studied their structural, morphological and crystalline properties. The magnetic studies suggest that the magnetic easy axis direction of $Co_{50}Ni_{50}$ alloy nanotubes changes from a perpendicular direction to the axial direction of nanotubes with the increase in aspect ratio from 15 to 120.

At last, we have also prepared some transition metal based core/shell hybrid nanostructures (Ni/NiO core/shell nano-heterostructures) by controlled oxidation of as-prepared transition metal based nanostructures (such as Ni nanowires). We have studied their structural, morphological, crystalline properties in details. Further, we have studied their electrochemical properties and found their technological application in supercapacitor electrodes as active electrode material. The highly porous nanolayer of NiO serves as the large platform for ion diffusion whereas the conductive Ni core provides the highway for fast transport of electrons to the current collector. The specific capacitance, cycle life, energy density and power density demonstrating the superior performance of the Ni/NiO core/shell nano-

heterostructures as supercapacitor electrode material. Further, electrical conductivity of supercapacitor electrode material (NiO) improved by hydrogenation process and introducing impurities via doping of one metal oxide material with other metal oxide material. The resultant products (H-Ni/NiO, Fe-Ni/$Fe_2O_3$-NiO and Co-Ni/$Co_3O_4$-NiO core/shell nano-heterostructures) exhibit enhanced electrochemical performance as a supercapacitor electrode materials.

## 6.2. Scope of future work

One can tightly control the structural parameter (diameter, density, and aspect ratio of pores, and even internal pore structures) of the anodic aluminum oxide (AAO) by appropriate selection of the anodizing conditions. These capabilities may offer large degrees of freedom for the template based syntheses of low-dimensional functional nanostructures, and also in the development of AAO-based advanced devices, allowing simple and cost effective non-lithographic fabrication of extended arrays of structures well-defined and identical nanostructures. These porous AAO membranes can be used for the synthesis of various nanowires and nanotubes, as masks for extended arrays of structurally well-defined surface nano-patterns, and also as platform materials for magnetic storage devices, molecule separations, drug delivery, photonic, and energy storage and conversion devices. All of these applications could be achieved through deliberate control over the dimensions of pores and the thickness of AAO membranes, and also through the appropriate engineering of surface properties of porous AAO.

For the last two decades, researchers have invented several composite materials for the advancement in the field of magnetic device applications. Among them an attractive composition results from the combination of a ferromagnetic (FM) and antiferromagnetic (AFM) materials coupled with the exchange interaction at the interface between them. The exchange coupling at the FM/AFM interface may induce unidirectional anisotropy in the FM below the Neel temperature of the AFM, causing a shift in the hysteresis loop, a phenomenon known as exchange bias (EB). The exchange bias phenomenon is of tremendous utility in magnetic recording. One can do the detail study of the exchange bias effect in core/shell Ni/NiO and

Co/CoO nano-hetrostructures because there is a possibility of exchange bias effect on the interface of FM (Ni & Co) and AFM (NiO & CoO), which might help in magnetic device applications. Magnetic nanotubes are also highly attractive due to their structural attributes, such as the distinctive inner and outer surfaces, over conventional nanowires and nanoparticles. Inner voids can be used for capturing, and releasing various molecules and outer surfaces can be differentially functionalized with environment-friendly probe molecules to a specific target. By combining the attractive tubular structure with magnetic property, the magnetic nanotube can be an ideal candidate for the multifunctional nano-materials toward biomedical applications, such as targeting drug delivery with magnetic resonance imaging capability. In addition, the effect of alpha particle irradiation on various nanostructures can be further extend work, to investigate the change in the multi-physical (magnetic, optical, electronic, etc.) properties of nanostructures after irradiation process.

Transition metal oxides (such as NiO, $Co_3O_4$, $MnO_2$, $Fe_2O_3$, $TiO_2$, $V_2O_5$ etc.) based nano materials have broad application in energy storage and conversion application such as supercapacitors. The capacitive performance of these supercapacitors strongly depends on the type and the nano-morphology of the electrode materials, researchers have been very enthusiastic in developing some new, unique nanostructures to maximize their energy storing capacity per unit volume as much as possible and it remains a challenge for them to optimize those properties. One can further optimize the capacitive performance of these transition metal oxide based nanostructures by incorporating them with highly conductive and high surface area materials such as graphene, Ni foams, etc. Moreover, the study of materials for multipurpose use has always been interesting and significant research attempt have been made to develop such materials. So, the search for the materials that can be used in the energy storage devices will always remain to be an area of active research in the future as well to cope with the ever growing need of these materials in our everyday life.

# Appendix

## *Part of this thesis work cited in Media*

**Cited by AIP publishing**

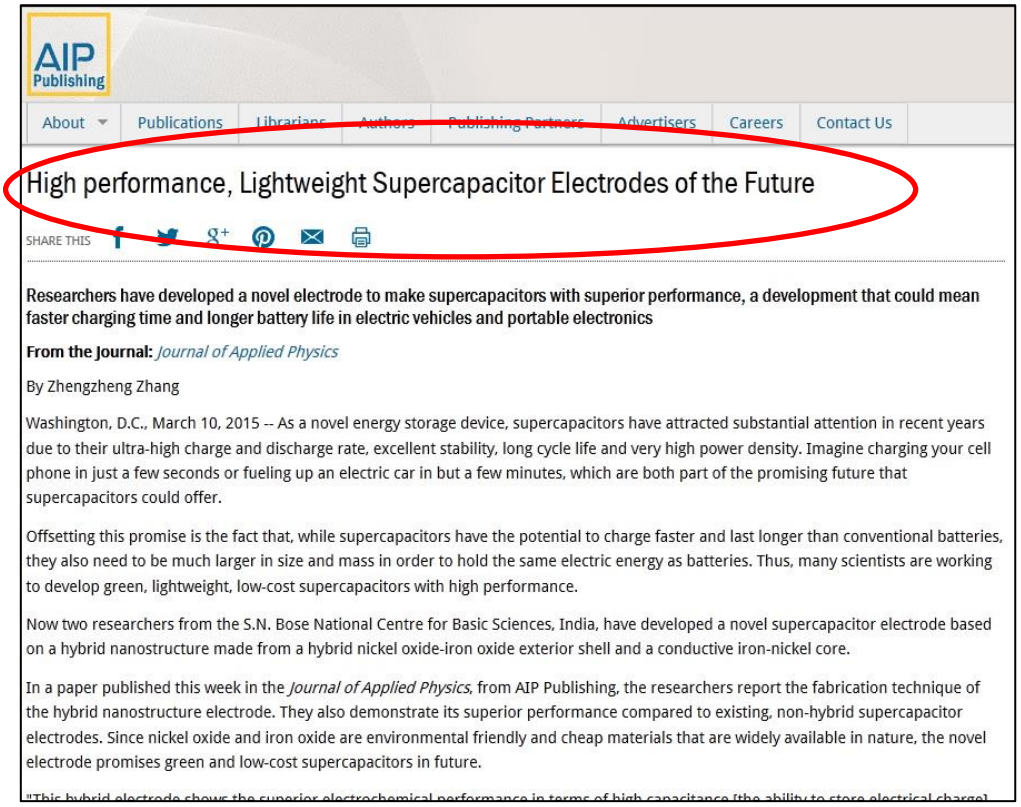

AIP Publishing

About | Publications | Librarians | Authors | Publishing Partners | Advertisers | Careers | Contact Us

### High performance, Lightweight Supercapacitor Electrodes of the Future

SHARE THIS

**Researchers have developed a novel electrode to make supercapacitors with superior performance, a development that could mean faster charging time and longer battery life in electric vehicles and portable electronics**

**From the Journal:** *Journal of Applied Physics*

By Zhengzheng Zhang

Washington, D.C., March 10, 2015 -- As a novel energy storage device, supercapacitors have attracted substantial attention in recent years due to their ultra-high charge and discharge rate, excellent stability, long cycle life and very high power density. Imagine charging your cell phone in just a few seconds or fueling up an electric car in but a few minutes, which are both part of the promising future that supercapacitors could offer.

Offsetting this promise is the fact that, while supercapacitors have the potential to charge faster and last longer than conventional batteries, they also need to be much larger in size and mass in order to hold the same electric energy as batteries. Thus, many scientists are working to develop green, lightweight, low-cost supercapacitors with high performance.

Now two researchers from the S.N. Bose National Centre for Basic Sciences, India, have developed a novel supercapacitor electrode based on a hybrid nanostructure made from a hybrid nickel oxide-iron oxide exterior shell and a conductive iron-nickel core.

In a paper published this week in the *Journal of Applied Physics*, from AIP Publishing, the researchers report the fabrication technique of the hybrid nanostructure electrode. They also demonstrate its superior performance compared to existing, non-hybrid supercapacitor electrodes. Since nickel oxide and iron oxide are environmental friendly and cheap materials that are widely available in nature, the novel electrode promises green and low-cost supercapacitors in future.

"This hybrid electrode shows the superior electrochemical performance in terms of high capacitance [the ability to store electrical charge]

**Cited by The Telegraph**

The Telegraph

Archives Select Date Search

March 23, 2015 | Monday

Go To: KnowHow

First Page 1 2 3 4 5 6 7 8 9 10 11 12 13 14 15 16 17 18 19 20 21 22 Last Page

IN TODAY'S PAPER

Front Page
Foreign
Nation
Bengal
Business
Today
Sport
Metro

PAGE THUMBNAILS

The Telegraph KnowHow 9

MONDAY 23 MARCH 2015

**CHARGED UP**

A device being developed in a Calcutta lab may make the lithium-ion battery redundant, says **T.V. Jayan**

YOUR HEALTH
DR GITA MATHAI

**When learning is a problem**

# *Part of this thesis work cited in Media*

**Cited by Science Daily**

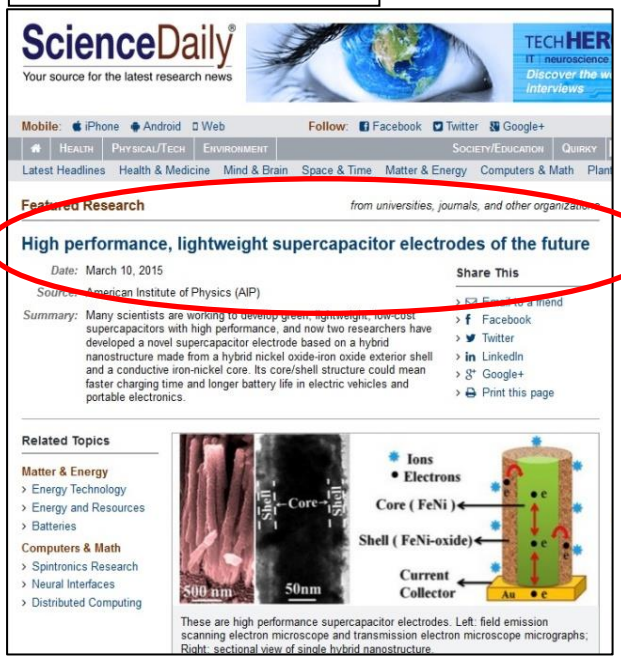


**Cited by Nature India**

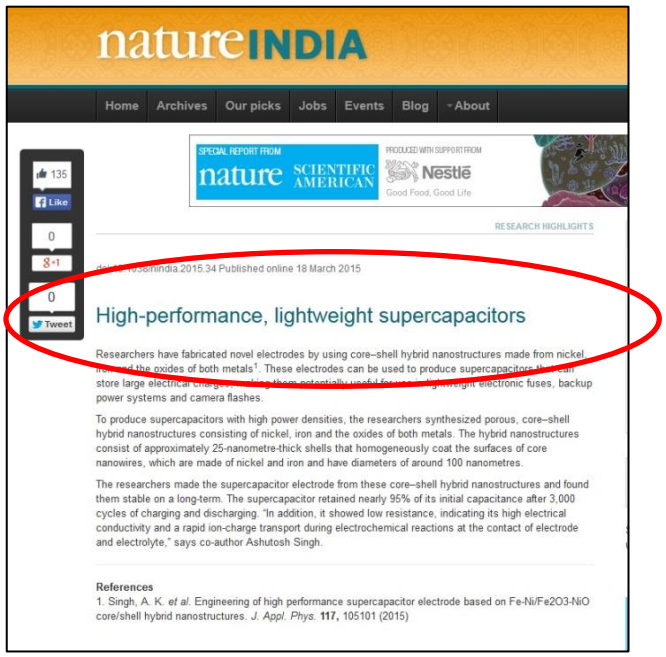


**Cited by The Telegraph**